UNIVERSITY OF OKLAHOMA

GRADUATE COLLEGE

Design and Utilization of Laser Physics to Collect, Model, and Analyze Lateral Drill String Vibration Data

A THESIS

SUBMITTED TO THE GRADUATE FACULTY

In partial fulfillment of the requirements for the

Degree of

MASTER OF SCIENCE

By

Cameron James Devers

Norman, Oklahoma

2019

Design and Utilization of Laser Physics to Collect, Model, and Analyze Lateral Drill String Vibration Data

A THESIS APPROVED BY

MEWBOURNE SCHOOL OF PETROLEUM AND GEOLOGICAL ENGINEERING

BY THE COMMITTEE CONSISTING OF

Chair, Dr. Catalin Teodoriu

Member, Dr. Ramadan Ahmed

Member, Dr. Deepak Devegowda

Dedication

To those who selflessly help others and expect nothing in return, you push the world forward.

Acknowledgements

First and foremost, I would like to thank PD Dr. Dr.-ing. Habil Catalin Teodoriu for his continued support these last two and a half years. Without him, this project, and my studies, never would have been finished. Additionally, I would like to thank Barrett Cross and Keyence for both their help in selecting tools necessary for the project completion but their continued outreach and aid. Also I would like to thank Dr. Carl R. Nave, founder of HyperPhysics, who helped tremendously in my understanding of vibrational systems and offered personal assistance in this work.

To Professor Fitzmorris from Electrical Engineering department, who kept my summers productive by sparking my interests in electronics and signal processing.

To Dr. Devegowda for continuously challenging me in my studies, in introducing me to many topics that spurred my interest in this work, and for serving on my committee

To Dr. Ahmed for first introducing me to the field of drilling, and for serving on my committee

To my mother Annette Devers for her continued love and support all these years

To my father Kevin Devers who has been a sturdy foundation in shaky times.

To all my friends and people who have made this process easier, through any and all means.

To all, my deepest appreciation and gratitude.

Cameron James Devers

Table of Contents

Table of Figures

Table of Tables

Abstract

This study focuses on measuring lateral drill string vibrations. First, the nature of drill string vibrations is discussed. Second, a review of previous experiments on drill string vibrations, both in the laboratory and field, is presented to highlight previous successes and potential improvements to be made in future research. The conclusion from the review of previous works is that historical methods of collecting data greatly restricted access to drill string vibration measurements, did not collect data at a high enough resolution, nor collected comprehensive data. This conclusion became the basis for the experimental design outlined in the document, with significant work performed to determine the best method of measuring and collecting drill string lateral vibration data. The method selected was incorporated into the drill string experimental model at multiple points along the drill string. A method of calibration was designed and incorporated to ensure the data collected from the model was accurate. An initial test was done to generate data needed to format a robust testing method. Results from the initial test indicated data needed to be primarily collected at high rotational speeds and sampled at 1 kHz for comprehensive data collection. Data was also down-sampled to 100 Hz and 10 Hz in order to study what information is lost at lower resolutions. Experiments were run at five rotary speeds at constant WOB with data sampled at 1 kHz, 100 Hz, and 10 Hz. Initial analysis of the tests verify large amounts of pattern-recognizable data is lost as sampling frequency decreases. Additionally, previous assumptions regarding the circular rotational patterns of the drill string when not constrained are brought into question as evidence suggests significant deformation of regular oscillatory patterns along the drill string during the onset of lateral vibrations. Lastly, Fast Fourier Transform (FFT) analysis concluded that there is substantial information aliased moving from 100 Hz to 10 Hz, with minor aliasing happening moving from 1 kHz to 100 Hz.

1. Introduction

In March 2016, the United States Energy Information Administration reported that "rig related costs can range from $0.9 MM to $1.3 MM making up 12% to 19% of a well's total cost" (E.I.A. 2016). That same report also lists drill times for many modern wells as taking over three weeks. If a problem were to occur during the drilling phase of the operation, there is a potential for significant fiscal setbacks as well as product delivery delay. In an effort to prevent that, substantial designing and planning goes into the drill plan, as well as careful monitoring of the drill process. Fundamentally, drilling can be controlled by two factors: weight-on-bit (WOB) and rotations-per-minute (RPM). These two factors are considered the primary driving parameters in the drilling rate-of-penetration (ROP), which is used as a metric for determining how fast the well is being drilled. These two factors are also the primary driving parameters in a series of commonly occurring drilling phenomena called drill string vibrations (DSVs). While not all occurrences of DSVs are detrimental, they can damage the bottom hole assembly, cause excessive wear, and create delays in the drilling process (Kapitaniak, et al. 2015, 324-337) (Younggang, et al. 2011) (Moradi and Ranjbar 2009). Therefore, it is important to understand how DSVs behave, and to predict and mitigate them.

1.1 What Are Drill String Vibrations

DSVs can be the result of the response of the drill string to several factors which include, but are not limited to: WOB, RPM, geology, drill string tools, drilling fluids, etc. These responses are commonly placed into three different modes: axial, torsional, and lateral (Sotomayor, Placido and Cunha 1997). The general behavior of these modes is illustrated in **Figure 1,** with each visual column labeled with both the vibrational mode and the most common drilling problem associated with that mode.

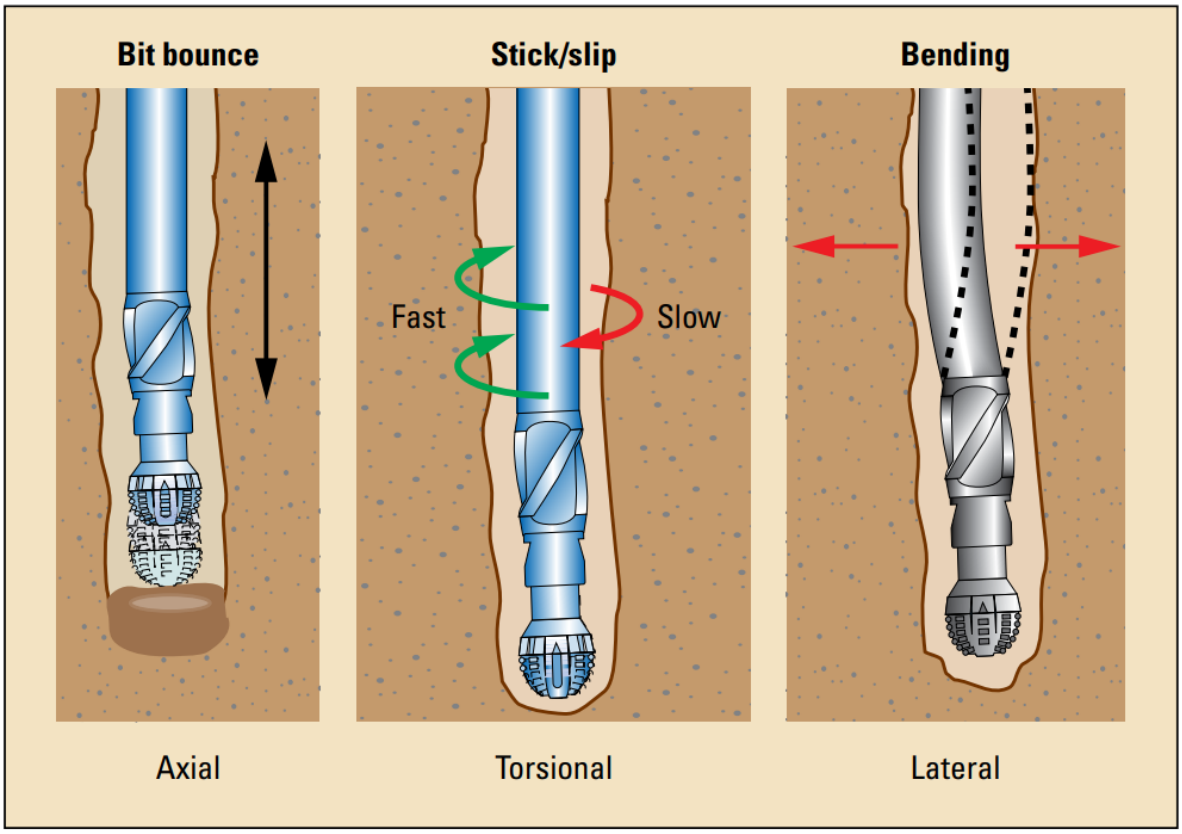

Figure 1. Vibration modes (Jardine, Malone, and Sheppard, 1994)

Further, axial vibrations result in the drill bit losing contact with the drilling surface at the bottom of the well and then dropping back down onto the surface. When this process becomes repetitive, it is known as bit bounce. Stick/slip, caused by torsional vibrations, can be described as a repetitive 'torsional pulse' in which the energy builds up, releases, and repeats resulting in inconsistent rotational speeds. The third mode, lateral vibration, can generate bending along the drill string. This onset of bending is also referred to as whirl, as it describes the motion of the drill sting and potentially the drill bit in the wellbore (Tucker and Wang 1999). Additionally, vibrations "may induce wellbore instabilities reducing the direction control and its overall shape" (Dunayevsky, Abbassian, and Judzis 1993). The primary focus of this paper is to assist in measuring and understanding lateral vibrations.

1.2 Why Study Drill String Vibrations

"Drilling vibrations are always present in drilling operations but they only become a problem when the oscillations in any axis (lateral, axial and/or torsional) come close to the natural frequencies of the system, thus reaching resonance" (Chacin 2017). To best predict DSVs, each mode must be monitored at the appropriate. Monitoring specific DSVs is problematic, and this is more clearly illustrated and presented by Esmaeili et al. (2012) shown as **Figure 2,** which is derived from field measurements presented in Macpherson et al. (1993). There is a large amount of overlap between the different vibrations occurring on a drilling rig, and many of the vibrations can be observed across several orders of magnitude. So, to study a particular type of vibrational behavior, a robust method with high resolution may be necessary.

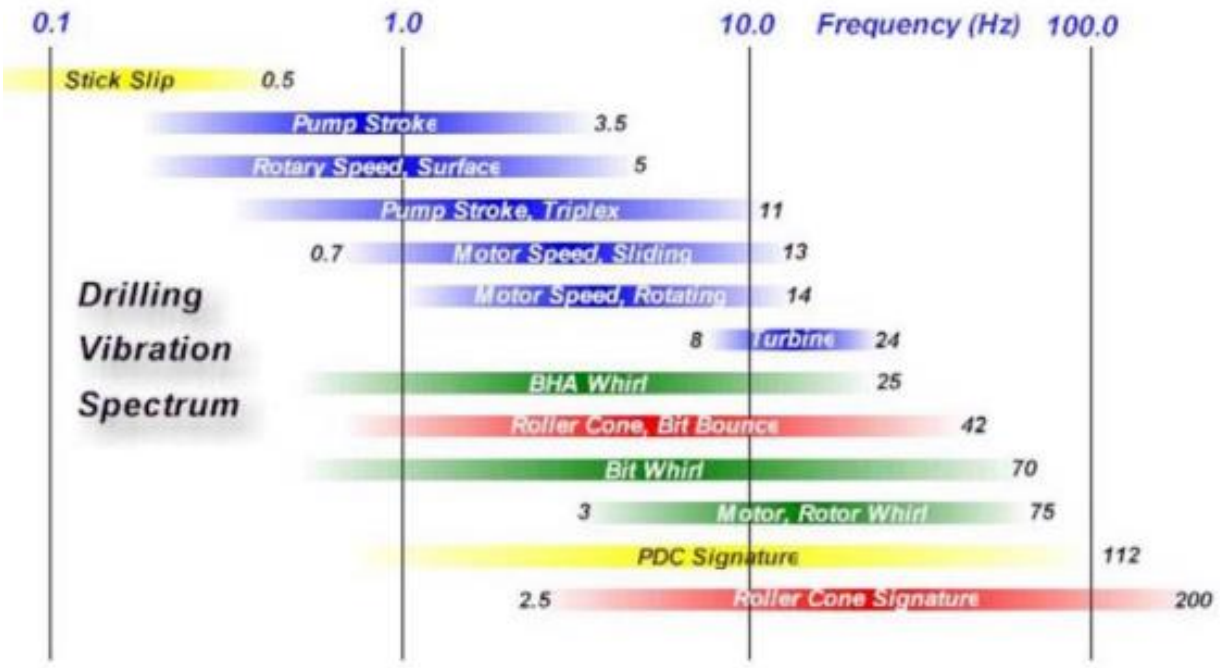

Figure 2. Ranges of frequencies at which vibrations may occur, (Esmaeili et al., 2012)

1.3 Drill String Vibrations as Waves

'Vibration' and 'Wave' are often used interchangeably in physics. This would suggest that DSVs can be viewed as waves. If so, principles relevant to waves and wave propagation could be most relevant to understanding DSVs.

1.3.1 Standing Waves

Wave propagation is a disturbance that travels through a medium. This disturbance induces oscillation, a regular back and forth motion, of the medium. If the medium is fixed in space perpendicularly to the direction of oscillation at two points along the string, the portion between the fixed points can be referred to as a special type of wave called a standing wave. In the context of DSVs, the drill string is the physical medium in which the disturbance propagates through. In a simple model, the drill string is a rotating pipe laterally fixed at two ends. The first fixed point can be considered to be either the drill bit or the drill collar, and for this experiment the drill collar is selected as the fixed point. The second fixed point is at the rig floor. This is considered fixed as the pipe is not allowed to move along the plane perpendicular to the axis of rotation. As there are two fixed points between which a system of oscillations occurs, the drill string may function as a standing wave.

While standing waves are normally associated with sound propagation, the concepts that define a sound wave can help to understand results from previous experimental works as well as frame new experimental designs. With the assumption that a drill string is a standing wave, there are two established equations that can be applied to the system (Ling, Sanny, and Moebs, 2017). **Equation 1** relates properties of the string to its fundamental frequency. **Equation 2** relates the frequency of the string to the wave velocity, harmonic number, and string length.

Eqn. 1 $$f_1 = \frac{\sqrt{\frac{T}{(\frac{m}{L})}}}{2L}$$

Eqn. 2 $$f = nv/2L$$

Where;

T = String tension (N)

m = string mass (kg)

L = string length (m)

v = Wave velocity (m/s)

n = harmonic number

f_1 = fundamental frequency (Hz)

f = frequency (Hz)

1.3.2 Damping

A dampening force prevents an oscillating system from returning to its previous or expected amplitude and inhibits a system's tendency to oscillate normally. In the realm of drilling, the most notable source of damping on the drill string is the drilling fluid in contact with the entire string. In order fully understand the importance of damping forces on the field data and the laboratory data, the behaviors of different types of damping need to be reviewed. Damping inherently alters the equilibrium state of the oscillating medium, so the magnitude of the damping force on the system is referred to as damping ratio (Kelly, 2012).

To understand what this means physically, Newton's Second Law is utilized, starting with **Equation 3 -** the basic form of the equation for equilibrium motion.

Eqn. 3 $$ma + cv + kx = 0$$

Acceleration is the second derivative of position with respect to time, and velocity is the first derivative with respect to time. This simplifies **Equation 3** into **Equation 4.**

Eqn. 4 $$m\frac{d^2x}{dt^2} + c\frac{dx}{dt} + kx = 0$$

This equation is in the form of a homogenous second order differential equation, and has a solution in **Equation 5,**

Eqn. 5 $$x = e^{\lambda t}$$

An equation for an auxiliary variable can be constructed in **Equation 6**

Eqn. 6 $$m\lambda^2 + c\lambda + k = 0$$

The damping coefficient is shown as **Equation 7**

Eqn. 7 $$\gamma = \frac{c}{2m}$$

Rearranging **Equation 6** into **Equation 8** results in the possible solutions for c and m

Eqn. 8 $$\lambda = \frac{-c \pm \sqrt{c^2 - 4mk}}{2m}$$

Solving **Equation 8** generates the following **Equations 9, 10 and 11:**

Eqn. 9 $c^2 - 4mk > 0$ **(Overdamped)**

Eqn. 10 $c^2 - 4mk = 0$ **(Critical Damping)**

Eqn. 11 $c^2 - 4mk < 0$ **(Underdamped)**

Where;

m, c, k = physical parameter constants
a = acceleration
v = velocity
x = position
γ = damping coefficient
λ = auxiliary variable

This series of equations result in the three solutions for the damped oscillator; each resulting in a unique physical behavior illustrated in **Figure 3**.

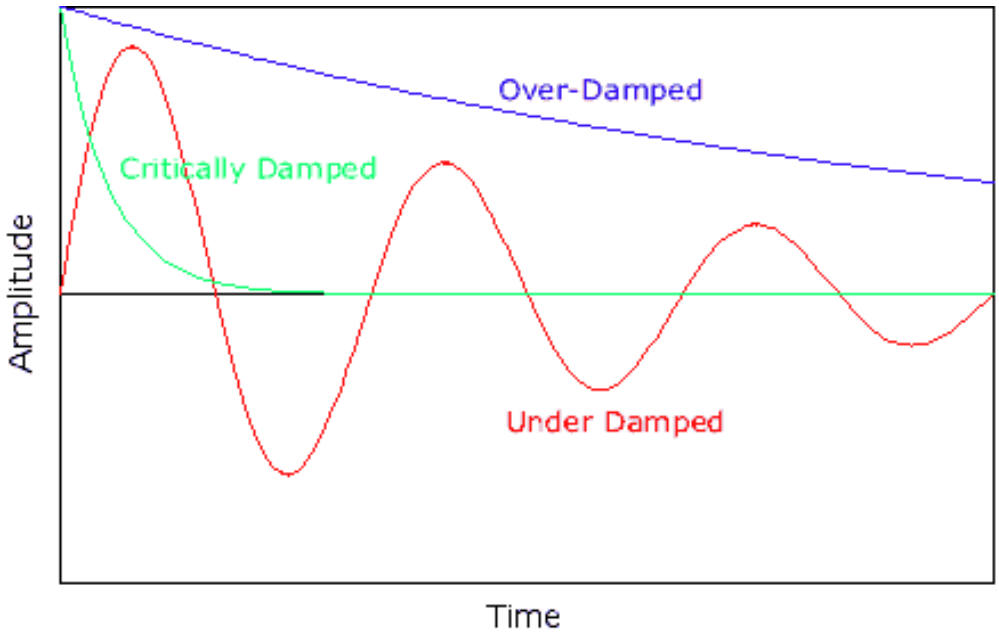

Figure 3. Simple graph depicting the three basic damping modes (Nave, 2017)

Thus far, the models have assumed the system experiences a one-time displacement force after which the oscillating body returns to equilibrium. Since drilling fluid is normally present along the drill string, the drilling fluid is constantly acting against the drill string. In this case, the driving oscillator would be the force of the drilling fluid on the drill string. Because of this, the boundary condition for solving Newton's Second Law is no longer set to zero, but instead equal to the driving force.

Since it is possible for the drilling fluid to either be circulating or still, the driving force is either sinusoidal or constant. A sinusoidal driving force is capable of being either resonant or non-resonant, which means the driving force can either increase the equilibrium amplitude or decrease the equilibrium amplitude. Constant applied forces typically diminish amplitude similarly to an under-dampened system, eventually resulting in either a greatly reduced equilibrium amplitude or termination of the oscillations entirely. Resolving this boundary condition often yields a two-part result, one part transient state and one part steady state. Examples of potential observations of this damping are provided in theoretical examples provided in **Figures 4** and **5.** The red waveform in **Figure 4** depicts a resonant sinusoidal excitation, which means that the force of driving oscillator is actually causing the maximum amplitude to increase, shown by the dotted red line. The green waveform is an example of non-resonant driving oscillator, where the waveform may behave non-normally and has a diminished amplitude, shown by the green dotted line. The red and purple waveforms in **Figure 5** are both theoretical waves experiencing two different constant damping forces, with the purple waveform subjected to the stronger of the two and therefore ceasing oscillation quicker.

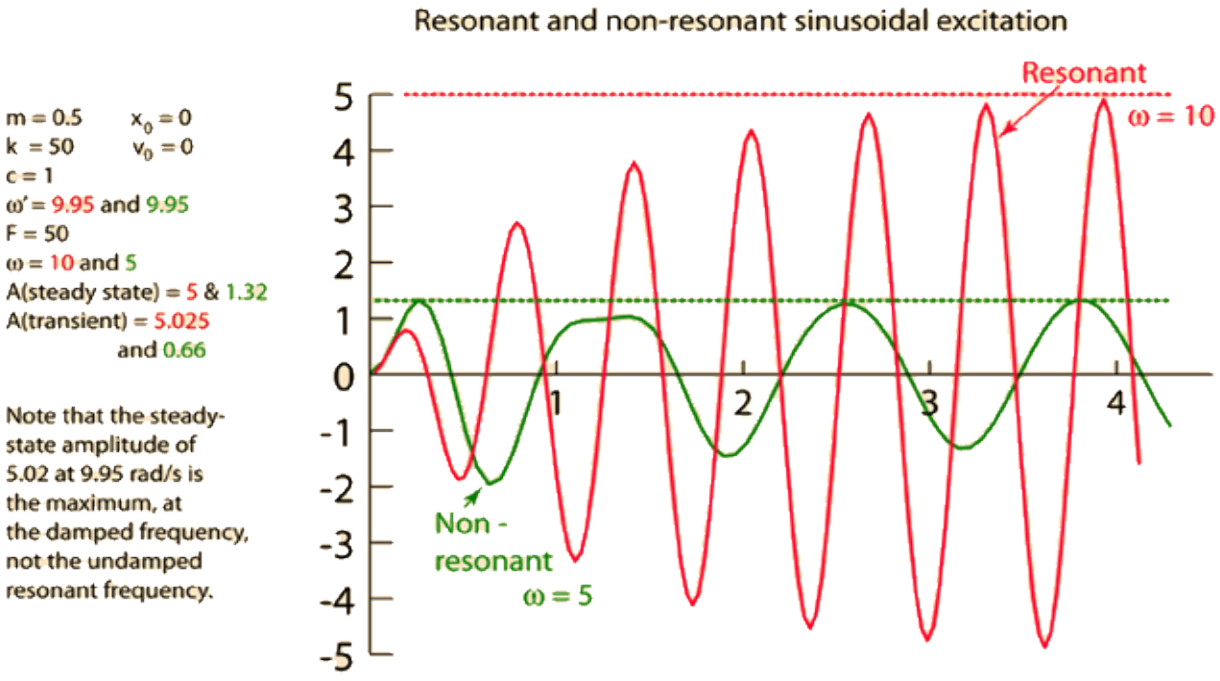

Figure 4. Illustration of impact of driving forced on sinusoidal oscillators (Nave, 2017)

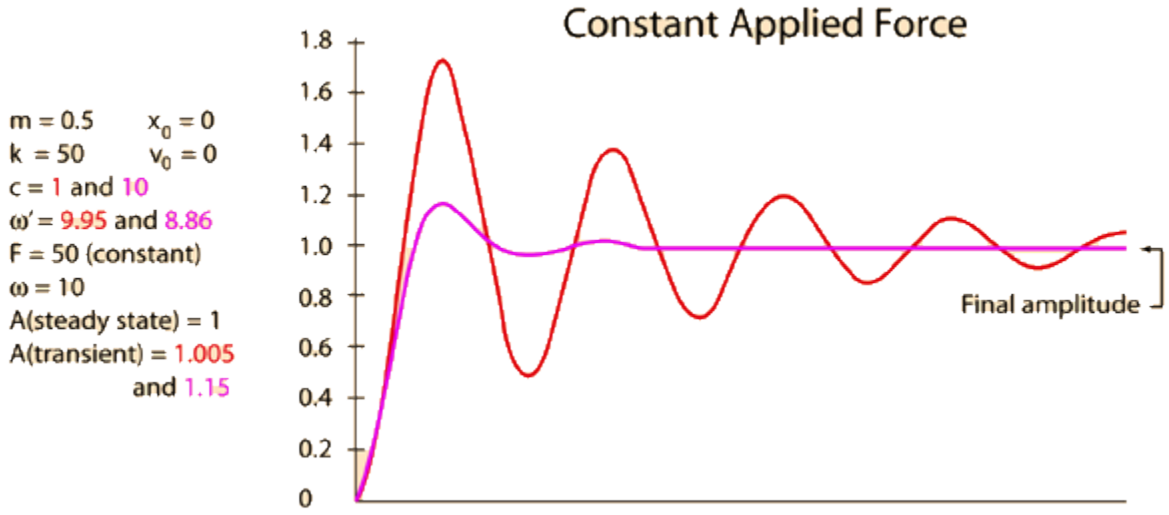

Figure 5. Illustration of the impact of relatively constant force on harmonic motion, courtesy (Nave, 2017)

2. Literature Review

Attempts to collect information regarding DSVs, both in the field and in laboratory environments, has been an ongoing endeavor since the 1960's. While earlier DSV experiments struggled to collect sufficient data to study axial vibrations, works today are collecting high resolution data of horizontal whirling (Deily et al., 1968; Lin et al., 2018).

2.1 Field Experiments

The Esso Production Research Company led many of the early field investigations into the behavior of DSVs in downhole conditions. These experiments were possible due to their "self-contained instrument for measuring and recording forces and motions at any point in the drill string under actual drilling conditions" (Deily et al., 1968). These devices had their data collection limited to "eight to nine minutes of recordings made on tape," where a "specific set of drilling conditions could be recorded for about 20 to 30 sec and then the recorder stopped" (Cunningham 1968). This suggests that in the early period of investigations into DSVs, prolonged data collection was simply not an option. Since data was being collected at live well sites and not a testing well, the test could not be replicated under the same conditions. This meant that every data set was unique and could not be cross checked by a data set collected at the same parameters. This results in potentially biased data. Not only could the tests not be replicated, but each test was difficult and cumbersome to execute. This idea is reinforced by **Figure 6**, as the sheer size of the tool required to obtain these measurements was a significant limitation to its usability. The tool had a nearly-uniform diameter of 6.75 inches at its largest section and weighed approximately 1250 lbs.

This added significantly to the tension on the string as well as completely preventing measurements from being collected in any small diameter wellbore operations. This, in turn, further limited the data set Esso was able to obtain in order to study DSVs.

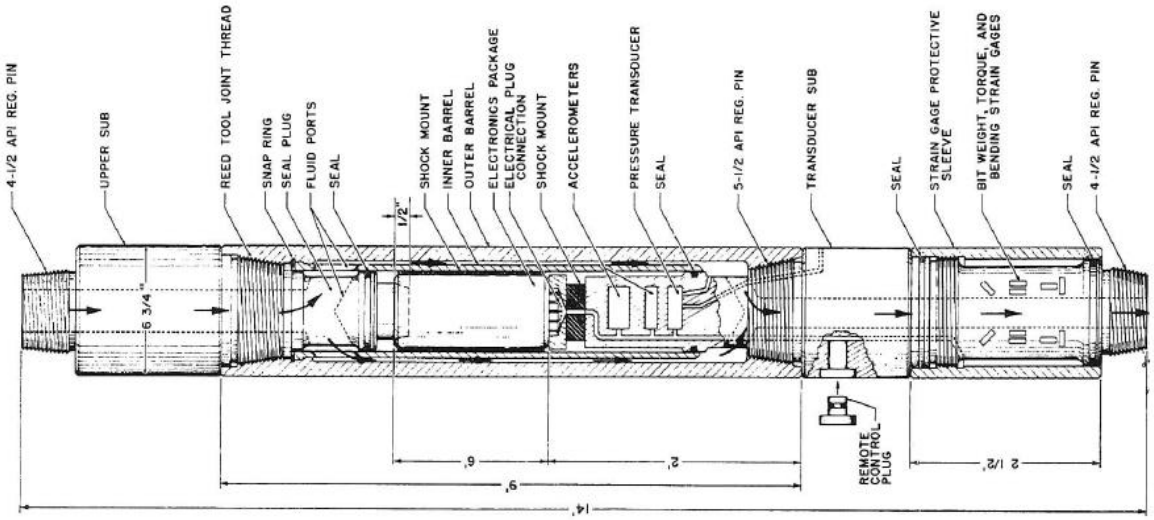

Figure 6. A 2D slice of the first mainstream tool used to measure downhole vibrational data (Deily et al., 1968)

Despite the technological limitations, it was still possible for a well to be sampled at a data collection frequency of approximately 10 Hz which is noted by the tick markings on the top axis of **Figure 7**, but the exact sampling rate is unclear and not specified in this early literature. This graph is one of the early pieces of evidence linking pressure variances in the drill pipe to the bit bounce phenomena associated with axial vibrations. The paper continues these investigations into bit bounce by observing bit weight with respect to other potentially relevant parameters. Though the results and conclusions focus primarily on axial vibrations, it marks the beginning of the industry putting importance on understanding the system of DSVs occurring during the drilling process.

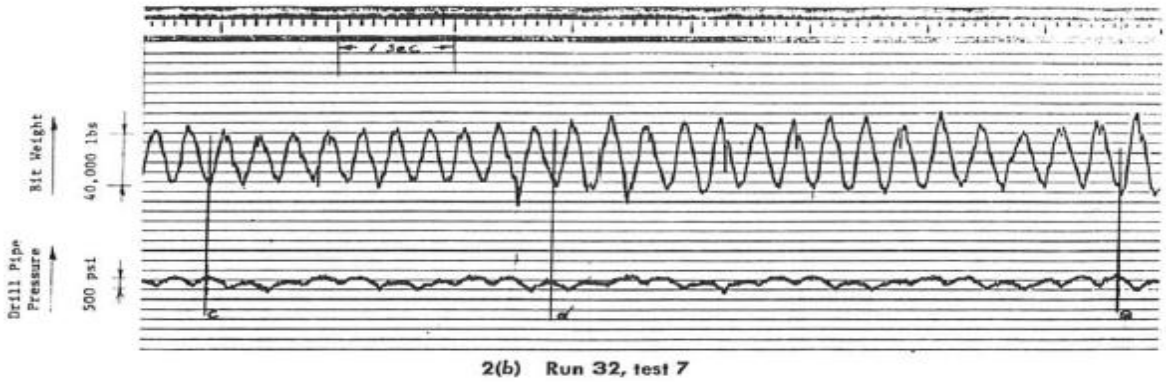

Figure 7. The Output graph for the tool designed by the Esso Company (Deily et al., 1968)

Improving data collection technology from bulky steel and strain gauges, the NL Industries company teamed up with the Shell Development Company to create the significantly sleeker and unobtrusive 'NL Wire Telemetry System'. The NL Wire Telemetry System was heavily tested in NL Industries research and development laboratories by drilling into cement-filled vertical wells to simulate formation penetration. This system was able to achieve a "maximum cumulative sampling rate of 650 samples/ second" (Wolf et al., 1985). The accumulation of testing and research lead to a joint operation with Shell Oil Company in which data was collected for 60 hours during the drilling operation of a straight, 8.75-inch hole in Quitman, Texas. This test was run approximately 20 years after Esso's initial investigations into downhole DSV under similar straight-hole conditions, but during the course of that time the data collection frequency had improved by roughly 6500% and the time of data collection improved by over 40,000%. Additional improvements in technology also include the operators' ability to "interrogate the downhole sensors through the data acquisition and control system" (Wolf et al., 1985). This technology generated more accurate data during the drilling process, allowing analysis to uncover any unexpected or unusual phenomenon.

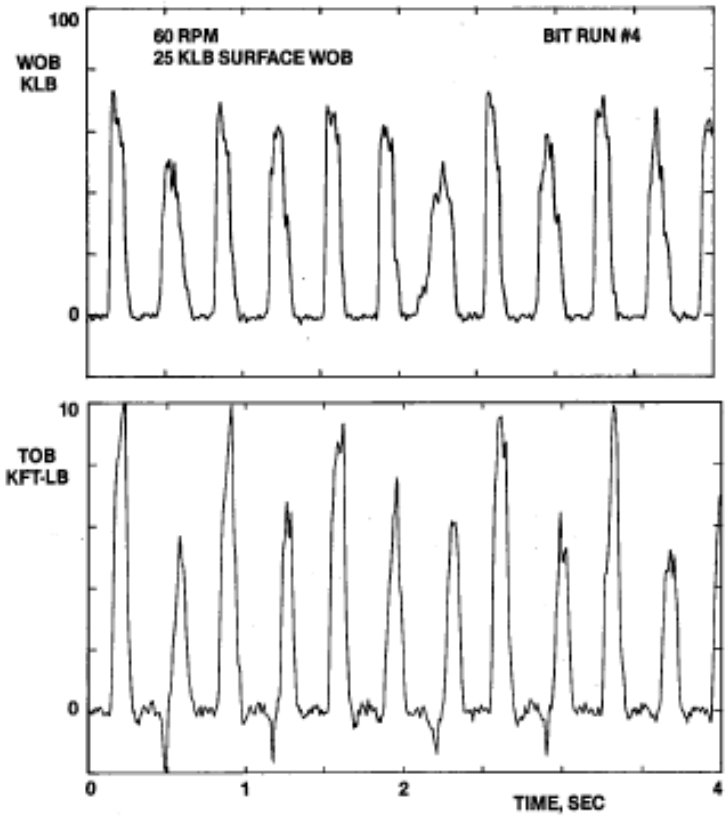

Figure 8. Graphs illustrating the increased resolution of the new NL and Shell tool (Wolf et al., 1985)

Figure 8 shows two different graphical representations of the data collected from the NL and Shell joint operation. The first of these two graphs is monitoring axial vibrations and the second is monitoring torsional vibrations. Comparing the first graph of **Figure** 8 to the results of Esso's 1968 results in **Figure 7**, the more modern results depict a more instantaneous change in WOB than the cyclic nature of the data Esso collected. This is likely due to the Esso tool collecting significantly less data per second compared to the wire telemetry system. Bit bounce as depicted by the NL tool is also more in line with what intuition would dictate, as bit bounce is the cyclic removal and subsequent impact of the drill bit to the bottom hole. This process is not a controlled process, as the movement of the drill string axially is not uniform during bit bounce. This is turn means that the change in WOB would be near instant.

2.2 Laboratory Experiments

Early laboratory experiments focused on simplifying the drill string down to the simplest model possible. This simplification resulted in the pendulum model, shown in **Figure 6**. This model was designed to study longitudinal and angular vibrations, not lateral vibrations. This parallels the field work done at the time, as the primary studies were investigating bit bounce. This model found success when comparing the results of the measured vibrations to those gathered from field models at the time (Darein and Livesay 1968). It is noted in the work, though, that the pendulum model does not account for friction, nor did it account for any damping forces that would have been present in field experiments. Despite this, the data was still reflective of field data, indicating that laboratory experiments could potentially simulate live well DSVs.

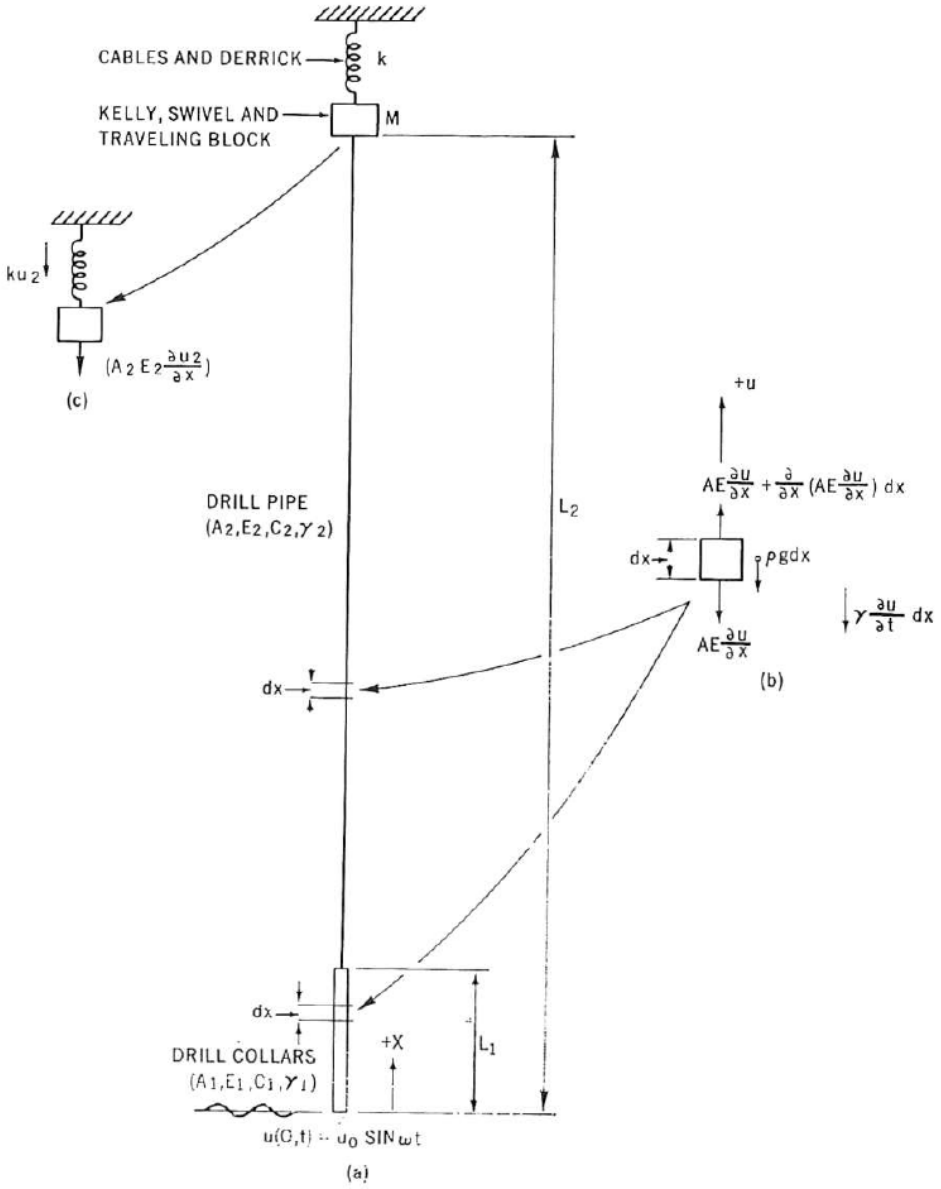

Figure 9. The general setup for the pendulum model experiments (Darein and Livesay, 1968)

As computational power improved, more complex and comprehensive models were developed for the purpose of better predicting dynamic drill string behaviors. An example of these newer models is shown in **Figure 9**, and is referred to as a "lumped mass torsion model" (Navarro-Lopez and Cortes, 2007; Shor, Pryor and Oort, 2014). This model breaks down the drill string into representational 'disks', with more added as the drill pipe is extended down hole.

Each of these ‘disks’ are treated as linear springs of torsional stiffness (Navarro-Lopez and Cortes 2007). While this method of modelling is vastly superior to the pendulum model, as the numbers of parameters are increased in the model the math becomes increasingly complex, eventually mandating simplifications be made to obtain a solution.

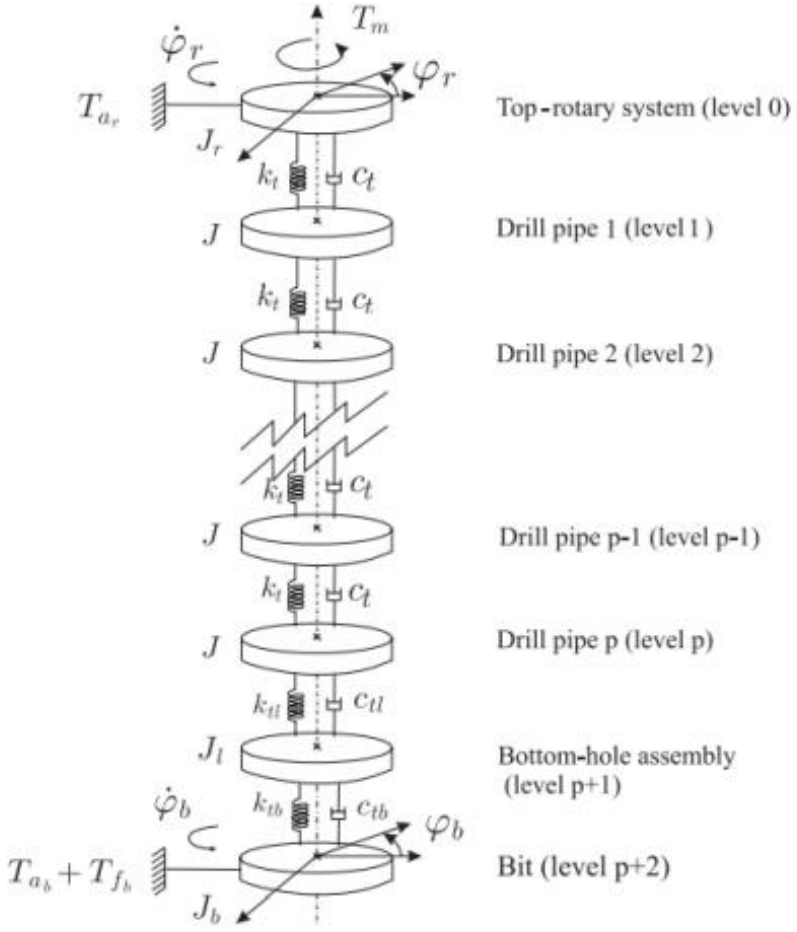

Figure 10. The breakdown of the lumped mass torsional model (Navarro-Lopez and Cortes 2007)

Moving away from complex analytic methods of predicting drill string behavior through use of sub-models, recent research emphasis has returned to physically modeling the drill string and recording data from the model. This has become possible due to rapid technological development and improved access to said technologies. As a recent result of this, more targeted experiments have begun to surface regarding lateral DSVs.

Constant improvement on laboratory based drill string models resulted in models robust enough to prove that managing WOB and RPM properly have direct effects on the mitigation and control of DSVs, a long held theory that had little comprehensive validation (Esmaeili et al., 2012). Work regarding complex physical modeling continued to develop to the point where it was possible to create a high-dimensional model of an experimental drilling rig using finite elements analysis (Kapitankiak et al., 2015). Then, in 2018, two different papers were published discussing precision measurement of lateral drill string vibration in a laboratory setting (Lin et al., 2018; Wen et al., 2018).

The first of the experiments utilized a completely horizontal model, with a fixed wellbore size and fixed measuring points along the drill string (Lin et al., 2018). This model, shown in **Figure 11,** used an electromagnetic motor for drill string rotation and additionally incorporated a force transfer device. The function of this device was to control 'pushing forces' on the drill string. Important observations from this experiment included noting that while the drill string was rotating the drill string "not only rotates around its own axis but also rotates around the wellbore axis" (Lin et al., 2018). This observation is recorded in the data, shown in **Figure 12,** by indicating that the acceleration of the drill string along the lateral axis (X axis) of the drill string in the experiment and of the vertical axis (Y axis) of the drill string in the experiment was mostly uniform but 'phased.' This makes sense as the expected rotation would be circular in nature.

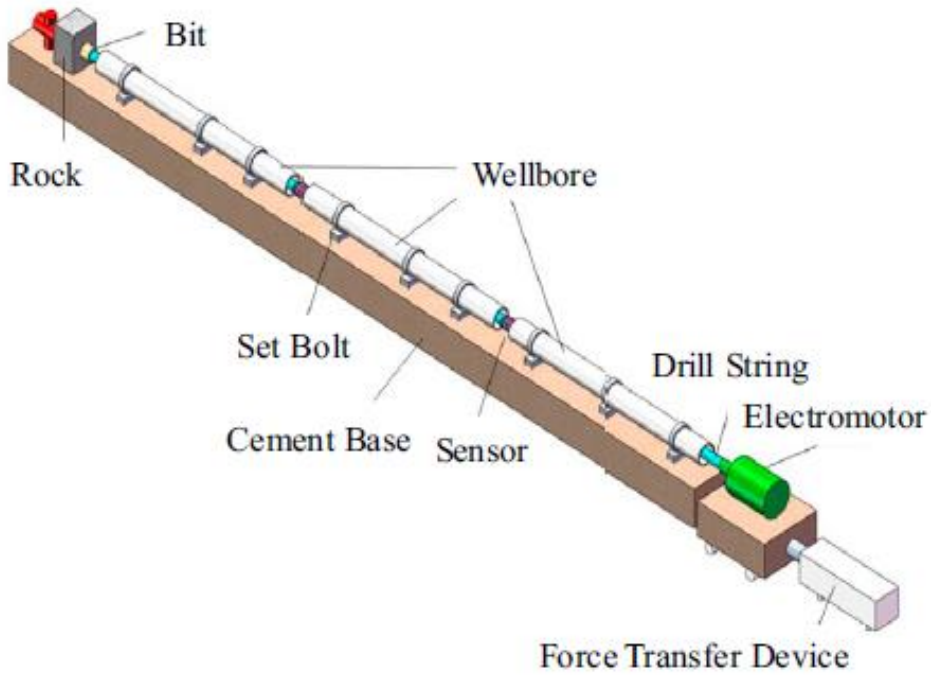

Figure 11. The design for horizontal lateral vibration testing (Lin et al., 2018)

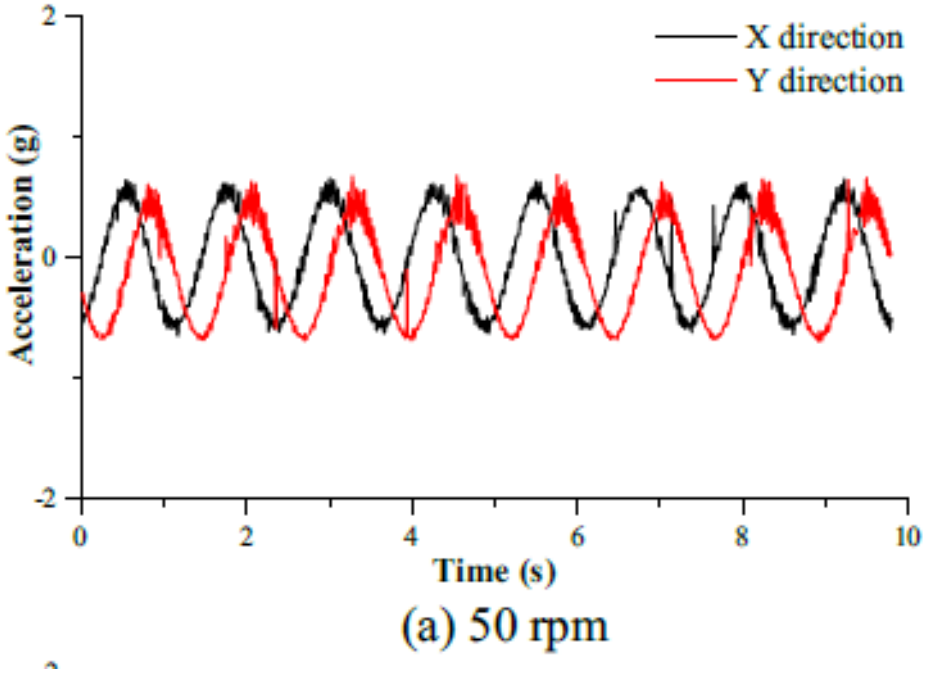

Figure 12. The breakdown of acceleration into X and Y components (Lin et al., 2018)

The second experiment captured data on a 'highly-deviated' wellbore model rather than a perfectly vertical one (Wen et al., 2018). Many of the experimental design features between the Wen experiment and the Lin one, but the Wen experiment was not locked in horizontal only experiments as it can adjust the deviation angle. Additionally, this experiment utilized 'Eddy Current sensors' to capture the lateral movement of the sensors. These are sensors which capture movement through the use of electromagnetic fields and are known to have high resolution (Nabavi and Nihtianov 2012). Due to this, there is a size and materials restriction on what drill strings can be measured without causing interference to the tool.

The results of this experiment lead to the conclusion that high WOB can inhibit lateral drill string vibrations, but as the rotary speed increases the WOB will have diminishing effects on the vibrational responses of the string (Wen et al., 2018). This, combined with the results of the other experiment, indicate that the original belief that RPM increases lateral vibrations while WOB inhibits it is seemingly valid. Additionally, it can be expected that as RPM goes up, there is a point at which the acceleration of the string will rapidly increase as well. This is reflected in the work done by Wolf et al. (1984) where as seen in **Figure 8** the bending moment jumped up rapidly. While both experiments expanded the knowledge base of lateral vibrations, the designs for the experiments limited testing parameters, highlighted in **Figure 11** by how the experiments have fixed wellbore dimensions, as well as fixed wellbore materials. Additionally, since both experiments incorporate bit responses from rock-bit interactions, the lateral vibration data produced also contain those interactions as a factor in the generated information, and is therefore not an isolated measure of WOB and RPM as control factors.

3. Experimental Design

Based on existing works, two things are clear. The first is that the method of data collection has been the limiting factor in experimental design, both in laboratory and in the field. The second is that physical drill string models are fully capable of being designed in such a way that they are a true representative model of a full-scale drilling rig. With these two facts in mind, as well as general wave theory, a series of design requirements were made for the purpose of studying lateral DSVs.

The experimental design:

1. Utilizes a drill string model that has a fully controllable WOB and RPM
2. Utilizes a drill string model which is representative of a full-scale drilling rig
3. Experiences minimal damping outside atmospheric conditions
4. Collects robust and comprehensive vibrational data in the lateral plane
5. Is not restricted by the method of data collection

As of the writing of this document, there is no available publication depicting an experiment that is capable of collecting high resolution data at any point along the drill string, nor collect data of any material or dimension of drill string. Because of this, there is not a current experimental set up capable of being completely modular or expandable. This is noteworthy because to be able to predict and prevent negative DSV occurrences, it is important to understand these vibrations as a complete system, as it is the "combined effect that is of practical importance" (Chin 2014). So, unless the tools used are capable of comprehensively measuring the system, there will always be missing information.

3.1 The Drill String Model

The data collected by any experiment is only as reliable as the methodology used to collect it. In the case of studying lateral DSVs, the data is only meaningful if it can directly correlated to full scale drilling operations. This makes it imperative that the drill string model used is a valid representation of a full-scale drill rig. This means, in theory, that the material used for the drill string model can relate to drill pipe, and that the methods of applying weight on bit and rotating the drill string are behaviorally the same as in the field. Because of this, this experiment utilizes a previously constructed drill string model that has been extensively studied and verified as an accurate model (Chachin 2017). This section will briefly discuss the components of the model and how it relates to the objectives of this work.

3.1.1 Top Drive

For the model drill string used in this experiment, the drill string is rotated in the same way a top drive would rotate a drill string. A Direct Current (DC) motor is fixed to the top of the drill string to simulate a top drive. A DC motor was selected for its ability to maintain constant voltage output resulting in the smooth transmission of torque throughout the drill string (Foster et al., 2010). Additionally, DC motors do not store torque while no power is supplied, ensuring zero residual energy is stored between experimental runs. Since the primary function of the model in this work is to be the source of the vibrations that are measured, it is important that the components employed do not contribute additionally to the operationally generated vibrations.

3.1.2 Drill String Material

A much more crucial element of the model downscaling to process is the selection of drill string material. This is critical because it is the drill string that vibrates, and therefore it is the drill pipe which will be most closely studied and compared to the full-scale vibrations. Unfortunately, this is also where most models must make concessions in the downscaling process. For example, unlike in the field where drill pipe is extended by connecting standpipes, there is no downscale method for making those connections. It is because of issues like this that it becomes important to understand the relationship between the drill string and DSVs, and "since the study of vibrations involves inertial behavior, the density and resulting linear mass of the selected string will become critical" (Srivastava and Teodoriu 2019). This work continued by deciding, for at least in the case of studying stick/slip, PVC material made for the best representative material of the drill string (Patil 2013). Additionally, is it known that PVC has "higher natural frequencies for the same mode of vibration" (Chachin 2017). That is not to say other options such as aluminum, steel, or structural steel polyethylene (PE) are poor candidates. In fact, the experimental setup is capable of using drill strings of all these material types, and each has well studied expected behaviors when used as such. PVC was selected among the four as it is both readily market available in the dimensions required to use as a drill string in the model, and projected to generate the least nodes per string length. A list of scaling factors relevant to the downscaling of the drill string was detailed by Westermann (2015), and is shown in **Table 1.**

Physical Parameter	Variable	Scaling
rev/min	n	$\phi_{n,\omega} = \phi_L^{-1}$
Angular velocities	ω	
Velocity	v	$\phi_{v,\grave{o},\sigma,p} = \phi_L^0 = 1$
Stress	$\grave{o}$	
Strain	σ	
Contact pressure	p	
Elastic deformation	Δl	$\phi_{\Delta l,c} = \phi_L^1$
Spring stiffness	c	
Forces	F	$\phi_{F,P} = \phi_L^2$
Power	P	
Weight	G	$\phi_{G,M,c,W} = \phi_L^3$
Torque	M_T	
Torsional stiffness	c_T	
Resisting torque	W_b, W_t	
Area moment of inertia	I_b, I_t	$\phi_1 = \phi_L^4$
Mass moment of inertia	J_b, J_t	$\phi_1 = \phi_L^5$

Table 1. List downscaling requirements for a model drill string (Westermann 2015)

In a perfect world, this table could be used as the go-to guide for downscaling field equipment into the laboratory setting. However, in the realm of drilling, this falls far beyond realism. Consider again the Quitman test well mentioned earlier. While that paper does not explicitly state its total depth; the paper does state the well was drilled into the Woodbine Sand. While the depth of this sand varies greatly due to updip, it is safe for this example to assume the well is drilled to at least 2000ft. If it was desired to model that well to verify data in the same space as this experiment has, the slenderness ratio would have to be maintained for both the length and the diameter. Since the 'five floor' model is the largest model Chachin proposed for construction, which would translate to roughly a 50 foot maximum model length, the resulting slenderness ratio would be 50:2000, or 1:40 (Chachin, 2017; Wolf et al., 1985).

That would mean whatever drill string material was used for the model would have to have a diameter $1/40^{th}$ of 8-¾ inch: that calculates out to just over a fifth of an inch, or just over 5.556mm. This, however, is a very generous ratio especially given the depths drilled to in modern times. Many wells drill to depths five times that great, and many labs don't have five times that space. So a modern well model might have a slenderness ratio of something close to 10:10000, resulting in a requisite diameter over just over a fifth a millimeter, which is not practical. This results in a classic problem regarding downscaling, and in this case the solution is to adapt the model to account for as many parameters as is practical. Therefore, the parameters selected were length, diameter, torque at surface, modulus of elasticity, and rotation stiffness. It is also noted that although certain slenderness ratios aren't strictly adhered to, the model is not invalidated, rather only applies to a portion of the full-scale drill string (Srivastava and Teodoriu 2019).

3.2 Data Collection

It is important to briefly discuss the complex world of signal processing, because, fundamentally, that is the object of this experiment. That means that in order to properly sample the signal in question, a few concepts need to be reviewed. The first of these concepts is time; precisely, discrete time versus continuous time. Discrete time can be thought of as a step function: it doesn't matter what the interval between the independent variable is, because the dependent value will change instantaneously when the independent variable achieves the next threshold. Continuous time, though, assumes that an event only occurs at its instantaneous point in time, much like a point on a parabola or slopped line.

In the context of this experiment, the position of the drill string along a plane is a continuous-time function, however; data cannot be collected 'infinitely' as continuous time behaves. That brings up the topic of sampling, which is defined as the process of regularly collecting values at a set interval of any given signal.

3.2.1 Data Signal

In the modern age, data is most often transmitted data from the tool or device reading the signal through a Data Acquisition (System) Card, or DAQ card. These cards are capable of collecting data from either digital or analog signals. Digital signals are signals which represent data as a sequence of discrete values (Dueck 2005). Analog signals are signals representing data continuously, and are therefore have an infinite range of values. This in turn makes analog more cumbersome to work with, but allows for user-designed sampling rates and filters to be applied to the generated signal. A major objective of this work is to investigate what sufficient data collection is, making controlling the sampling rate is important and therefore analog the preferred signal type to work with.

3.2.2 Sampling and Aliasing

With it established the data signal desired is analog and that sampling rates will be manually selected, it becomes important to discuss what happens when the signal is poorly sampled. This primarily refers to the problem of aliasing, a phenomenon that causes misidentification of signals due to improper sampling. Highlighted in **Figure 13**, the red line represents a potential alias of the actual wave.

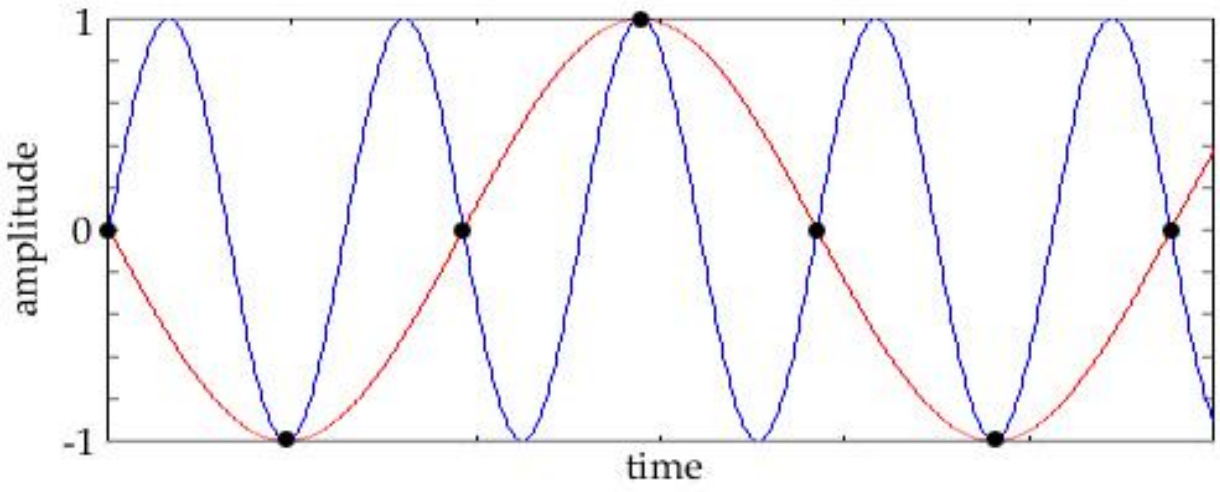

Figure 13. A simple illustration depicting the simplest form of information aliasing, (Burk et al., 2011)

This wave would be created due to a failure to sample enough data points per second, also known as failing to sample at a high enough frequency. The mathematics surrounding this phenomenon is quite complex, however; thanks to the endeavors of Claude E. Shannon in 1949 in 'Communication in the Presence of Noise', a proof was developed that eventually lead to the establishment of the Nyquist-Shannon Sampling Theorem. This theorem established the condition of when sufficient sampling occurs. While the explicit proof is more complex, and less general, it can be assumed the basic principle of the proof applies to this research model, as the ideal behavior of the model can be expressed as simple sinusoids. Additionally, without much laboratory precedent to work from, this theorem functions as a strong starting condition. This condition can be satisfied by meeting the Nyquist Criterion; which states that the sampling frequency must be twice the bandwidth of the signal being sampled. Since the drill string model is being approached as a single signal, the sampling rate needs to be twice the frequency of the lateral oscillations. It needs to be stressed that this body of work is investigatory in nature, and it is not known if these assumptions are valid. However, in the completely ideal case where the conditions and assumptions previously stated are true, the assumptions would be valid.

3.2.3 Laser Measurement

With it made clear that there exists the potential for large amounts of information to be generated, the tool which collects the DSV data must be equally capable of high-frequency data collection. Further, the tool cannot make contact with the drill string. The measurement method pursued in this work is derived technology first developed practically by Theodore H. Maiman in 1960. 'Light Amplification by Stimulated Emission of Radiation', or lasers, are tools which transmit waves, traditionally infrared (Maiman 1960). These waves contribute zero damping to the drill string, and transmit data at a minimum of 30 GHz; a frequency well above what a physical model can achieve.

3.2.4 Laser Doppler Vibrometers

Initially, Laser Doppler Vibrometers (LDVs), scientific instruments used to make non-contact vibrational measurements of a surface, was investigated as the method of colleting DSV data. Best explained with the aid of the diagram in **Figure 14** diagram, LDVs begin with the propagation of laser beam, or light wave, from the source.

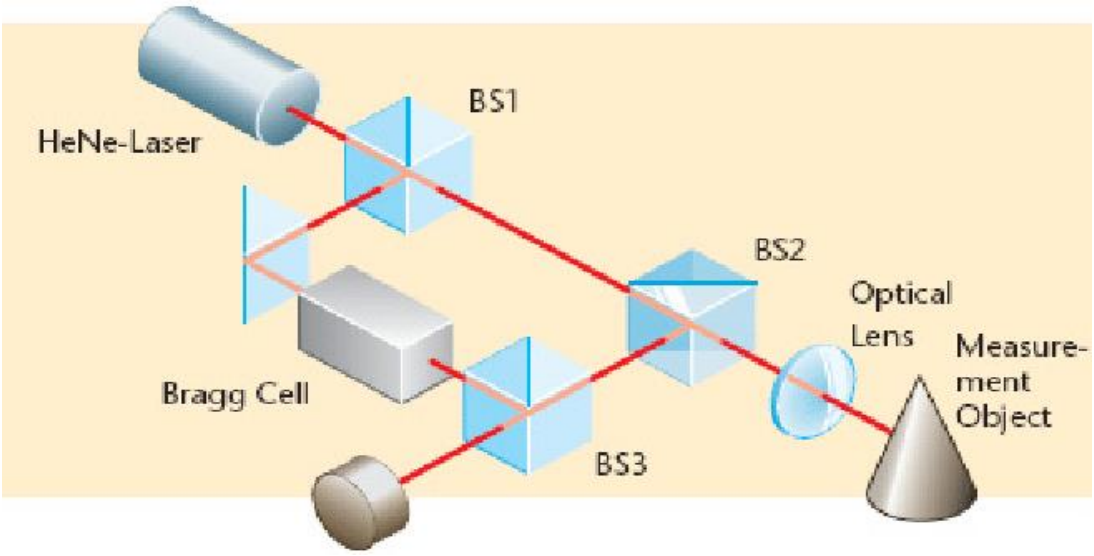

Figure 14. Simple design for an LDV, showing individual components (Qu et al., 2010)

That laser is aimed at a beam splitter, which allows that same wave to propagate through it and reflect at a 90-degree angle away from it. The wave which was split from the original is then reflected off a mirror and is passed through a Bragg Cell. Without discussing the complexity of the Bragg Cell, it is a device, usually made of quartz, which shifts the frequency of the light wave using sound waves. This shift adds a known frequency to the propagating wave in addition with the initial wave. While this occurs, the initial, unmodified wave makes contact with the object that is desired to be measured and reflected back. This back reflection of unknown frequency is then passed through a lens, then the beam splitters to reach the photodiode where the two waves interfere with each other.

By causing this interference, information can be extracted as there is enough known information present in the wave to remove it from the information collected by the photodiode. The information that is left is the information of interest concerning the object that was intended to be measured. This solution, objectively, has a lot of positives as a solution. The tool is well studied, with a large number of scholastic and industry uses across a plethora of industries making information on different design options readily available. Additionally, the tool is easy to build. However, the cost of these parts are significant, and this very fundamental setup is only designed to measure movement along one line across one plane; so some parts would need to be purchased in higher quantities than illustrated in order to capture a more complete dataset. A rough breakdown of the construction cost is found in **Table 2**.

Quantity	Object	Provider	Cost/Item	Total
1	Laser – 405 nm	THORLABS	656.84	656.84
3	Beam Splitter - Economy	THORLABS	34.91	104.73
1	Bragg Cell	THORLABS	2678.25	2678.25
1	Mirror – UV Enhanced	THORLABS	101.65	101.65
1	Photodiode – Si 405 nm	THORLABS	53.05	53.05
1	Lens – Bi-Convex no Coat	THORLABS	24.13	24.13
Total				3,618. 65 USD

Table 2. A breakdown of the construction cost for a simple LDV

While a cost of just over 3600 USD is not bank-breaking, there is a large aspect of inexperience and design challenge to be addressed. As mentioned before, this design is meant to measure movement along a single line, and the model drill string will be moving in both the X and Y planes. This means both the 'Object' and 'Reference' lasers would have to be split and redirected to interact with the object perpendicularly and would require a second photodiode to pick up the resultant interference wave. Additionally, the tool would have to be carefully calibrated and moved each time there was a need or desire to measure the string at a different height. Because of the constant movement of delicate and difficult to calibrate parts, renders this a non-ideal laboratory tool. Additionally, another deficiency of this design is that it relies on the point laser easily being able to make contact with and reflect off the object in motion.

The model drill string in question can reach diameters as small as one millimeter. Since this may be incredibly difficult to align, it could be viewed as a limitation on drill string parameters and therefore fails to align with the experimental objectives. Furthermore, that target could be moving around in a space over an order of magnitude greater than its own size, so it is not likely the laser will be able to constantly or consistently measure the vibrations. All of this, of course, falls on top of the technical inexperience of constructing the device. This all cumulates into a simple verdict: good in theory, poor in practice. With this information, a more user-friendly solution was sought out.

3.2.5 The Keyence Solution

After surveying the market for laser-based solutions for measuring complex planer movement, one company stood out as the primary provider of a plethora of options, the Keyence Company. Keyence refers to themselves "As a leading supplier of sensors, measuring systems, laser markers, microscopes, and machine vision systems worldwide." Focused mainly in the world of automation, their large catalogue of tools doesn't limit themselves to providing solely to any one particular industry. After looking into some of their products and meeting with some of their trained representatives, an investigation into the possibility of if using their High-speed, High-accuracy Digital Micrometer LS-7030 would meet the experimental requirements; the exact specification of which can be found under Appendix A as **Figure A-1**. The 7000 series of digital micrometers Keyence produces functions in a similar method to a LDV. While the exact method the device utilizes is proprietary to the company, the general idea can be explained with the aid of **Figure 15**. The exact physics and principles that are present in the device are beyond the scope of this work; however, the device was demonstrated before more advanced testing occurred.

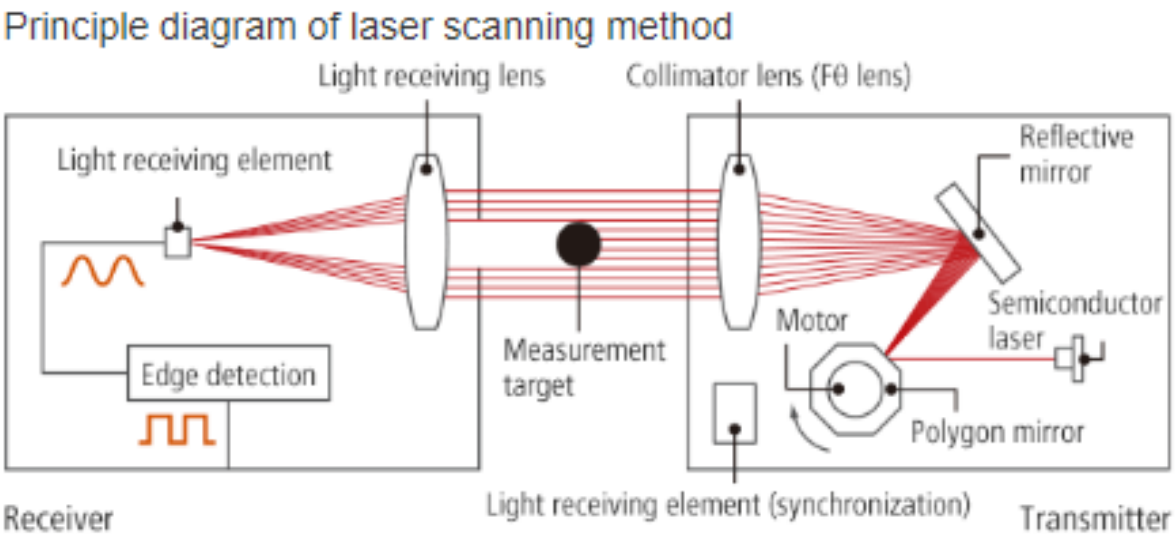

Figure 15. A diagram depicting the fundamental operating procedure of the Keyence equipment, courtesy Keyence

The ‘measurement target’ is placed within the ‘laser bridge’ that is formed by the array of parallel lasers. This object then obscures some portion of that bridge from passing through the receiving lens to the receiver. This obstruction in information is what is then translated into position. That position is the position parallel to the lenses and perpendicular to the propagation of the lasers. This means that the lasers running across the ‘vertical’ position are measuring position in the ‘horizontal’ axis and to capture movement along and X-Y plane; two sets of these lasers are needed. The two laser bridges would be placed offset by the smallest distance possible without overlapping to prevent interference while also keeping the measurements as true to ‘planar’ as possible. From a top down prospective, it would look as **Figure 16** depicts.

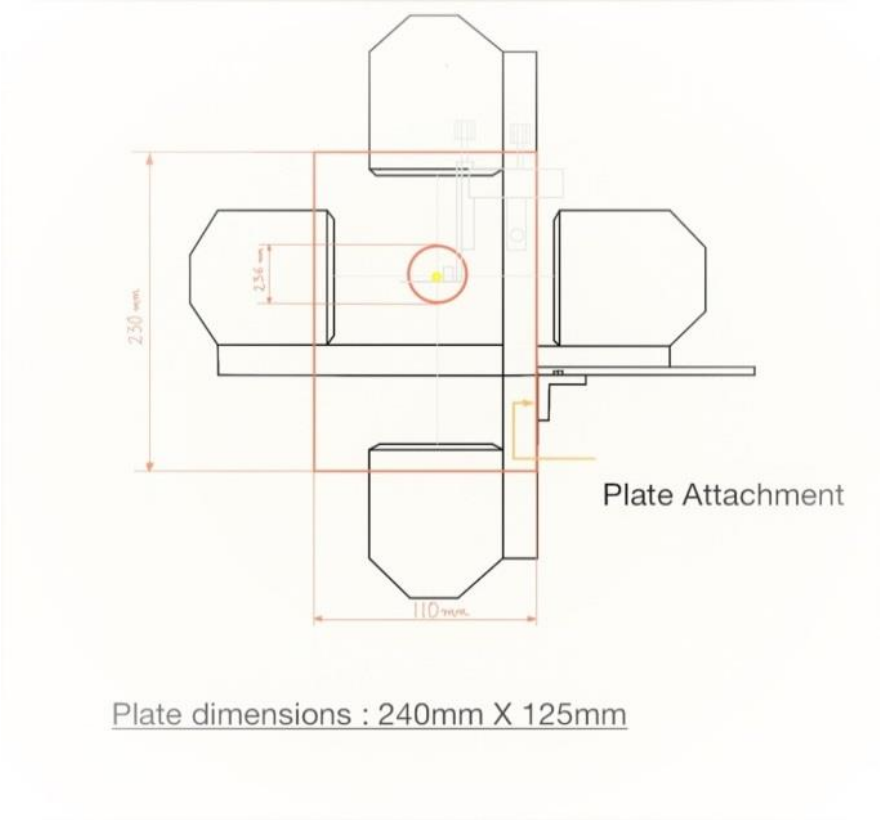

Figure 16. The Schematic for setting up the measurement lasers

This design comfortably allows the for the potential use of the entire almost 30mm of direction allowance of both laser bridges; just under 15mm from center in all directions. This means that if a 2mm diameter drill string model is used, the string would have to oscillate over seven times its own diameter before the laser would no longer be able to measure the behavior. This allowance was determined to be completely acceptable, as oscillations of that magnitude are incredibly violent and very unlikely to occur. Additionally, the string will eventually be confined within a model wellbore, which will not have such allowance for motion, making the point moot. After carefully studying the capabilities of the LS-7030, and negotiating its price, it was selected as the optimal method of collecting the positional data of the model drill string. From here, a position to mount the laser along the drill string, as well as the mount itself, had to be addressed; as well as how to transmit, collect, store, and process the data measured by the LS-7030. This makes the next limiting factor the method of transmitting the data from the device to a computer.

National Instruments tells us that “data acquisition (DAQ) is the process of measuring an electrical or physical phenomenon such as voltage, current, temperature, pressure, or sound with a computer,” and that “DAQ hardware acts as the interface between a computer and signals from the outside world. It primarily functions as a device that digitizes incoming analog signals so that a computer can interpret them.” To select an appropriate DAQ card, a few parameters have to be addressed, some of which relate to the measurement device and others to the software one wishes to utilize to process the data. The LS-7030 data sheet states that the sampling cycle of the device is 2400 samples/second; meaning the DAQ card used should, at least, be able to transmit data at a rate of 1200 Hz to avoid data loss. However, in this case, it was deemed necessary to ensure all data was captured for data processing purposes and the minimum parameter for the DAQ card was set to 2400 Hz. The next important parameter on a DAQ card is how many channels, or how many different measurements are being transmitted. The LS-7030 transmits the measured position in analogue as a function of volts. Each position along the plane requires a voltage relative to the x direction and the y direction of the plane. That means, for every plane measured, 2 slots on the DAQ card are needed that can sample at a rate of at least 2400 Hz. Allowing for experimental expansion, for example, acquisition of additional lasers, and for the incorporation of additional measurement devices, it was decided that a minimum of eight channels would be needed.

Finally, the LS-7030 has a maximum voltage transmission of 10 volts. Therefore, the DAQ card used must be able to accept voltages within that range. The USB-1608G Series by Measurement Computing offers a 16 analog, 8 digital channel input card easily capable of sampling data, clocking in at a maximum sampling rate of 500kS/s, or 500,000Hz. The DAQ cards' computer software drivers are well integrated into both LabVIEW and DASYLab, two popular programs used for the controlling of digital measurement and the collection of data from the tools. The DAQ is easily connected to the computer by use of USB connections, and is tethered to the LS-7030 by standard electrical wiring. This is important because the long term goals of the drill string model will result in potentially having to run cable for dozens of feet, so it is important that the cabling used it not overly complex or expensive to run in long lengths. More details regarding the selected DAQ card can be found on **Figure A-2**.

3.3 Integrating the Keyence Laser Sensors

With the confidence in the tools of established, the next step was to install the data measurement and collection equipment. Since these were preliminary investigations into measuring the drill string, the full experimental setup was not utilized at this point. This means is that the maximum possible length of the drill string was not used, but only 30 ft. This resulted in the position of the bottom of the drill string being close to the target computer and therefore made access to the bottom laser easy. This was critical as the bottom laser was the first laser installed and is where all the critical calibrations occur. It also made the wiring process easier for both power and data transmission, and in the connection of the second laser, which was added at a later point. The resultant design is simplistically illustrated in **Figure 17**.

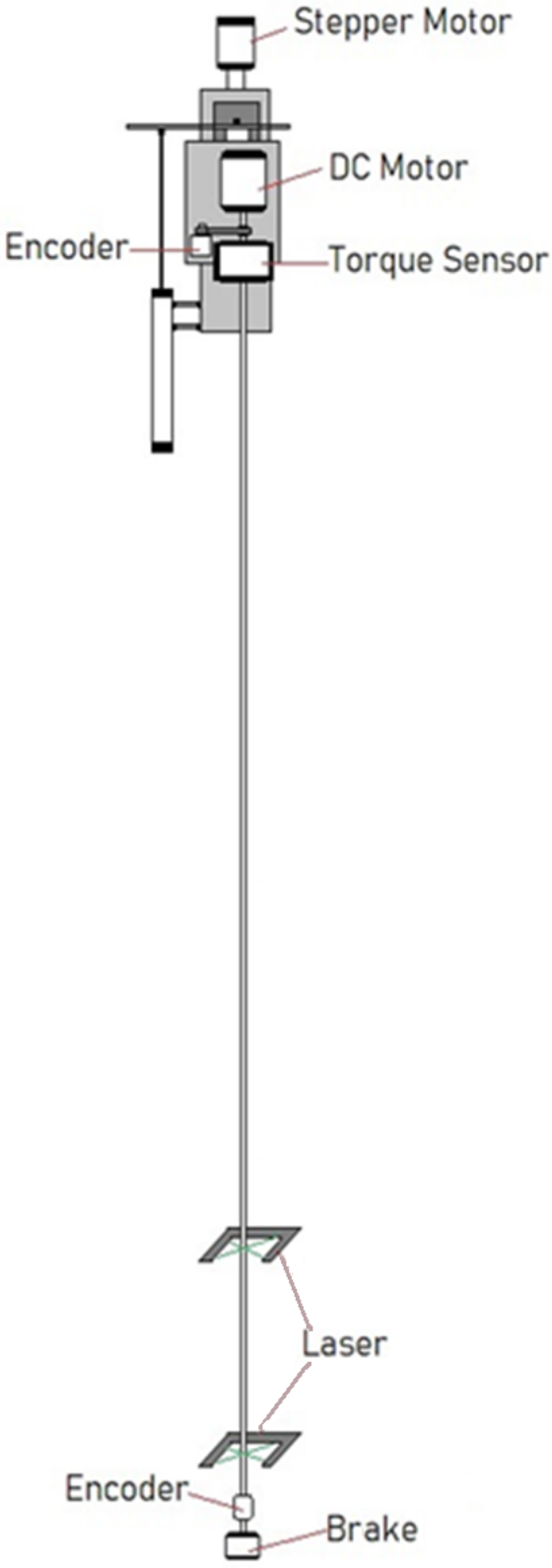

Figure 17. General illustration for the large-scale experimental set-up

While the schematic does not have dimensions, it is roughly to scale, with the LS-7030 lasers located roughly 0.1 foot and 6.5 feet above the encoder along a 30ft drill string. The intent of the diagram illustrates primarily that the drill string is tethered at the top and at the bottom, emphasizing the previously discussions regarding wave nodes. At this point in the experiment, the intent of the lasers was not to capture the 'node' and 'anti-node' behavior but a 'point of order' and a 'point of disorder'. What is meant by this, simplistically, is that the goal was to compare what the string looked like close to a fixed point and some distance away from that fixed point that likely was not a node. To achieve this, the second laser was placed 6.5 feet above the first, which was placed six inches above the fixed point. For a node to possibly occur at that point of 6.5 feet, the wave would have to achieve its 5^{th} harmonic. This was considered highly unlikely to occur. It is believed that in most cases it is far more likely that distance is closer to an antinode, as it is approximately $1/4^{th}$ up the string, which is the location for an antinode when three nodes are present. These considerations were incredibly important in initial data collection because collecting data exactly at the node, in perfect conditions, would generate zero lateral displacement. Since the intent of this investigation was primarily to capture the phenomenon of lateral vibration, it would be counterproductive.

3.4 Data Processing

There was debate when it came to the optimal method of collecting and storing the data generated from laser measurements. The mechanics of the drill string model itself are controlled via LabVIEW and is a program well suited towards the task of accepting, processing, and storing data. However, DASYLab is a far more streamlined system for reading in, neatly illustrating, and saving the data. This becomes important to consider given the sheer quantity of data collected in extended runs.

For reference, the size of an excel file containing just 60 seconds of information, compressed, is 54 megabytes. During early calibration, the laser would be transmitting data for several minutes. By separating the operating software from the data collection software it reduced the work load of the program and allowed for easier termination in the case of memory overload during data collection. As mentioned before, the DAQ card selected has preexisting software integration into DASYLab, allowing for seamless integration with the DAQ card to the program. The code for reading in, processing, and storing the data was added to a block diagram from a menu of different options from within DASYLab. Considering how the measurement device transmitted data to the computer, a small series of operations was selected. First the DAQ card was selected and the channels for accepting data were defined. The displays were added so that the data point being brought into the computer could be verified real time by comparison with the digital display on the laser itself. Then, since the value imported into the program was voltage, a conversion was applied to the value and also displayed. This second display was used to primarily ensure quality of data during data collection. The laser has a finite amount of measurable space, so certain displacements cannot be captured by the laser sensors. By being able to check for this real time, it saves time and effort as tests easily collect millions of data points. Penultimate, the data points were plotted onto polar graphs to help visualize the positional pattern of the drill string. The graphs were not saved and only plotted for a set number of points at a time. This was done so that in extended testing, anomalies could be noted with a time stamp and referred to in the data later. Finally, the data was collected in serialized excel files bound by a predetermined block size. This was to prevent the computer from freezing while attempting to create an overly large file. This led to having to merge files at a later point, but also resulted in smoother data collection.

4. Results

This chapter contains a large number of tables and graphs that correspond to a selection of five different extended measurements of the drill string at two different positions along the drill string, and is prefaced by calibration data and an initial, much smaller experiment. The calibration data serves only to verify that the motion occurring matches what is being transmitted to the computer. This was done by use of a 2D caliper attached to the laser measuring sensor (the LS-7030), seen in **Figure A-3**. The minor experiment helped to establish the parameters for the extended test, as well as to highlight how the data is to be organized to be best understood from a visual perspective. Finally, the full experiments had parameters set as a result from information gathered from the smaller experiment.

4.1 Calibration

Calibrating the lasers for use in the experiment is slightly different from the standard definition of calibration. Since the human hand is not precise enough to operate at the magnitude the laser is capable of detecting motion, perfectly centering the lasers around the drill string is near impossible by hand. To deal with this, an alternative method of calibration was performed to ensure that the drill string was always seen by the LS-7030. Since the objective of the experiment is to capture the entire motion of the string, it is more important that all the motion be captured than it is to be perfectly centered. In order to guarantee that the drill string would always be seen by the LS-7030, a straight rod was attached perpendicularly to the previously mentioned caliper to the laser. This caliper could be adjusted by hand in such a way that made it possible to move the rod along the maximum oscillating diameter set by the steel plate seen in **Figure A-3**.

Data was collected as the rod moved along the edge, and if at any point the LS-7030 could not see the rod, the device would output a preset maximum reading, which was in the case 10V. If this occurred, as it did in **Figure 18**, it meant that the drill string could possibly oscillate outside the target range of the LS-7030, so the center had to be adjusted. In order to see how to adjust the center, the same 2D caliper was positioned in the center, and was moved to the maximum positive and negative X and Y direction. This process would generate a cross, like the one seen in **Figure 19**. The X and Y displacement from center was adjusted for on the physical modal my moving the base of the laser, and then rechecking until the cross shape aligns with the axes as much as possible, such as in **Figure 20**. When the graph was this closely aligned, it meant that no data would be out of the target zone for the LS-7030, and testing could begin. For note, the significant digits of the points on **Figure 18** and **20** are accurate, and the reason for the decrease removal of the digits in **Figure 19** was a stylist choice for readability during the process of calibration, as the process of calibration does not require any data to be saved. Additionally, the output of these graphs is voltage; this is because the analog signal from the LS-7030 sends an output voltage ranging from negative to positive 10V, which corresponds to a positional range of negative to positive 15 mm. Since calibration data was not analyzed, it was never converted to position units.

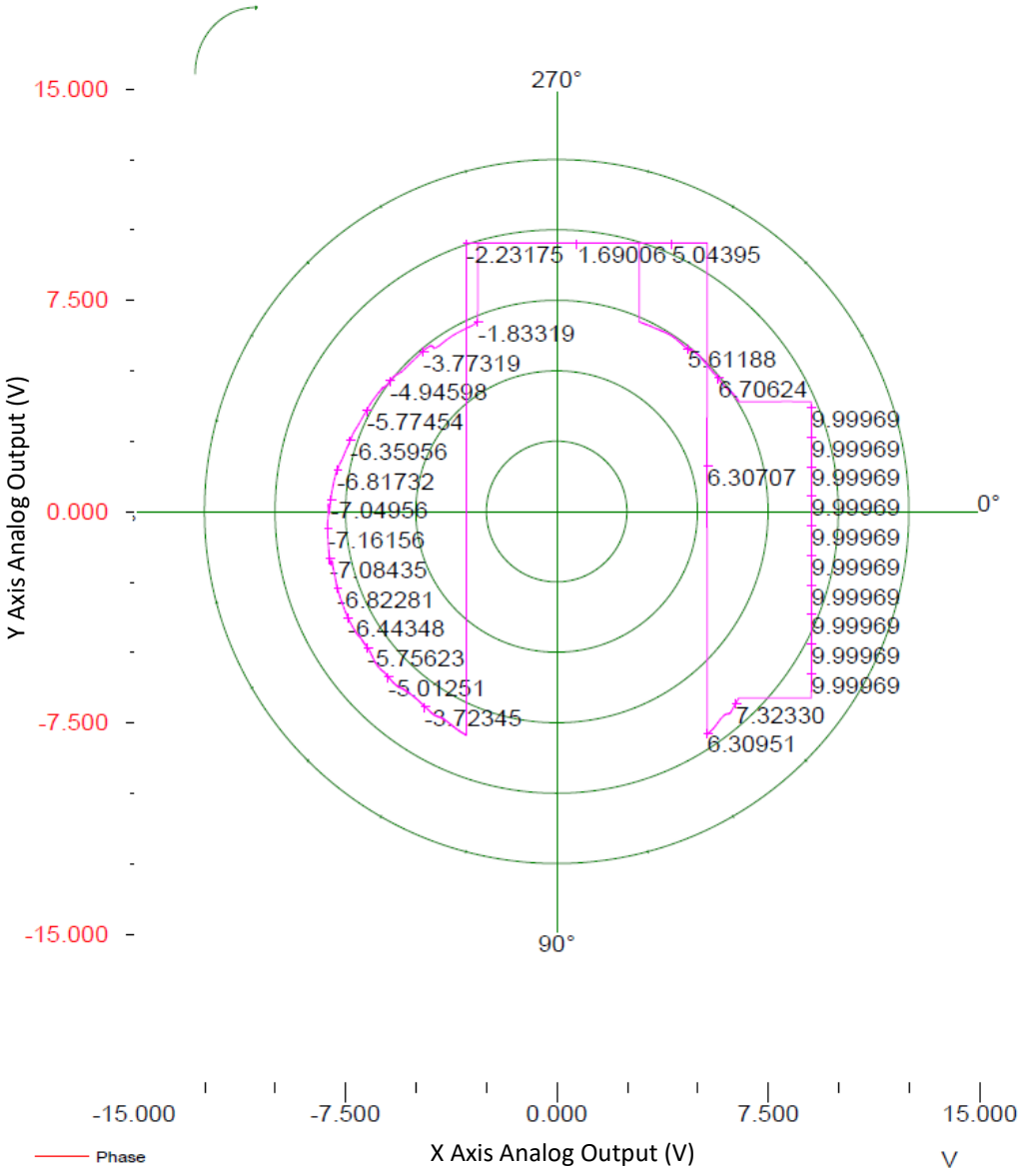

Figure 18. Initial calibrating graph illustrating invalid laser placement

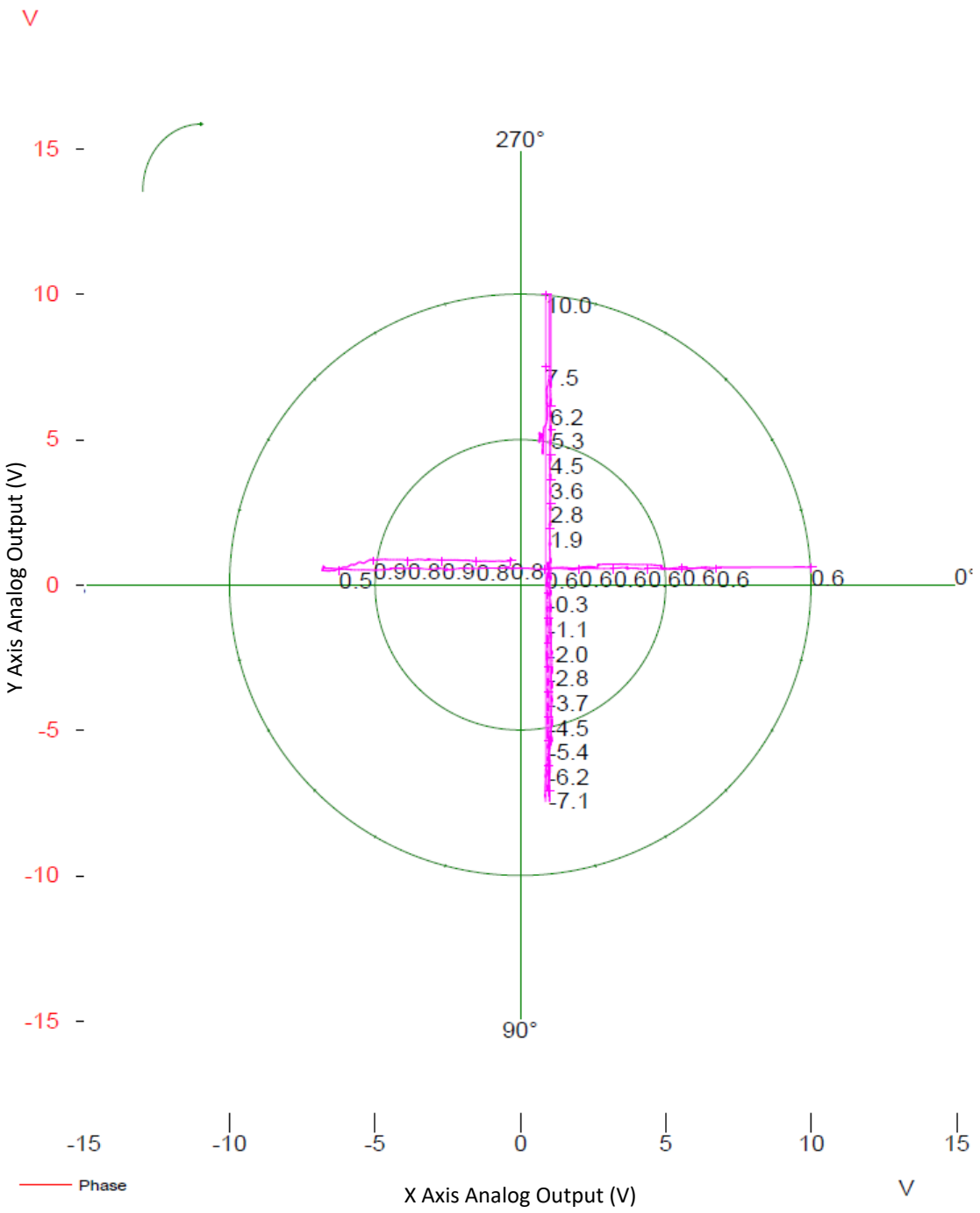

Figure 19. Calibration showing how off-center the laser was placed

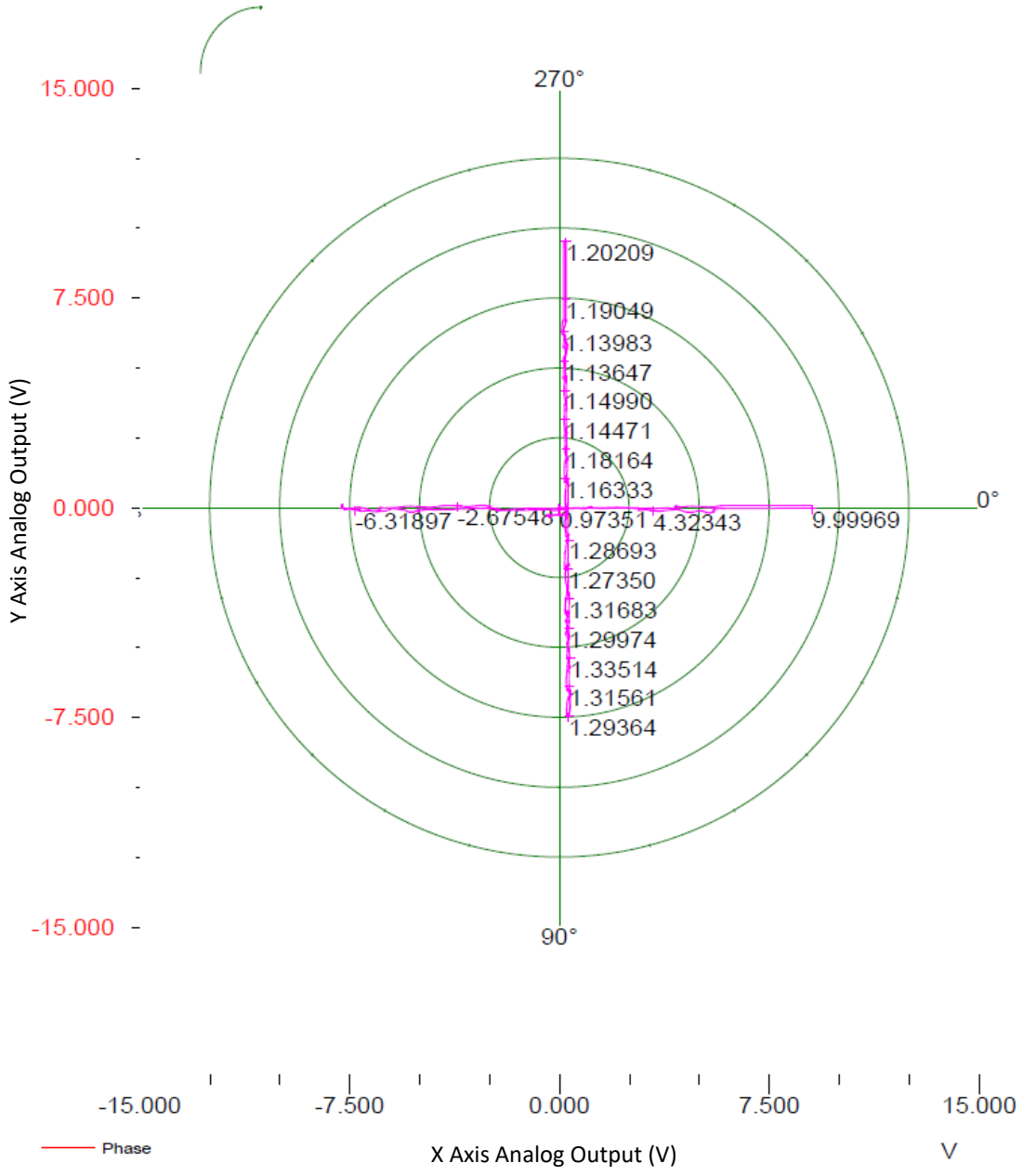

Figure 20. Calibration graph depict more optimal placement of the laser

4.2 Initial Experiment

The minor experiment was initially designed with the intent of confirming the experimental setup was indeed capable of measuring, transmitting, and storing the data at a resolution that was comprehensive and analyzable. In order to verify this, data was collected at a 'medium-high' RPM with low WOB, relative to the capability of the setup. This would be expected to generate drill string rotations with relatively large lateral movement, which is the exact type of behavior desired for generating information. The reason for not noting the exact RPM is because the intent was to look for completeness of information and ability to discern that information. Additionally, it was desirable that the information from this experiment not be directly compared to the full experiments in terms of exact values. Shapes, trends, and behaviors were the target observations, not exact values. This data was recorded simultaneously at 1 kHz, 100 Hz, and 10 Hz. This was done by recording the data three different times in the DASYLab system. This data was then assembled into two different visuals; the first as a 2D positional plot across all times, and the second as a waveform graph for both X and Y. The 2D positional graphs plot X and Y position against each other. The waveform graph plot X and Y positions against time in seconds. This data is compiled together and presented as **Figure 21**. The intent of presenting the data in this method was to look at the same information from two different viewpoints to gather as much insight into the behaviors of the system as possible, as well as look for any loss in visual information; an idea discussed in more detail in the next chapter.

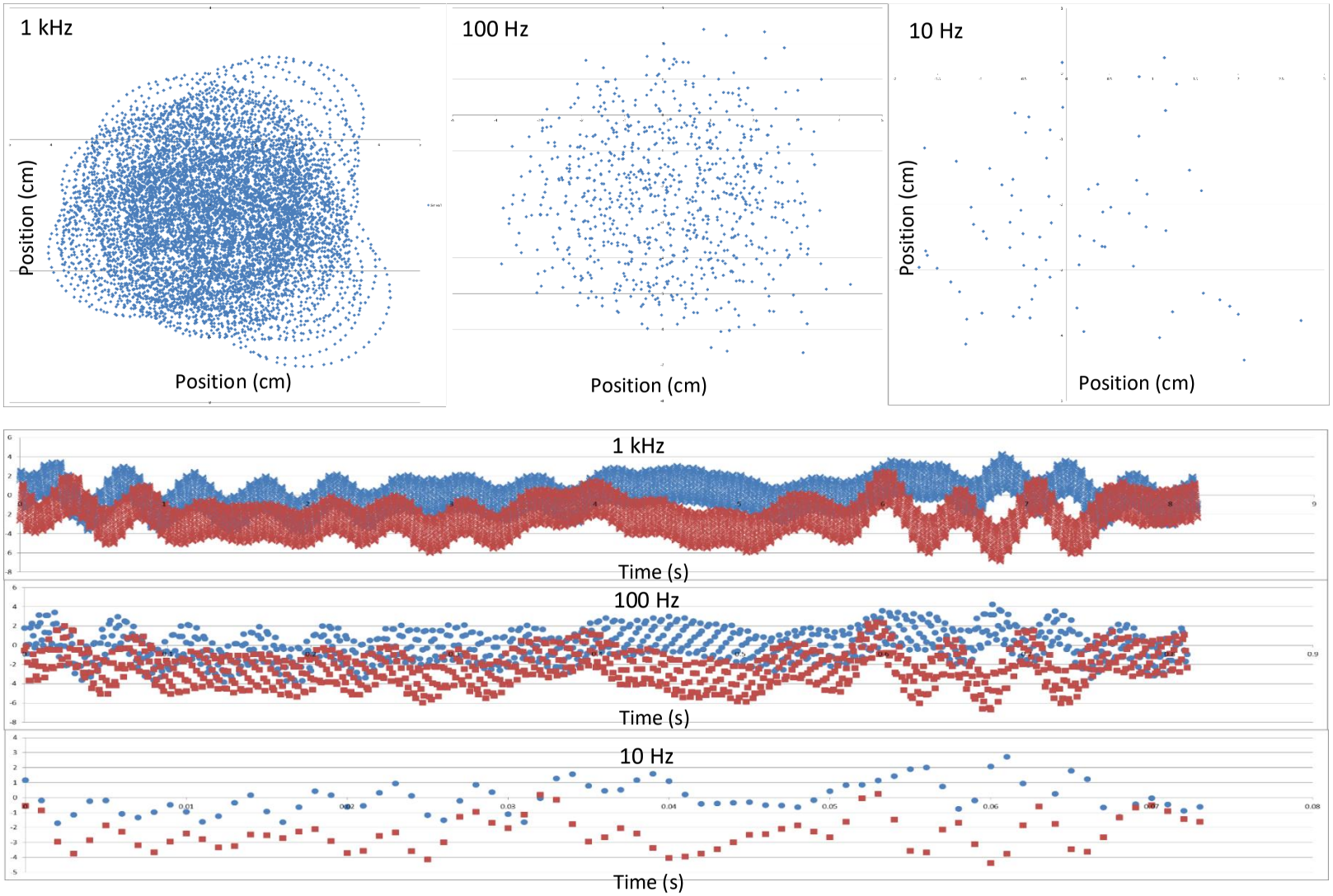

Figure 21. A Composite graphic of the initial, minor experiment at 1 kHz, 100 Hz, and 10 Hz in both positional and frequency

4.3 Full Experiment

Insights from the minor experiment lead to two major conclusions regarding the design of more detailed experiments. The first, and the primary conclusion, was the lasers were fully capable of collecting robust data from high-energy experiments. This meant testing at the highest RPM was allowable. The second conclusion was that there was definitely information loss at data collection frequencies cited by prior literature. To better detail the extent of information loss; data should continue to be collected at three frequencies of different magnitude. Furthermore, for all five experiments a WOB of 1Kg was kept constant. As this is a primary investigation, it was decided that only one parameter change should be observed. RPM was decided as the independent variable as it was both easier to change in the preexisting set up and it was thought to be the parameter that increases lateral movement as it goes up. The experiments are labeled as 6V, 7V, 8V, 9V, and 10V; corresponding to the voltage sent to the DC motor to control the RPM. Due to the large amount of data generated from this experiment, more data is collected than can be reasonably included within this chapter. An incredible large amount of data is generated from just one run; defined as a data collection interval of 35 seconds or longer plus a 5 second window at the start to allow for a reduction in noise from starting the setup. The data collection was always started after the drill string model is started and terminated before the model has been stopped. Additionally, data is collected at two points along the drill string, as described in Chapter 3.

In just one set of 35 seconds, over 1.4 million data points are recorded, and two experimental sets include extra information that was used for additional analysis. For each experiment, two polar graphs and two frequency-domain graphs were generated for each position and for each data collection frequency to more concisely convey the data generating 60 unique graphs. Only the results from experiment 10V are presented in this chapter; the complete data from all five experiments can be found at the end of this work in Appendix B. All graphs that are referenced out of that appendix will be referenced in the format **Figure B-X**, where **X** is the sequential number the figure appears in the appendix. For note, ‘Laser T’ refers to the laser further away from the drill bit, while ‘Laser B’ refers to the laser closest to the drill bit.

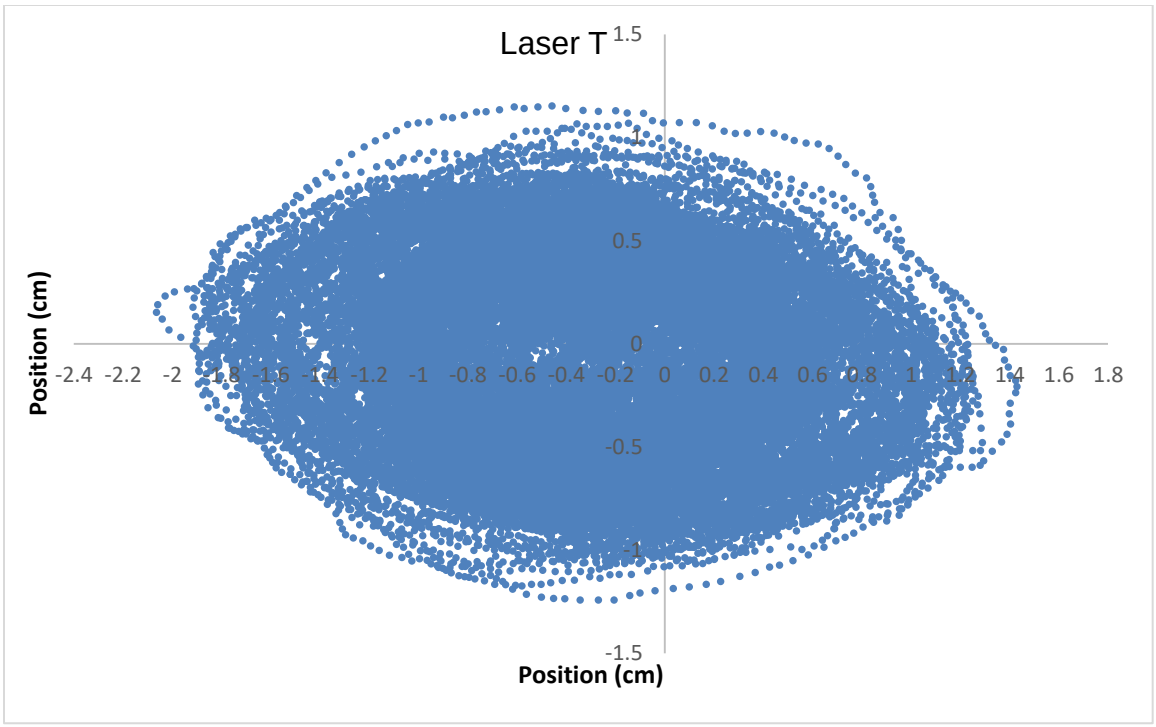

Figure 22. The top positioned planer behavior of the drill string of experiment 10V; 1 kHz

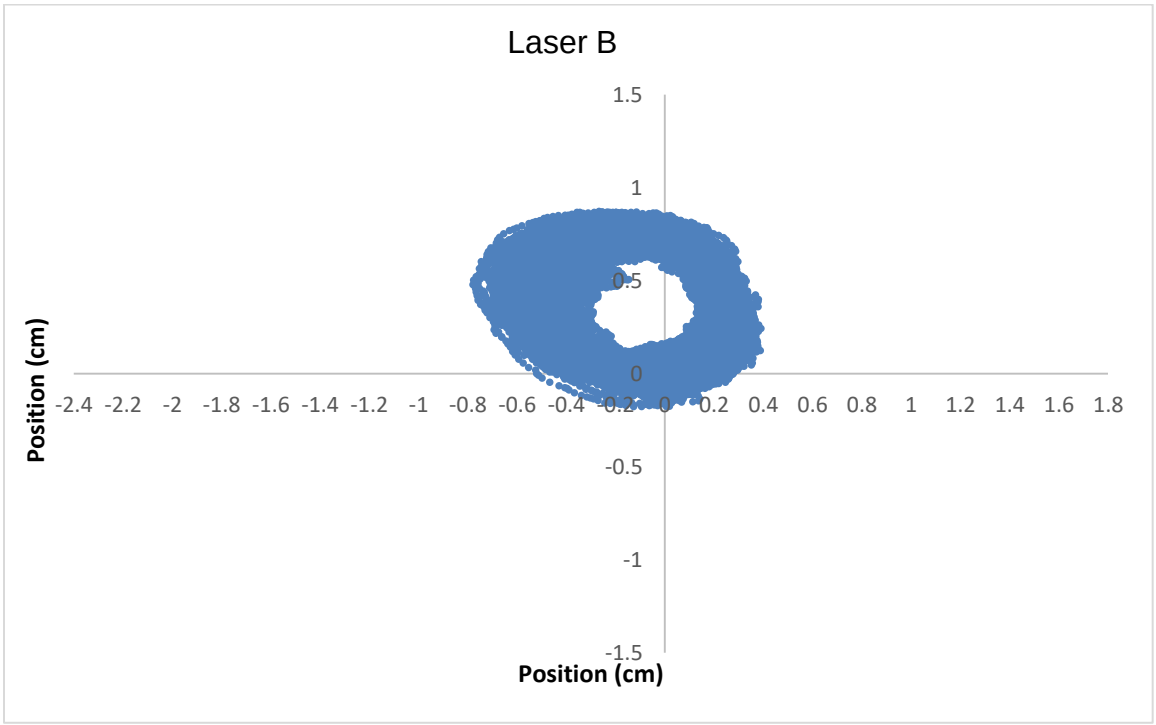

Figure 23. The bottom positioned planer behavior of the drill string of experiment 10V; 1 kHz

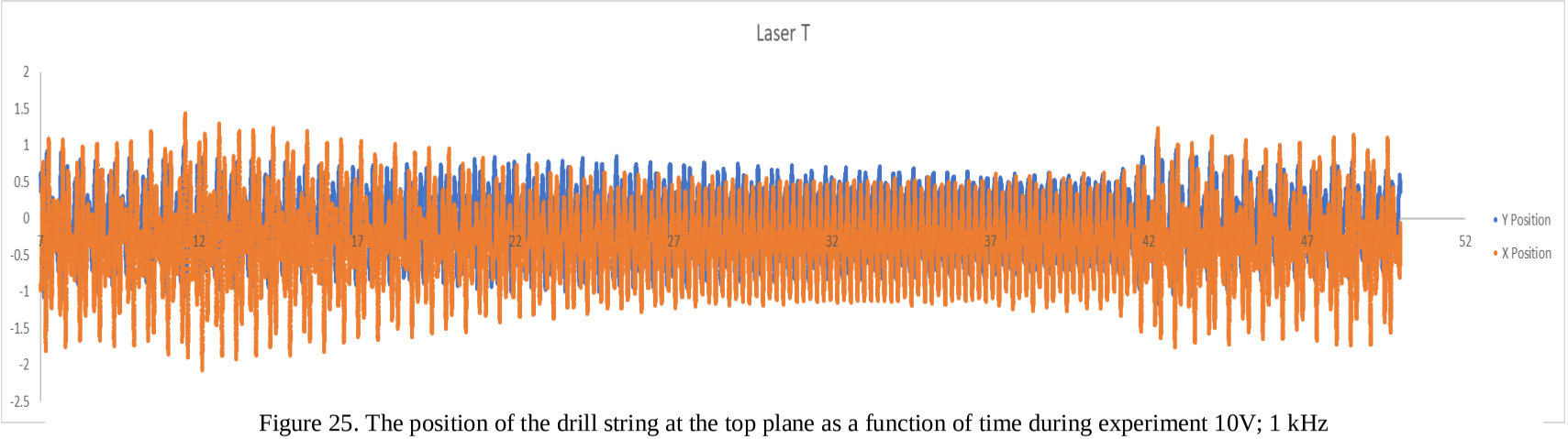

Figure 25. The position of the drill string at the top plane as a function of time during experiment 10V; 1 kHz

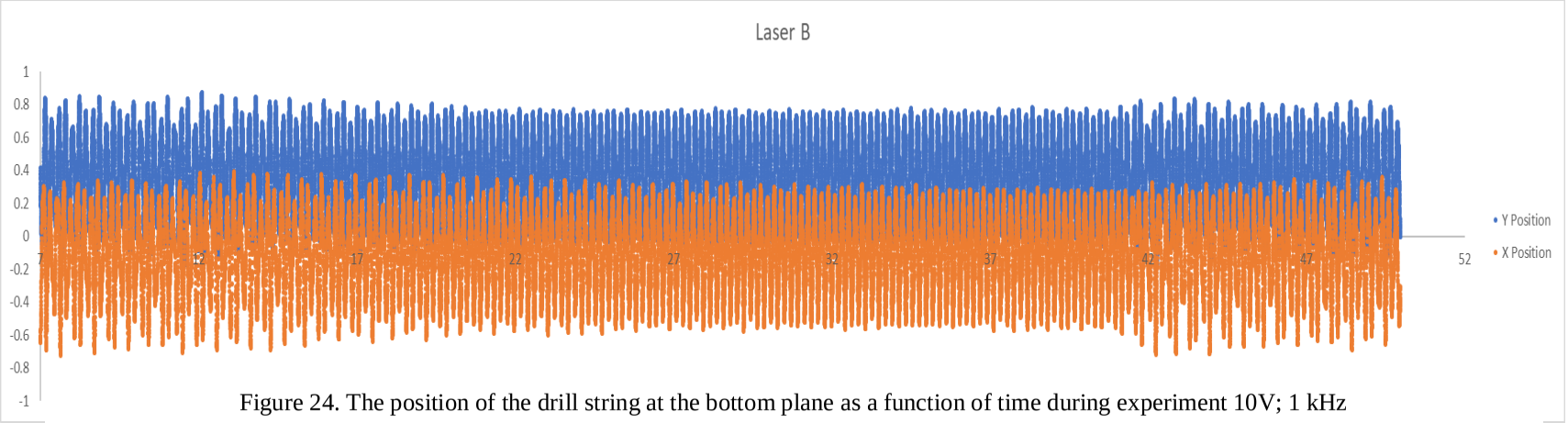

Figure 24. The position of the drill string at the bottom plane as a function of time during experiment 10V; 1 kHz

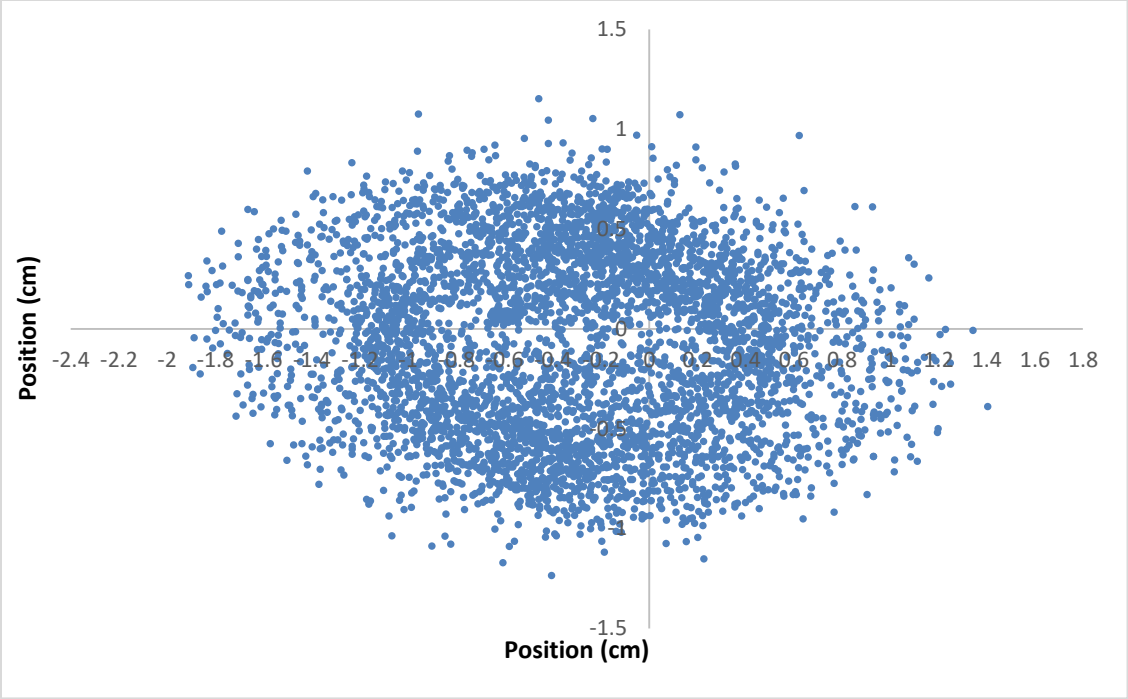

Figure 26. The top positioned planer behavior of the drill string of experiment 10V; 100 Hz

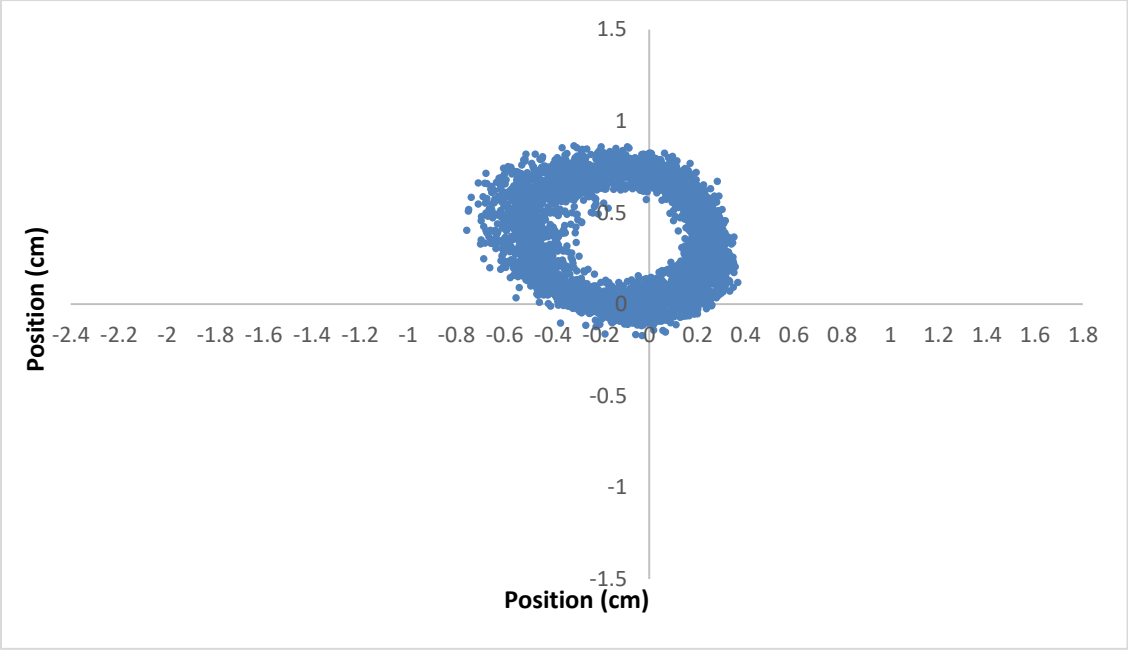

Figure 27. The bottom positioned planer behavior of the drill string of experiment 10V; 100 Hz

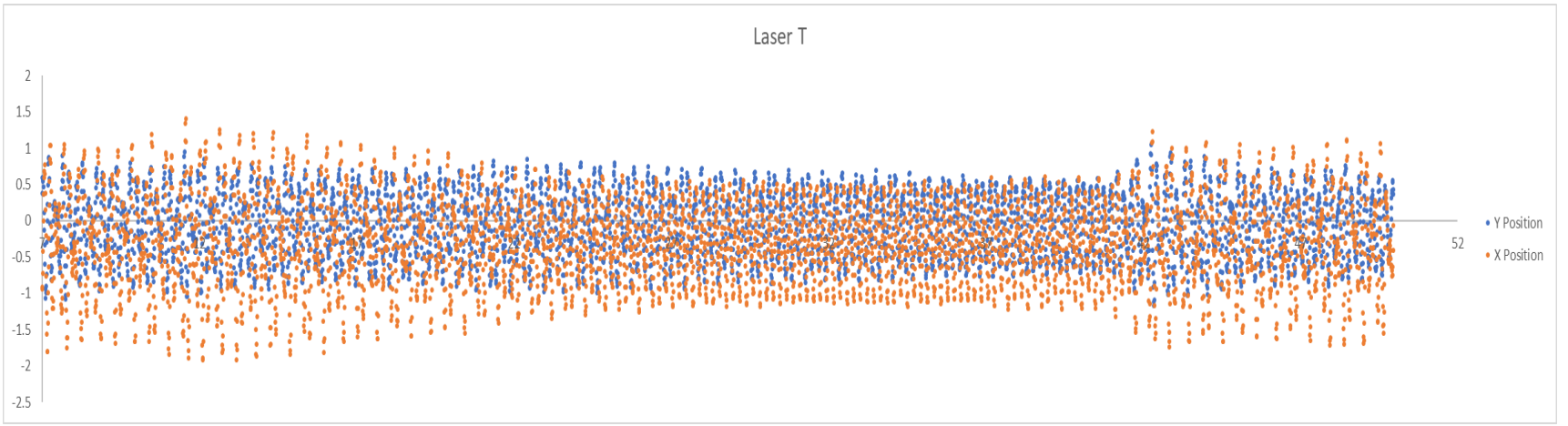

Figure 29. The position of the drill string at the top plane as a function of time during experiment 10V; 100 Hz

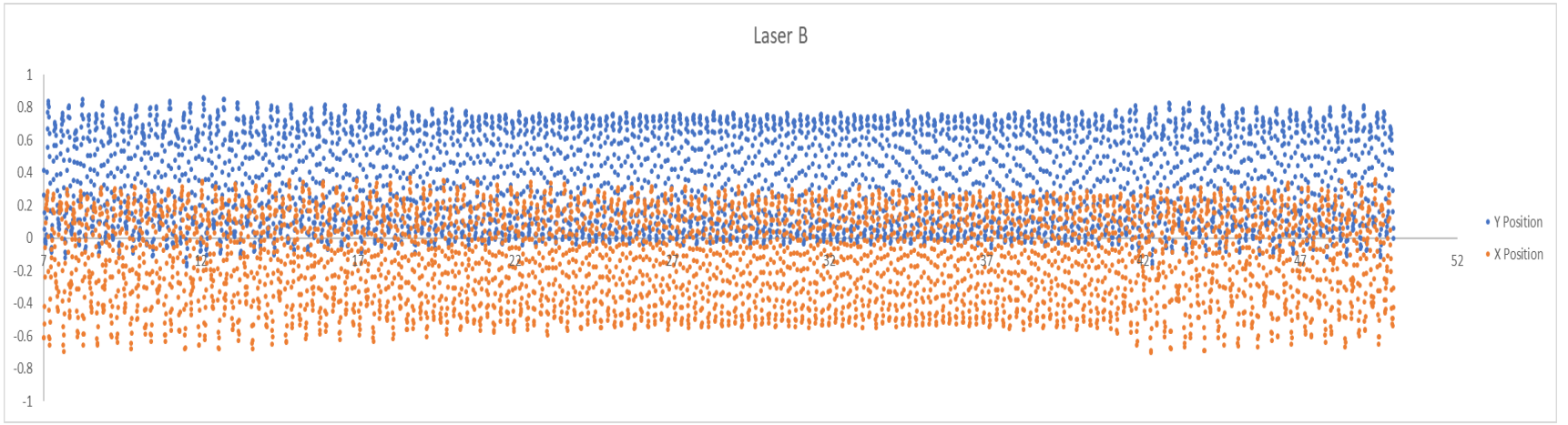

Figure 28. The position of the drill string at the top plane as a function of time during experiment 10V; 100 Hz

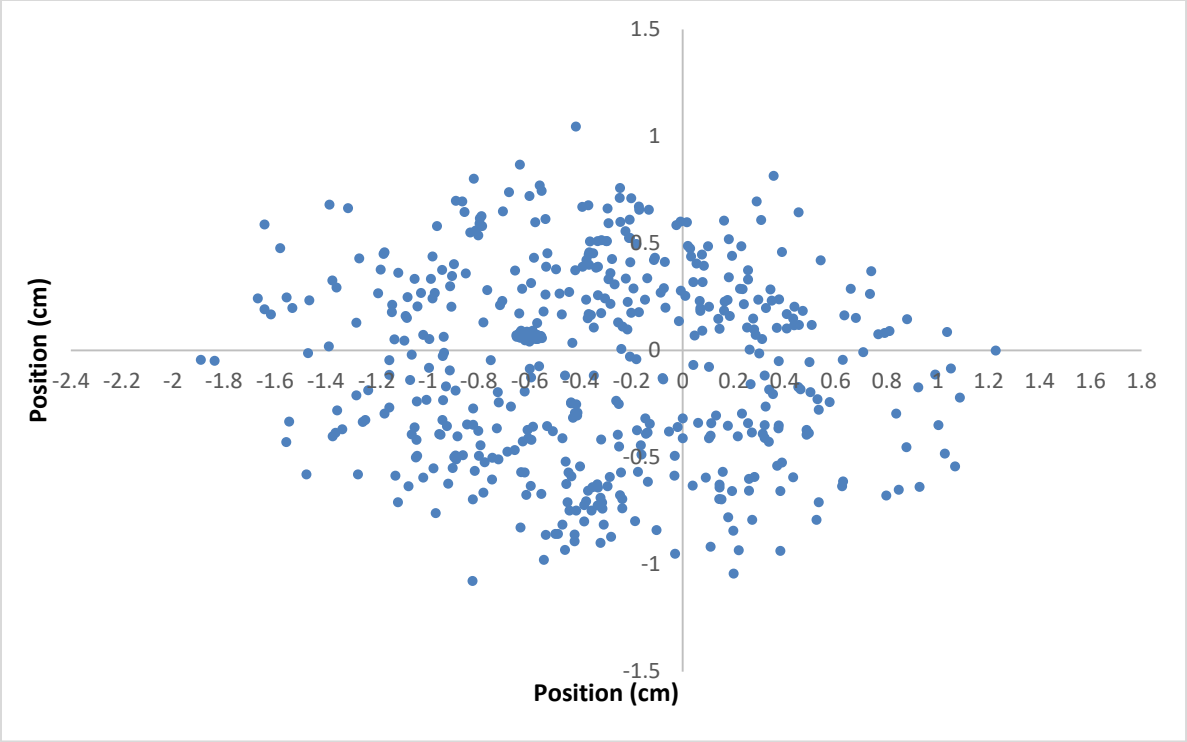

Figure 30. The top positioned planer behavior of the drill string of experiment 10V; 10 Hz

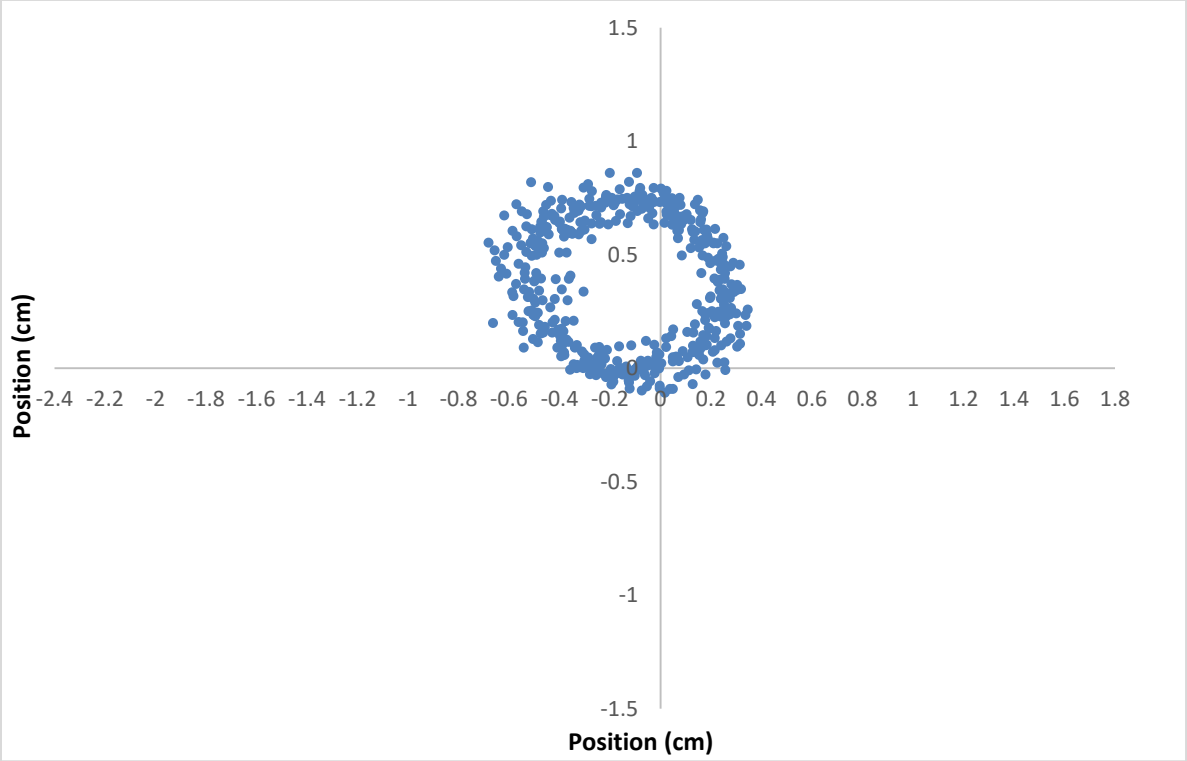

Figure 31. The bottom positioned planer behavior of the drill string of experiment 10V; 10 Hz

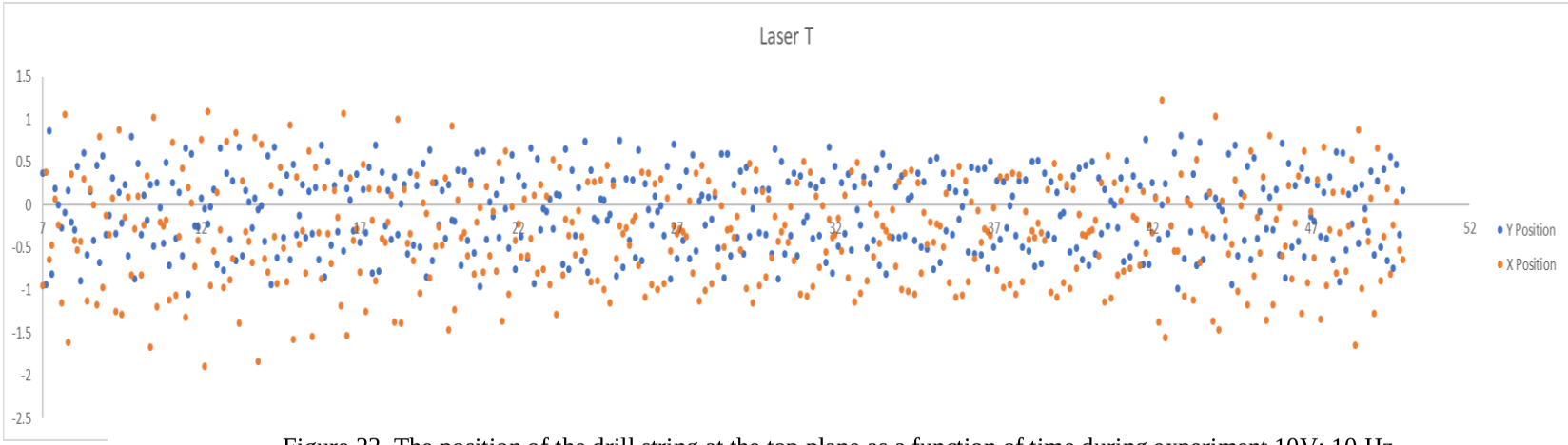

Figure 33. The position of the drill string at the top plane as a function of time during experiment 10V; 10 Hz

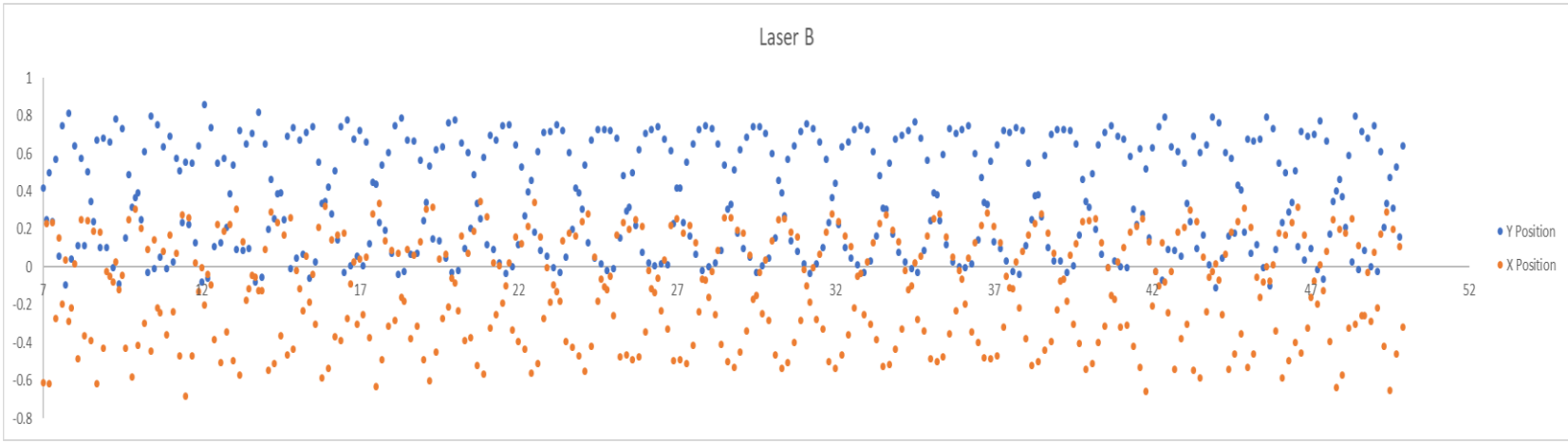

Figure 32. The position of the drill string at the bottom plane as a function of time during experiment 10V; 10 Hz

5. Data Analysis and Results

The analysis in this chapter is broken into three parts. The first part discusses the results from the minor experiment that lead to the decisions in setting the parameters for the major experiment. The second part discusses the results relative to the intended purpose of the experiment. This refers to assessing the experimental method in terms of its ability to collect adequate information and identify if there is indeed a significant loss of information between the different sampling rates. The third part of this chapter discusses insights and conclusions drawn from information gathered from high-resolution data sampling. These insights inform how best to continue future works relating to the experiment.

5.1 Minor Experiment Analysis

Referring back to **Figure 21,** there were two major insights gleaned from the graphical presentation of the data. While all six graphs in the figure contain information regarding the same experiment, the amount of information contained and the way the information is displayed is varied. The major distinctions between the two ways in illustrating the data are in the type of pattern information they reveal. The graphs that illustrate position along the X-Y plane give insight specifically into motion behavior in two dimensions. In the case of **Figure 21**, it can be seen that the experiment generated a large number of circular oscillations around a non-consistent center. Additionally, it can be seen that the majority of those circles fall within a general density, with only a few traveling paths moving outside of that area.

However; when looking at the same graph type but with data collected at one frequency magnitude less, the appearance of multiple circular traveling paths is lost, but the general density of data falls within the same region.

This means at the 100 Hz data collection range, a strong sense of general behavior is maintained but exact patterns – within the two-dimensional plane- are lost. Additionally, the level and behavior of outlying movement is completely lost, as only a few outlier points are still visible. Continuing this, by moving on to the 10 Hz version of the graph, all sense of shape and pattern are completely lost. Even the center of density is shifted away from what it was in the prior two iterations of this graph. This leads to the initial conclusion that the 1 kHz sampling rate is the most complete data set in terms of pattern profiling, and that 10 Hz is completely inadequate, but also that 100 Hz may be sufficient enough collection rate to define the important patterns and occurrences in the drill string.

To investigate this conclusion before moving on to the major experiment, the one-dimension position plots versus time were scrutinized. It is apparent in the 1 kHz version of the graph that both the X and Y position oscillate along a general sinusoidal curve, which at certain times experiences significant deviations. Looking at the 100 Hz version of this same graph type reveals almost all the same information. Both the oscillating behaviors and the deviations are clear; with the only notable loss in information being the overlap in the two positions. It is unclear from this experiment what, exactly, that overlap represents. It is only being noted as it is the only visually notable loss in information between 1 kHz and 100 Hz. However, when looking at the 10 Hz graph, it is seen again that all meaningful information has been lost. This 10 Hz graph could most easily be described as a potential 'trace' or average of the 1 kHz graph. The general shape of the sinusoid is shared, but the oscillations and the degree of deviation is completely lost. The total loss in visual information from both the two-dimensional and one-dimensional graphs further establishes the importance of at least sampling at 100 Hz.

Additionally, since most visible information was retained moving from 1 kHz to 100 Hz, it was deemed unnecessary to model the data at the maximum sampling frequency of 10 kHz.

5.2 Initial Discoveries

Initially, after all the data was collected, the primary investigation into the data was centered on the extent of data lost between each time the sampling was reduced and if the level of data loss was comparable between RPMs. By reviewing **Figures 22-33**, it is apparent that there is less information as the frequency of data collection decreases, and although this statement may seem redundant since each subsequent figure set inherently contains only 10% of the information than the previous, the extent of "lost information" extends past that literal number of points. Referring back to the results and conclusions from the Minor Experiment section, the two observations being investigated in the graphs are behavioral changes in the one-dimensional plots and the path and density center changes on the two-dimensional plots. Observing the graphs in pairs is the best method for understanding or noting any major visual data loss. By first reviewing **Figure pairs 22-23, 26-27, and 30-31,** the analysis begins the same way as it did in the minor experiment.

One of the first observations, and a deviation from the minor experiments, is that across all three tiers of measurement, Laser B's shape and shape density seems to be unchanged as data sampling decreases. More so, when looking at the graphs for Laser T, it seems that density may be better visualized in the 100 Hz graph versus the 1 kHz graph. This is likely due to the sheer number of points on the graph, and the trend would be clearer if the graphical indicators could be smaller. This does point out an issue of data clutter that is important to note, however; as it does make identifying patterns more difficult.

This appearance of overly-dense data points is evident in the one-dimensional graphical representations of the data as well, however; in this case the data loss is not nearly as forgiving. Just as in the minor experiment, this graph clearly outlines the sinusoidal traveling path taken by the drill string in each direction. Additionally, the deviations from the initial sinusoidal shape can be seen very clearly around the 25 second mark on Laser T, noted in **Figures 24 and 28**. This event is not nearly as apparent on **Figures 25 and 29**, but this is expected due to Laser T being located far away from a harmonic node and therefore subject to larger bending moments while Laser B is practically at the node, a point of stabilization along the wave. Looking at data loss across the data sampling rates, a return to the results observed in the minor experiment is seen, where by the time the data is being collected at 10 Hz, the oscillations and the deviation points lose a large amount of definition.

5.3 Hidden Findings

Since it is apparent that displaying all the data from the experiment at once at 1 kHz is too much information on one graph for detailed examination, but also apparent from the one-dimensional graphs that there is a change in behavior around the 25 second mark, magnified isolation graphs were generated. Since the phenomenon is notable primarily in the upper portion of the drill string at Laser T, but still notable to some degree at Laser B, a magnification of the data at 1 kHz of both lasers is considered, shown in **Figures 34 and 35.** Additionally, the data is presented at the lowering sampling rates in **Figures 36-39**. While the bottom laser graphs retain the general trend of maintaining their shape as sampling frequency decreases, the top lasers quickly fail to retain any form and take on a chaotic shape, with **Figure 38** losing any sense of visible order.

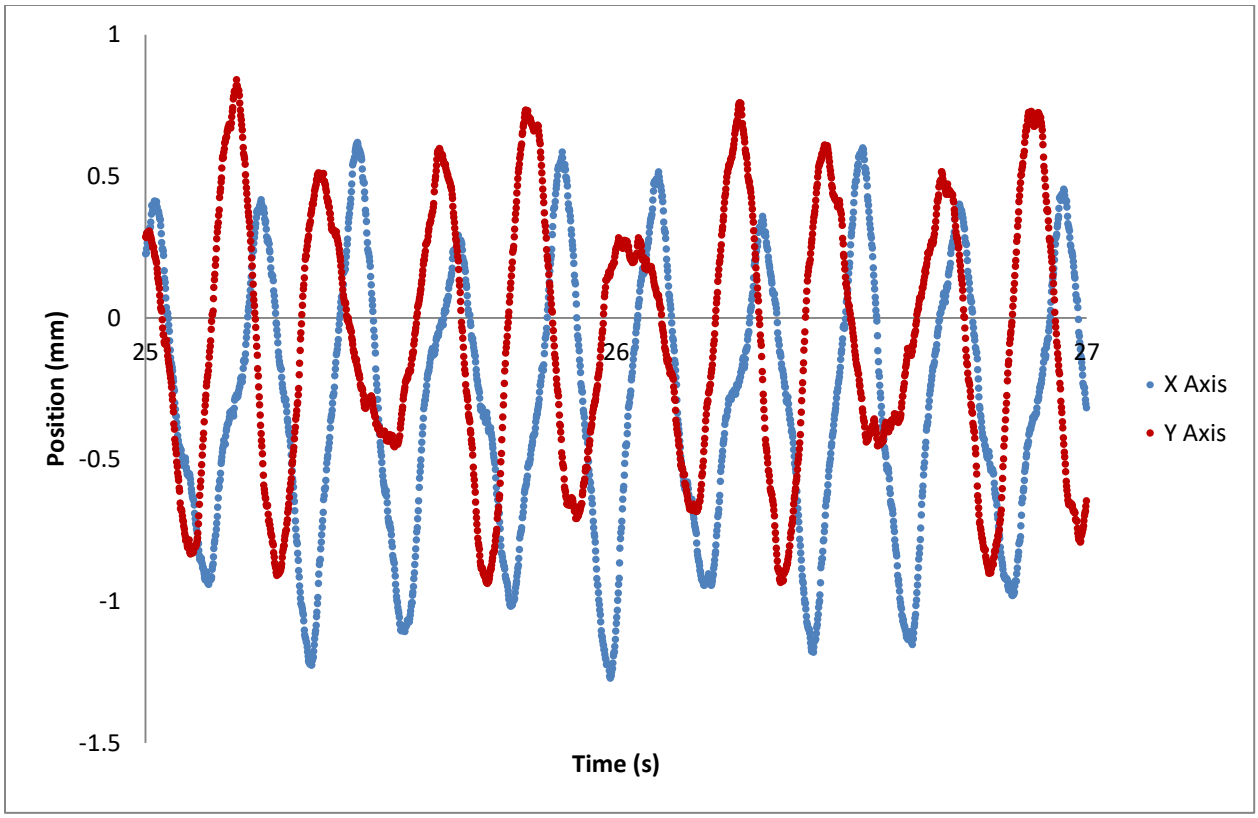

Figure 34. The deviation response across the X and Y axis during the 10V experiment at Laser T at 1 kHz

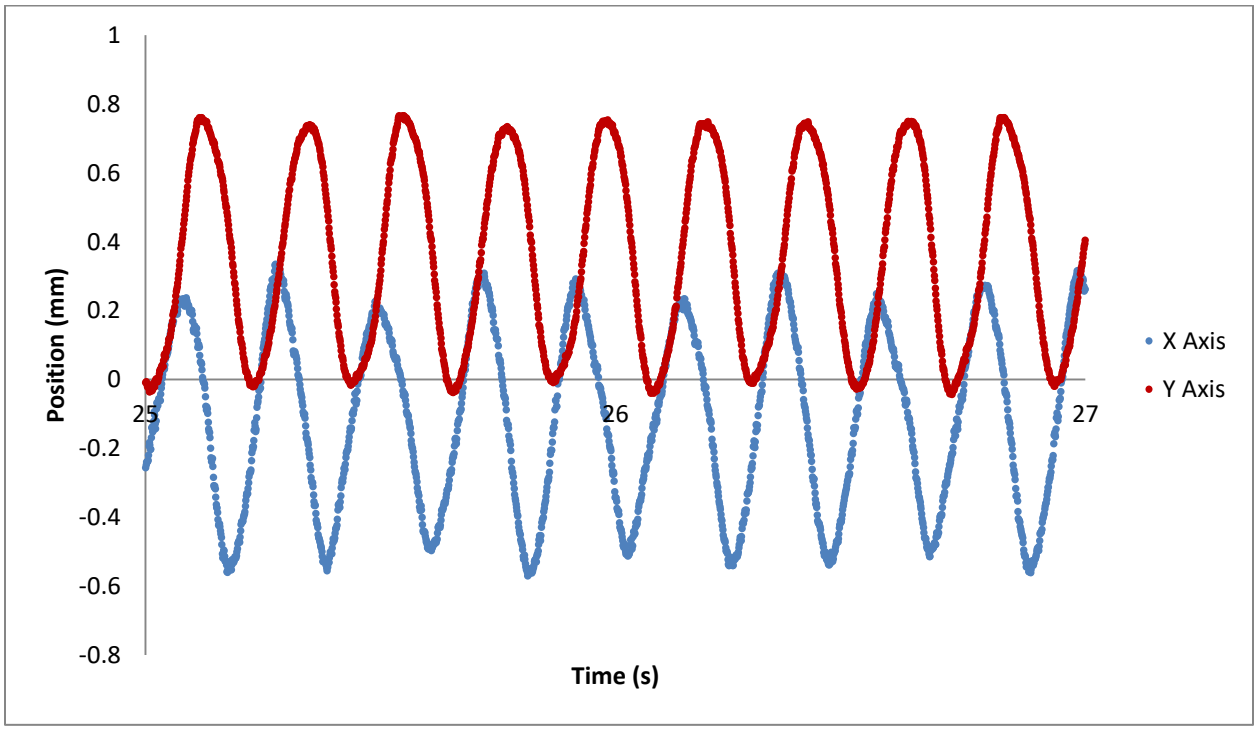

Figure 35. The deviation response across the X and Y axis during the 10V experiment at Laser B at 1 kHz

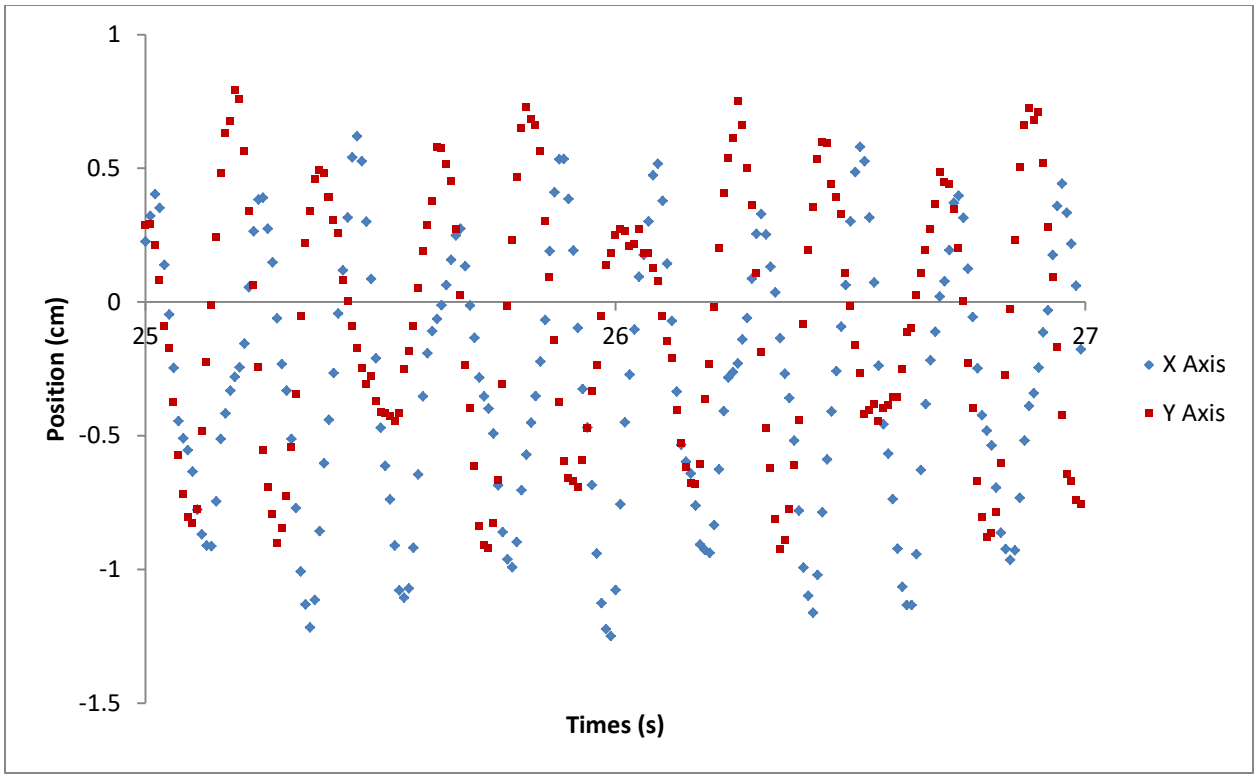

Figure 36. The deviation response across the X and Y axis during the 10V experiment at Laser T at 100 Hz

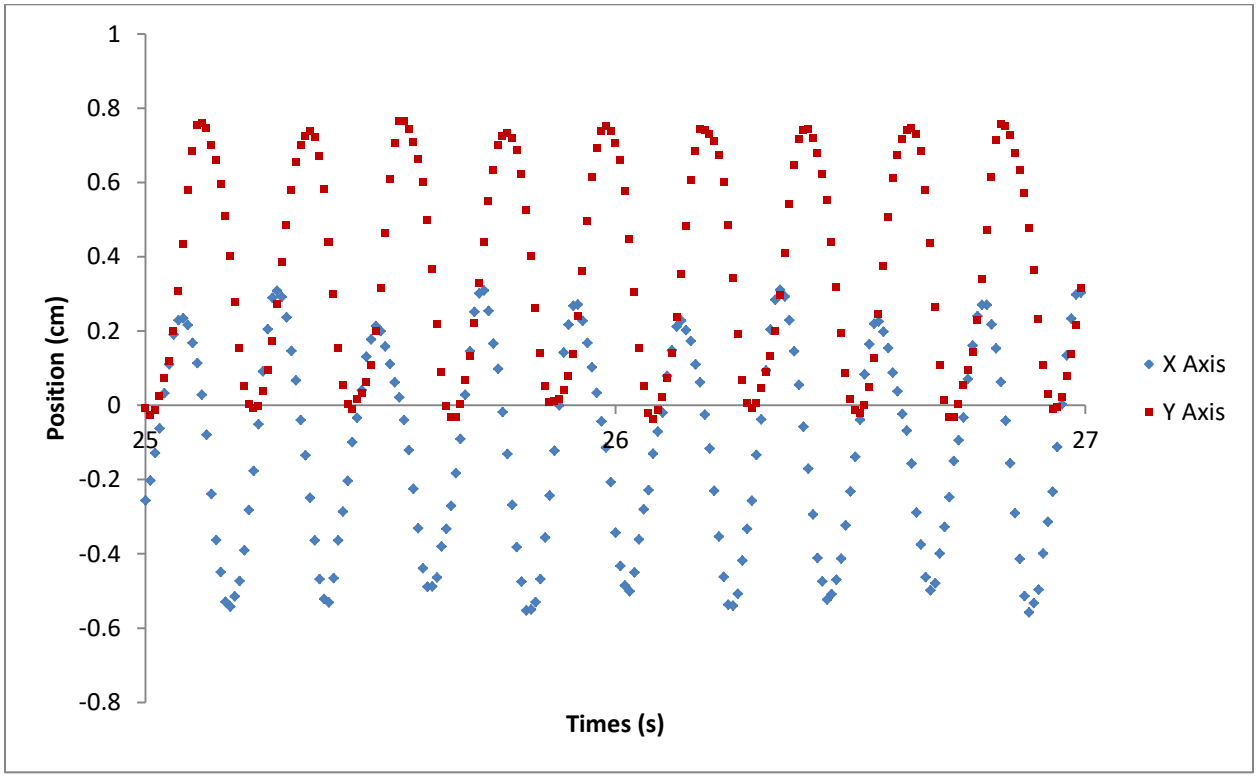

Figure 37. The deviation response across the X and Y axis during the 10V experiment at Laser B at 100 H

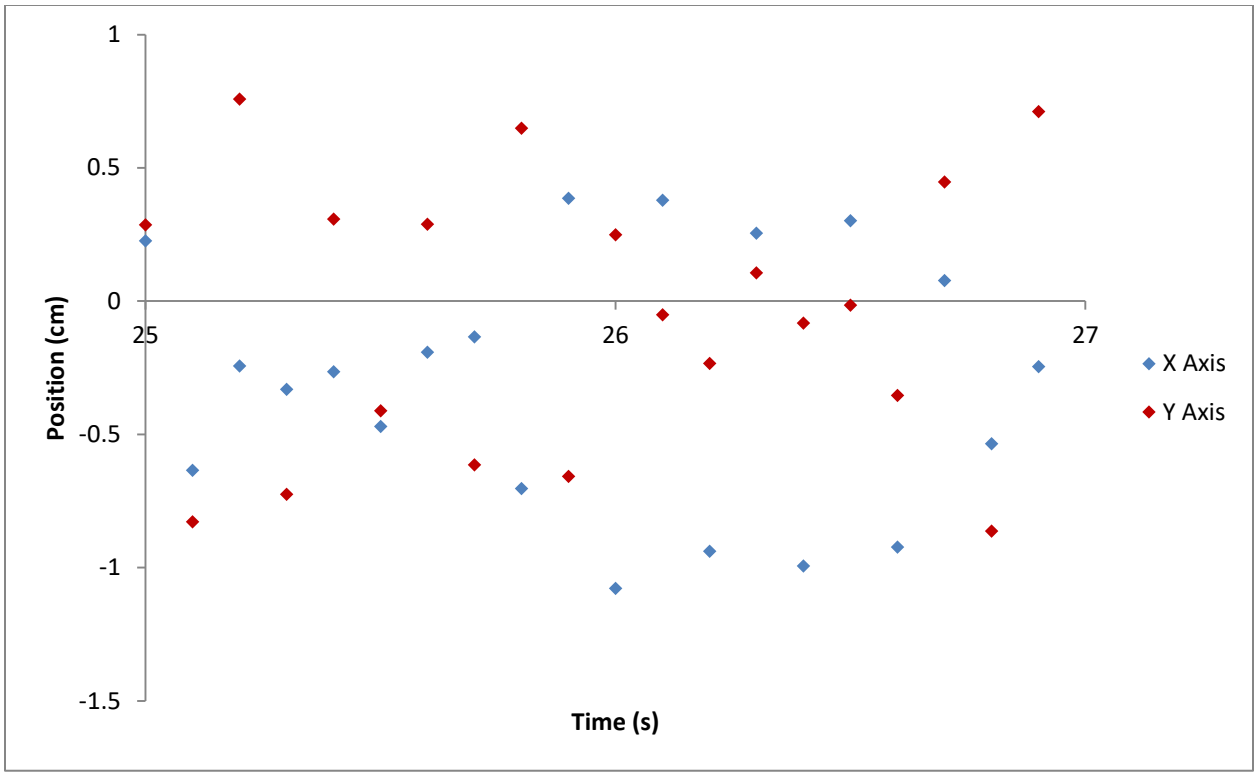

Figure 38. The deviation response across the X and Y axis during the 10V experiment at Laser T at 10 Hz

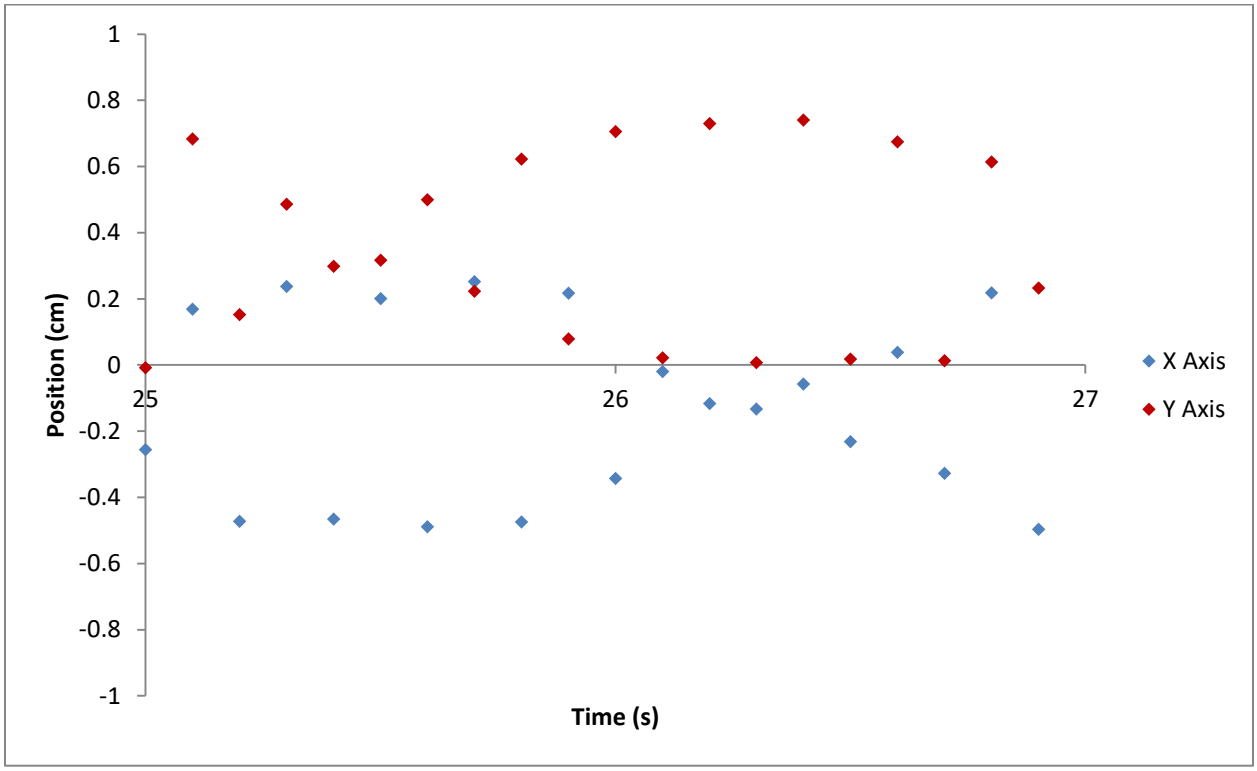

Figure 39. The deviation response across the X and Y axis during the 10V experiment at Laser B at 10 Hz

One of the more obvious observations that can be drawn from this data of the 10V test is that the center point of oscillation at Laser T is slightly different from Laser B. This could be either the drill string not being at a perfect 90-degree angle to the floor and ceiling, or it could be a result of the experiment itself. The offset centers are made more apparent by adjusting the scaling on **Figures 40 and 41** to share the same dimensions. This difference in center is noted across all five data sets and can be seen clearly in **Figure Pairs C-3,4, C-9,10, C-15,16, C-21,22,** and **C-27,28.** Additionally, another piece of information, though somewhat obvious and expected, is that the X and Y axis are fairly comparable to a Sine and Cosine waveform, evident by the slight offset. This is a far more apparent observation in Laser B than in Laser A, but it is loosely a requirement for circular rotation, as graphing Sine vs Cosine would result in a perfect circle.

In Laser B, the amplitude of both the X axis waveform and the Y axis waveform seem to have, mostly, the same amplitude. This agrees with **Figure 23**, which is more circular than elliptical. When looking at **Figure 34** the same offset between the waves is apparent, but the general shape of the wave is not nearly as neat and uniform enough to simply call them Sine and Cosine waves, respectively. At this resolution of the data, it appears that the X axis exhibits a phenomenon where every other oscillation displays some form of deviation from the expected wave form, where the increasing slope starts shallow and then half way through the increase, the slope sharply increases to account for the difference. While this is not noted on the Y axis, the Y axis displays its own unique behavior in that is does not constantly return to the minimum or maximum amplitude every time, in fact it does not even come close to hitting those points. Since the reason for this occurrence is unknown, it was thought to take an enhanced look at the two-dimensional graphs for the respective experimental run. At first glance, **Figures 40 and 41** exhibit the generally expected composite travelling path shape.

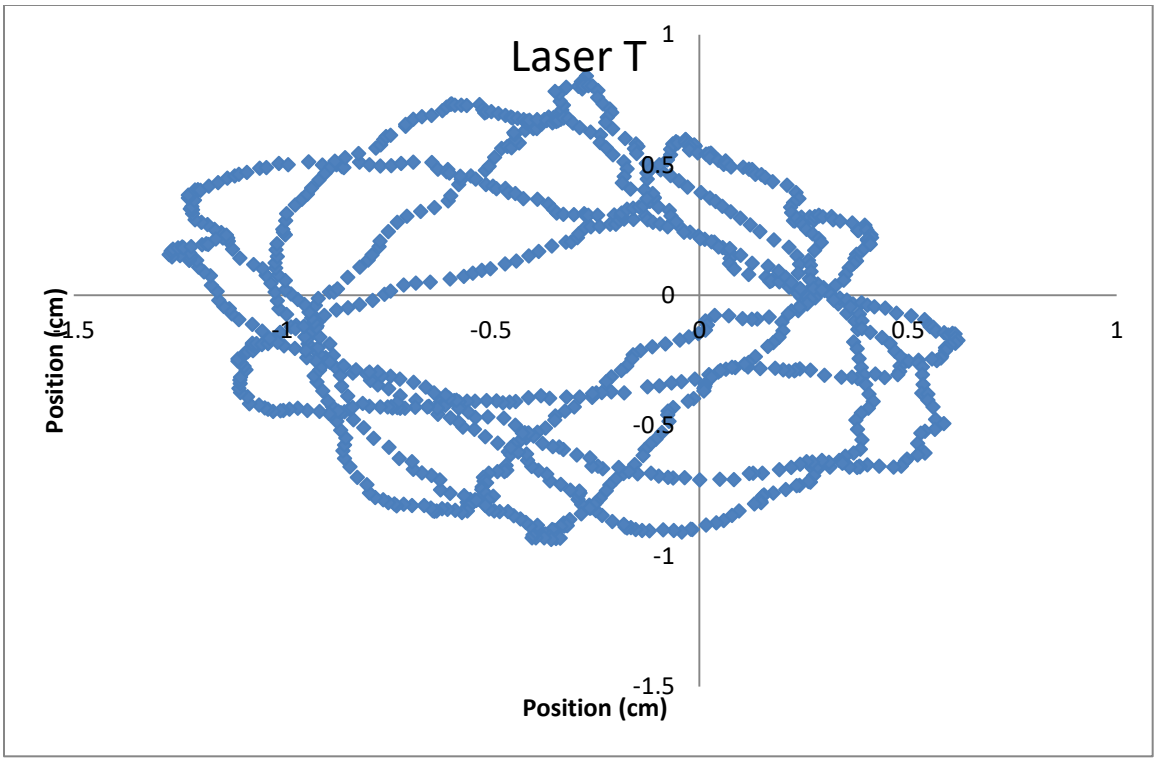

Figure 40. DSV position from 25 to 26 seconds during the 10V test at Laser T

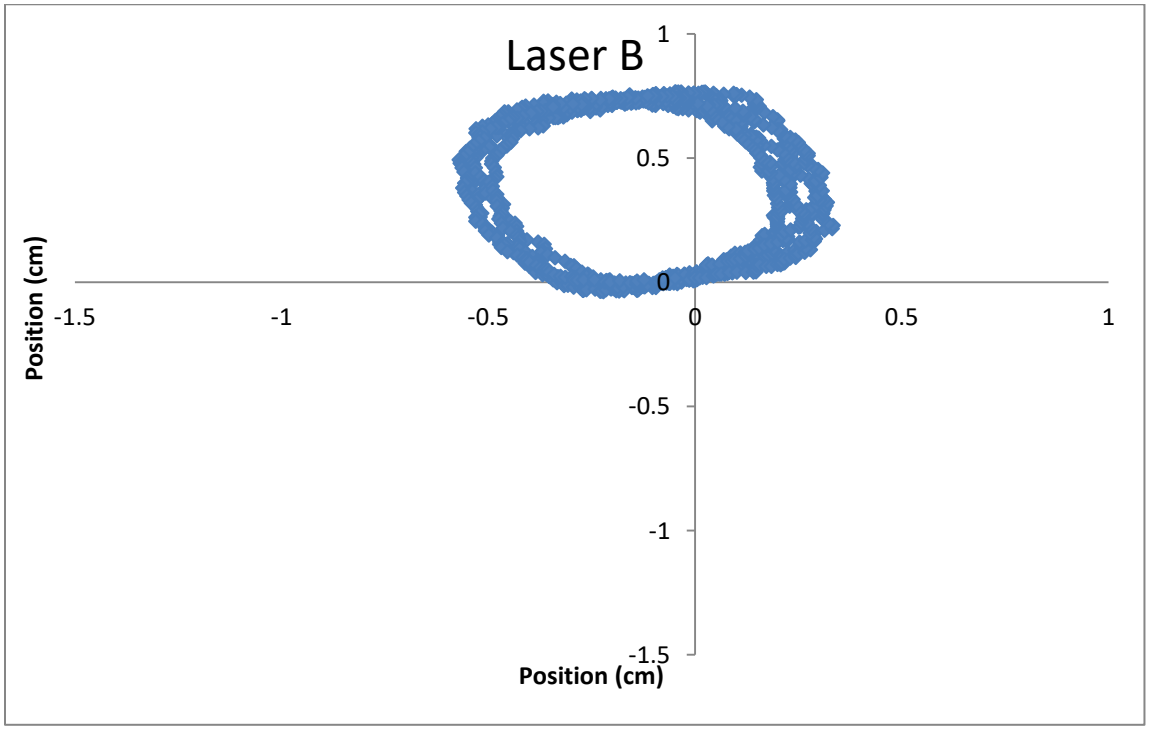

Figure 41. DSV positions from 25 to 26 seconds during the 10V test at Laser B

These graphs only contain one second of data, more precisely the first half of the data from **Figures 34 and 35**. When referring back to those figures, the graph clearly repeats behaviors from second 25 to 26 during second 26 to 27. Because of this, it is acceptable to only look at one second. At first glance, these plots seem like representative samples of the original **Figures 22 and 23**. The shape of **Figure 41** is of uniform shape and smaller size as seen previously. The shape of **Figure 40** is more elliptical, elongated in the X plane, just like the previous graph shows. However, since the data is thinner, it becomes apparent that the traveling path in **Figure 40** is not as uniform as previously thought. In order to investigate this, graphs of approximately one period, which is deemed one-third of a second, were constructed for Laser B and T for all experiments.

While just the graphs for 10V are contained within this work, all the graphs are contained in **Appendix C** at the end of this work. These graphs make it very apparent that the behavior of the drill string at Laser T is much more prevalent than expected. Additionally, it is seen that an increased RPM does in fact increase the oscillations per minute, as **Figures C-5 and C-6** do not contain one complete loop but **Figure 42** and **43 (**or **C-27 and C-28)** contain almost one and a half oscillations. The nature of the traveling path in **Figure 42** is difficult to truly determine due to its 'heart with a cross shape,' and we can see similar odd behaviors across all the position plots for Laser T graphs. This would mark yet another potential correlation or phenomenon that large data sets could help to better understand.

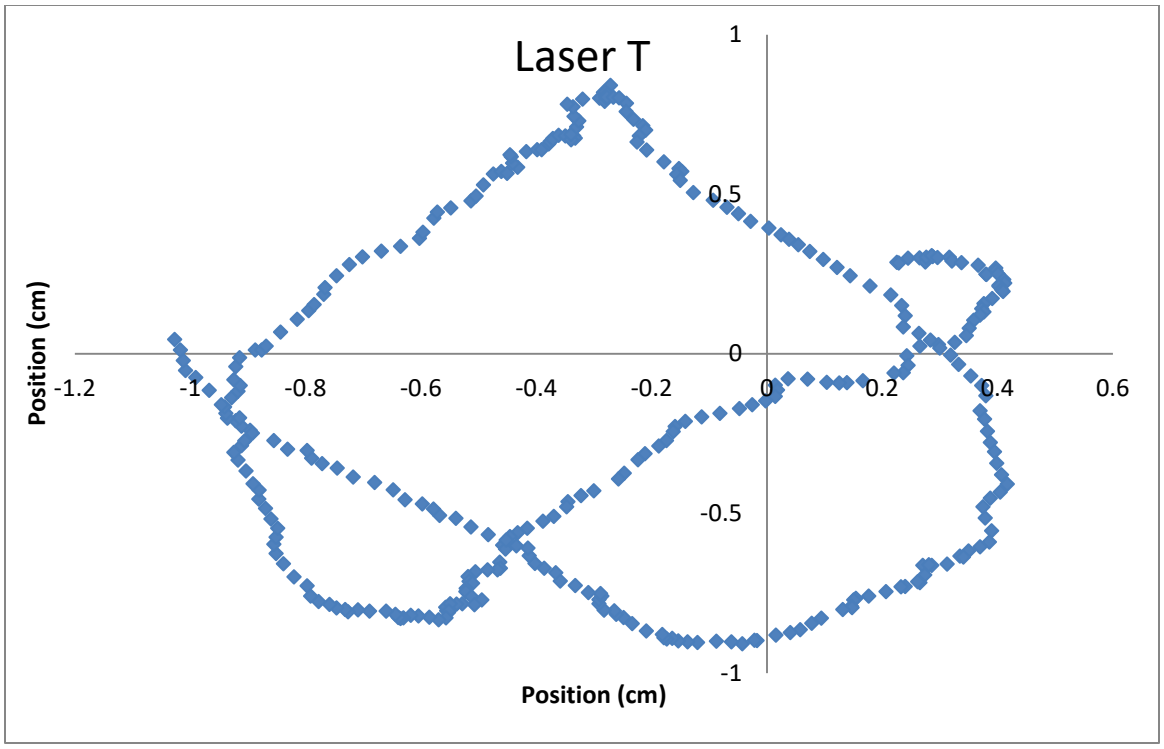

Figure 42. Data from Laser T during test 10V from 25 to 25.333 seconds

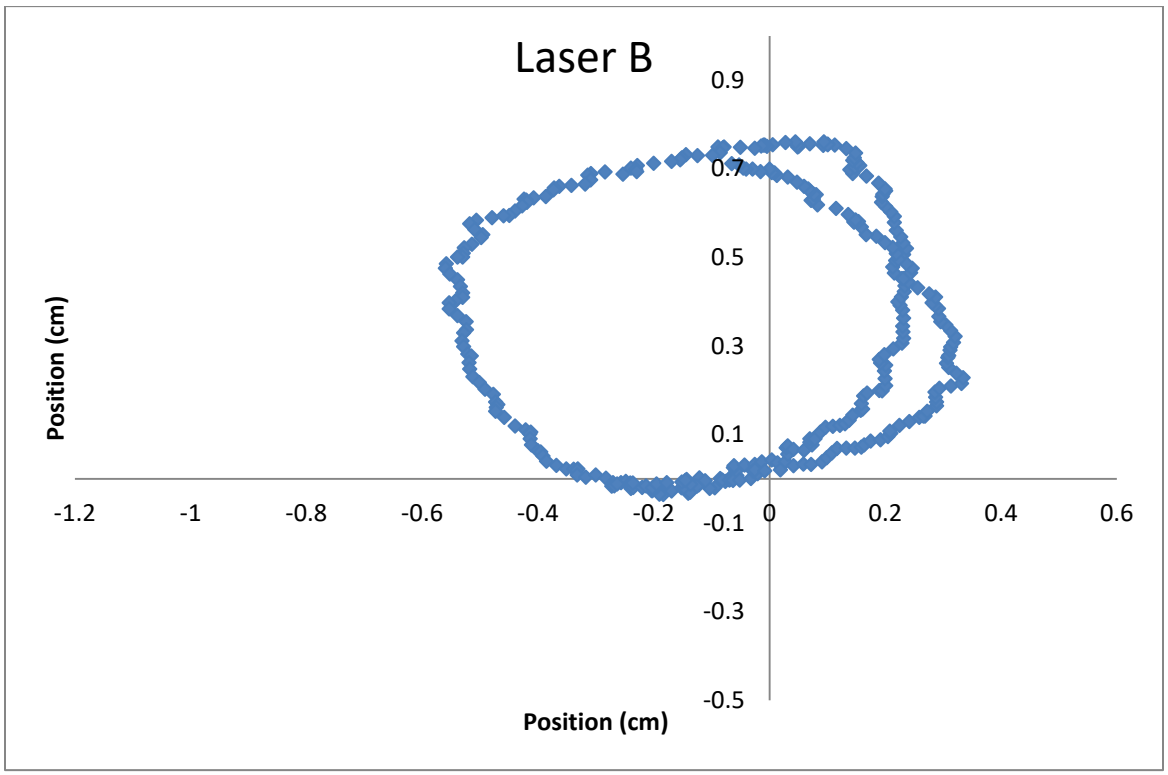

Figure 43. Data from Laser B during test 10V from 25 to 25.333 seconds

5.4 Analytic Confirmation

Visually, it appears information is being lost at each decrement of sampling frequency, there is also evidence that 1 kHz is too great a sampling rate. While the zoomed in visuals at 1 kHz reveal things such as approximate rotational frequency and shape of the traveling path, when sampling at 100 Hz does not seem to be much information loss. Conversely, the information lost moving from 100 Hz to 10 Hz seems to be great. Since all these statements are based on qualitative analysis, a qualitative method of analysis is needed to confirm the initial visual conclusions.

5.4.1 Fourier Transforms

Figures 34 and **35** indicate definable repetition in the waveform, and because of this a type of analysis called discrete Fourier transforms (DFT) becomes a clear choice in approach for analysis. DFT is a transform which, in short, converts a waveform such as the one in **Figure 34** into individual sinusoidal waveforms of uniform amplitude. A common algorithm for computing the DFT is the fast Fourier transform (FFT), and has grown to be so useful that it is an inherent function in computational programs such as MATLAB. Graphs generated through this process plot peaks at frequencies along the X axis, with their normalized amplitude along the Y axis. In an ideal transform, there would be a completely smooth line any time there is not an instant peak or a triangle-like peak. In non-ideal transforms, noise can cause the flat line to be jagged. By importing the data from all the experiments at all the frequencies, FFTs were generated that correspond to each imported wave form, generating 60 unique figures, with an additional 20 figures created to zoom in on the 1 kHz FFT. The FFT plots contained within the body of work are those corresponding to the 10V test, while all five tests can be found in **Appendix D**.

5.4.2 Fast Fourier Transform Plots

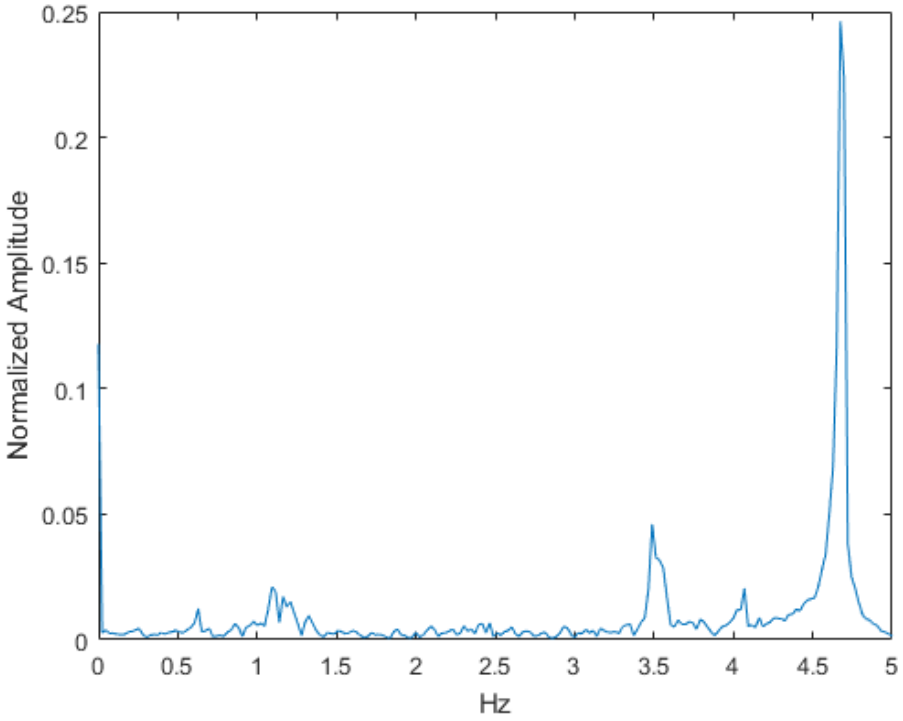

Figure 44. FFT of the X axis of the bottom laser during the 10V test at 10 Hz

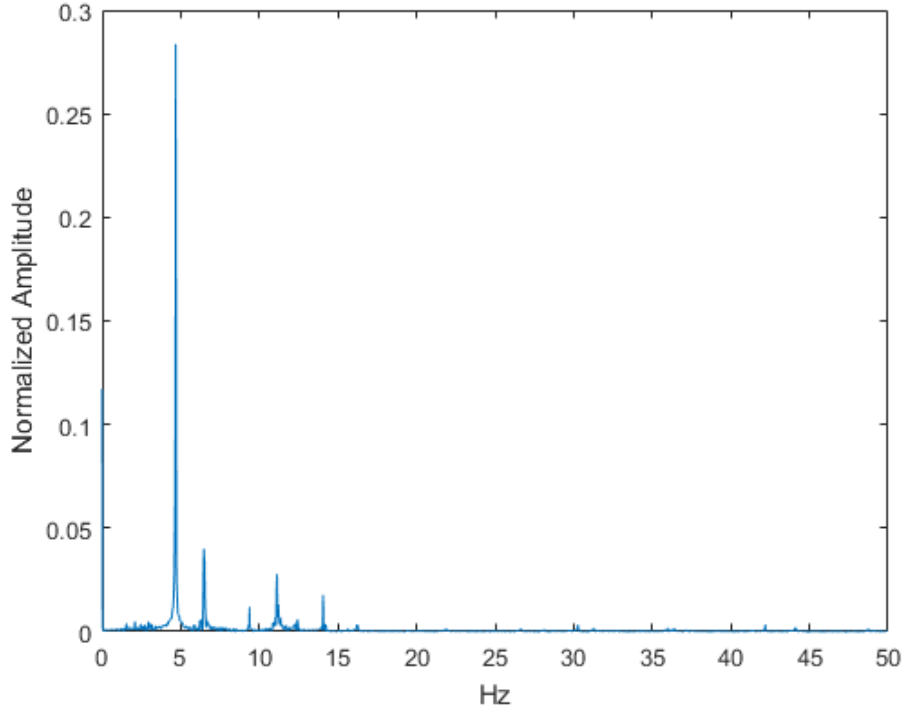

Figure 45. FFT of the X axis of the bottom laser during the 10V test at 100 Hz

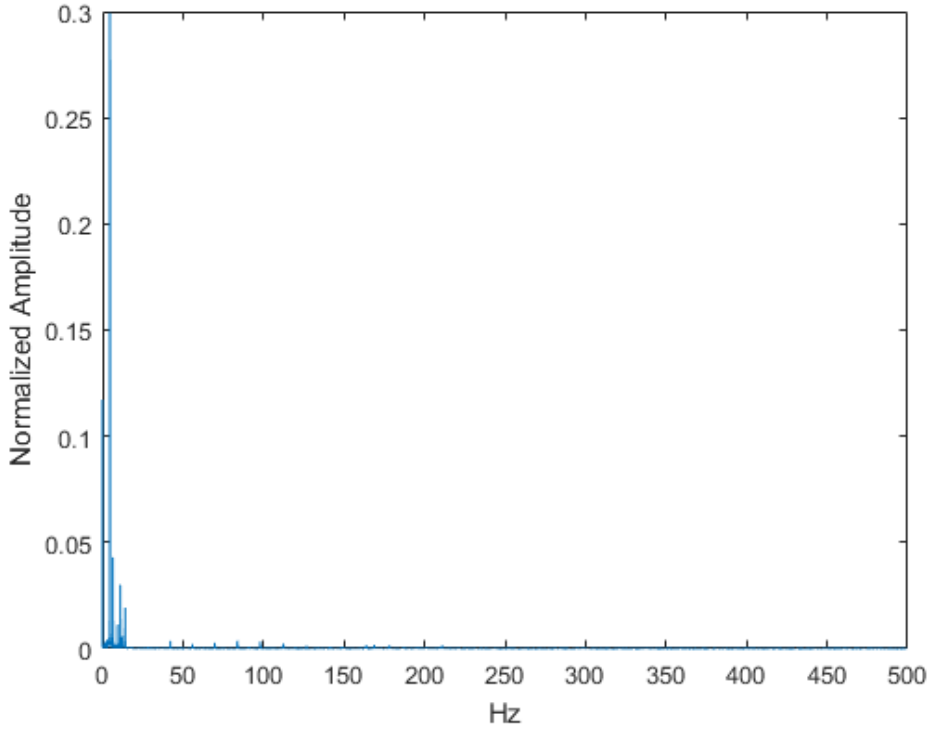

Figure 46. FFT of the X axis of the bottom laser during the 10V test at 1 kHz

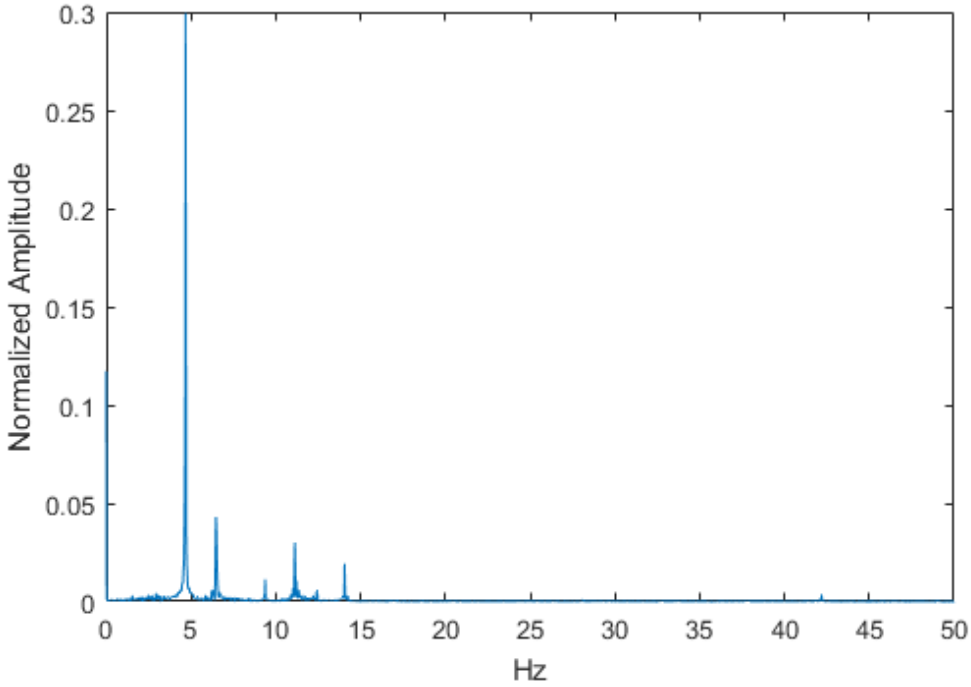

Figure 47. FFT of the X axis of the bottom laser during the 10V test at 1 kHz

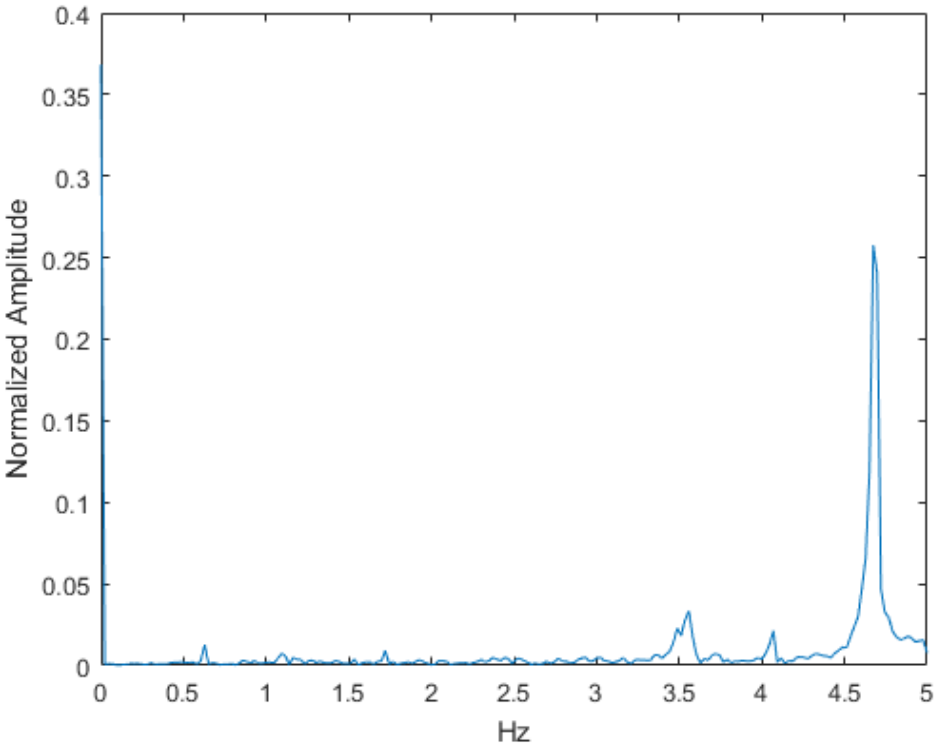

Figure 48. FFT of the Y axis of the bottom laser during the 10V test at 10 Hz

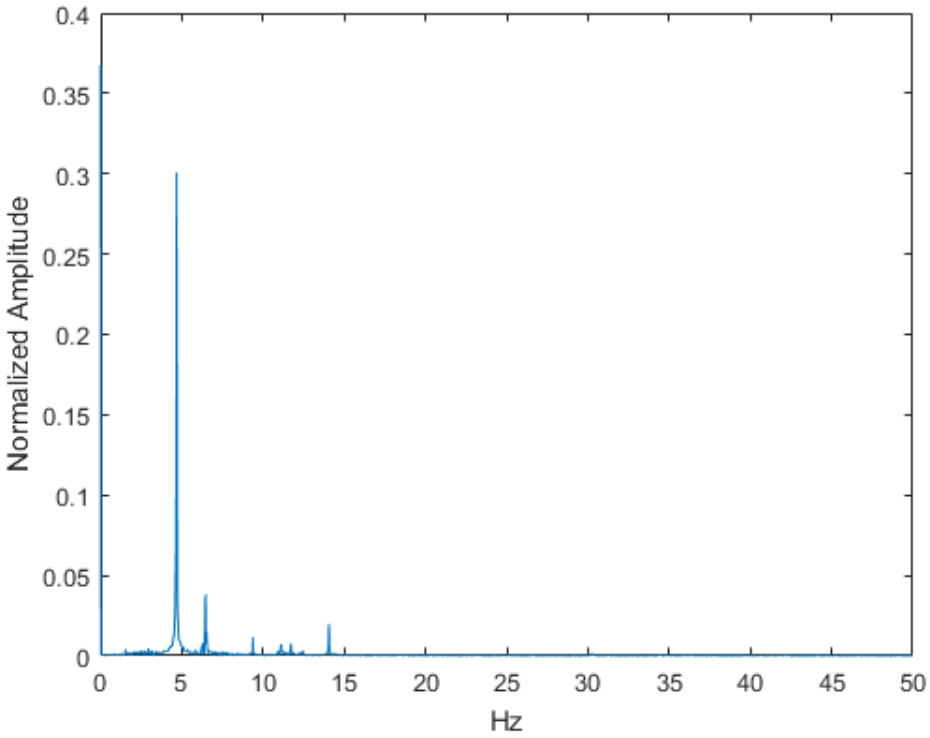

Figure 49. FFT of the Y axis of the bottom laser during the 10V test at 100 Hz

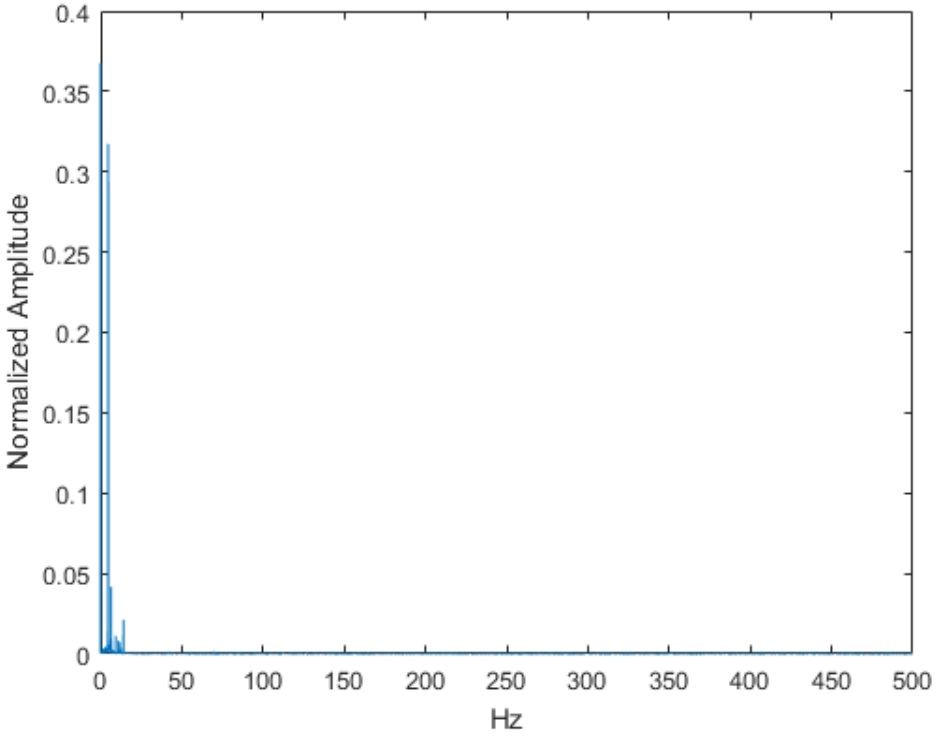

Figure 50. FFT of the Y axis of the bottom laser during the 10V test at 1 kHz

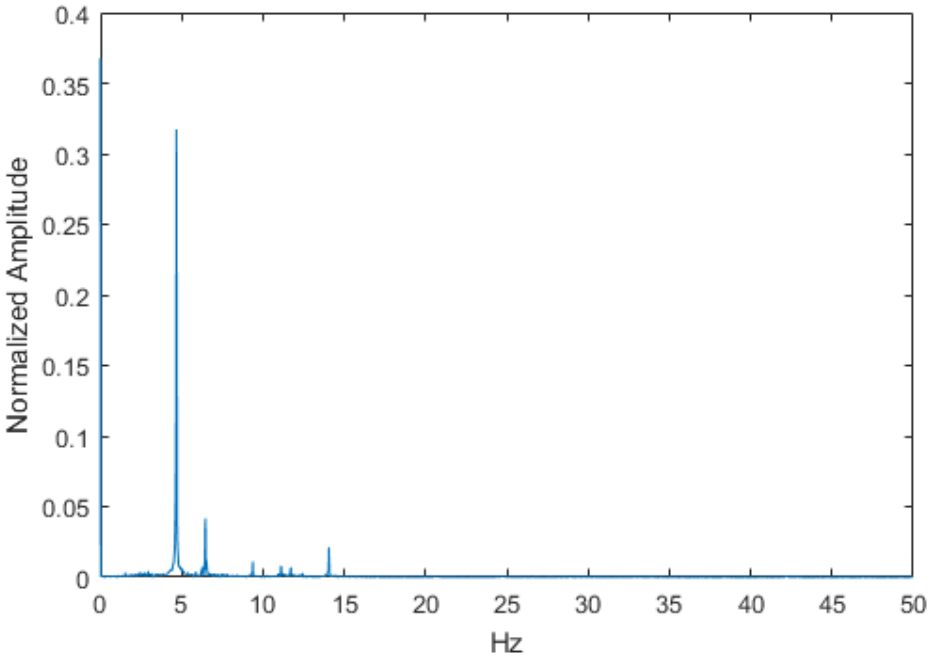

Figure 51. FFT of the Y axis of the bottom laser during the 10V test at 1 kHz zoomed in

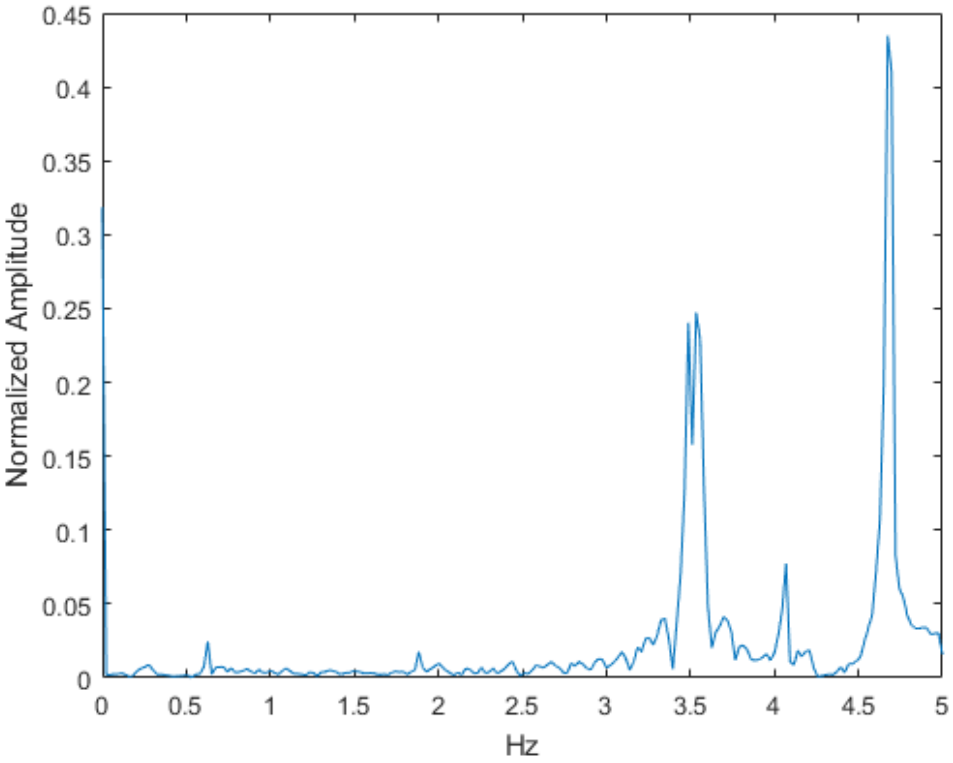

Figure 52. FFT of the X axis of the top laser during the 10V test at 10 Hz

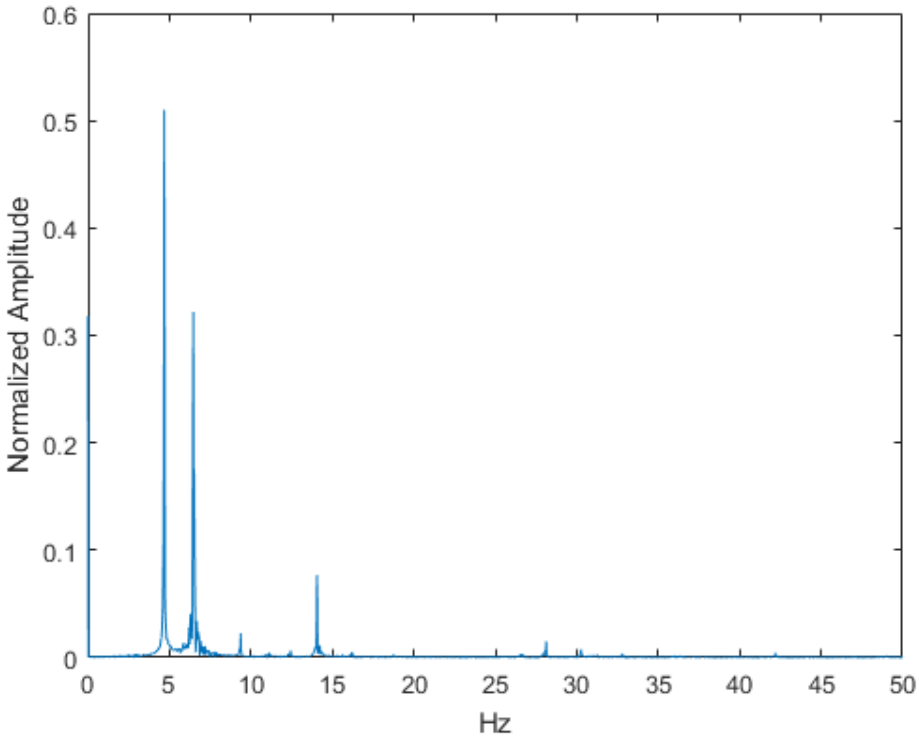

Figure 53. FFT of the X axis of the top laser during the 10V test at 100 Hz

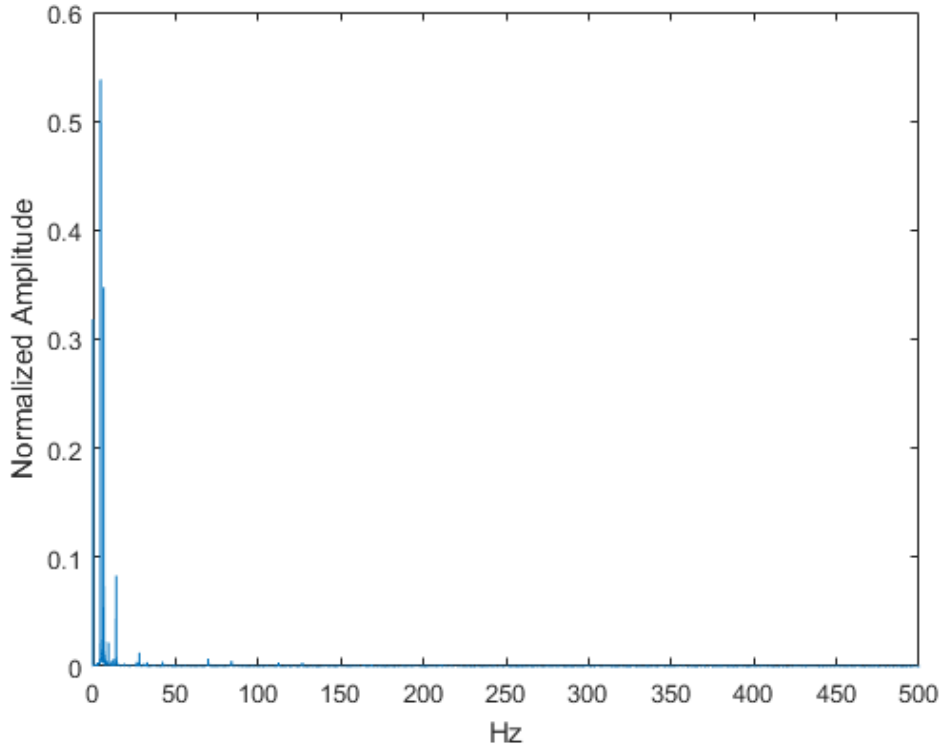

Figure 54. FFT of the X axis of the top laser during the 10V test at 1 kHz

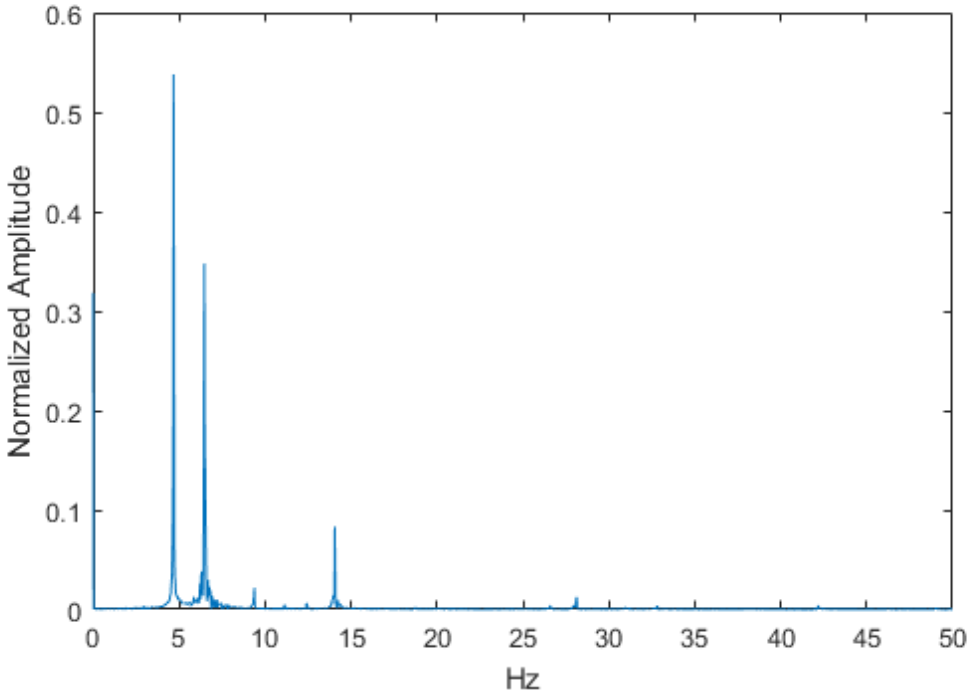

Figure 55. FFT of the X axis of the top laser during the 10V test at 1 kHz zoomed in

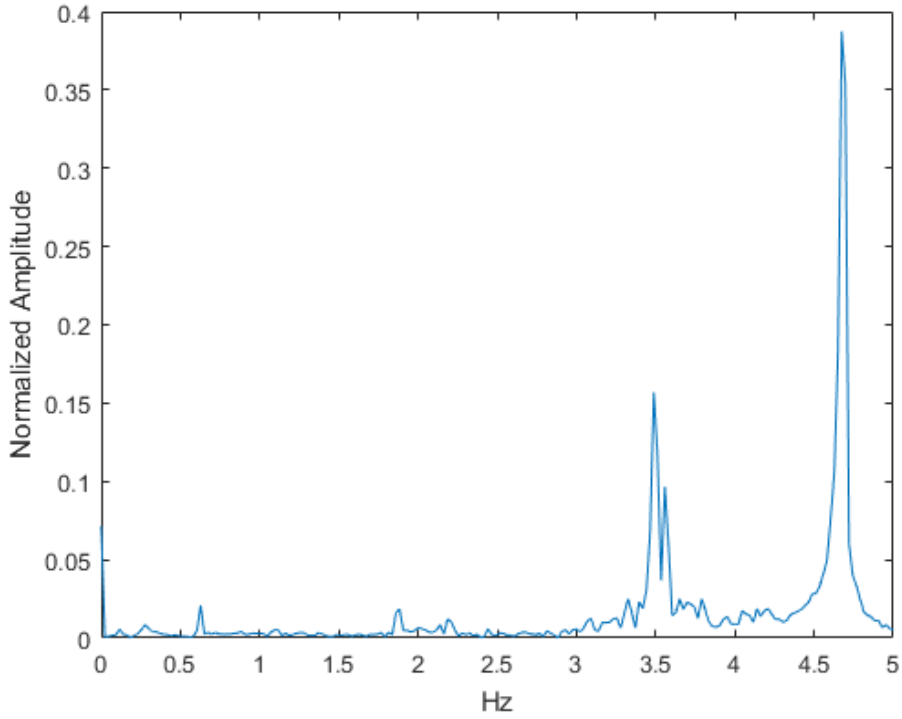

Figure 56. FFT of the Y axis of the top laser during the 10V test at 10 Hz

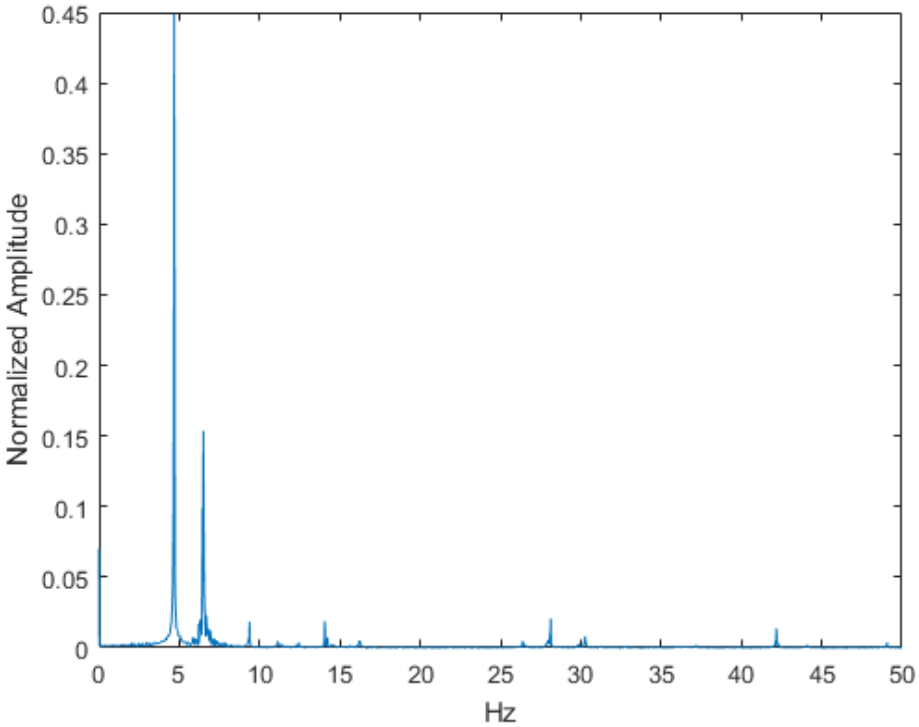

Figure 57. FFT of the Y axis of the top laser during the 10V test at 100 Hz

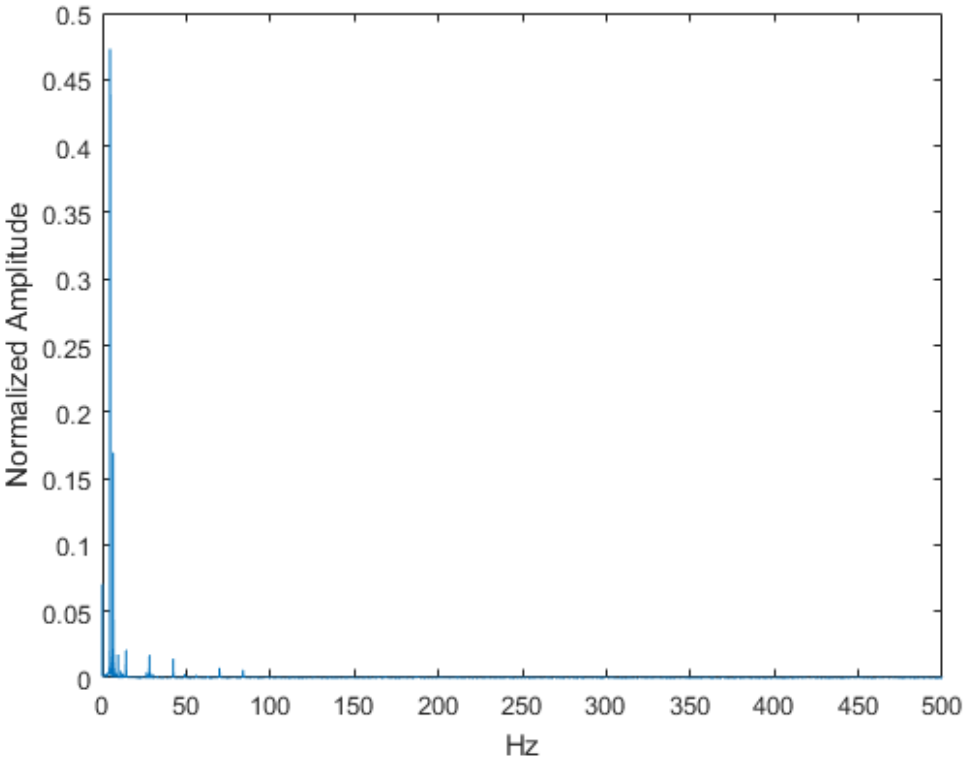

Figure 58. FFT of the Y axis of the top laser during the 10V test at 1 kHz

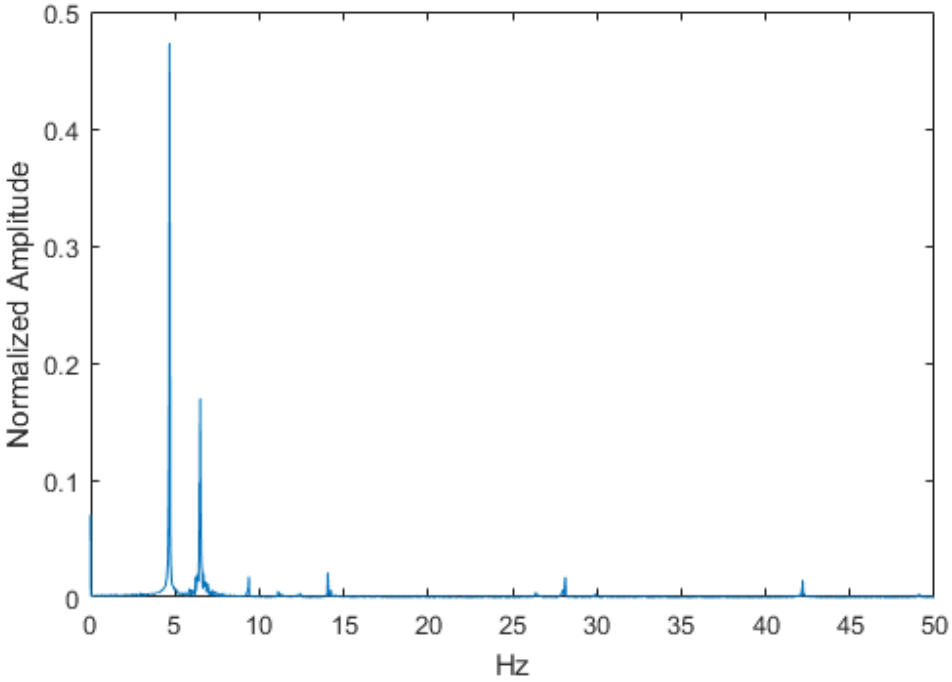

Figure 59. FFT of the Y axis of the top laser during the 10V test at 1 kHz zoomed in

5.4.3 FFT Insights

Initially, it becomes clear that only very minor contributions to the waveform occur after the 15 Hz mark. While it is tempting to disregard the frequency peaks occurring after 15 Hz, similar frequency peaks occur at during all five tests. Since the primary goal of this was to target information lost as sampling frequency is decreased, it is important to note patterns both across tests and across sampling frequencies. The second obvious insight is that because most peaks occur before 15 Hz, it is difficult to draw conclusions from the 1 kHz graphs. This caused the need for an inclusion of a magnification of the graphs to 50 Hz. This range was selected as it is the same range as the 100 Hz FFTs, which is important because discrepancies between data contained in the 100 Hz graphs and 1 kHz graphs could potentially be aliasing or other issues.

Moving past the initial, surface level conclusions from the FFTs, the actual plotted amplitudes were reviewed. The first conclusion drawn from the peaks in this set of figures is that every single plot has its largest peak right after 4.5 Hz. This makes sense as it was noted in **Figures 42** and **43** that the drill string rotated around its center just over 1.5 times in a 0.333 second period, resulting in just over 4.5 revolutions per second. In the 100 Hz and 1 kHz graphs, the next three largest amplitudes, in order, occur at roughly 6.5 Hz, 14 Hz, 9 Hz, and 27 Hz. This is important because three of those frequencies do not occur on a 10 Hz FFT, yet a peak occurs at roughly 3.5 Hz on every single 10 Hz FFT that does not occur on the other sampling frequencies. This is likely due to the initial waveform having been aliased, resulting in an incorrect FFT being systematically generated across all tests. A far less major occurrence of this phenomenon exists at a peak at roughly 31 Hz that appears on the 100 Hz FFTs but not at the 1 kHz FFTs, but is systematic across all tests.

Comparing the X axis FFTs to their respective Y FFTs generates insights to even more phenomenon observed in the qualitative analysis. In the top laser of every test, the 6.5 Hz normalized amplitude in the Y axis ranged from one-half to two-thirds the normalized amplitude in the X direction, making the X axis FFTs have the larger normalized amplitude every time when compared to their Y axis FFT counterparts. This phenomenon ties back to how the top laser positional graphs are elliptic in nature, with the X axis as the major axis and the Y axis as the minor axis. Due to the more controlled nature of the bottom laser, the 6.5 Hz amplitude is far less great across all tests respective to their top laser counterparts, but there is still a trend of the Y axis waveform consistently generating 6.5 Hz peaks of lower amplitude than the X axis counterparts.

Finally, the most interesting observation is how greatly some peaks in the FFT graphs change across RPMs, while other peaks stay practically the same. First, the FFT consistently plot the revolution frequency as the predominate peak. Then, the 6.5 Hz peak would be the second most, but the range across tests varies from 0.05 to over 0.3. This does not increase or decrease linearly with RPM, which was unexpected. Initial thoughts would be that it is a function of how many nodes are occurring in the wave, but the two largest amplitudes actually occur during the 6V and the 10V tests, with 8V – the middle test – having the lowest amplitude at this frequency. Why this occurs is unclear at this point and warrants further testing. The final insight from comparing samples is that in tests 6V, 7V and 8V, there is a frequency peak at roughly 11Hz and 14 Hz, but at 9V a third peak appears between the two, then finally at 10V the 14 Hz peak becomes much larger, with the 11 Hz and 12.5 Hz peaks still present. Other than a linear frequency increase as testing RPMs increase, this is the only other phenomenon that develops relative to RPM. This means that if further testing occurs, this should be a target of investigation.

6. Conclusions

In summary, the following objectives have been met:

1. Reviewed existing literature regarding vibrational data collection

This showed little to no work has been done in the realm of high frequency collection, nor had much work been done on lateral vibrations with physical data. The work that is done on lateral vibrations is primarily reserved to computer modeling.

2. Successfully integrated laser measuring system into a pre-existing physical drill string model

These measuring systems are fully capable of capturing high speed motion at resolutions above 1 kHz at multiple points along the drill string, as well as transmit that data to a computer real time to be analyzed and stored.

3. Proved that collecting data along the drill string at frequencies below 100 kHz may result in dramatic losses in information both quantitatively and qualitatively

Additionally, it was proved that there is less sampling loss when data is collected at less than 1 kHz, but this information is more useful for complex analysis than for immediate conclusions.

7. Moving Forward

This work sets up for continued work in two different ways. The first is continued work in this same vain. This work only changes RPM and it only tests 5 of them. A more comprehensive data set will generate more insight into how different parameters influence the motions along the drill string in different ways and run FFT to see if the trends noted here are noted through different combinations of untested RPM and WOB. The second is by applying the data collected in these tests to machine learning techniques, a growing interest in the Oil and Gas field. Preliminary investigation into the application of machine learning show that a technique referred to as Recurring Neural Networks shows promise with handling the data sets.

Final recommendation would be to further press into both of these continued works, as an increased data set will inherently elevate the level of work done with machine learning techniques. Additionally, since the lasers are Z axis mobile, it is recommended to repeat these tests measuring at an expected node to further test the assumption that the wave functions as a standing wave.

References

Burk, Phil. *Music and Computers: a Theoretical and Historical Approach*. Key College Pub., 2005.

Chacin, Antonio Rafael Marquez. “Investigation of Drillstring Vibrations Using Finite Element Method Simulations and Design and Implementation of Experimental Setup.” *University of Oklahoma*, 2017.

Chin, Wilson C. *Wave Propagation in Drilling, Well Logging, and Reservoir Applications*. Scrivener Publishing, Wiley, 2014.

Cunningham, R. A. (May 1, 1968). "Analysis of Downhole Measurements of Drill String Forces and Motions." ASME. *J. Eng. Ind*. May 1968; 90(2): 208–216. https://doi.org/10.1115/1.3604616.

Deily, F. H., Dareing, D. W., Paff, G. H., Ortloff, J. E., and Lynn, R. D. (May 1, 1968). "Downhole Measurements of Drill String Forces and Motions." ASME. *J. Eng. Ind*. May 1968; 90(2): 217–225. https://doi.org/10.1115/1.3604617.

Darein, D. W., and B. J. Livesay. 1968. "Longitudinal and Angular Drillstring Vibrations with Damping." Journal of Engineering for Industry 671-679.

Dunayevsky, V., Abbassian, F., & Judzis, A. (1993). Dynamic stability of drillstrings under fluctuating weight on bit. SPE Drilling and Completion, 8(2), 84–92.

Esmaeili, A., B. Elahifar, R. K. Fruhwirth, and G. Thonhauser. 2012. "Laboratory Scale Control of Drilling Parameters to Enhance Rate of Penetration and Reduce Drill String Vibration." SPE Saudi Arabia Section Technical Symposium and Exhibition. Al-Khobar, Saudi Arabia: Society of Petroleum Engineers.

Heisig, G., & Neubert, M. (2000, January 1). Lateral Drillstring Vibrations in Extended-Reach Wells. Society of Petroleum Engineers. doi:10.2118/59235-MS.

Jardine, S, Malone, D, and Sheppard, M. Putting a damper on drilling's bad vibrations. Netherlands: N. p., 1994. Web.

Kapitaniak, Marcin, Vahid V Hamaneh, Joseph Paez Chavez, Krishnan Nandakumar, and Marian Wiercigroch. 2015. "Unveiling complexity of drill-string vibrations: Experiments and modelling." International Journal of Mechanical Sciences 324- 337.

Kelly, S. Graham. *Mechanical Vibrations: Theory and Applications, SI*. Cengage Learning, 2012.

Ling, Samuel K, Sanny, Jeff, and Moebs, Bill. “16.7: Standing Waves and Resonance.” *Physics LibreTexts*, Libretexts, 17 Mar. 2020, phys.libretexts.org/Bookshelves/University_Physics/Book%3A_University_Physics_(OpenStax)/Map%3A_University_Physics_I_-_Mechanics%2C_Sound%2C_Oscillations%2C_and_Waves_(OpenStax)/16%3A_Waves/16.07%3A_Standing_Waves_and_Resonance.

Lin, T., Zhang, Q., Lian, Z., Xiao, Z., Wang, T., Li, G. and Ding, J. 2018. “Experimental study on vibrational behaviors of horizontal drillstring.” Journal of Petroleum Science and Engineering. Elsevier. 311-319.

Macpherson, J. D., and J. S. Mason. 1993. "Surface Measurement and Analysis of Drillstring Vibrations." SPE/IADC Drilling Conference. Amsterdam, Netherlands: SPE/IADC.

Maiman, T. Stimulated Optical Radiation in Ruby. *Nature* **187,** 493–494 (1960). https://doi.org/10.1038/187493a0.

Moradi, S., and K. Ranjbar. 2009. "Experimental and computational failure analysis of drillstrings." Engineering Failure Analysis 923-933.

National Instruments “What Is Data Acquisition?” *What Is Data Acquisition? National Instruments*, National Instruments, www.ni.com/data-acquisition/what-is/.

Navarro-Lopez, E. M., and D. Cortes. 2007. "Avoiding harmful oscillations in a drillstring through dynamical analysis." Journal of Sound and Vibration 151- 171.

Nave, Rod. *HyperPhysics*, Georgia State University, hyperphysics.phy-astr.gsu.edu/hbase/hframe.html.

Patil, P. A. 2013. Investigation of Torsional Vibrations in a Drillstring Using Modeling and Laboratory Experimentation (Doctoral Dissertation). Clausthal University of Technology: Papierflieger-Verlag.

Qu, Y. Wang, T. and Zhu, Z. "Vision-Aided Laser Doppler Vibrometry for Remote Automatic Voice Detection," in *IEEE/ASME Transactions on Mechatronics*, vol. 16, no. 6, pp. 1110-1119, Dec. 2011.

Shannon, Claude E. "Communication in the Presence of Noise," in *Proceedings of the IRE*, vol. 37, no. 1, pp. 10-21, Jan. 1949.

Shor, R. J., M. Pryor, and E. Van Oort. 2014. "Drillstring Vibration Observation, Modeling and Prevention in the Oil and Gas Industry." ASME 2014 Dynamic Systems and Control Conference. San Antonio, TX: ASME.

Srivastava, Saket & Teodoriu, Catalin. (2019). An extensive review of laboratory scaled experimental setups for studying drill string vibrations and the way forward. Journal of Petroleum Science and Engineering. 182. 106272. 10.1016/j.petrol.2019.106272.

Sotomayor, Gabriel P.G, Joao Carlos Placido, and J.C Cunha. 1997. "Drillstring Vibration: How to Identify and Suppress." Fifth Latin American and Caribbean Petroleum Engineering Conference and Exhibition. Rio de Janeiro, Brazil: Society of Petroleum Engineers, Inc. (Tucker and Wang 1999).

Thorlabs "Product Catalog." *Thorlabs*, www.thorlabs.com/navigation.cfm.

Tucker, R. W, and C. Wang. 1999. "An Integrated Model for Drill-String Dynamics." Journal of Sound and Vibration 123-165.

U.S. Energy Information Administration, Independent Statistics & Analysis. (2016). *Trends in U.S. Oil and Natural Gas Upstream Costs*. Retrieved from https://www.eia.gov/analysis/studies/drilling/pdf/upstream.pdf.

Wen, X., Guan, Z., Zhou, Y., Zhang, B. 2018 “Experimental Research on Lateral Vibration of Drill String in the Highly Deviated Well.” Offshore Technology Conference Asia, Kuala Lumpur.

Wolf, S. F., Zacksenhouse, M., & Arian, A. (1985, January 1). Field Measurements of Downhole Drillstring Vibrations. Society of Petroleum Engineers. doi:10.2118/14330-MS.

Younggang, Liu, Li Fangpo, Xu Xin, Yang Biyu, and Lu Caihong. 2011. "Simulation Technology in Failure Analysis of Drill Pipe." 2011 SREE Conference on Engineering Modeling and Simulation. Elsevier. 236-241.

Appendix A Specification Sheets

SPECIFICATIONS

Model		LS-7030M
Type		Standard
Classification		with monitor camera
Measurement range		0.3 to 30 mm 0.01" to 1.18"
Smallest detectable object		0.3 mm 0.01"
Transmitter/receiver distance		160 ±40 mm 6.30" ±1.57"
Repeatability		±0.15 µm ±0.000006"*1
Measurement accuracy		±2 µm ±0.00008"*2
Sampling cycle		2,400 samples/sec.*3
CCD scanning range		Approx. 33 mm 1.30"
Light source		GaN green LED
Monitor camera		Provided
Environmental resistance	Enclosure rating	IP64*4
	Ambient temperature	0 to +50 °C 32 to 122 °F
	Relative humidity	35 to 85 % RH (No condensation)
Weight		Transmitter: Approx. 420 g, Receiver: Approx. 570 g, Base: Approx. 430 g

*1 The value of ±2σ when the outer diameter of a rod 10 mm 0.39" in diameter is measured at the center of the measuring area while the number of averaging measurements is set to 512.
*2 The error when a moving rod 10 mm 0.39" in diameter is measured in the measuring area of 10 x 20 mm 0.39" x 0.79".
*3 1,200 samples/sec. when the mutual interference prevention function is used.
*4 The connector section is excluded.

Figure A-1. Table of specifications for the Keyence Lasers used for measuring movement of the drill string

KEY HIGHLIGHTS

The USB-1608G Series of high-speed multifunction USB data acquisition (DAQ) devices are ideal for low to medium channel count applications, and provide analog along with digital and counter/timer functions. Up to two analog outputs are available. OEM versions are available for embedded applications.

ANALOG INPUT		
CHANNELS	RESOLUTION	MAX SAMPLE RATE
16 SE/8 DIFF	16-bit	Up to 500 kS/s
SAMPLING	RANGES	ISOLATION
Multiplexed	±10 V, ±5 V, ±2 V, ±1 V	—

ANALOG OUTPUT		
CHANNELS	RESOLUTION	SPEED
Up to 2	16-bit	Up to 500 kS/s

DIGITAL I/O		
CHANNELS	COUNTER/TIMERS	ENCODER
8	2/1	—

SOFTWARE		POWER
OS SUPPORT	DRIVERS	POWER
Windows®, Android™, and Linux®	Universal Library™ SW Suite	Bus powered

Figure A-2. Table of specifications for the DAQ used to transmit data to the computer

Figure A-3 Bottom Laser with steel plate and 2D caliper

Appendix B Complete Graphs

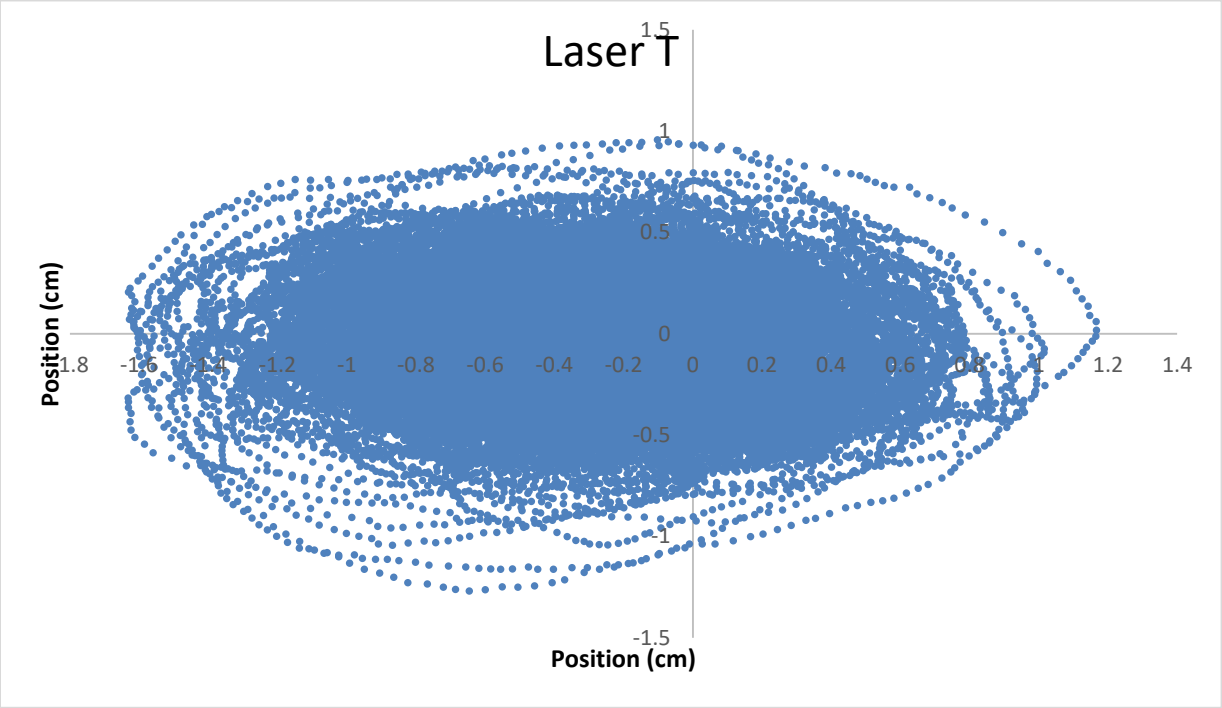

Figure B-1. The Top positioned planer behavior of the drill string during the 6V test; 1 kHz

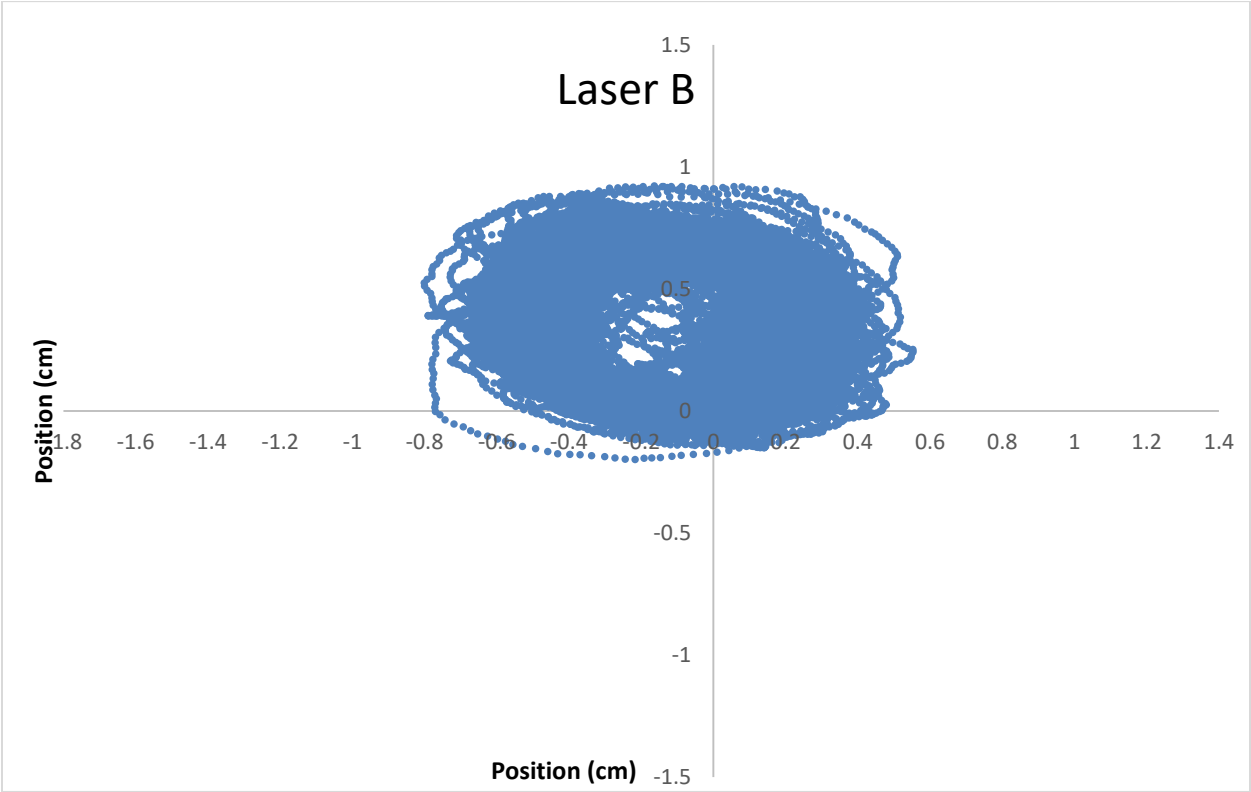

Figure B-2. The bottom positioned planer behavior of the drill string during the 6V test; 1 kHz

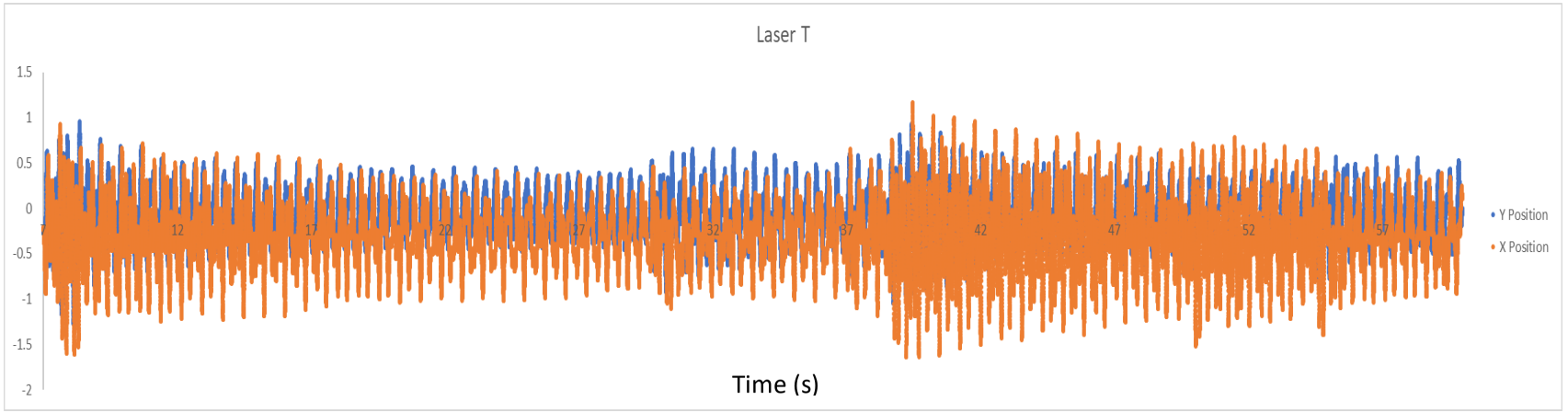

Figure B-3. The position of the drill string at the top plane as a function of time during the 6V test; 1khz

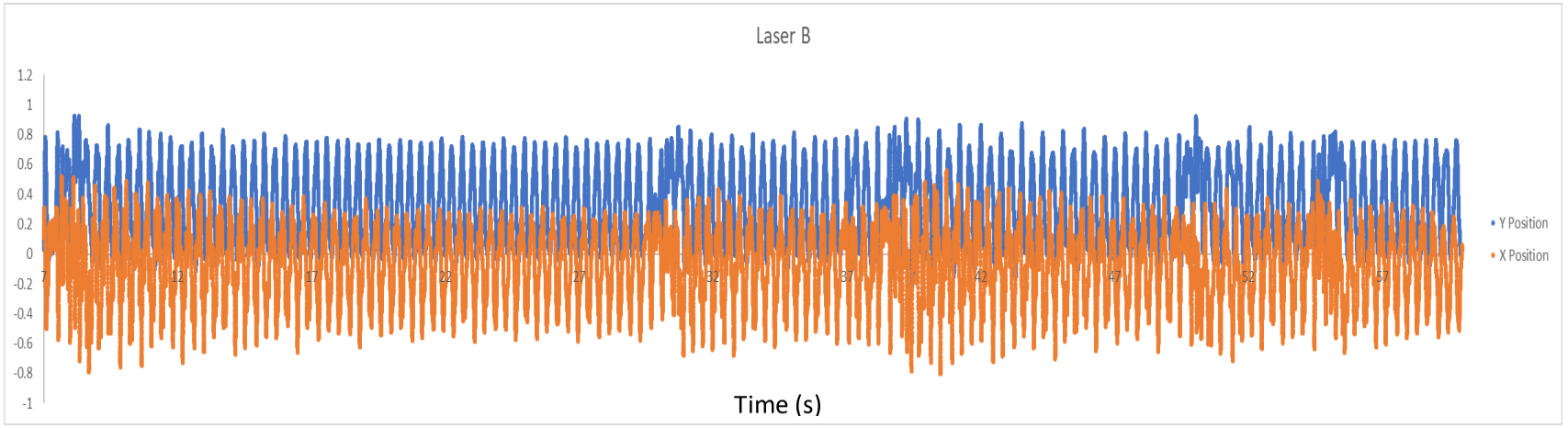

Figure B-4. The position of the drill string at the bottom plane as a function of time during the 6V test; 1 kHz

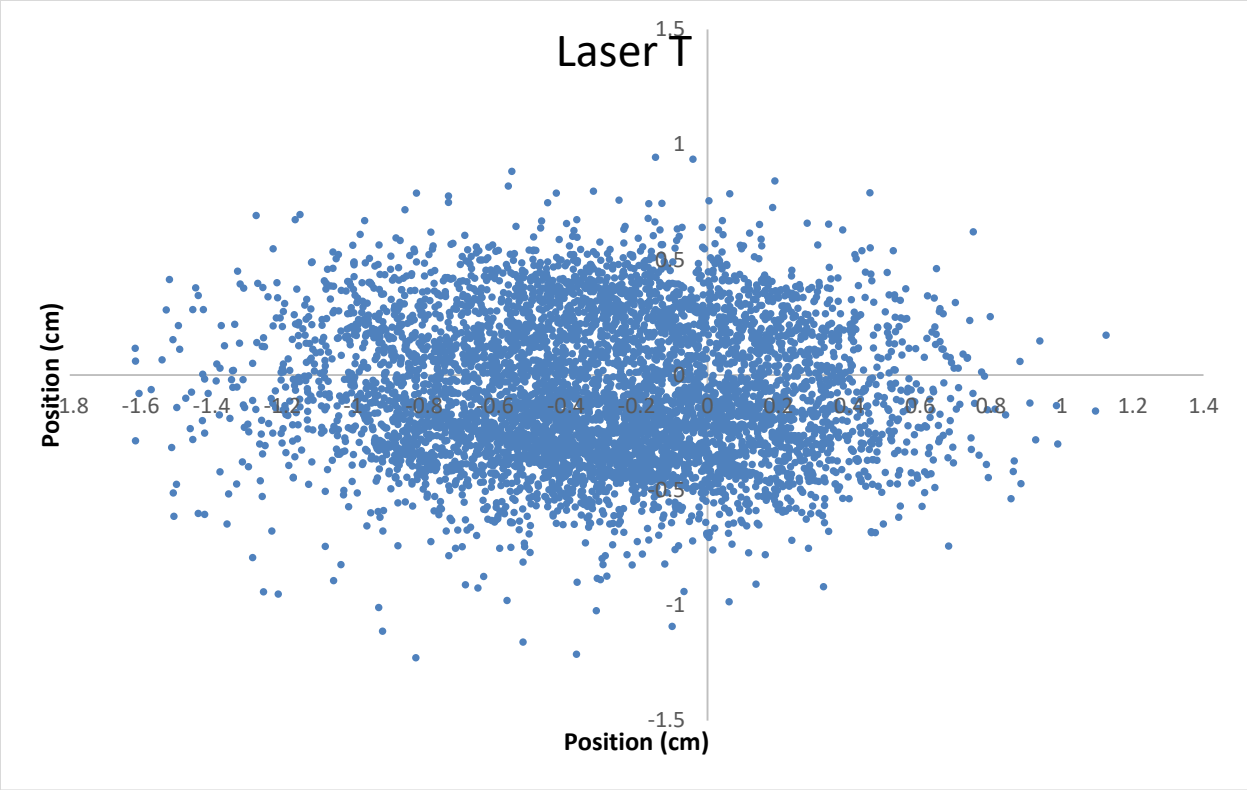

Figure B-5. The top positioned planer behavior of the drill string during the 6V test; 100 Hz

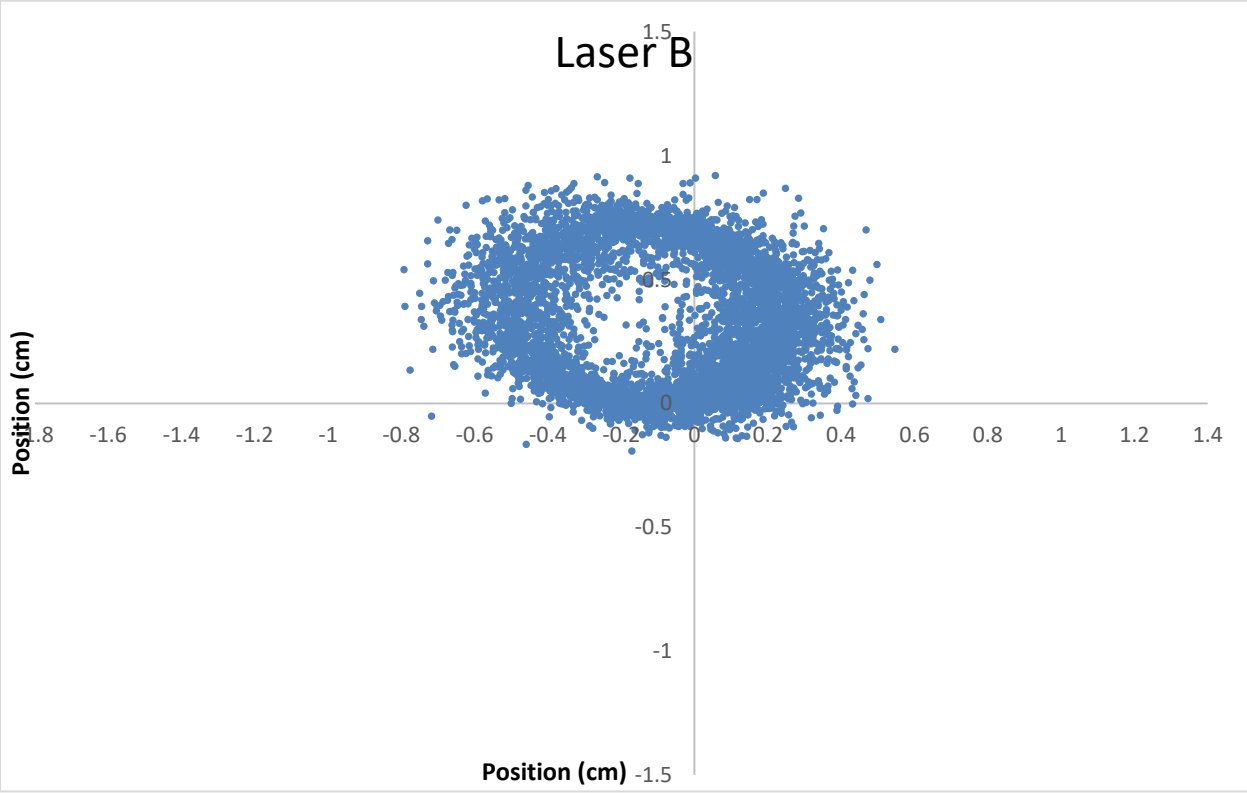

Figure B-6. The bottom positioned planer behavior of the drill string during the 6V test; 100 Hz

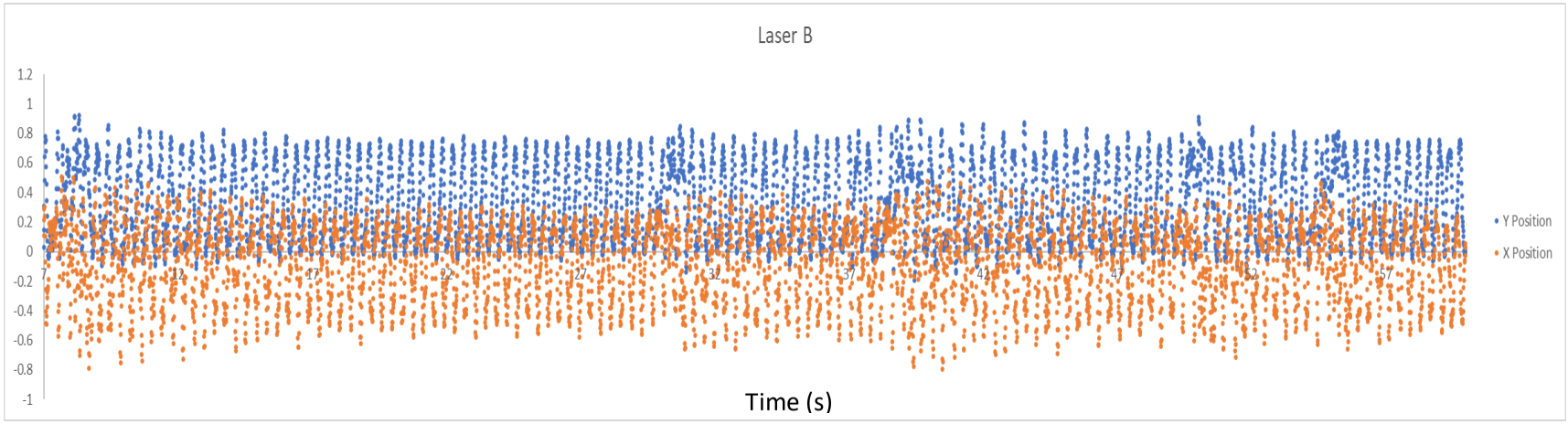

Figure B-7. The position of the drill string at the top plane as a function of time during the 6V test; 100 Hz

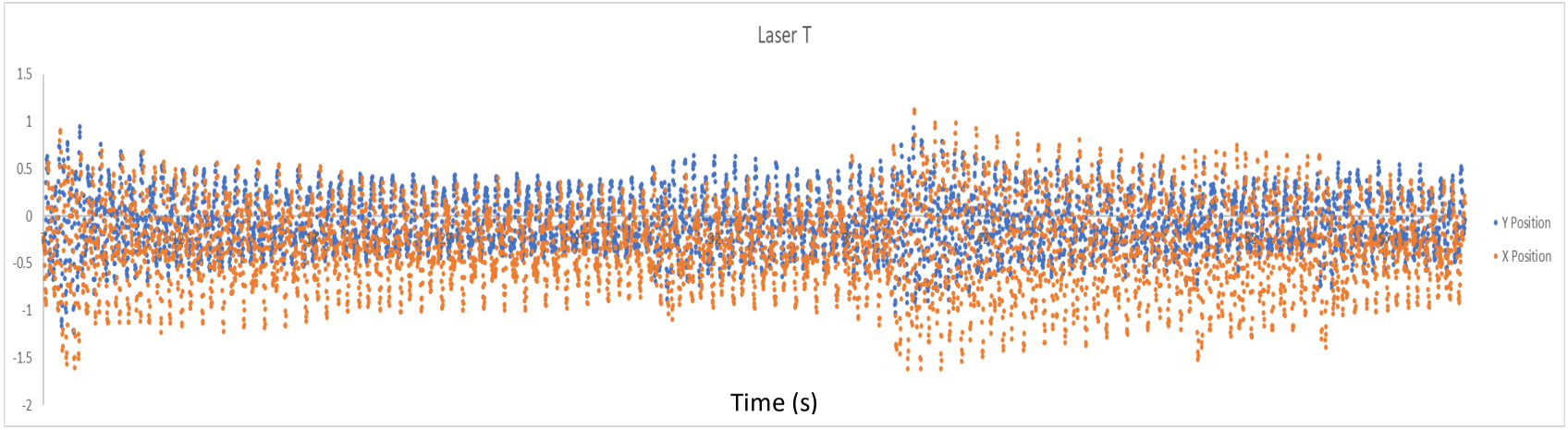

Figure B-8. The position of the drill string at the bottom plane as a function of time during the 6V test; 100 Hz

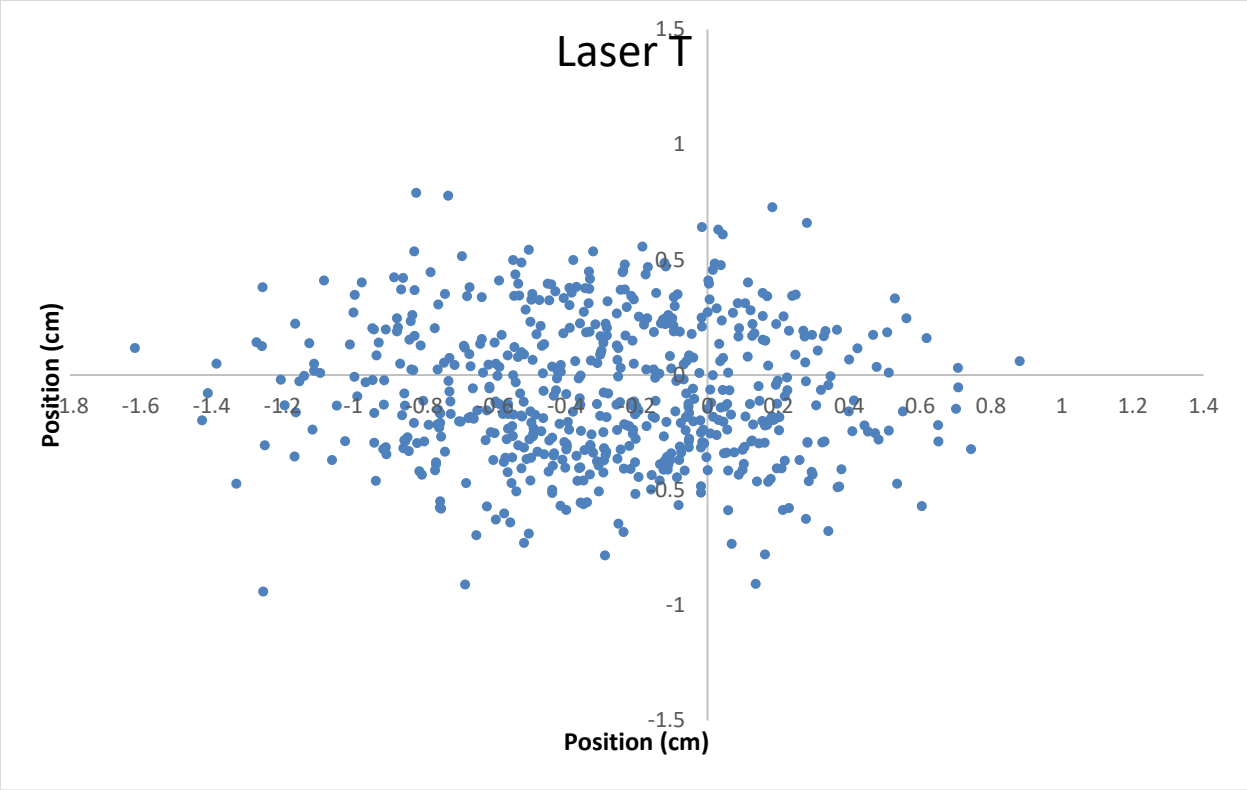

Figure B-9. The top positioned planer behavior of the drill string during the 6V test; 10 Hz

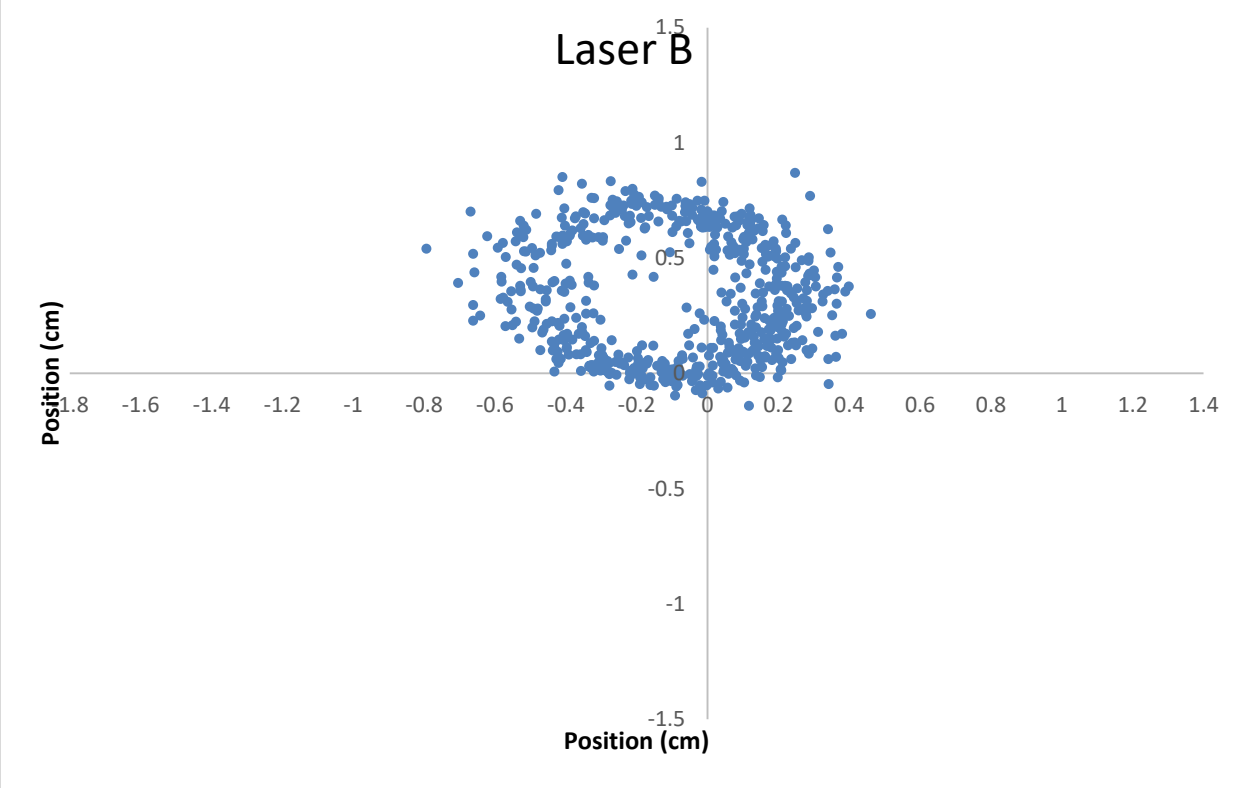

Figure B-10 The bottom positioned planer behavior of the drill string during the 6V test; 10 Hz

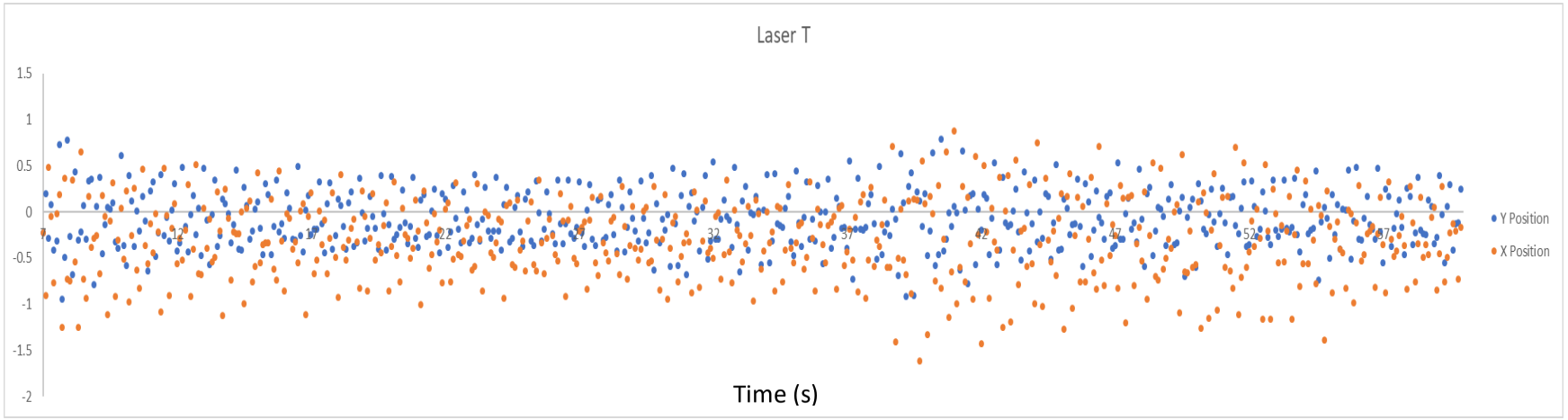

Figure B-11. The position of the drill string at the top plane as a function of time during the 6V test; 10 Hz

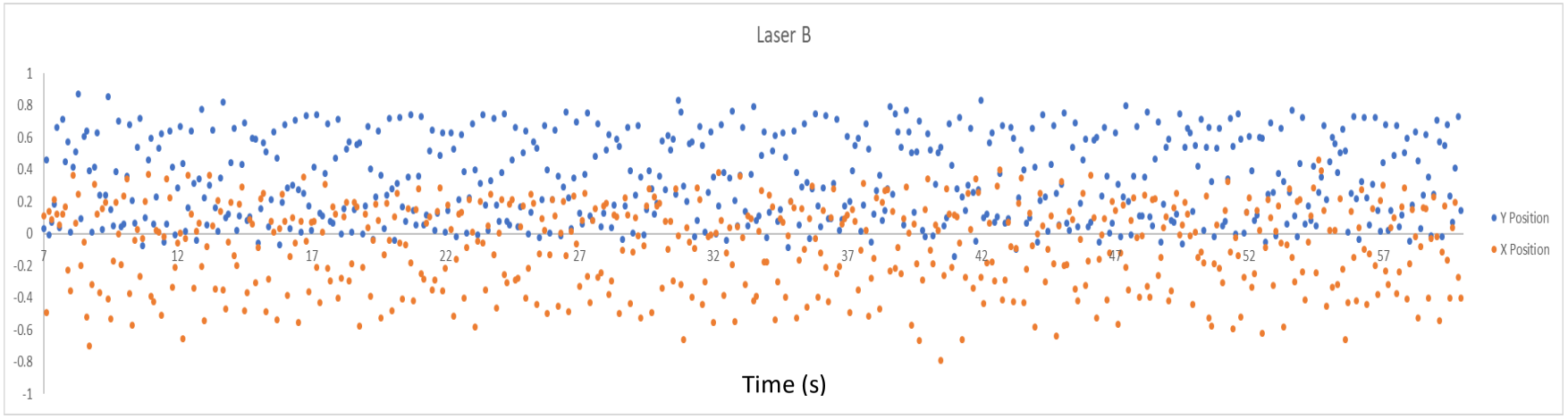

Figure B-12. The position of the drill string at the bottom plane as a function of time during the 6V test; 10 Hz

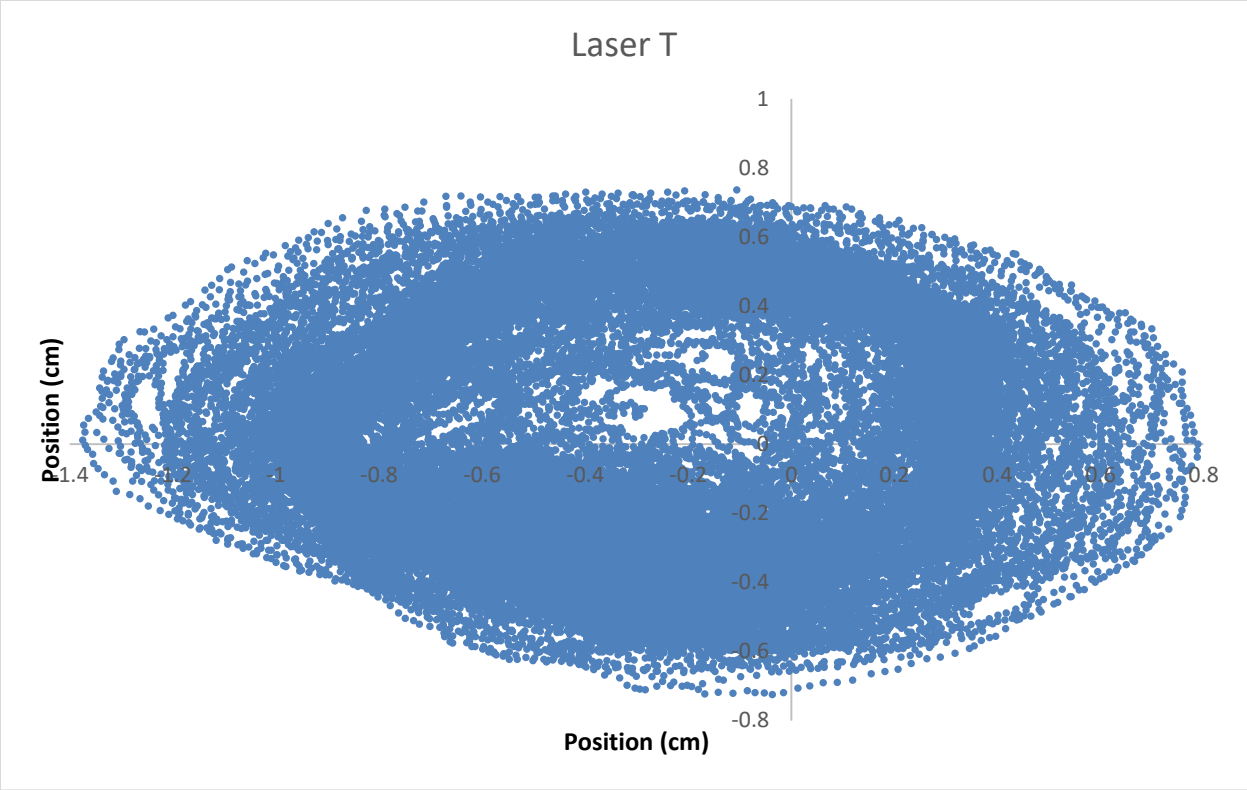

Figure B-13. The top positioned planer behavior of the drill string during the 7V test; 1 kHz

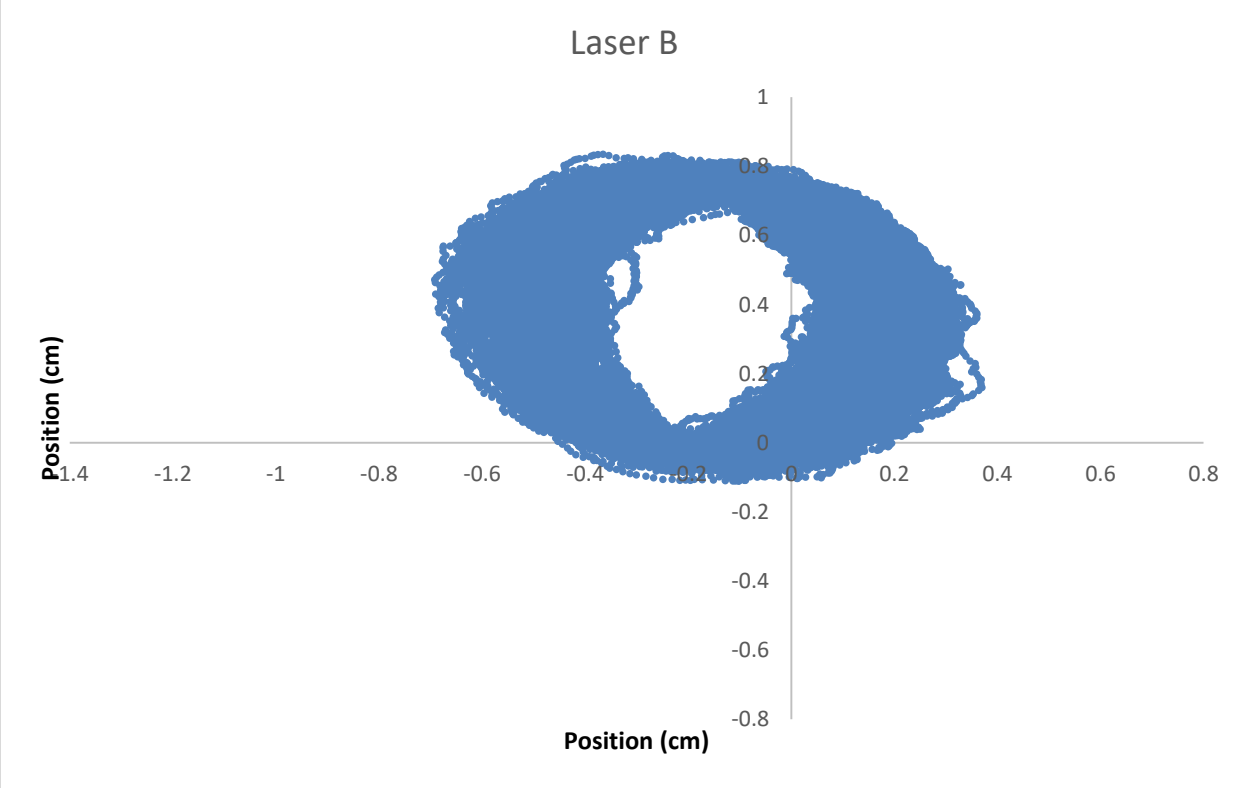

Figure B-14. The bottom positioned planer behavior of the drill string during the 7V test; 1 kHz

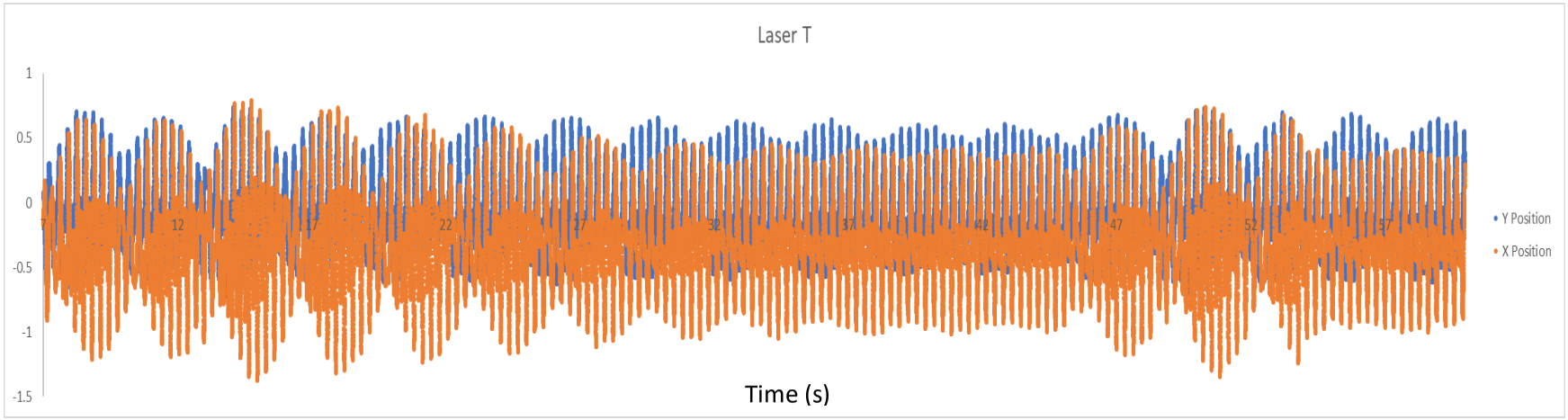

Figure B-15. The position of the drill string at the top plane as a function of time during the 7V test; 1 kHz

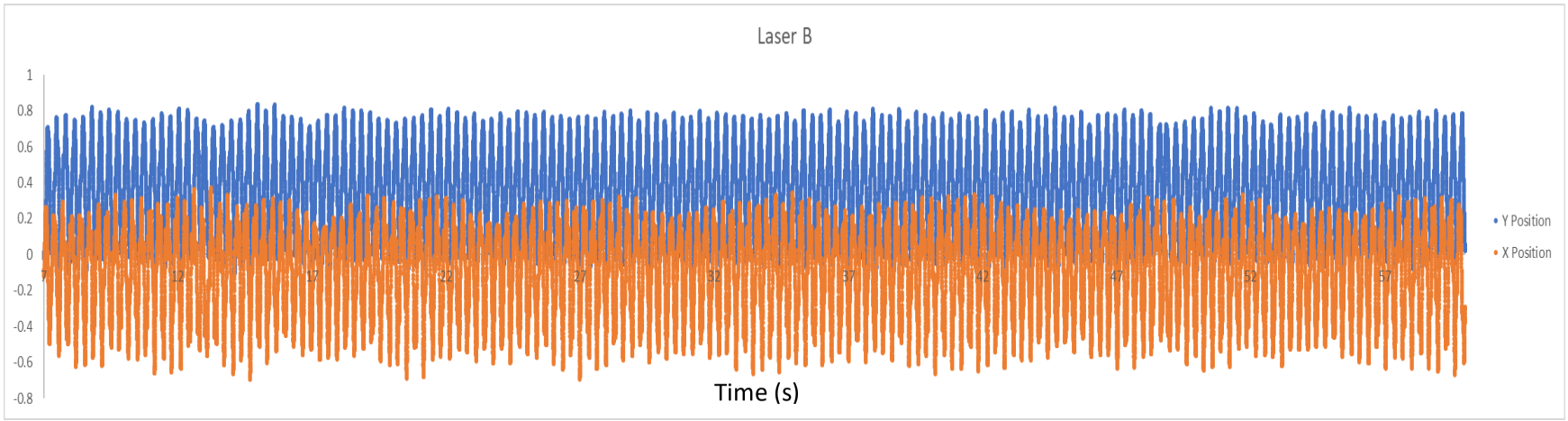

Figure B-16. The position of the drill string at the bottom plane as a function of time during the 7V test; 1 kHz

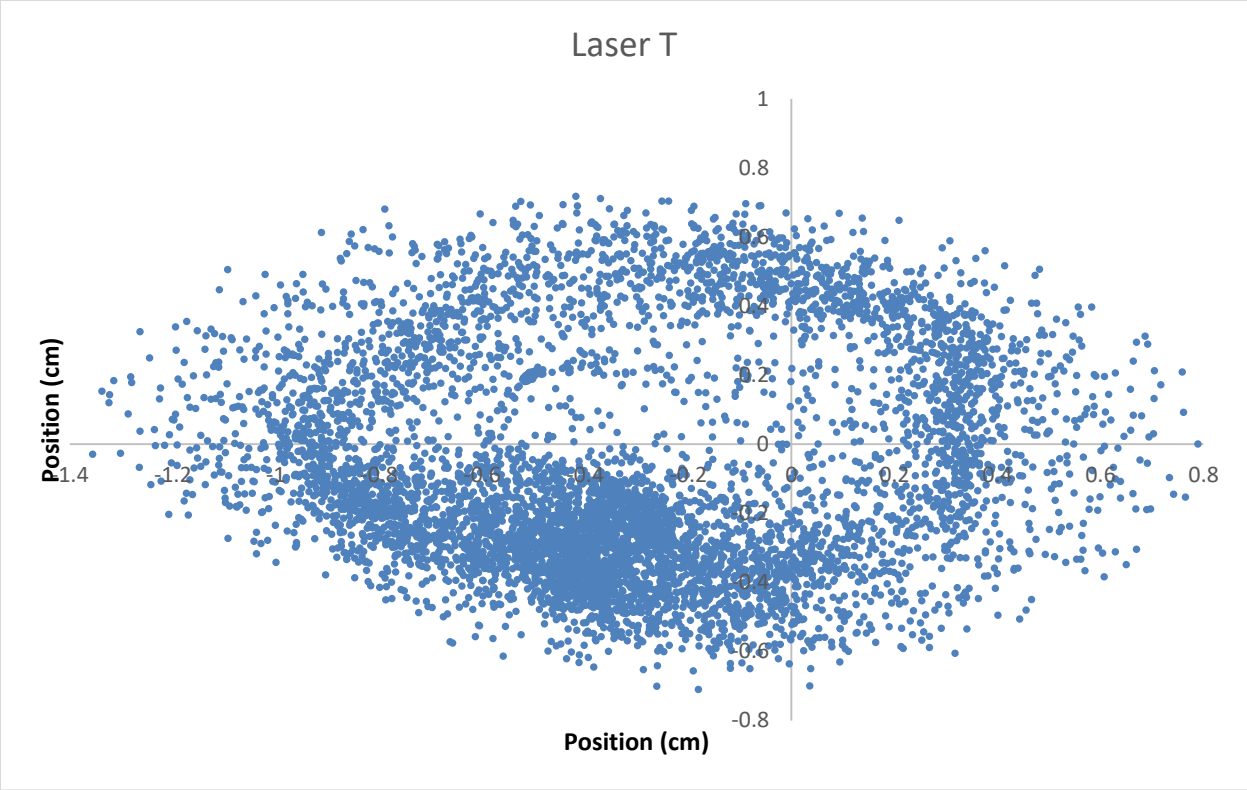

Figure B-17. The top positioned planer behavior of the drill string during the 7V test; 100 Hz

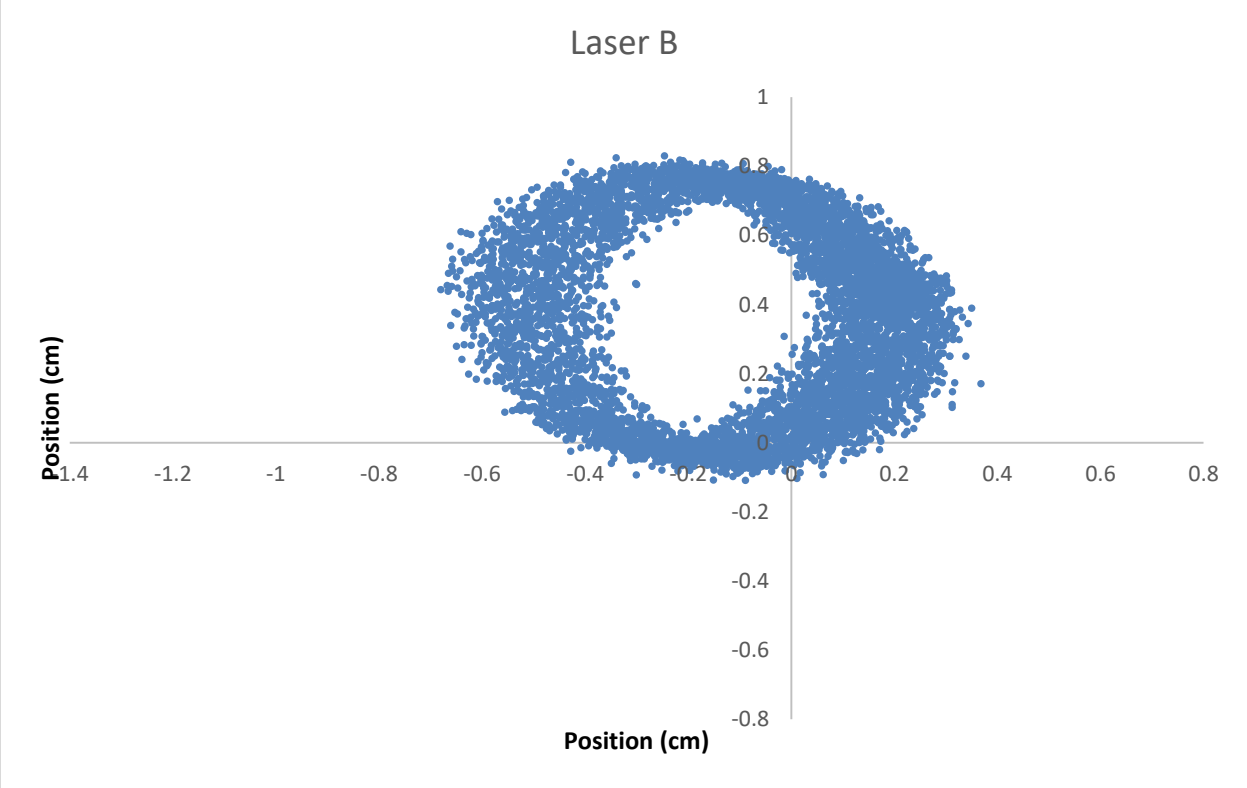

Figure B-18. The bottom positioned planer behavior of the drill string during the 7V test; 100 Hz

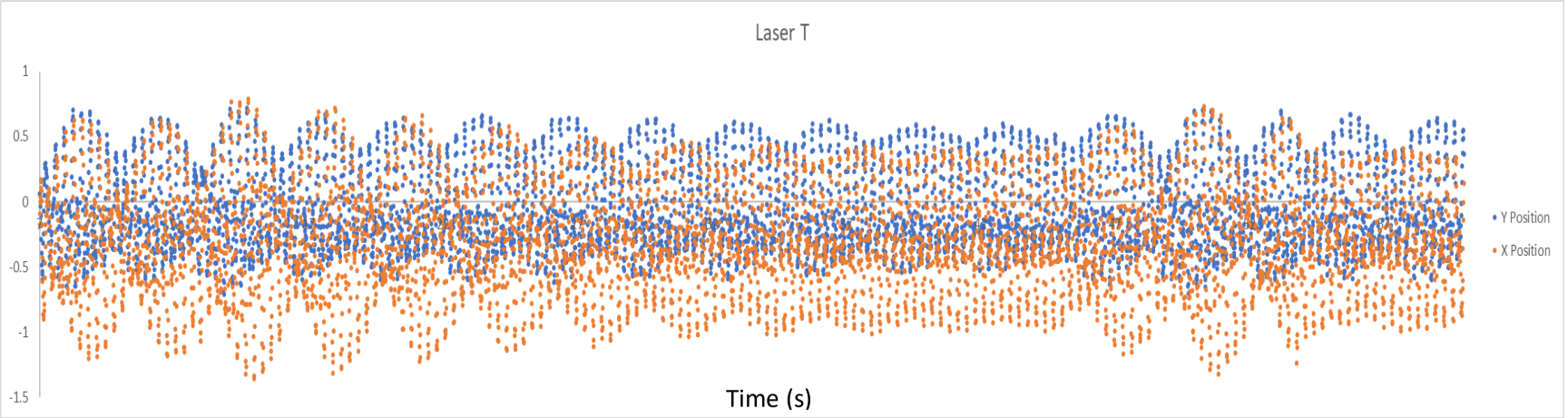

Figure B-19. The position of the drill string at the top plane as a function of time during the 7V test; 100 Hz

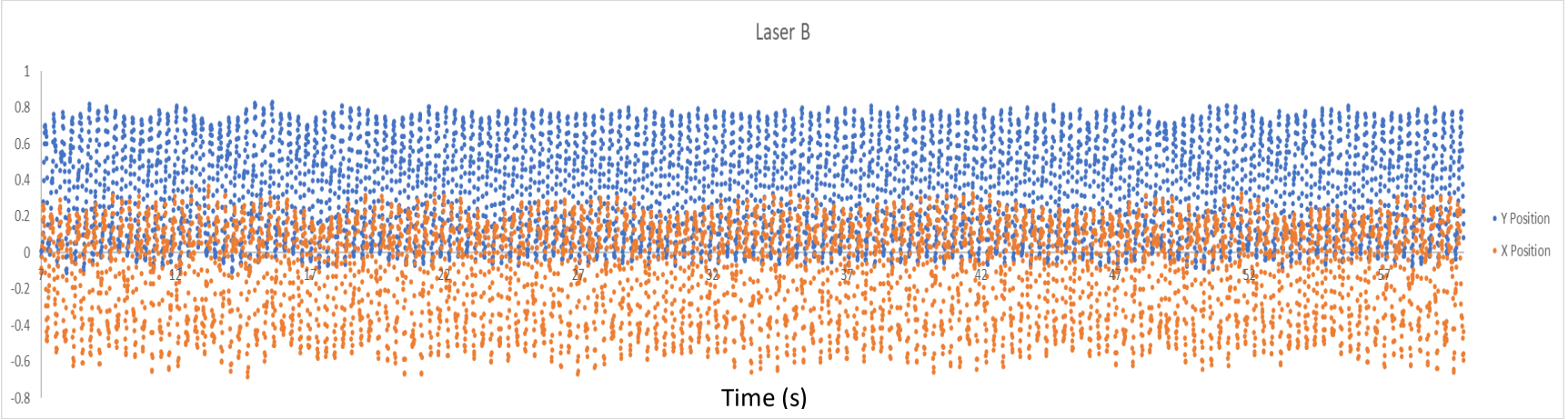

Figure B-20. The position of the drill string at the bottom plane as a function of time during the 7V test; 100Hz

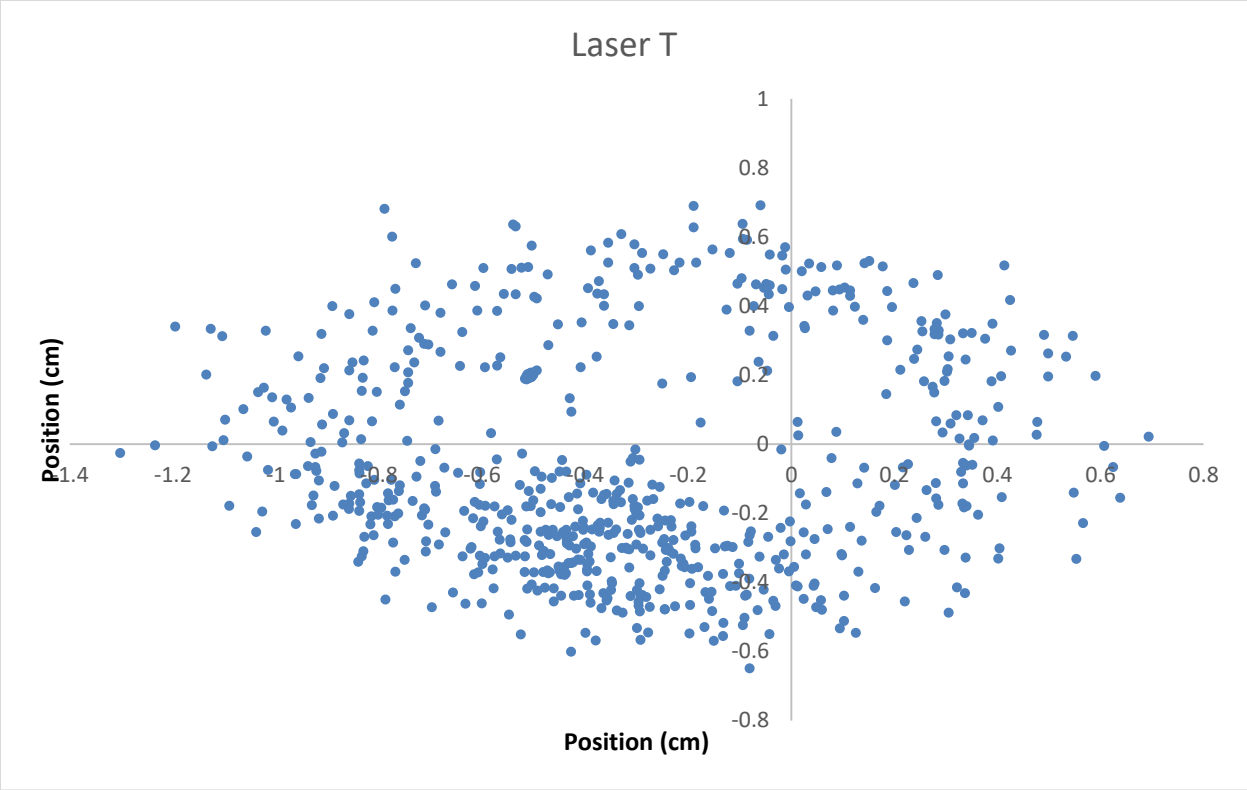

Figure B-21. The top positioned planer behavior of the drill string during the 7V test; 10 Hz

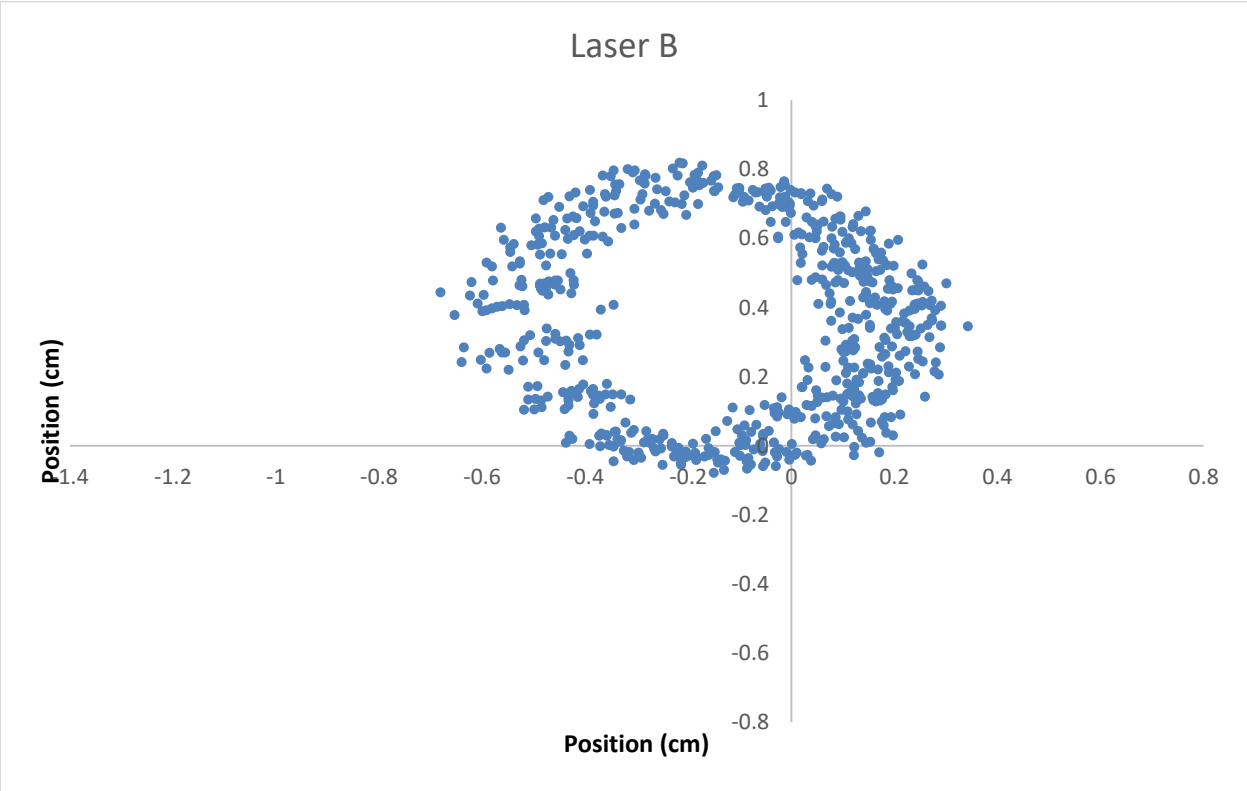

Figure B-22. The bottom positioned planer behavior of the drill string during the 7V test; 10 Hz

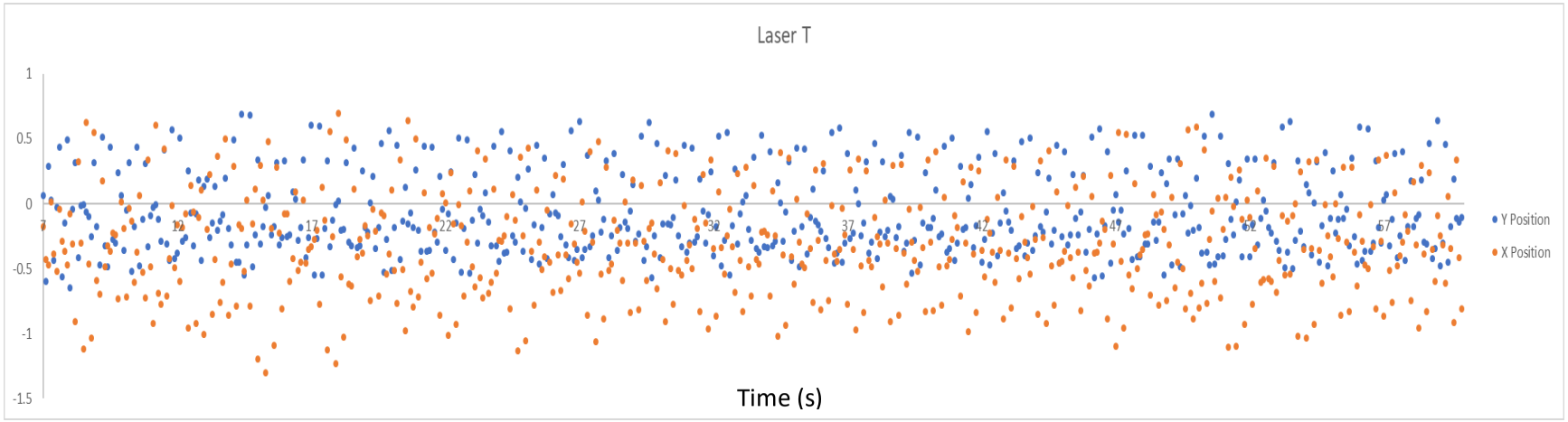

Figure B-23. The position of the drill string at the top plane as a function of time during the 7V test; 10 Hz

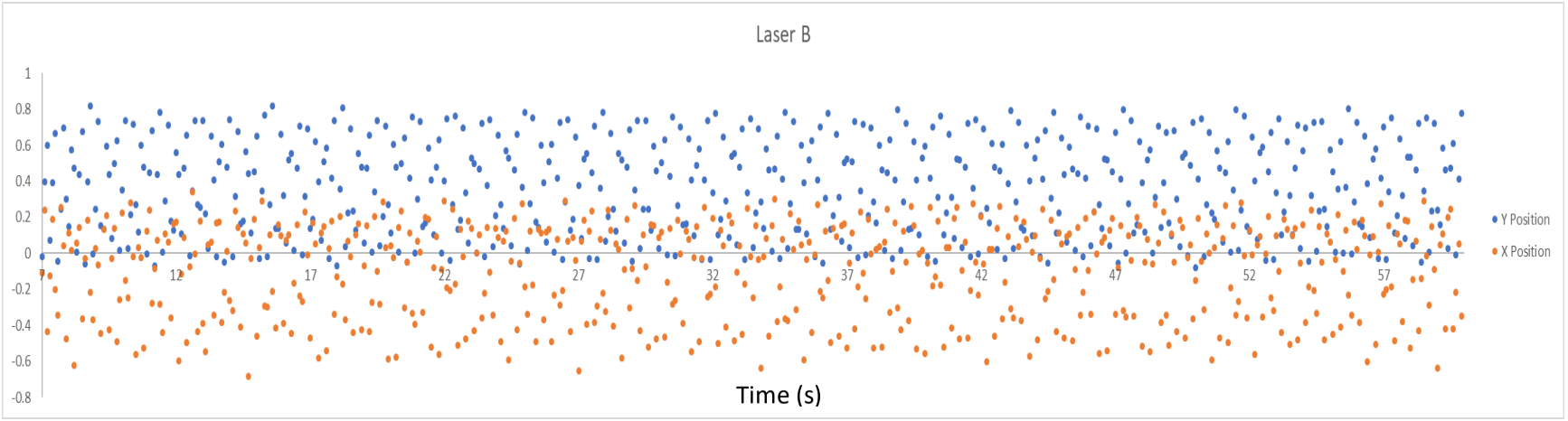

Figure B-24. The position of the drill string at the bottom plane as a function of time during the 7V test; 10 Hz

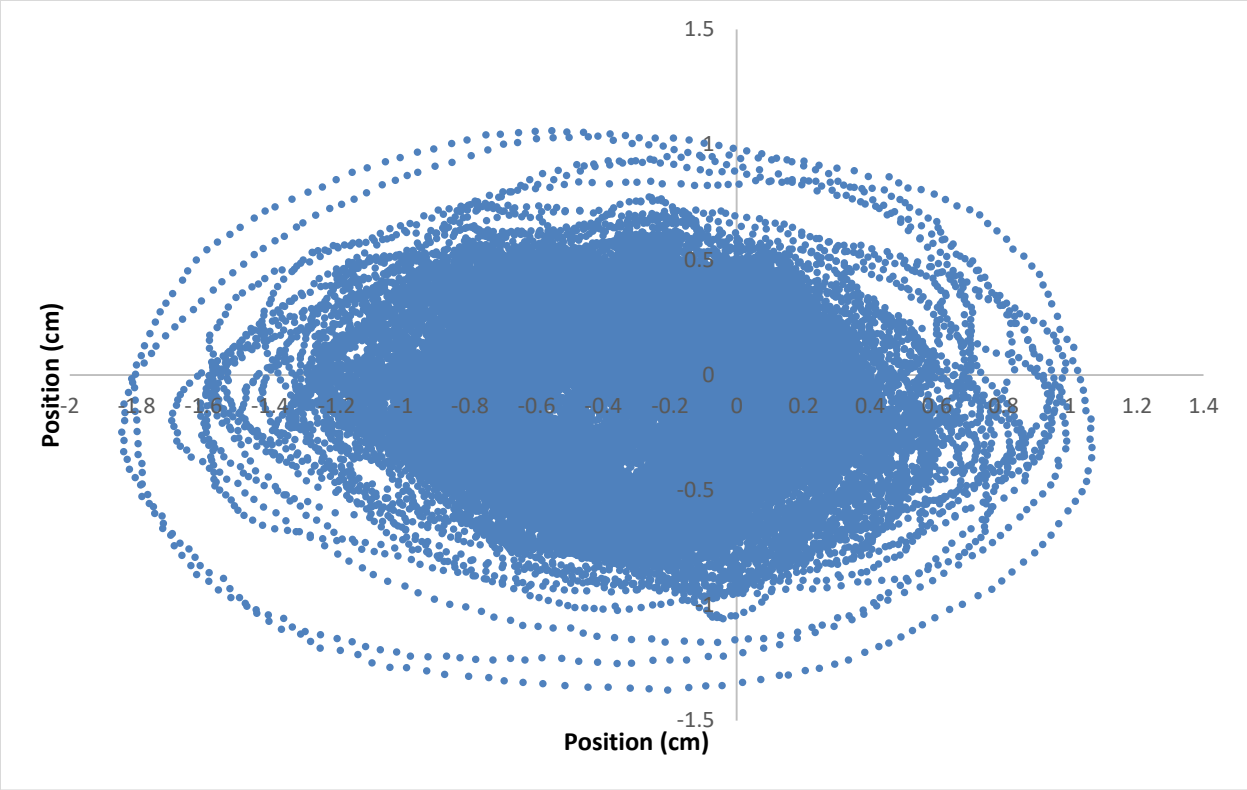

Figure B-25. The top positioned planer behavior of the drill string during the 8V test; 1 kHz

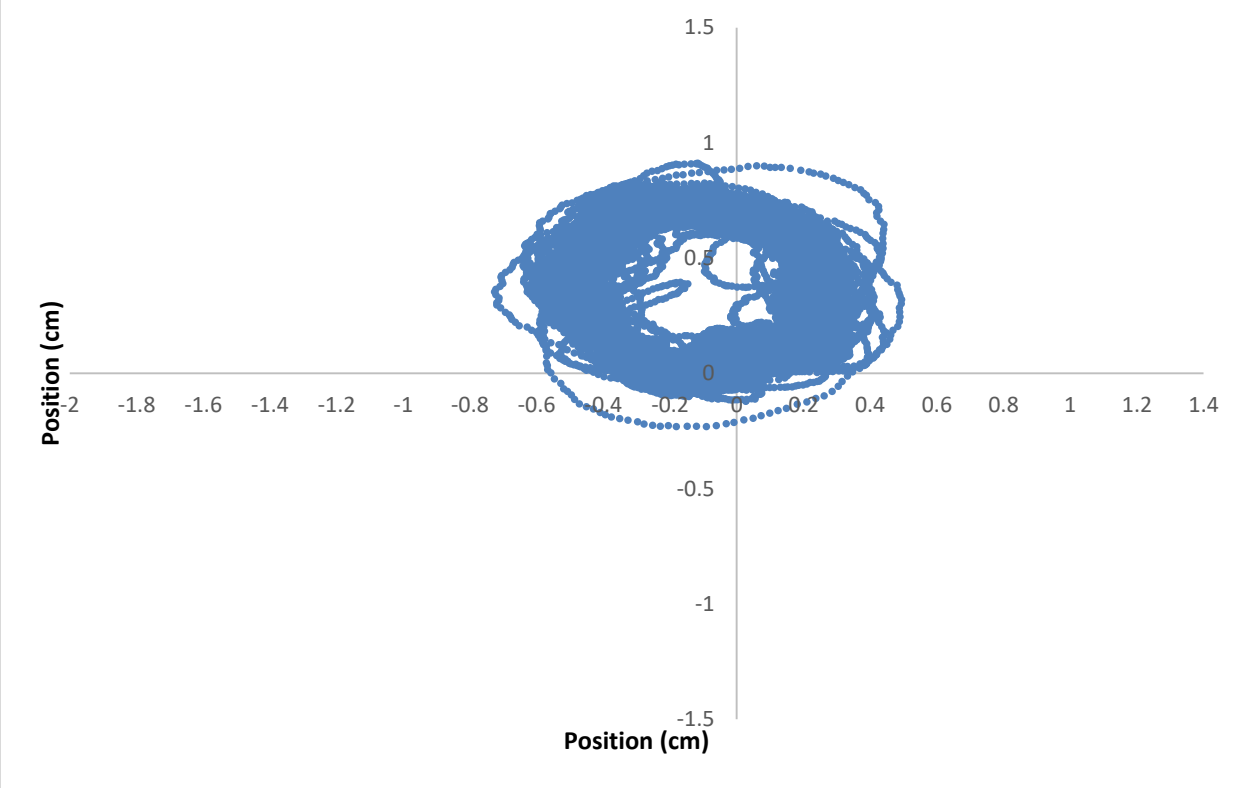

Figure B-26. The bottom positioned planer behavior of the drill string during the 8V test; 1 kHz

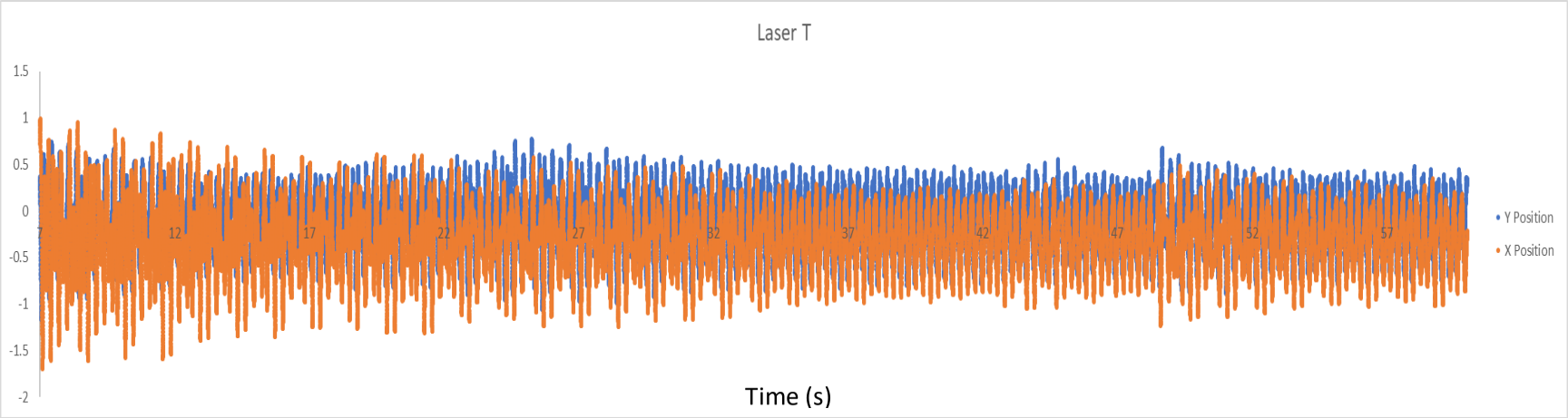

Figure B-27. The position of the drill string at the top plane as a function of time during the 8V test; 1 kHz

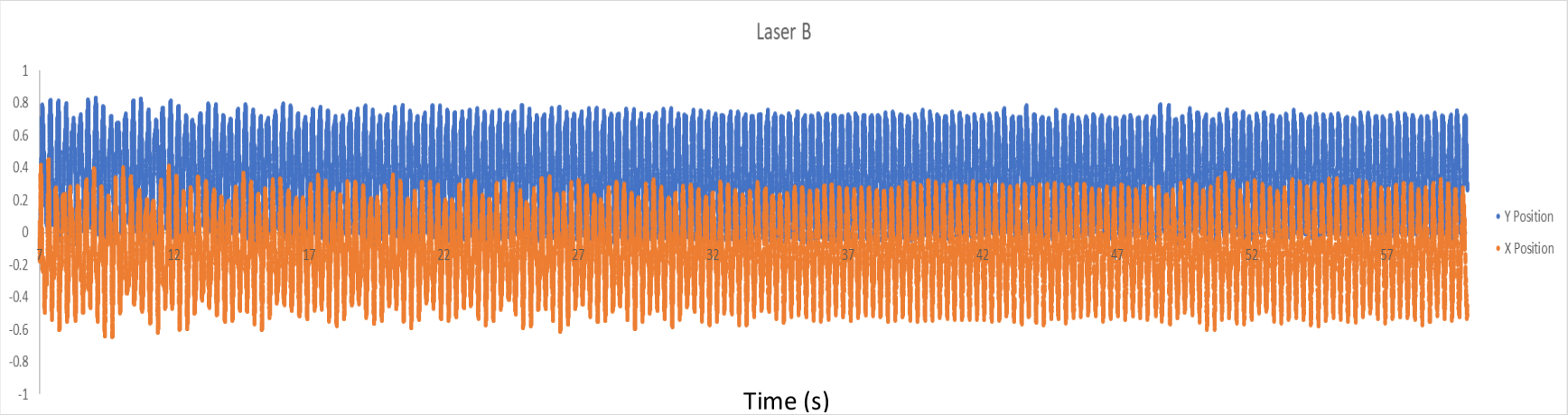

Figure B-28. The position of the drill string at the bottom plane as a function of time during the 8V test; 1 kHz

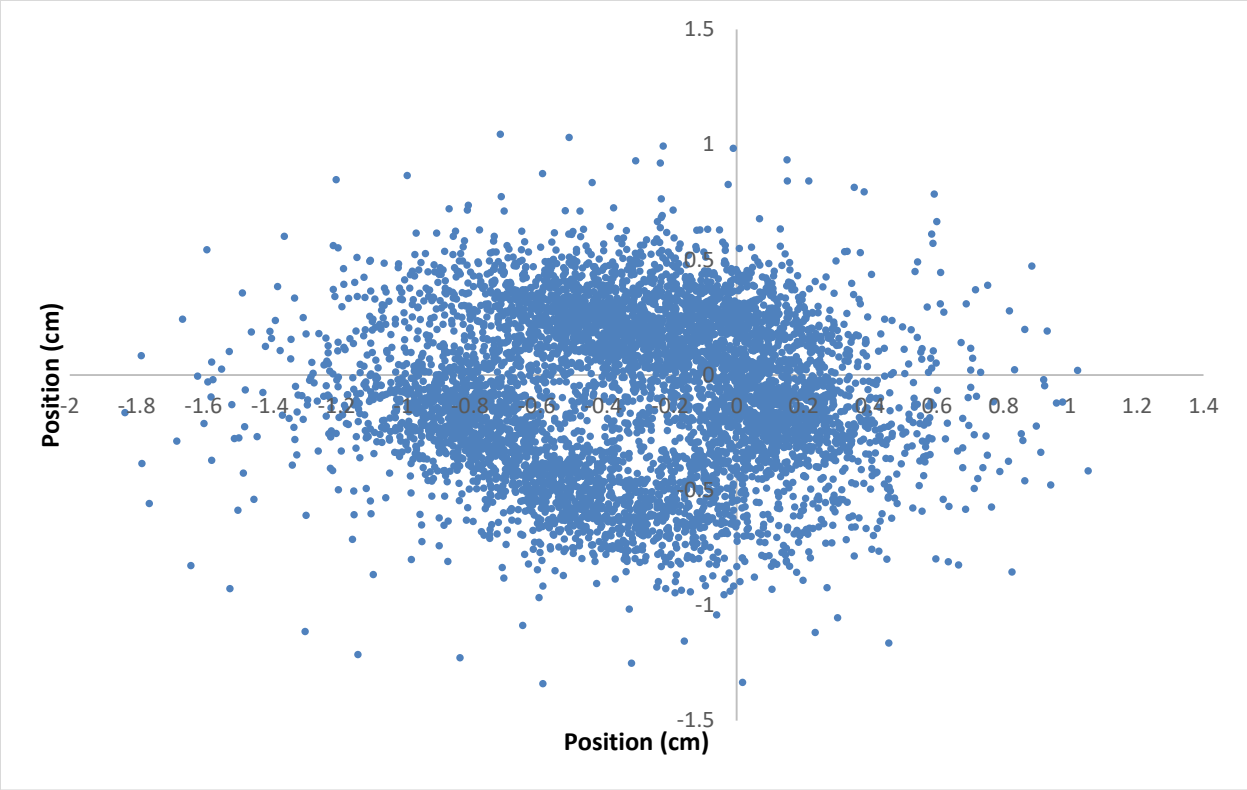

Figure B-29. The top positioned planer behavior of the drill string during the 8V test; 100 Hz

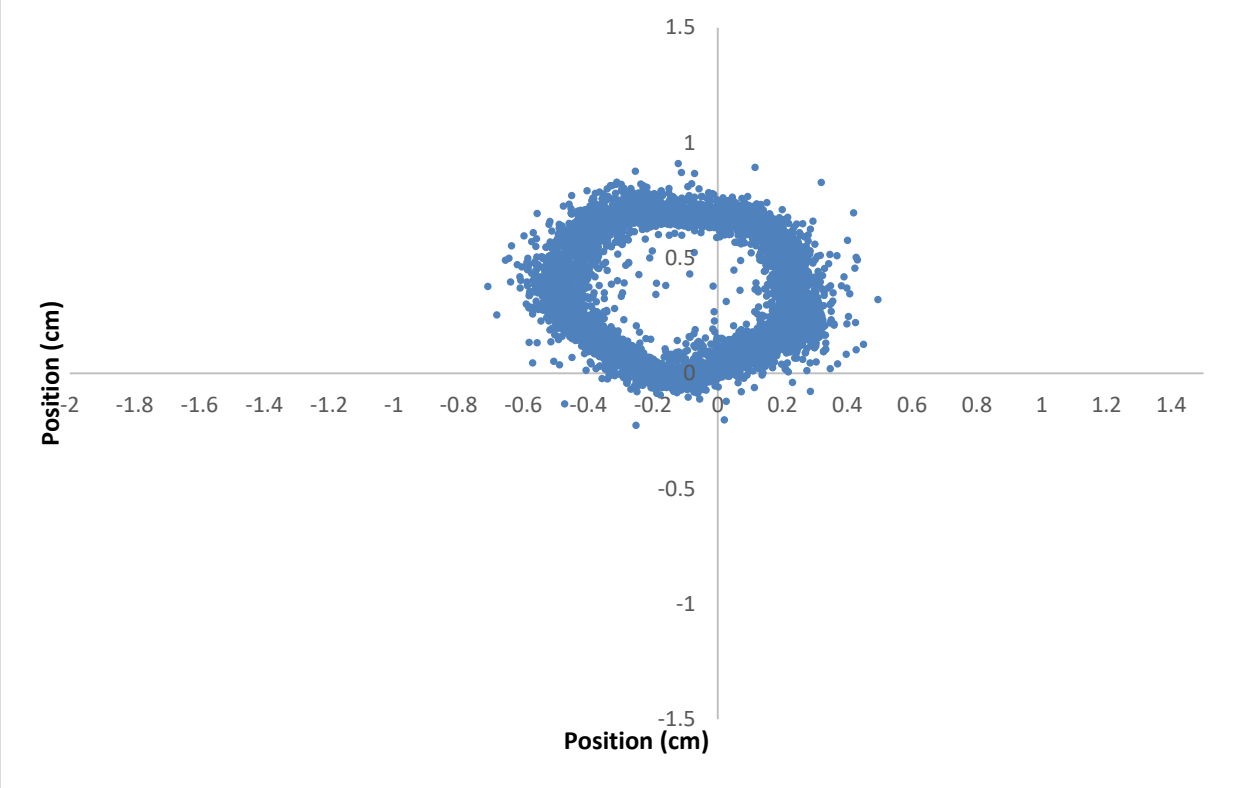

Figure B-30. The bottom positioned planer behavior of the drill string during the 8V test; 100 Hz

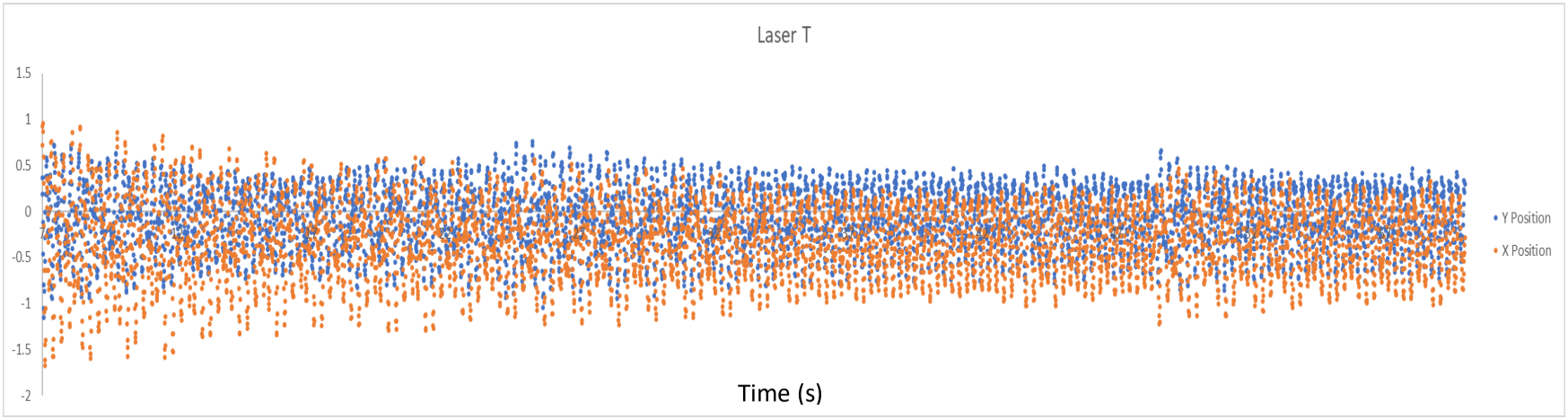

Figure B-31. The position of the drill string at the top plane as a function of time during the 8V test; 100 Hz

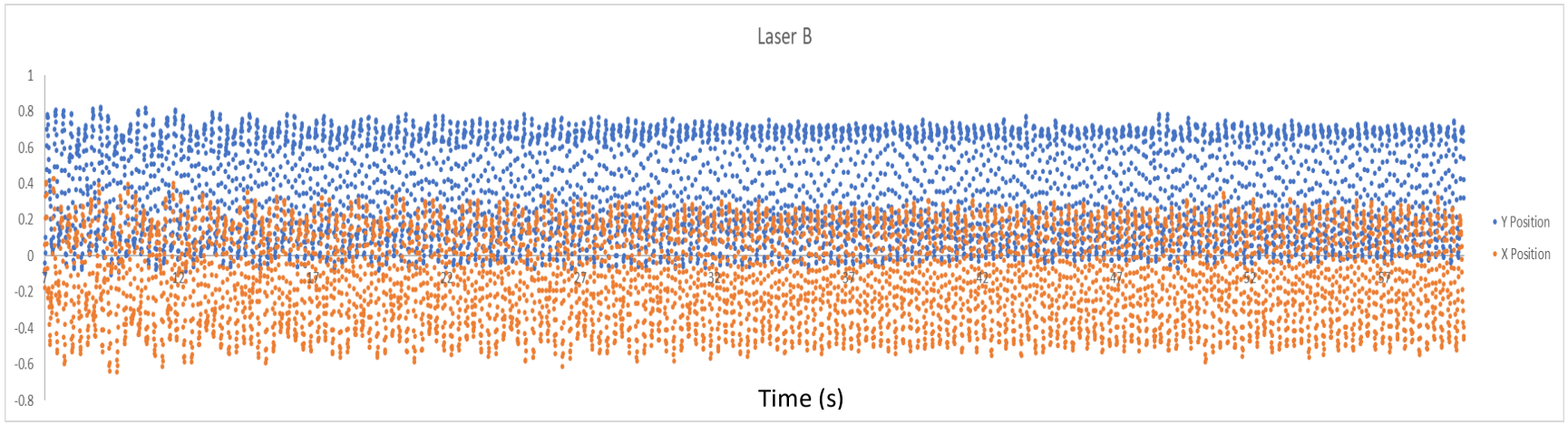

Figure B-32. The position of the drill string at the bottom plane as a function of time during the 8V test; 100 Hz

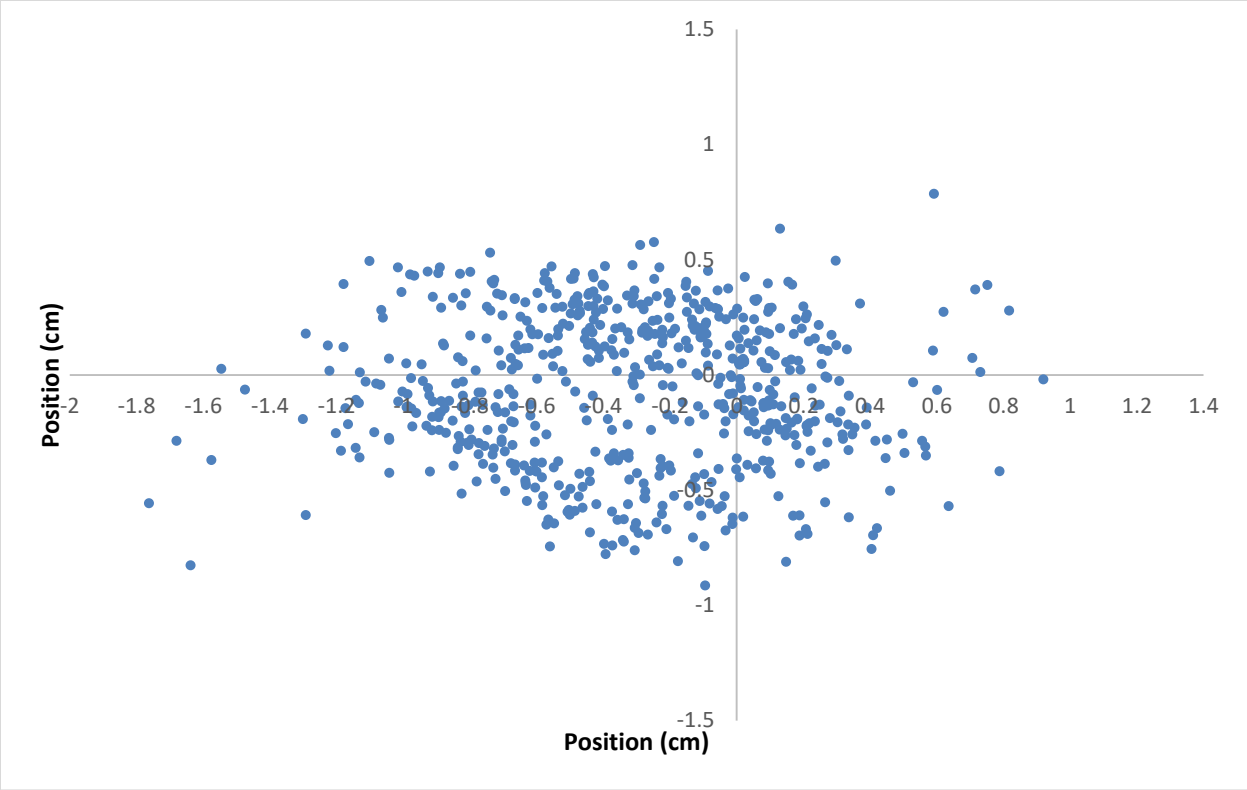

Figure B-33. The top positioned planer behavior of the drill string during the 8V test; 10 Hz

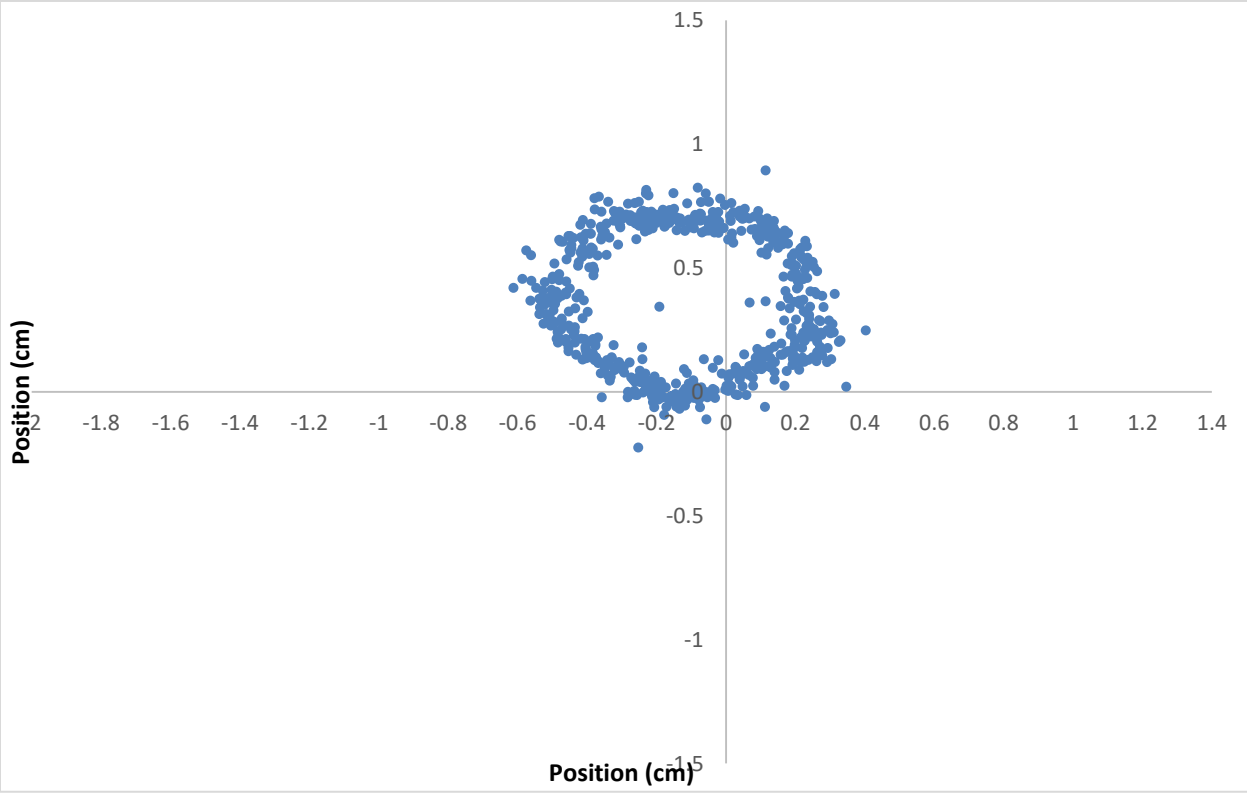

Figure B-34. The bottom positioned planer behavior of the drill string during the 8V test; 10 Hz

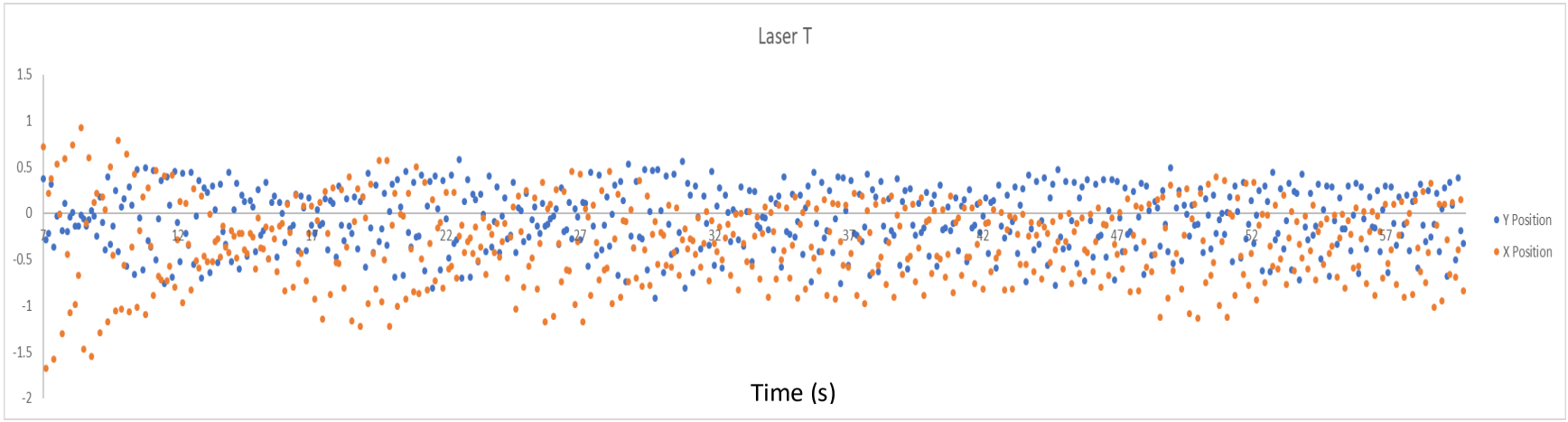

Figure B-35. The position of the drill string at the top plane as a function of time during the 8V test; 10 Hz

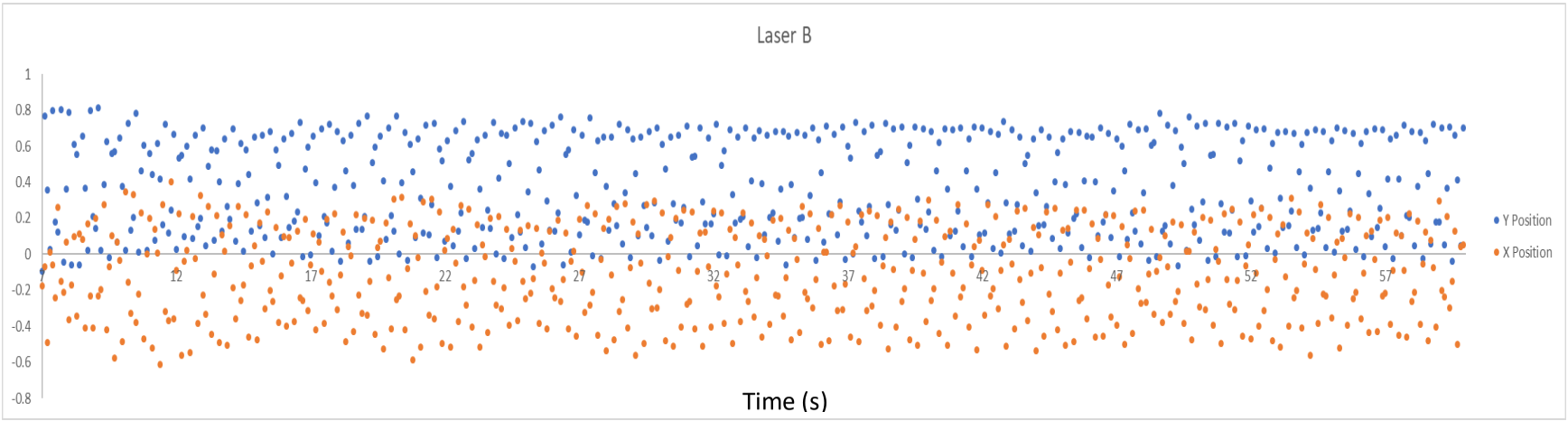

Figure B-36. The position of the drill string at the bottom plane as a function of time during the 8V test; 10Hz

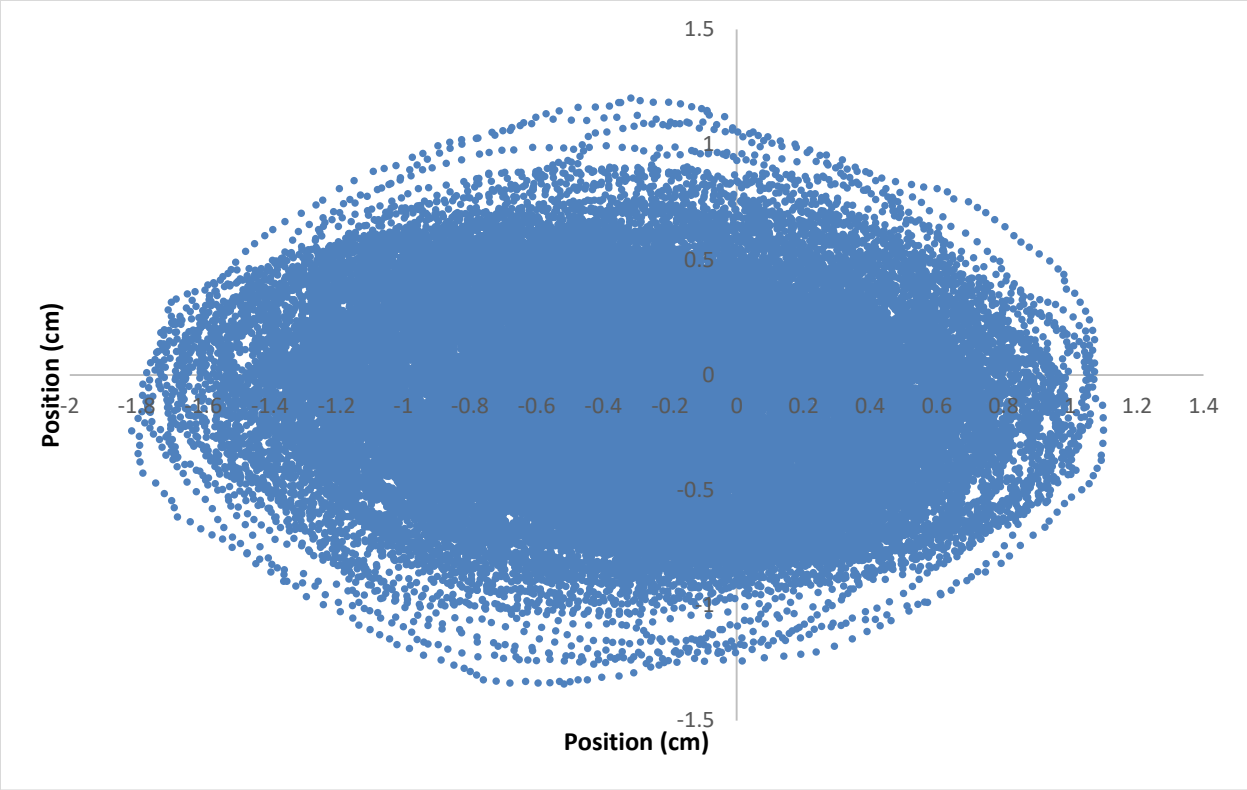

Figure B-37. The top positioned planer behavior of the drill string during the 9V test; 1 kHz

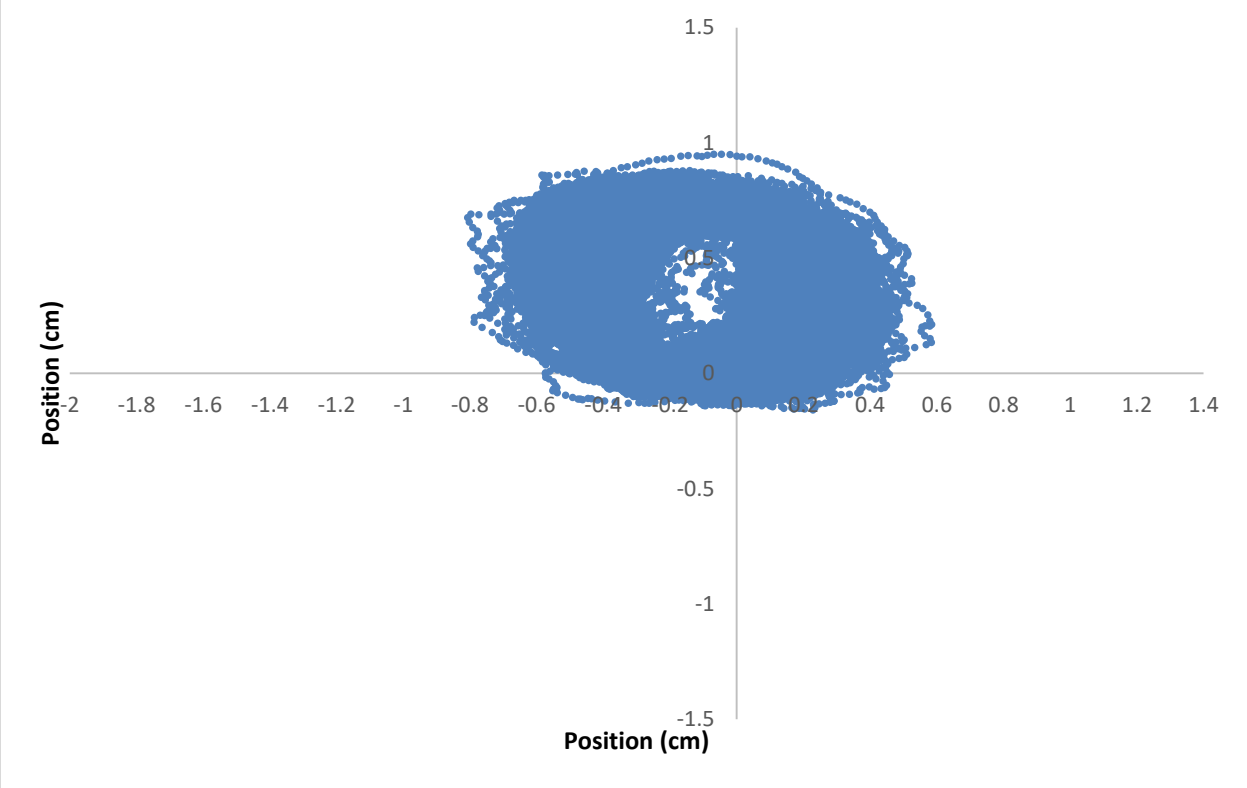

Figure B-38. The bottom positioned planer behavior of the drill string during the 9V test; 1 kHz

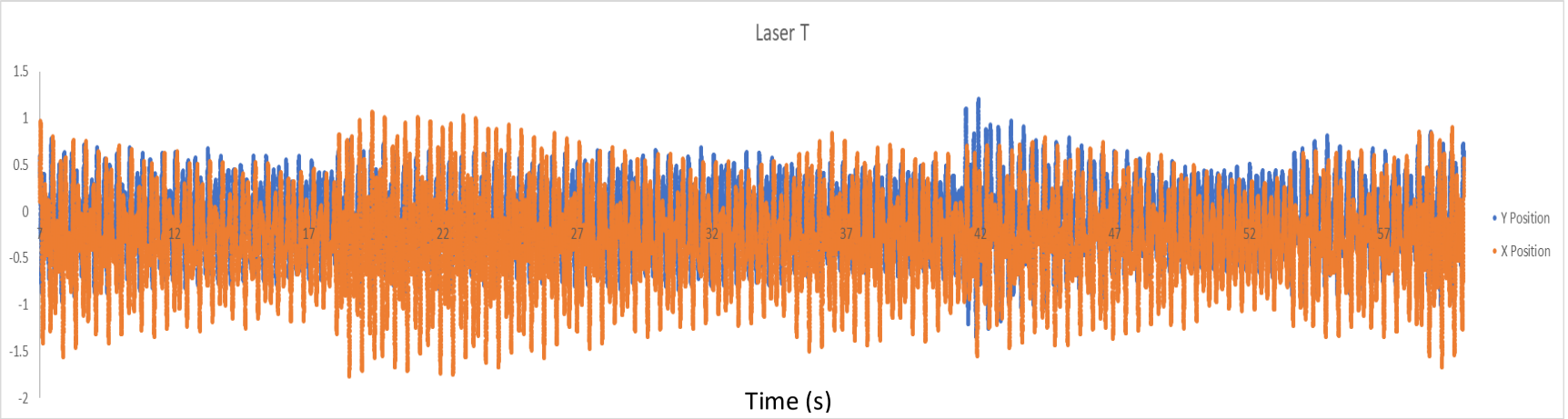

Figure B-39. The position of the drill string at the top plane as a function of time during the 9V test; 1 kHz

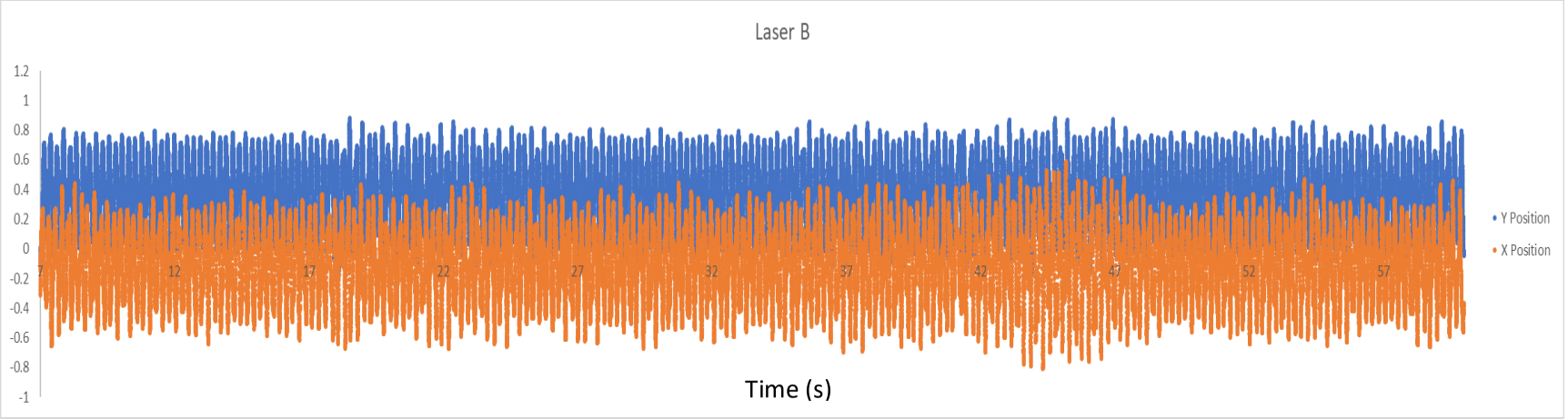

Figure B-40. The position of the drill string at the bottom plane as a function of time during the 9V test; 1 kHz

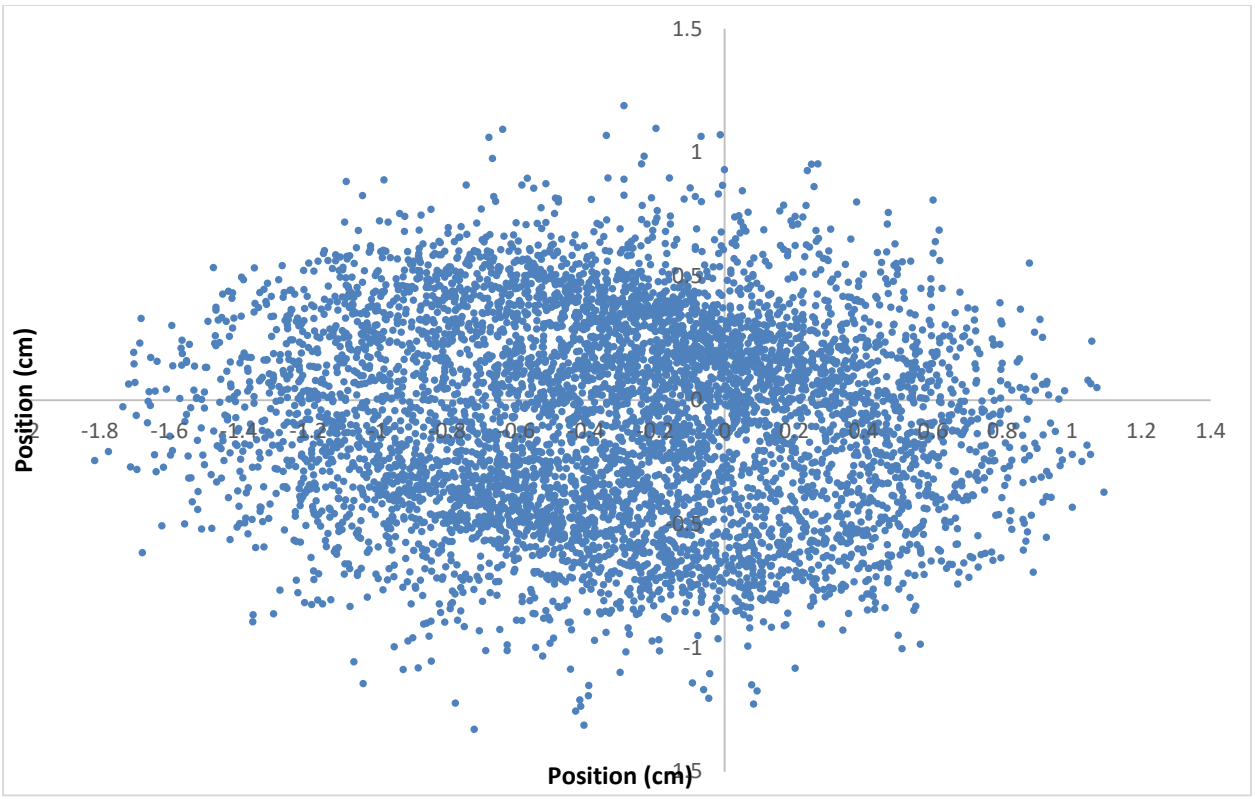

Figure B-41. The top positioned planer behavior of the drill string during the 9V test; 100 Hz

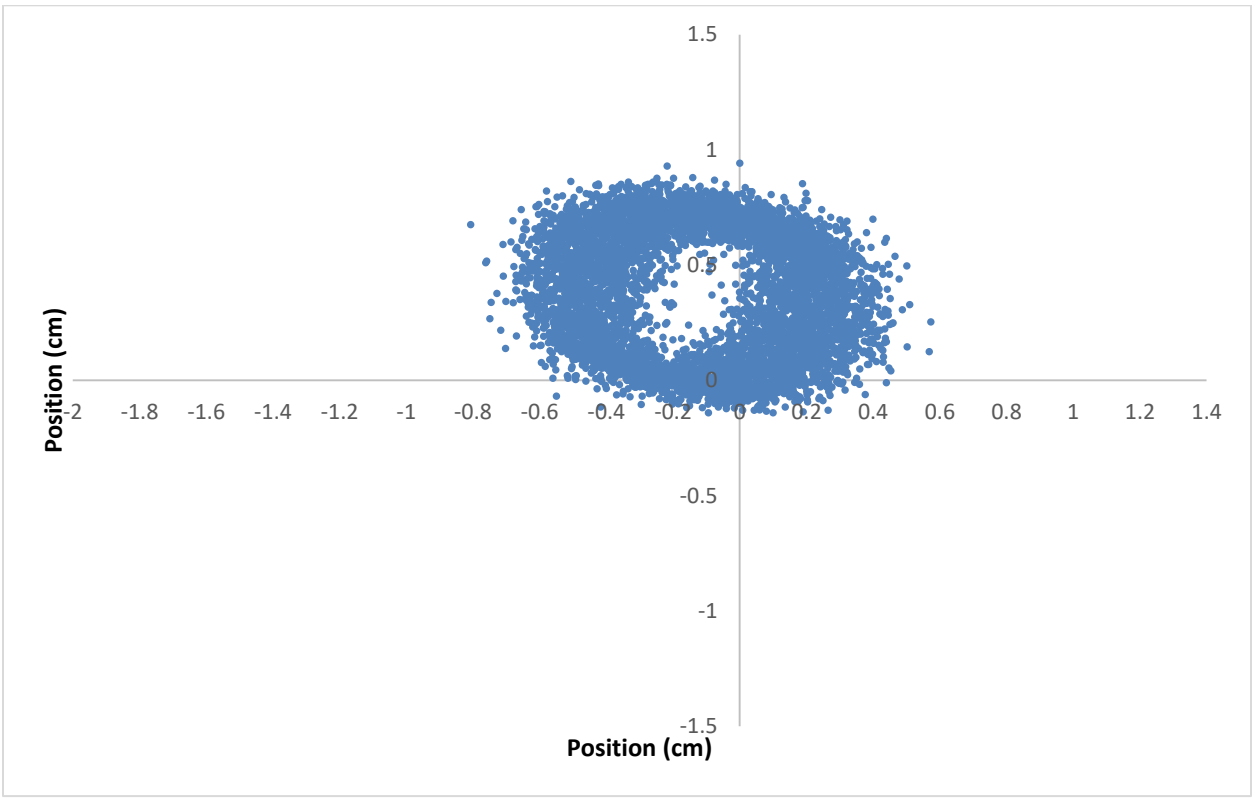

Figure B-42. The bottom positioned planer behavior of the drill string during the 9V test; 100 Hz

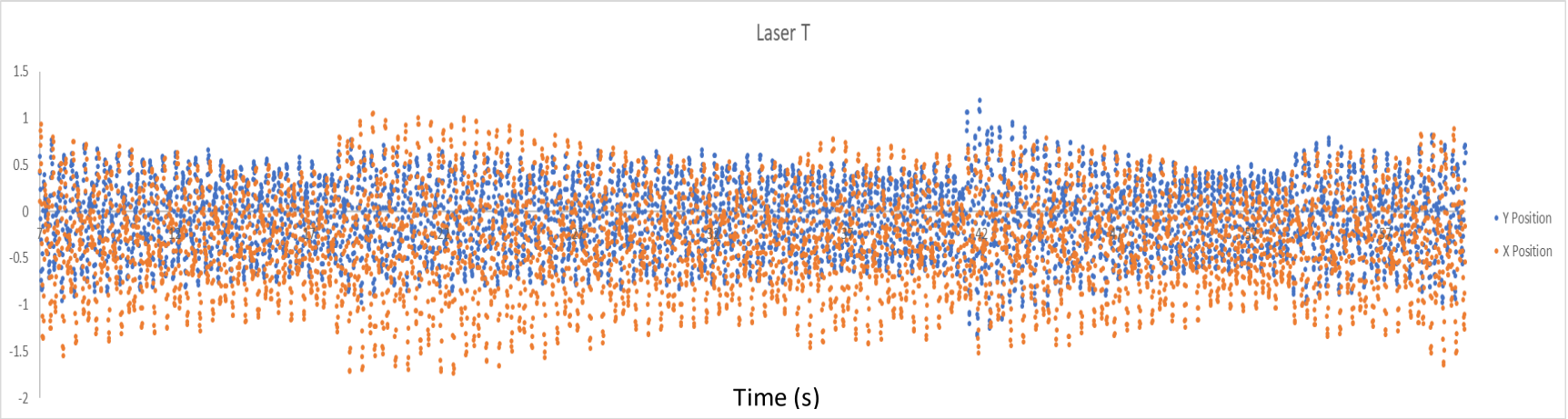

Figure B-43. The position of the drill string at the top plane as a function of time during the 9V test; 100 Hz

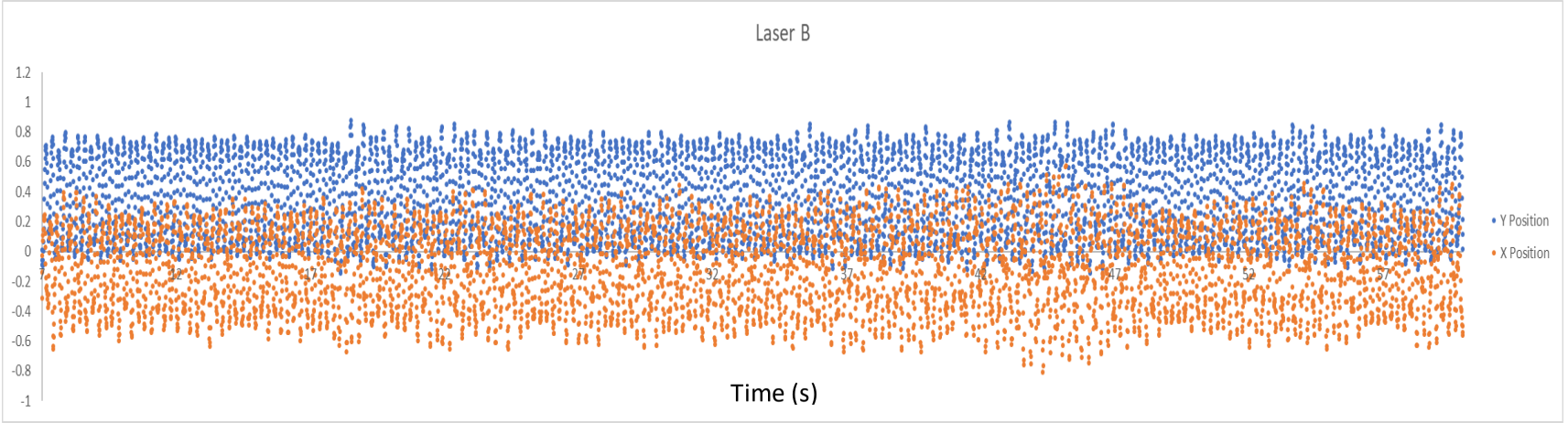

Figure B-44. The position of the drill string at the bottom plane as a function of time during the 9V test; 100 Hz

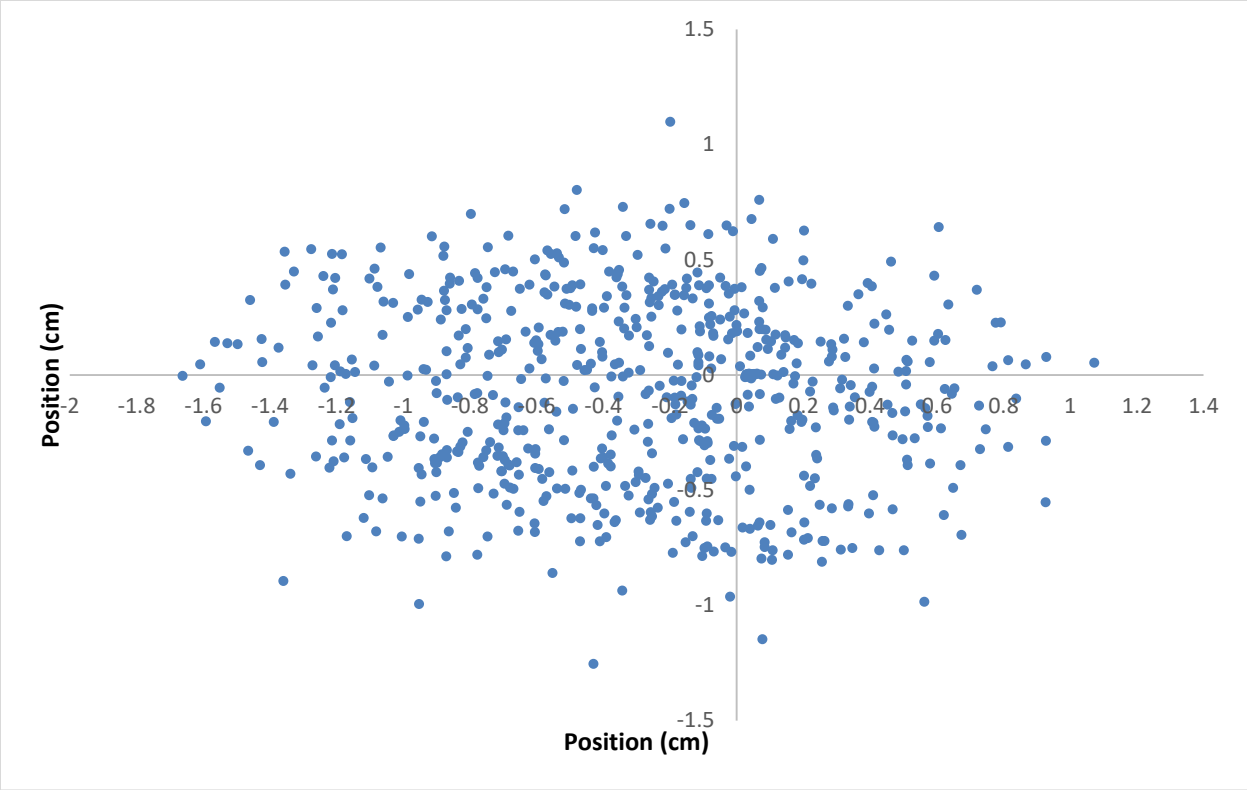

Figure B-45. The top positioned planer behavior of the drill string during the 9V test; 10 Hz

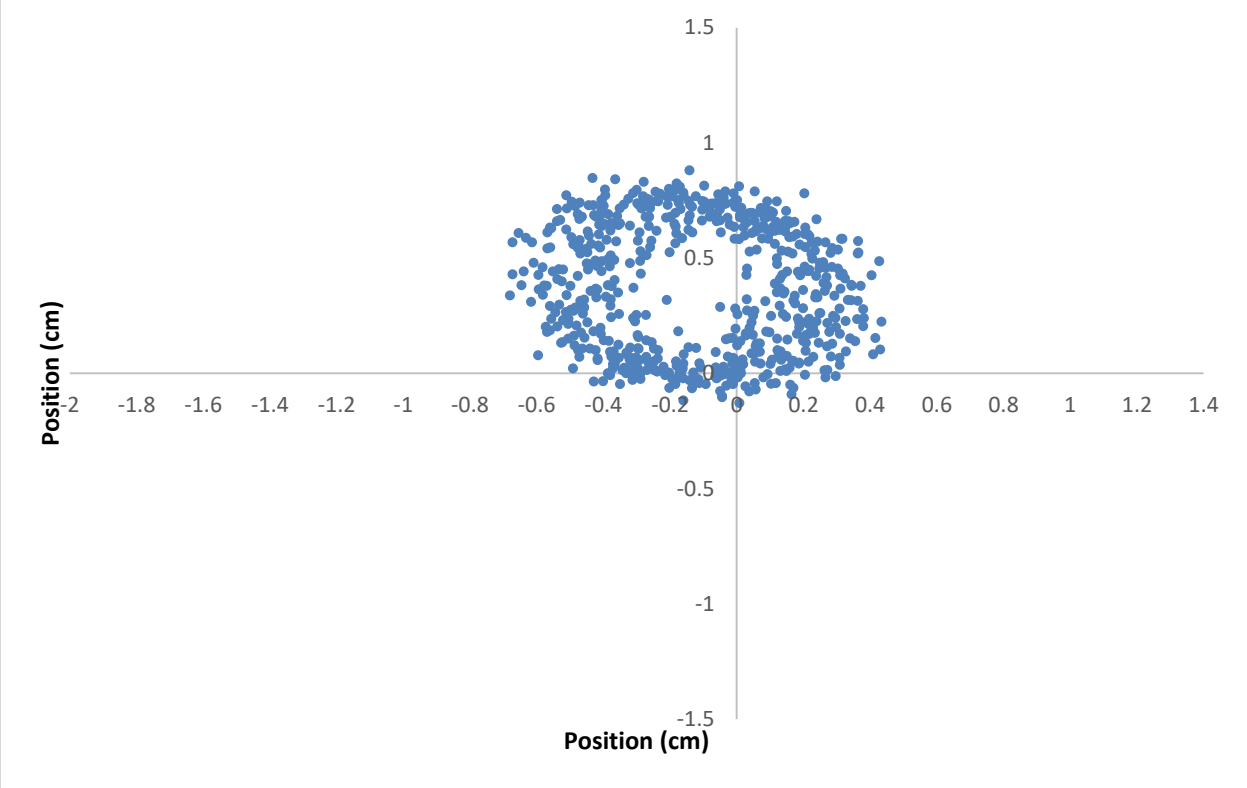

Figure B-46. The bottom positioned planer behavior of the drill string during the 9V test; 10 Hz

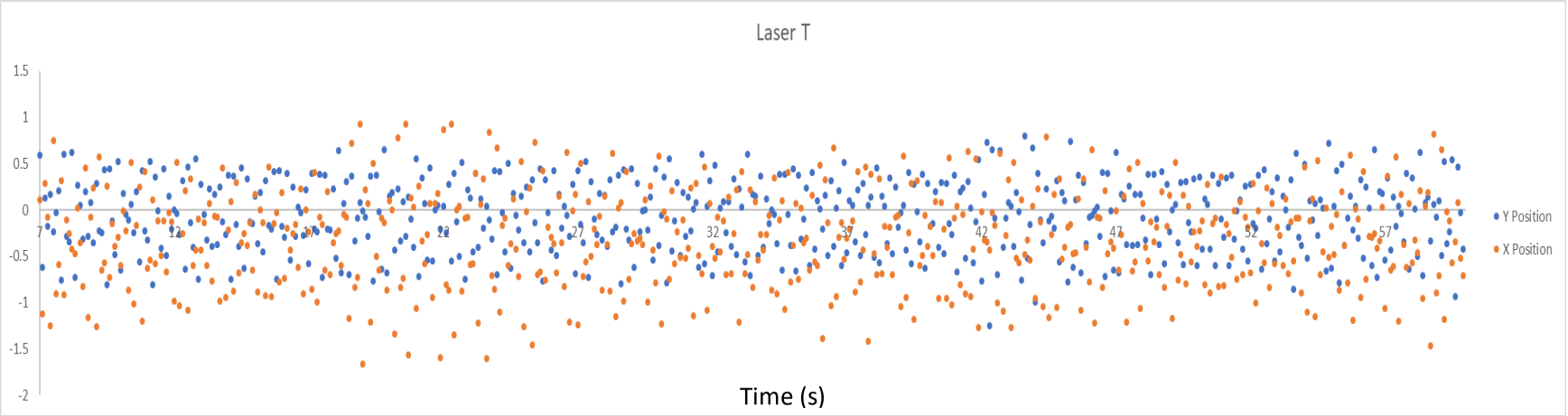

Figure B-47. The position of the drill string at the top plane as a function of time during the 9V test; 10 Hz

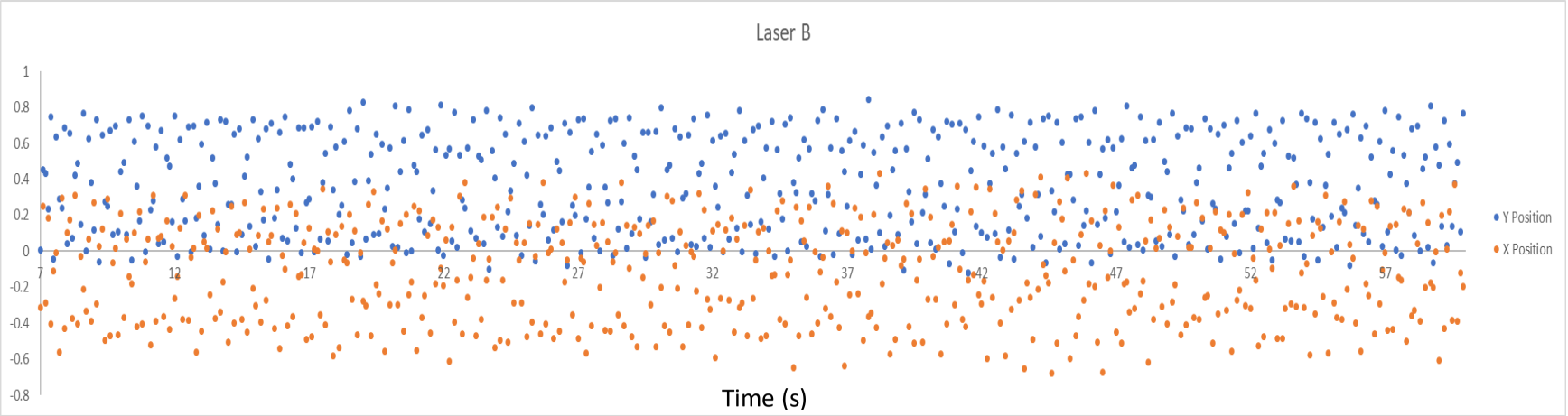

Figure B-48. The position of the drill string at the bottom plane as a function of time during the 9V test; 10 Hz

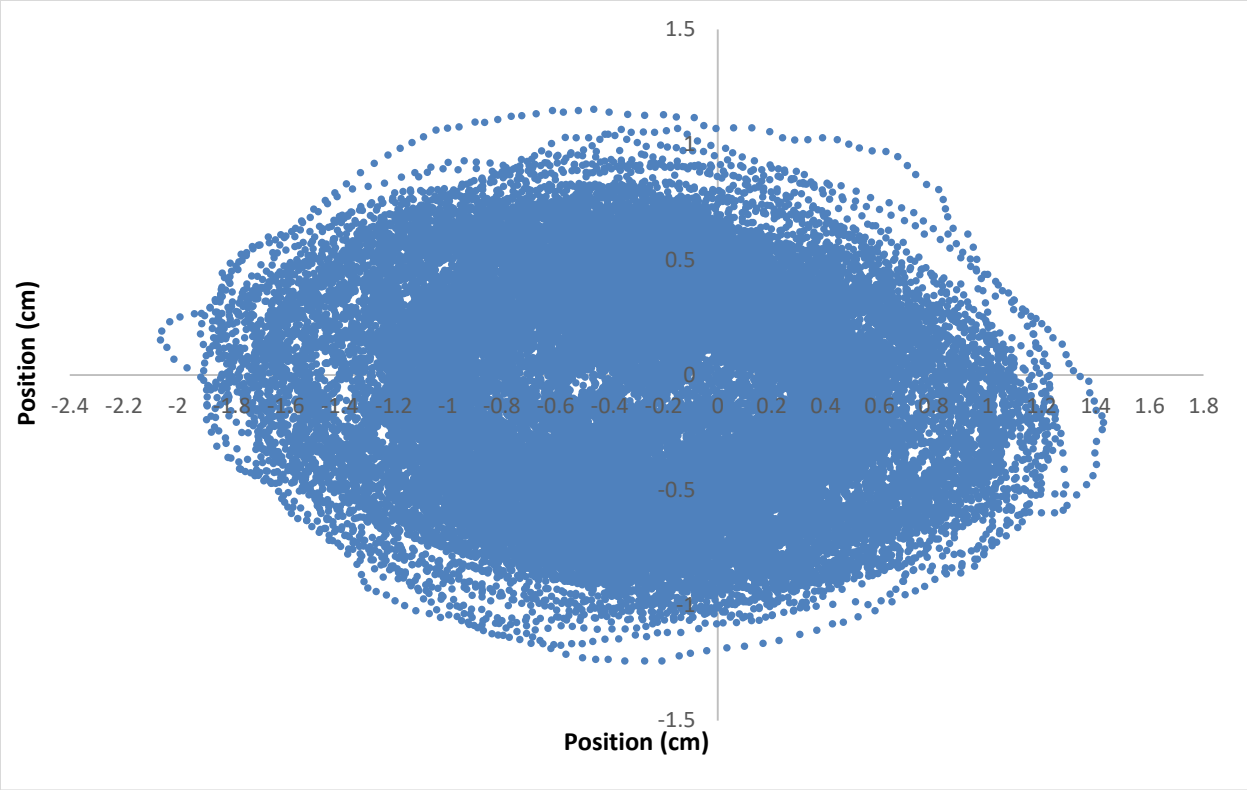

Figure B-49. The top positioned planer behavior of the drill string during the 10V test; 1 kHz

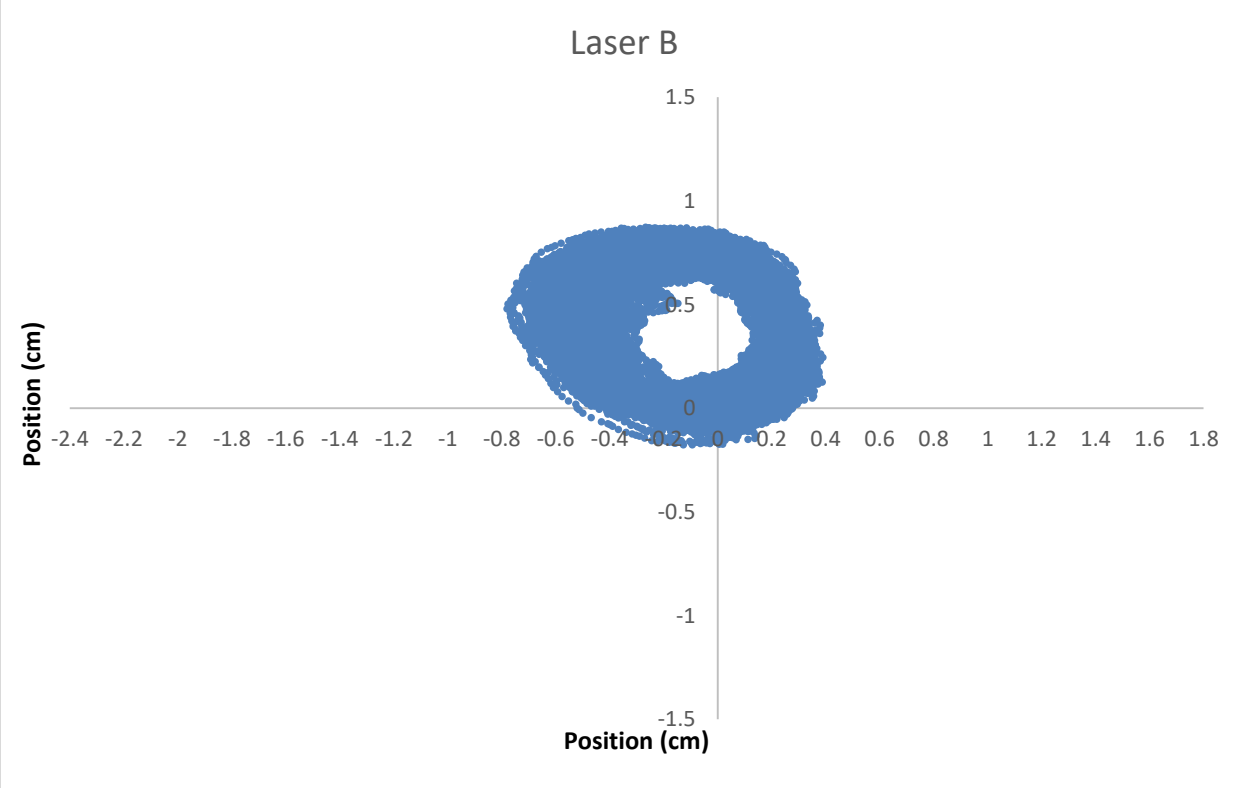

Figure B-50. The bottom positioned planer behavior of the drill string during the 10V test; 1 kHz

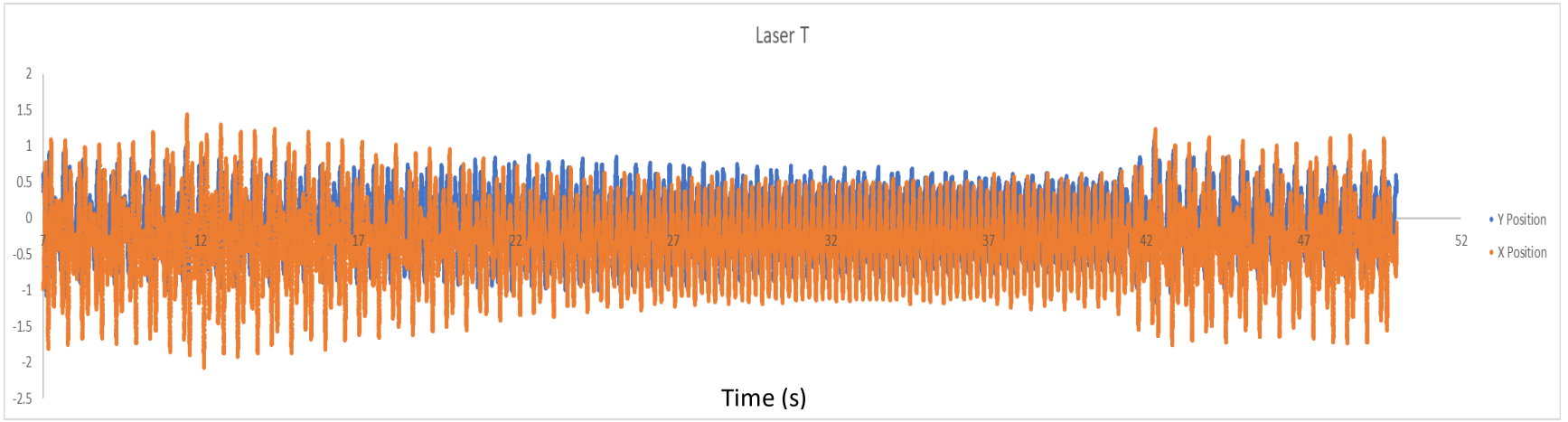

Figure B-51. The position of the drill string at the top plane as a function of time during the 10V test; 1 kHz

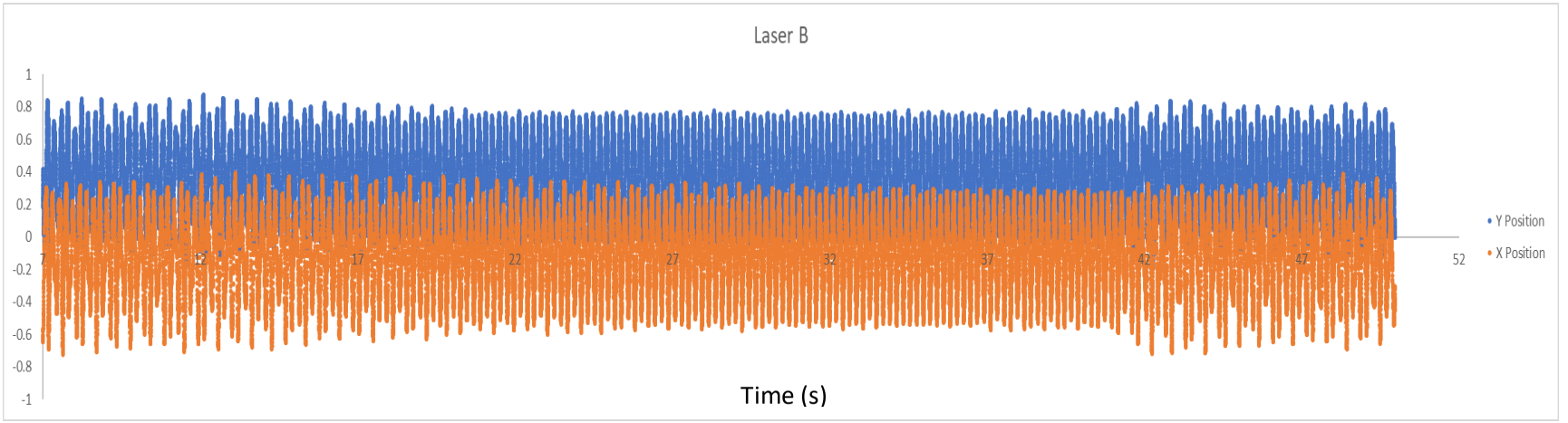

Figure B-52. The position of the drill string at the bottom plane as a function of time during the 10V test; 1 kHz

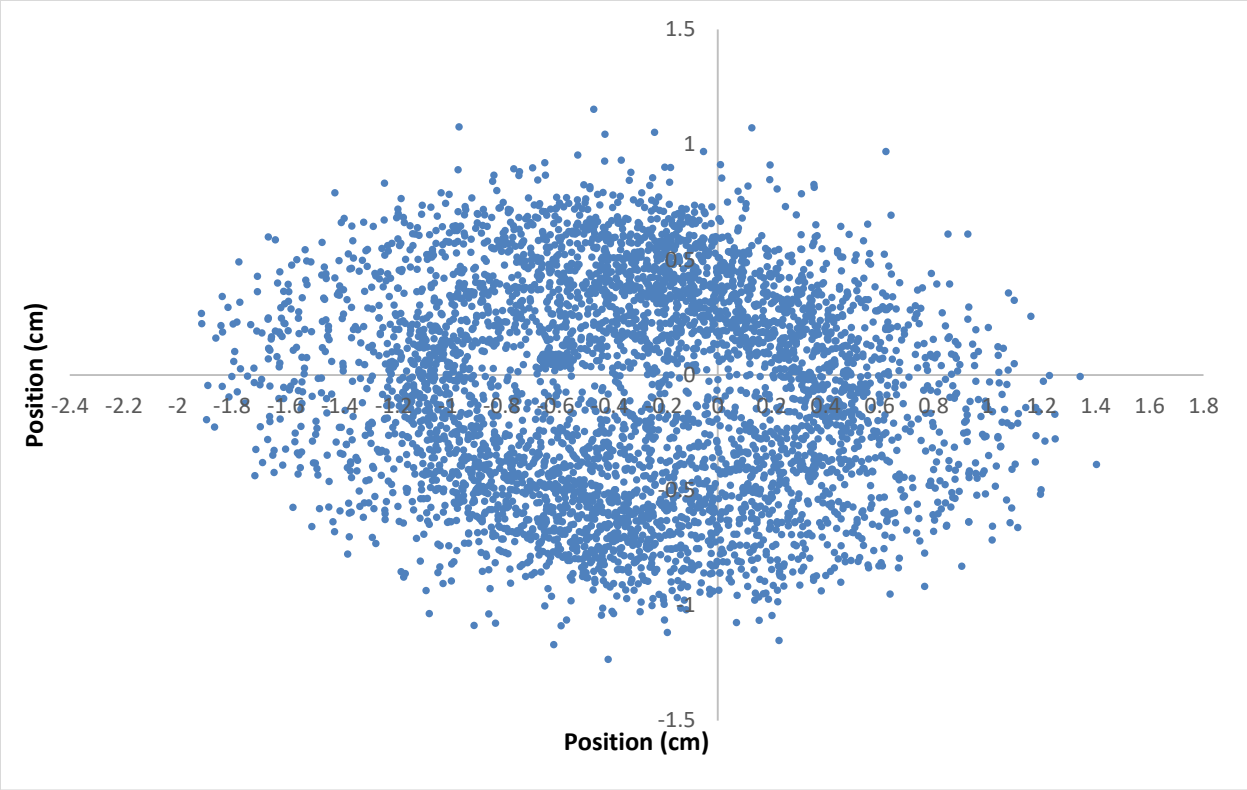

Figure B-53. The top positioned planer behavior of the drill string during the 10V test; 100 Hz

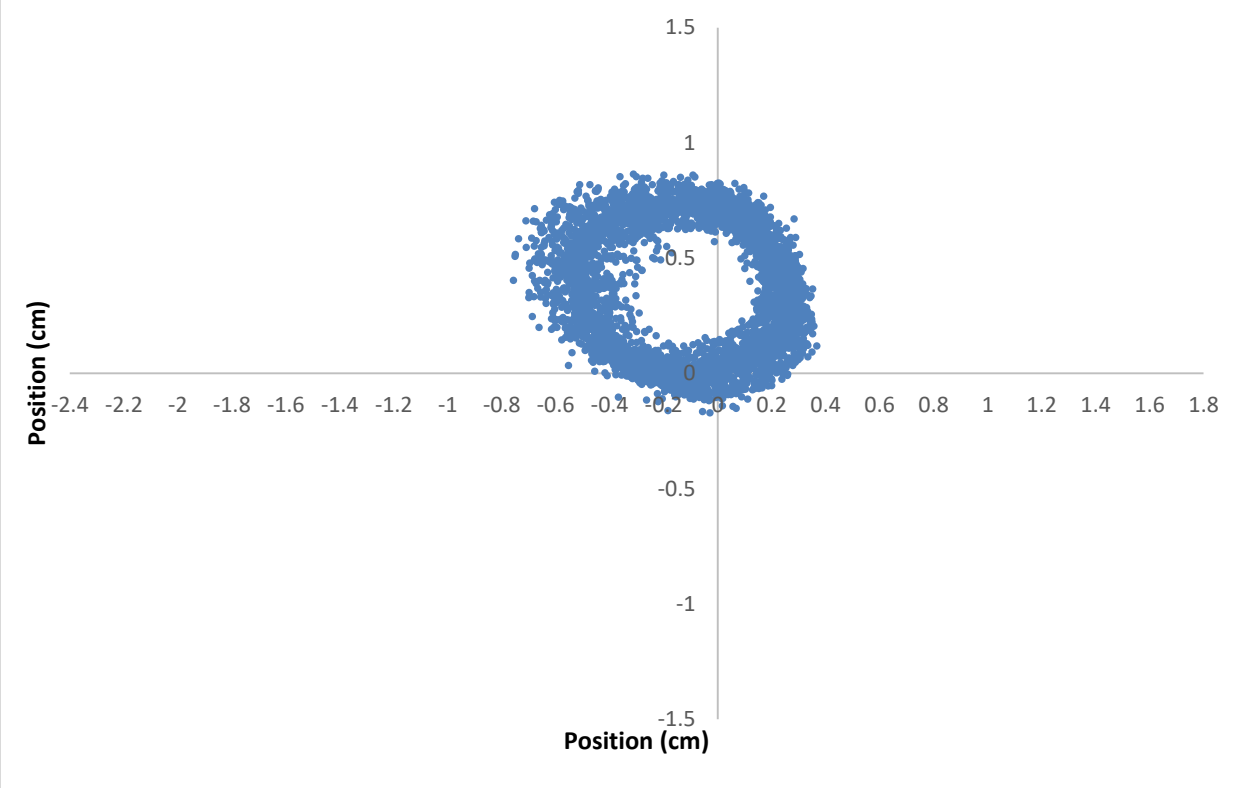

Figure B-54. The bottom positioned planer behavior of the drill string during the 10V test; 100 Hz

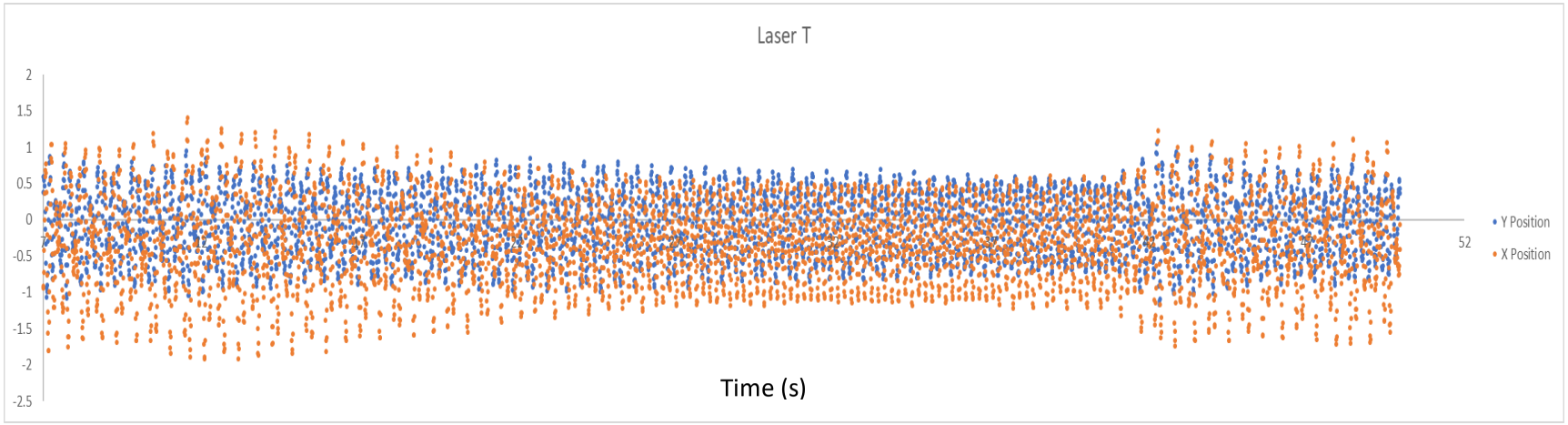

Figure B-55. The position of the drill string at the top plane as a function of time during the 10V test; 100 Hz

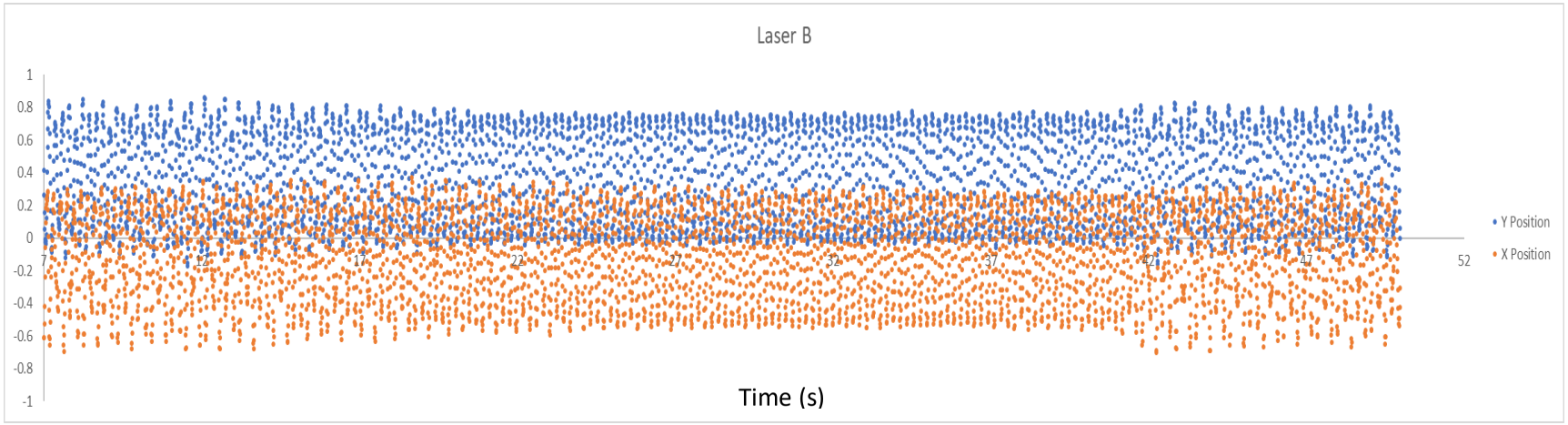

Figure B-56. The position of the drill string at the bottom plane as a function of time during the 10V test; 100 Hz

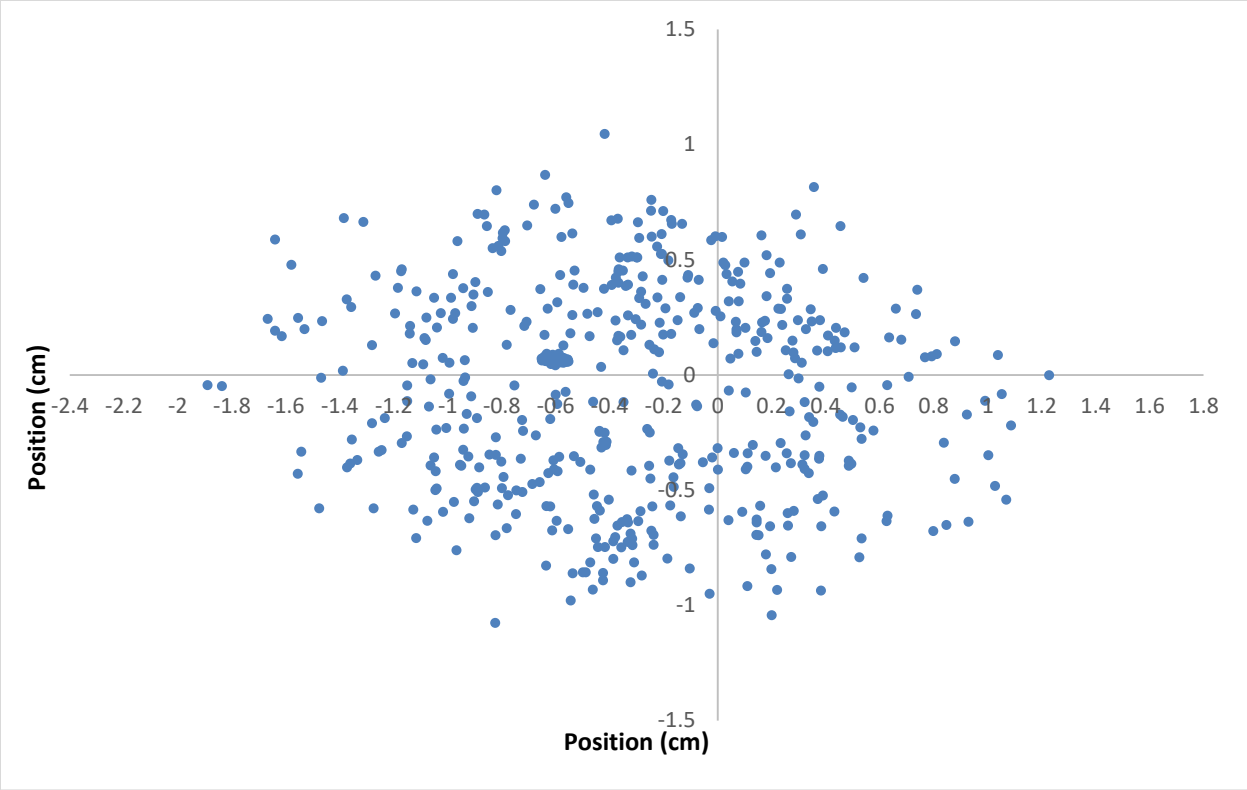

Figure B-57. The top positioned planer behavior of the drill string during the 10V test; 10 Hz

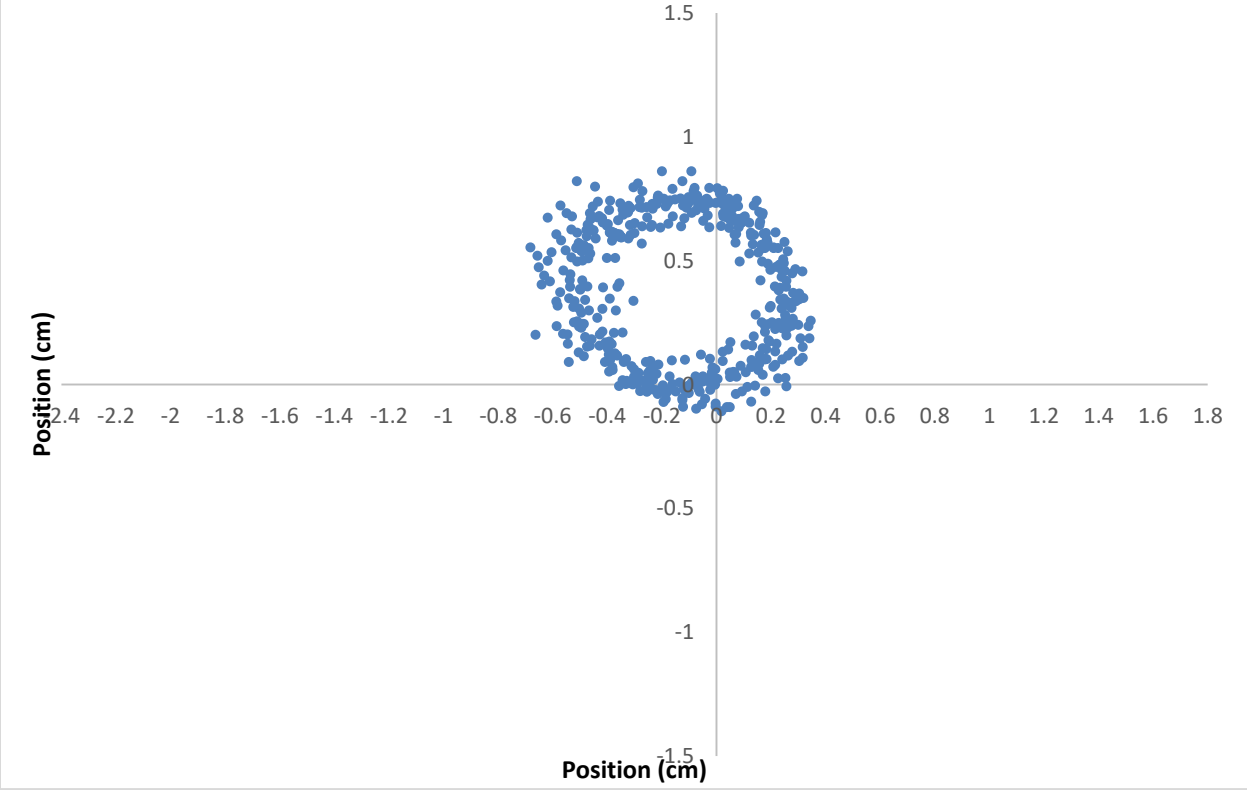

Figure B-58. The bottom positioned planer behavior of the drill string during the 10V test; 10 Hz

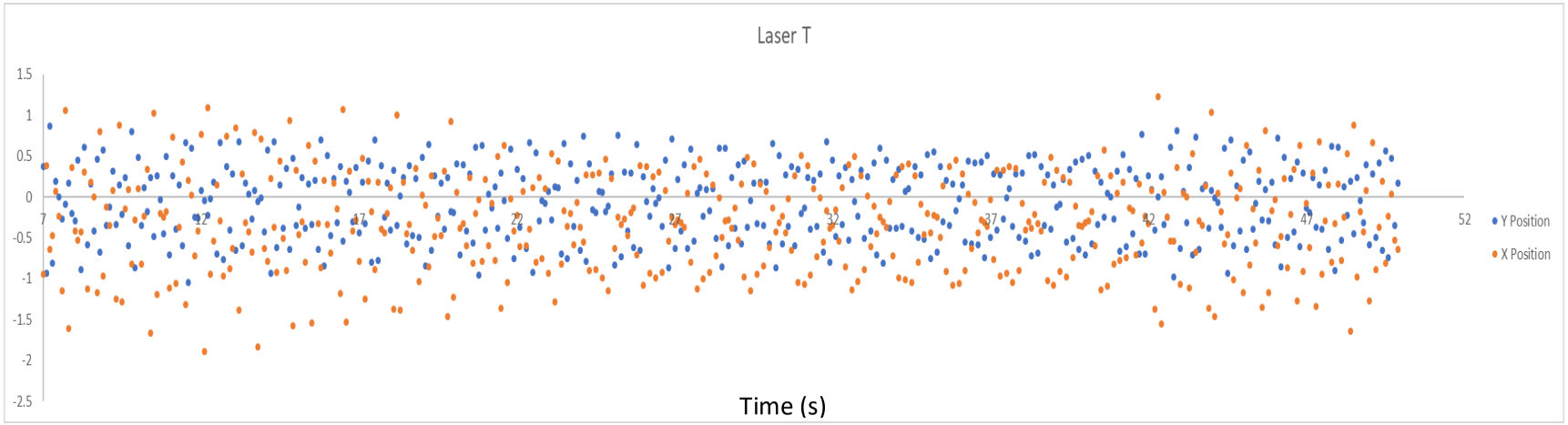

Figure B-59. The position of the drill string at the top plane as a function of time during the 10V test; 10 Hz

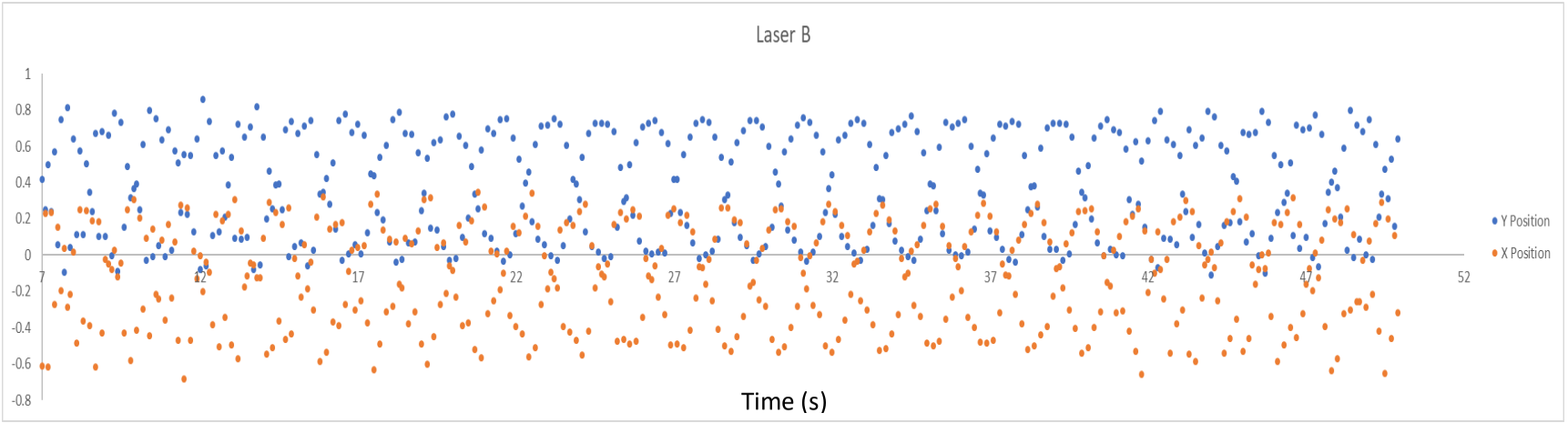

Figure B-60. The position of the drill string at the bottom plane as a function of time during the 10V test; 10 Hz

Appendix C Auxiliary Graphs

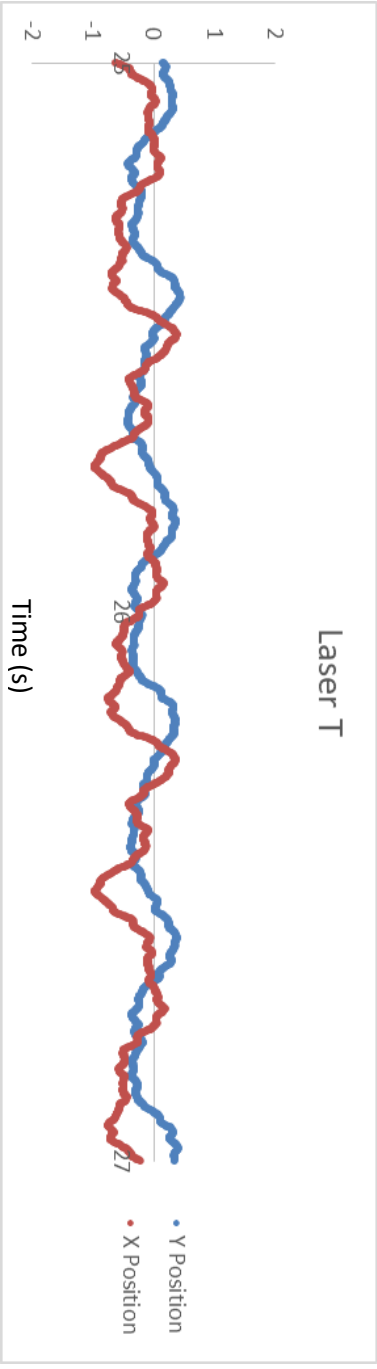

Figure C-1. The behavior of the drill string during the 6V test from 25s to 27s away from the drill bit

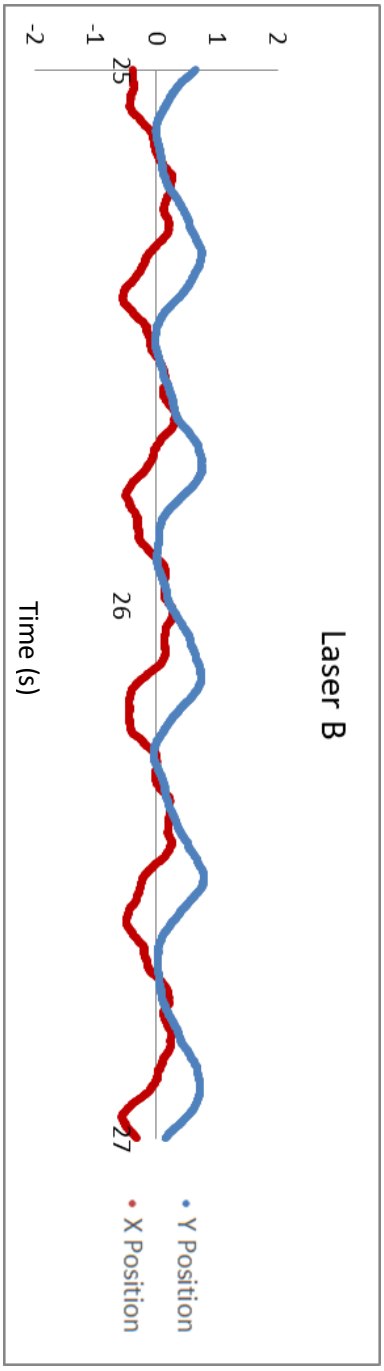

Figure C-2. The behavior of the drill string during the 6V test from 25s to 27s near the drill bit

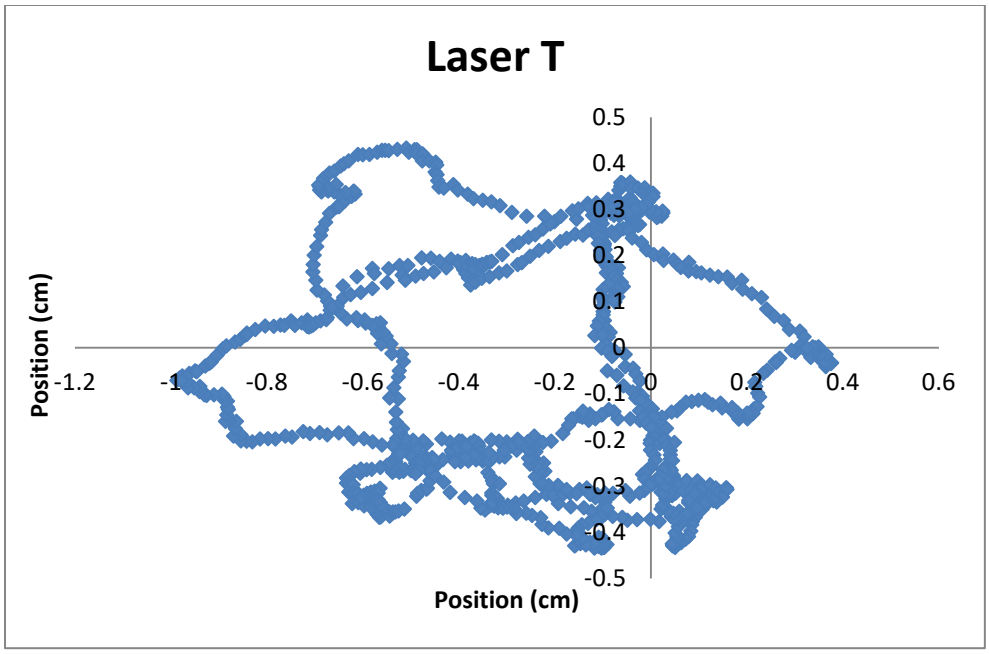

Figure C- 3. Position trace of the drill string far from the drill bit from 25s to 26s during the 6V experiment

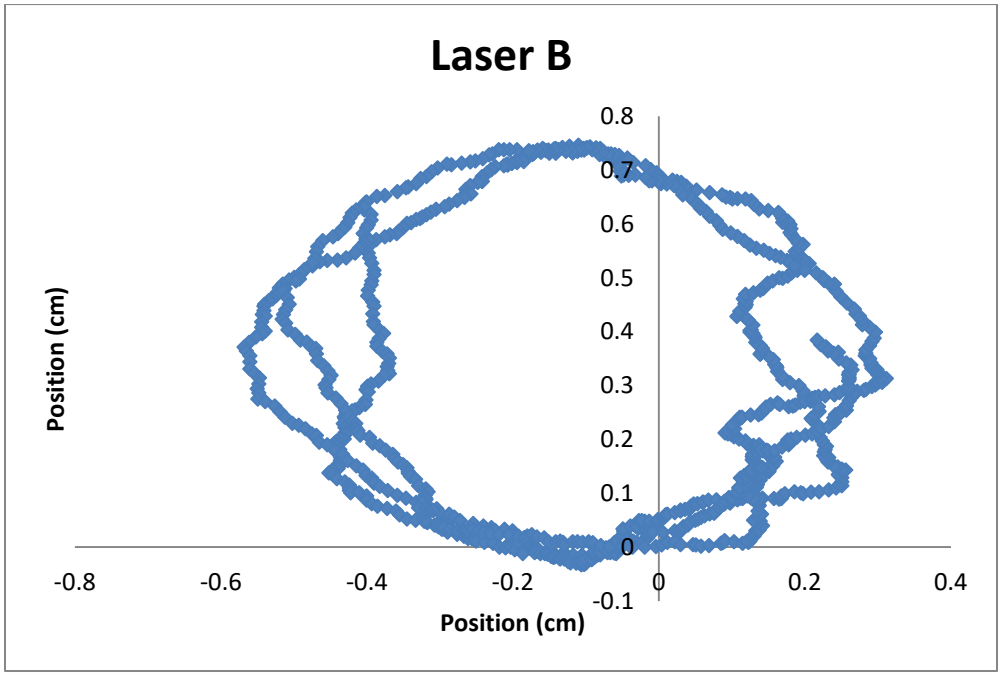

Figure C- 4. Position trace of the drill string near the drill bit from 25s to 26s during the 6V experiment

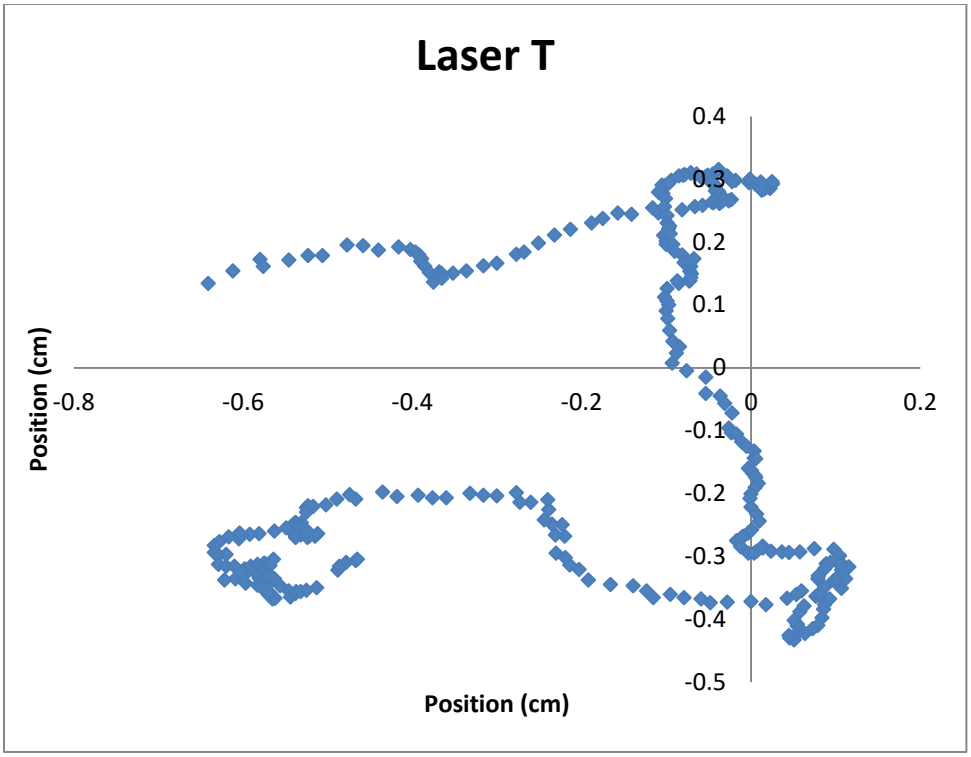

Figure C-5. Position trace of the drill string far from the drill bit from 25s to 25.333s during the 6V experiment

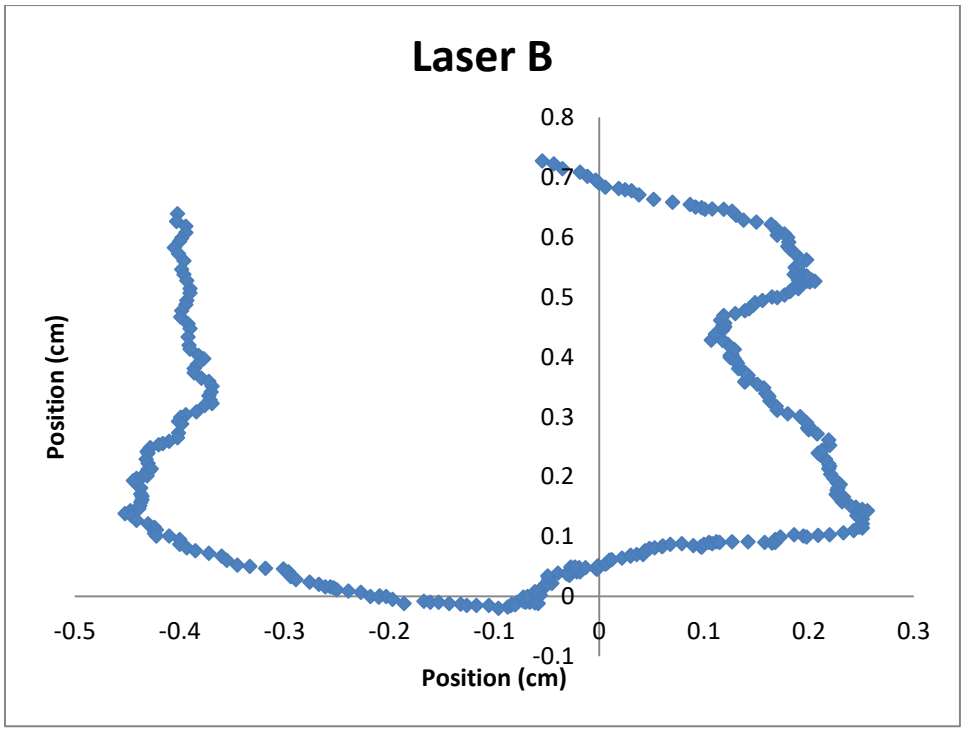

Figure C-6. Position trace of the drill string near the drill bit from 25s to 25.333s during the 6V experiment

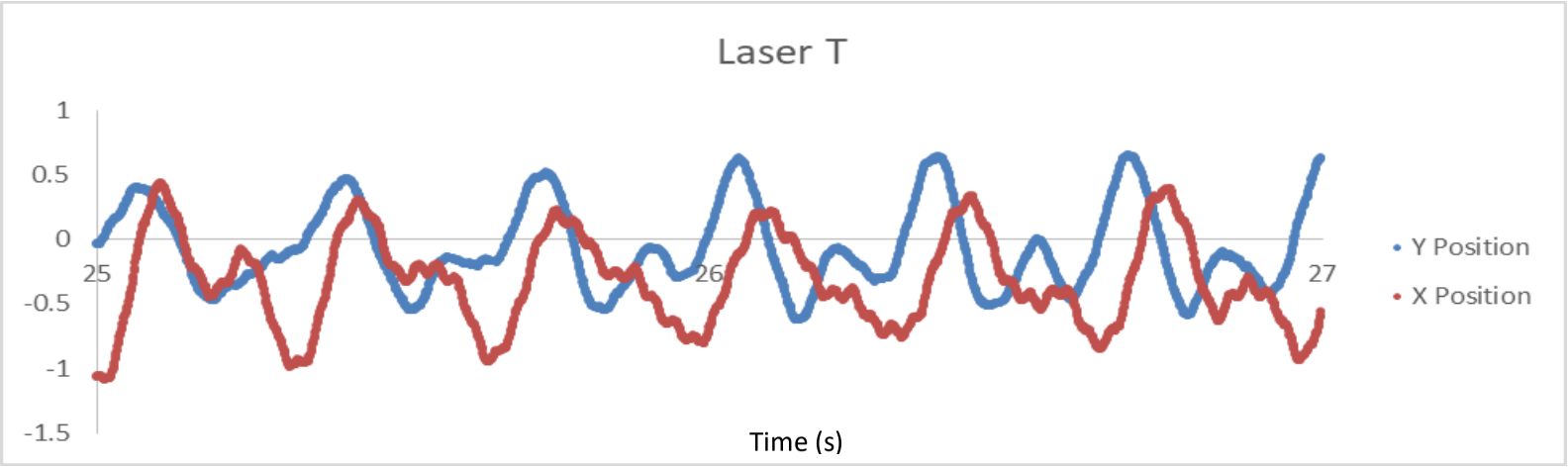

Figure C-7. The behavior of the drill string during the 7V test from 25s to 27s far from the drill bit

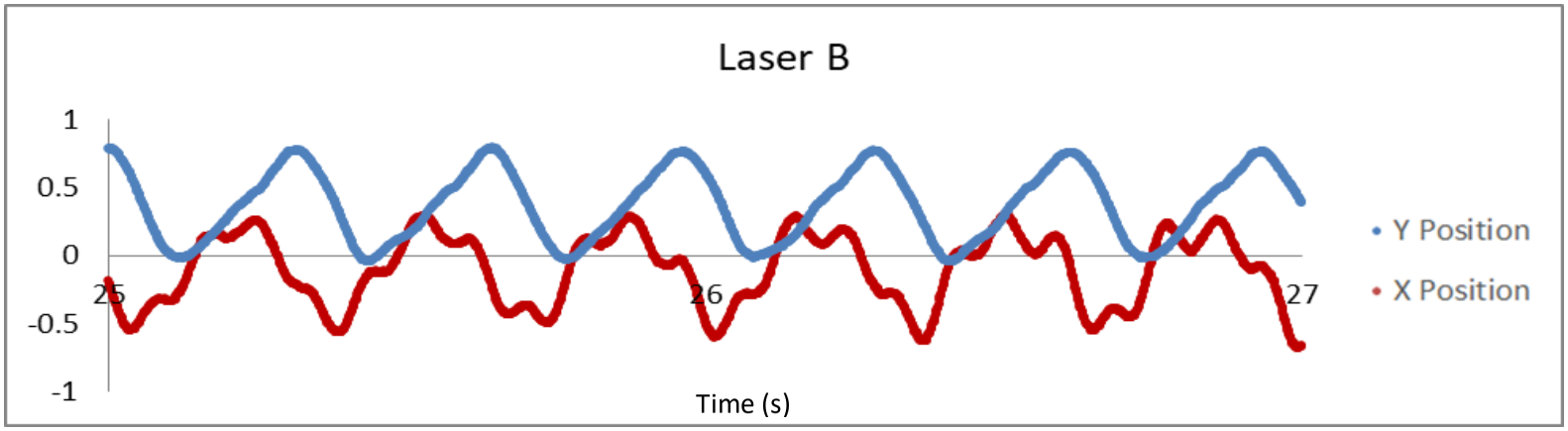

Figure C-8. The behavior of the drill string during the 7V test from 25s to 27s near the drill bit

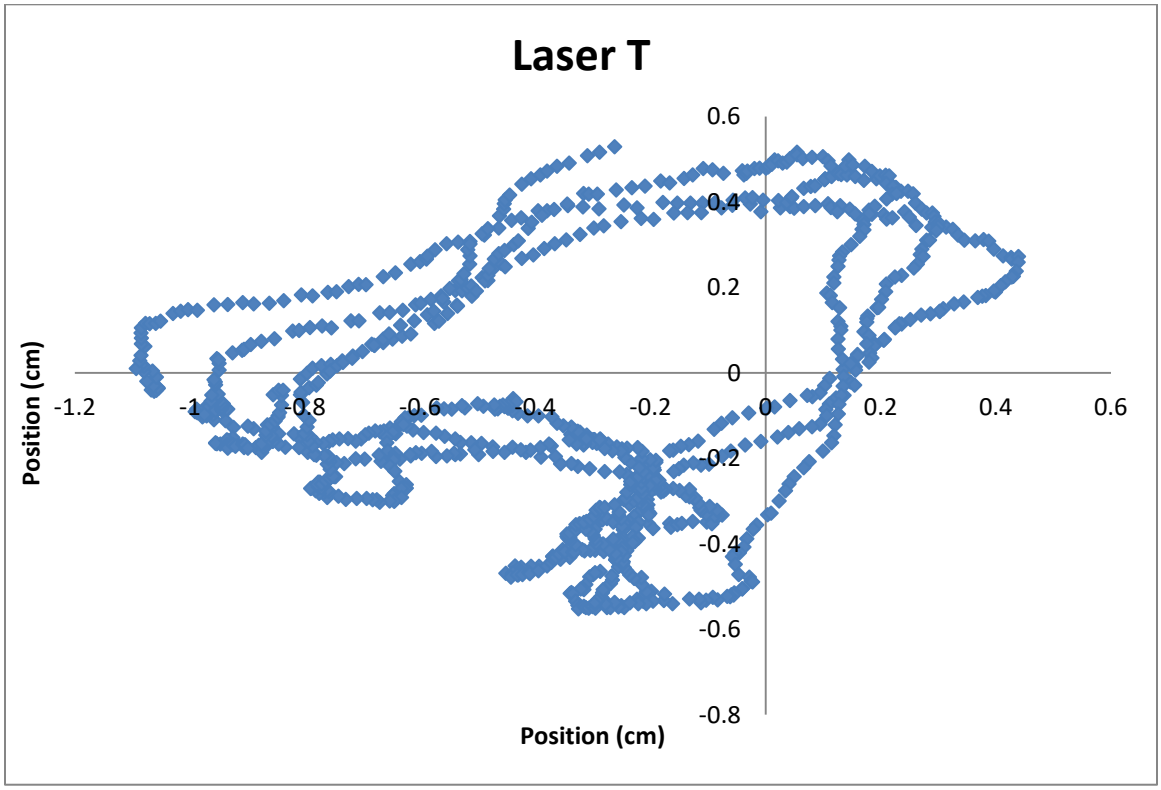

Figure C-9. Position trace of the drill string far from the drill bit from 25s to 26s during the 7V experiment

.

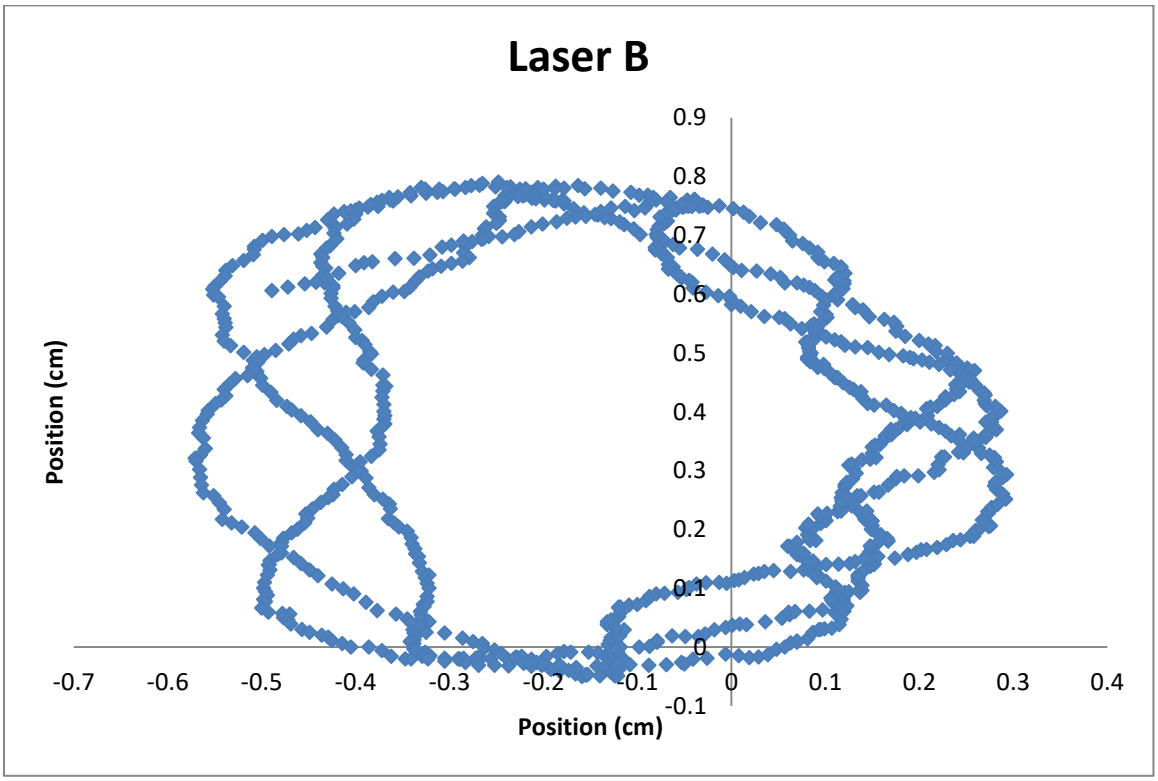

Figure C-10. Position trace of the drill string near the drill bit from 25s to 26s during the 7V experiment

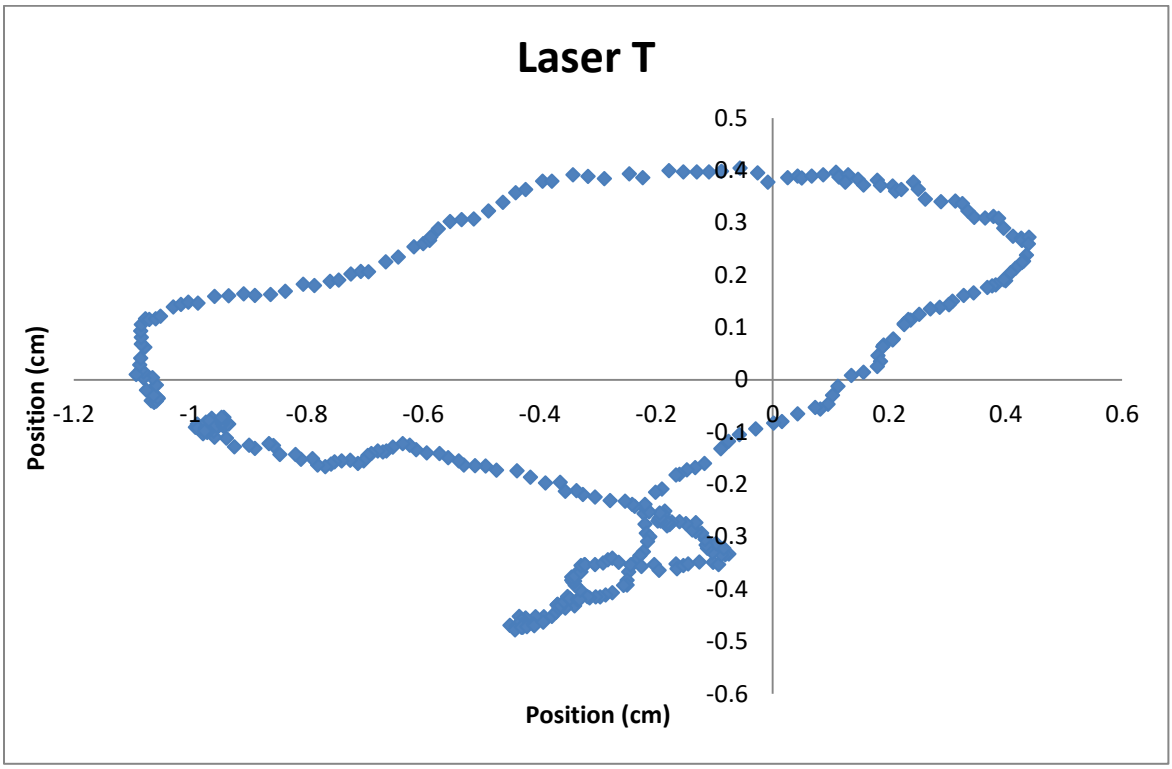

Figure C-11. Position trace of the drill string far from the drill bit from 25s to 25.333s during the 7V experiment

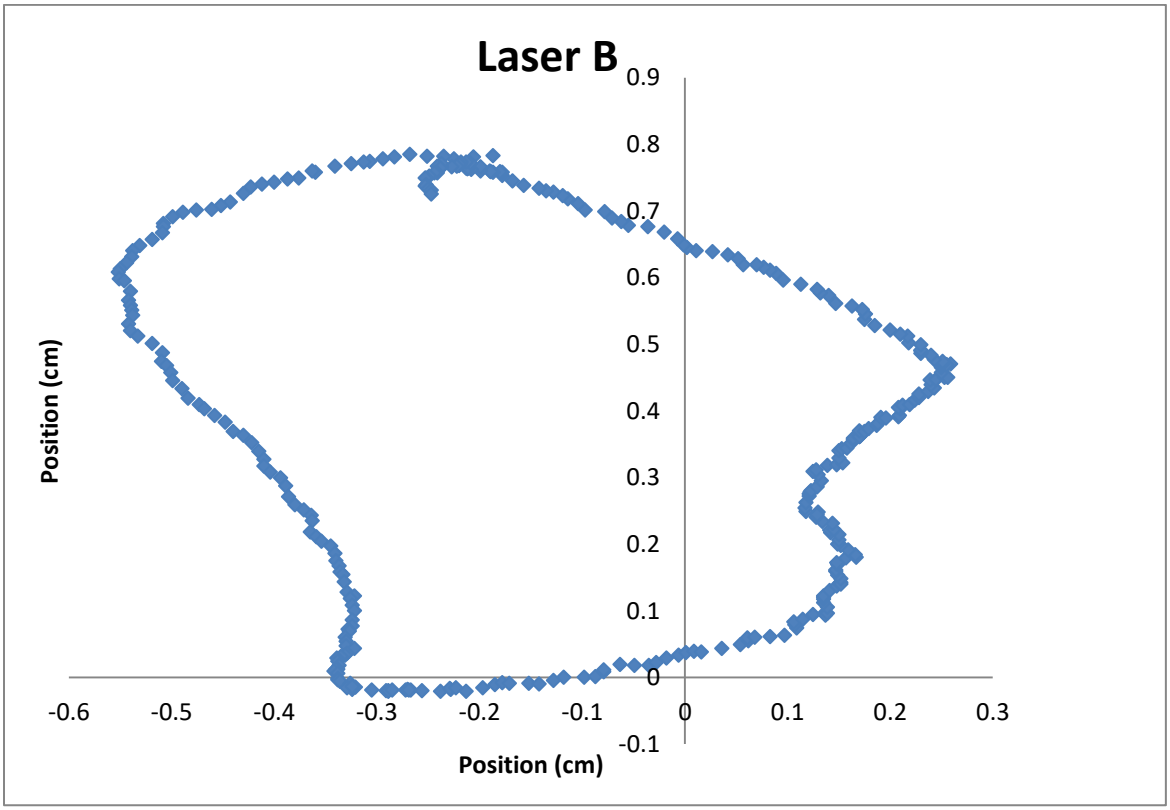

Figure C-12. Position trace of the drill string near the drill bit from 25s to 25.333s during the 7V experiment

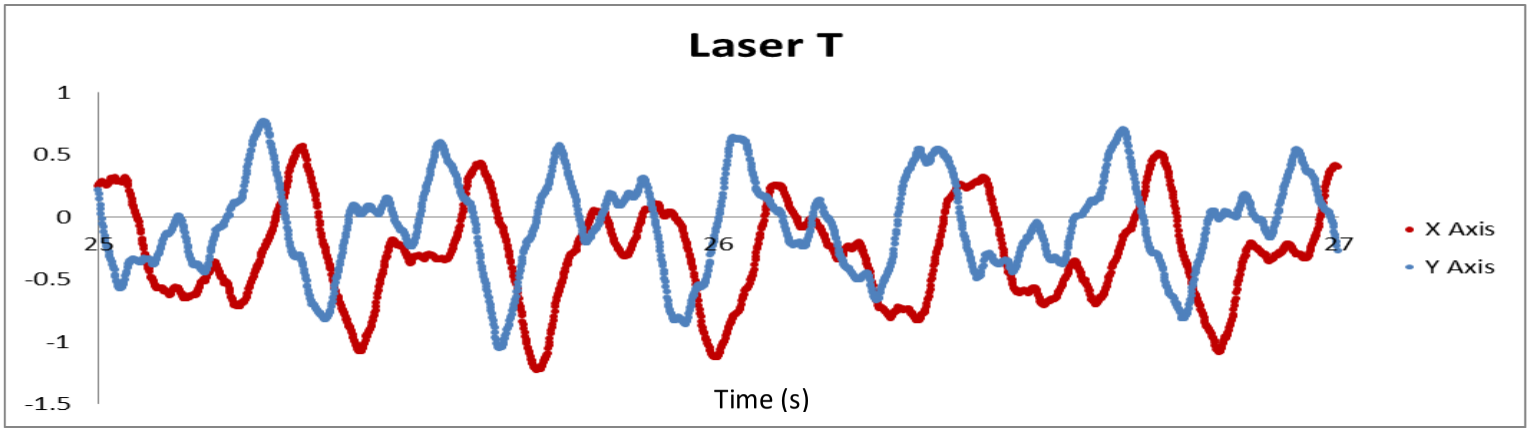

Figure C-13. The behavior of the drill string during the 8V test from 25s to 27s far drill bit

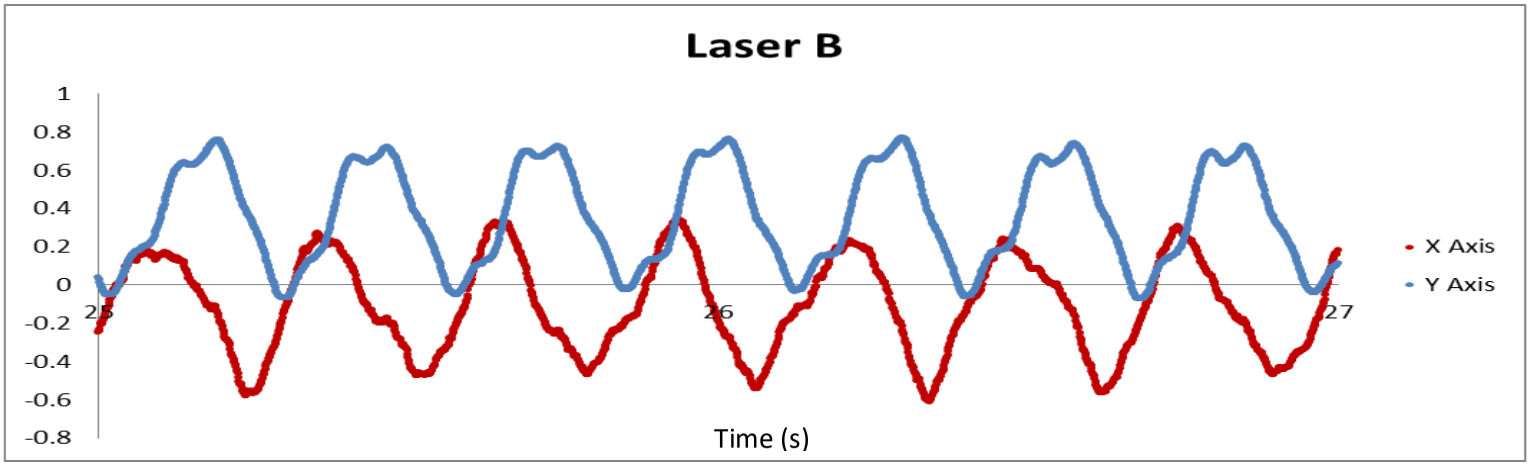

Figure C-14. The behavior of the drill string during the 8V test from 25s to 27s near the drill bit

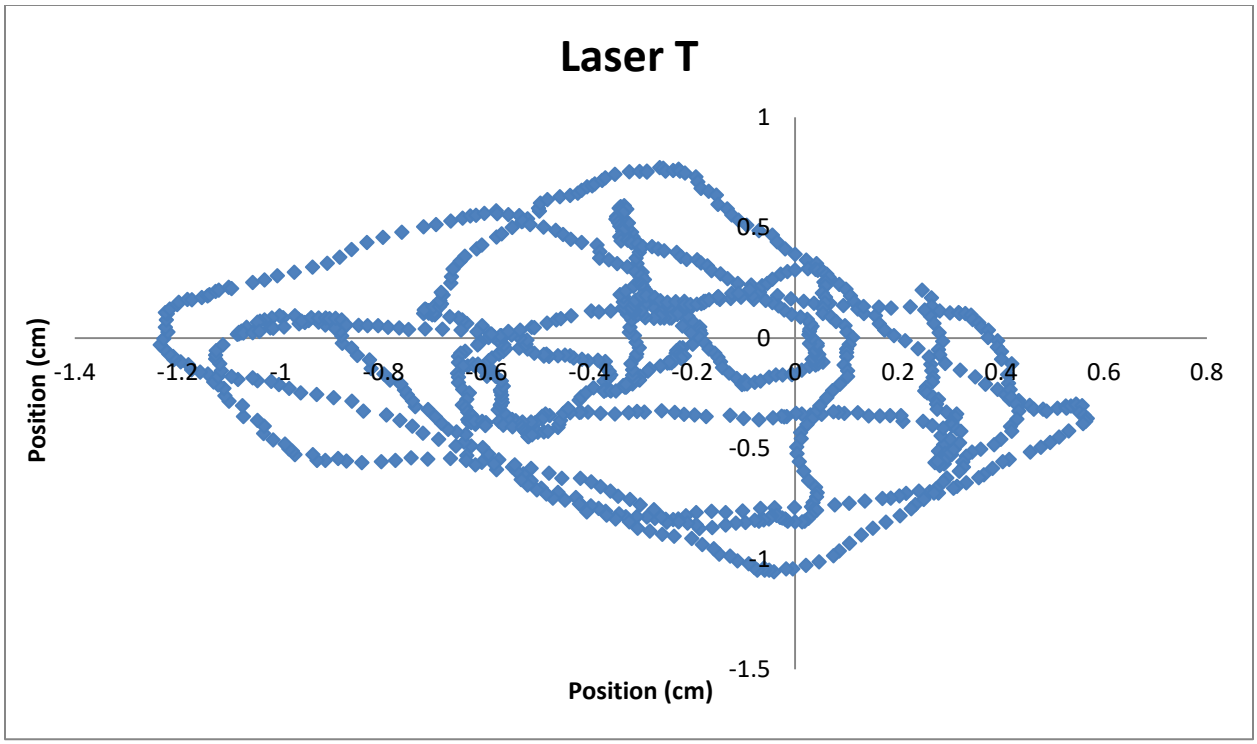

Figure C-15. Position trace of the drill string far from the drill bit from 25s to 26s during the 6V experiment

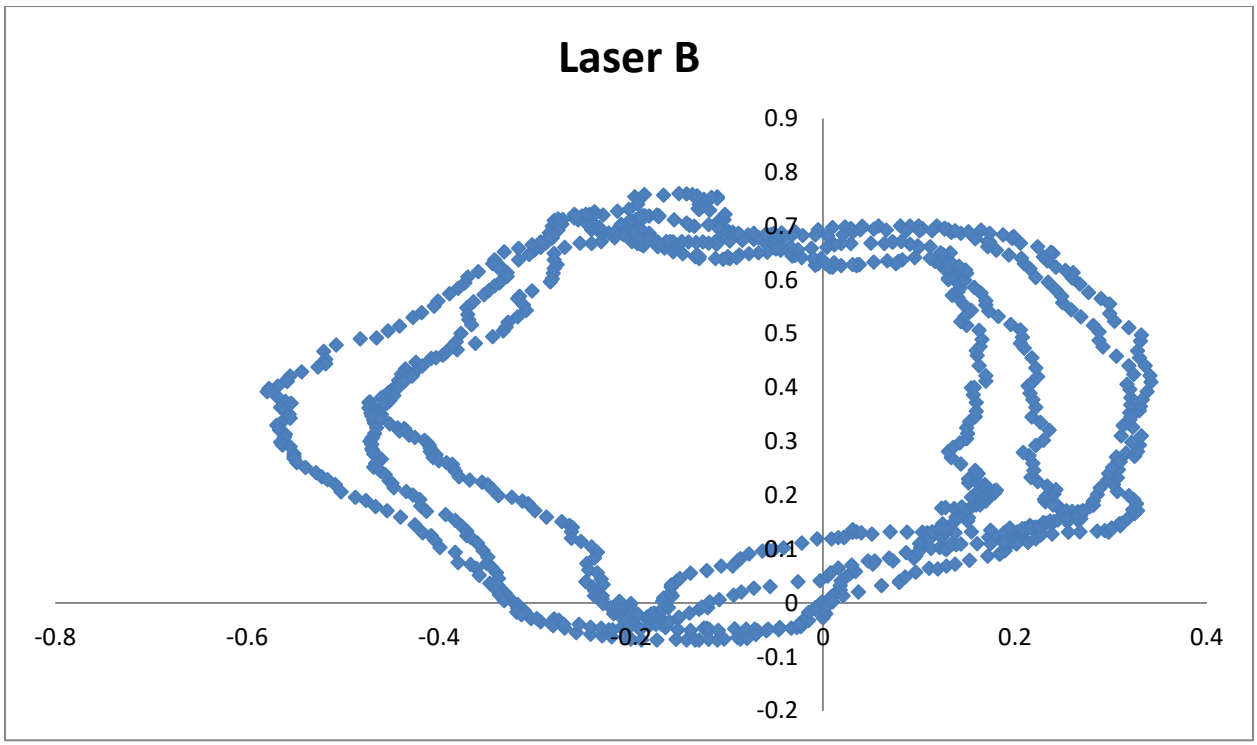

Figure C-16. Position trace of the drill string near the drill bit from 25s to 26s during the 8V experiment

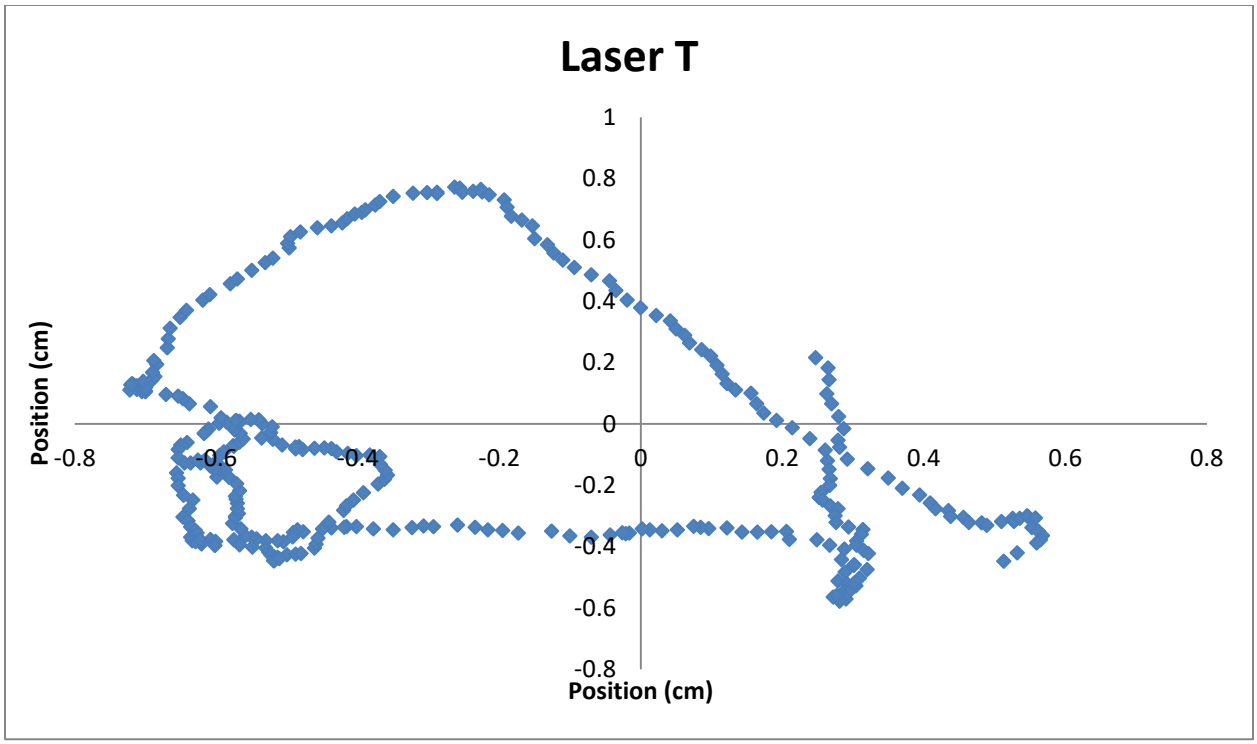

Figure C-17. Position trace of the drill string far from the drill bit from 25s to 25.333s during the 8V experiment

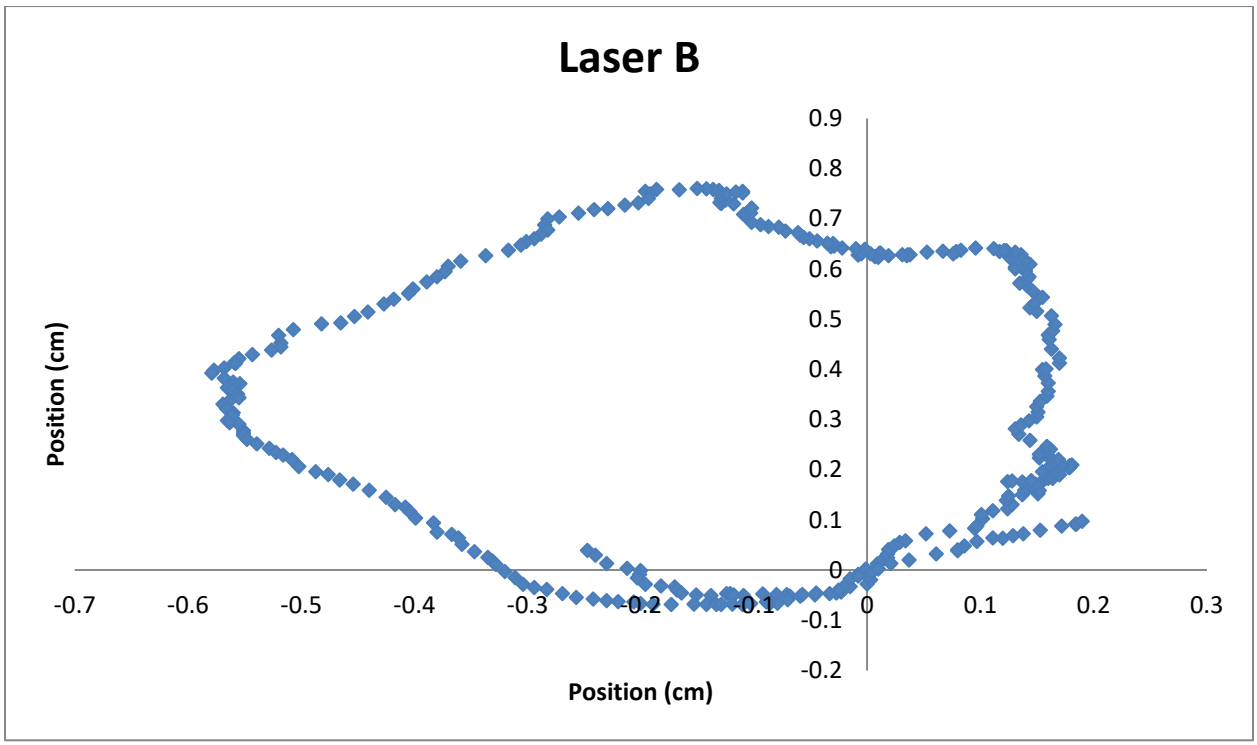

Figure C-18. Position trace of the drill string near the drill bit from 25s to 25.333s during the 8V experiment

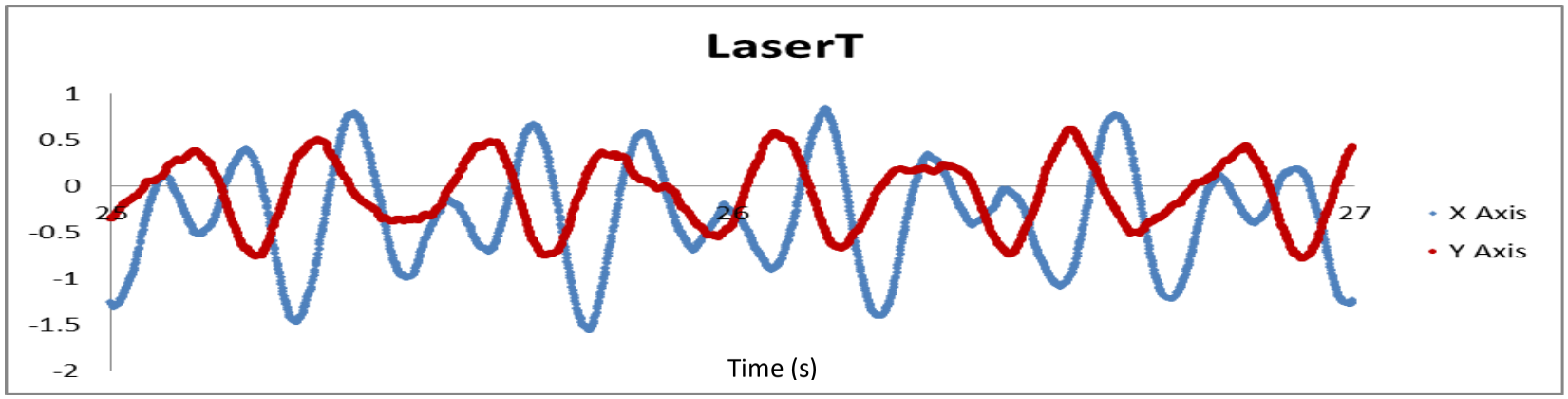

Figure C-19. The behavior of the drill string during the 9V test from 25s to 27s far from the drill bit

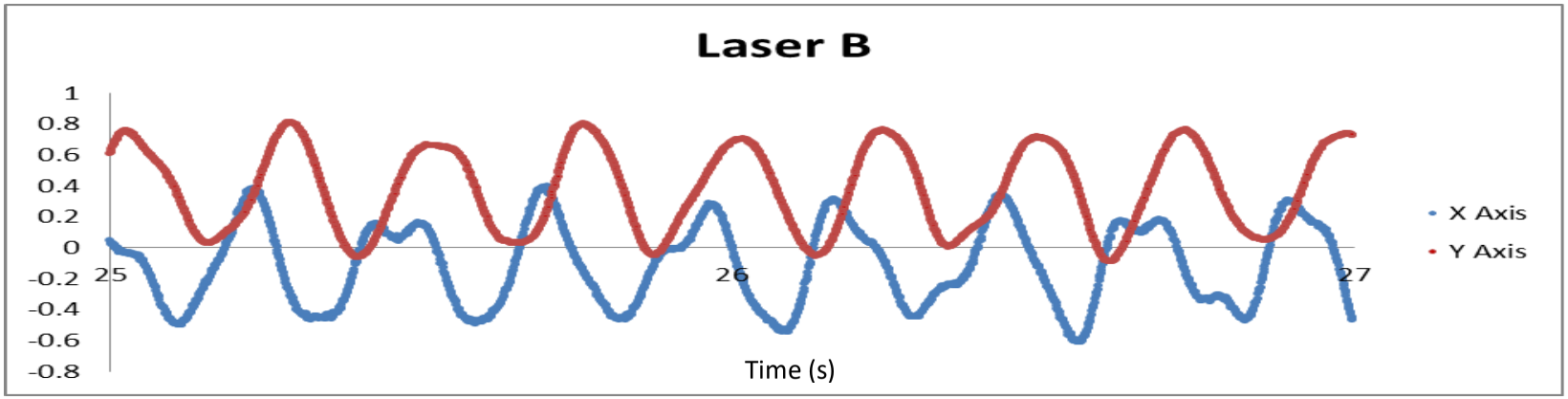

Figure C-20. The behavior of the drill string during the 9V test from 25s to 27s near the drill bit

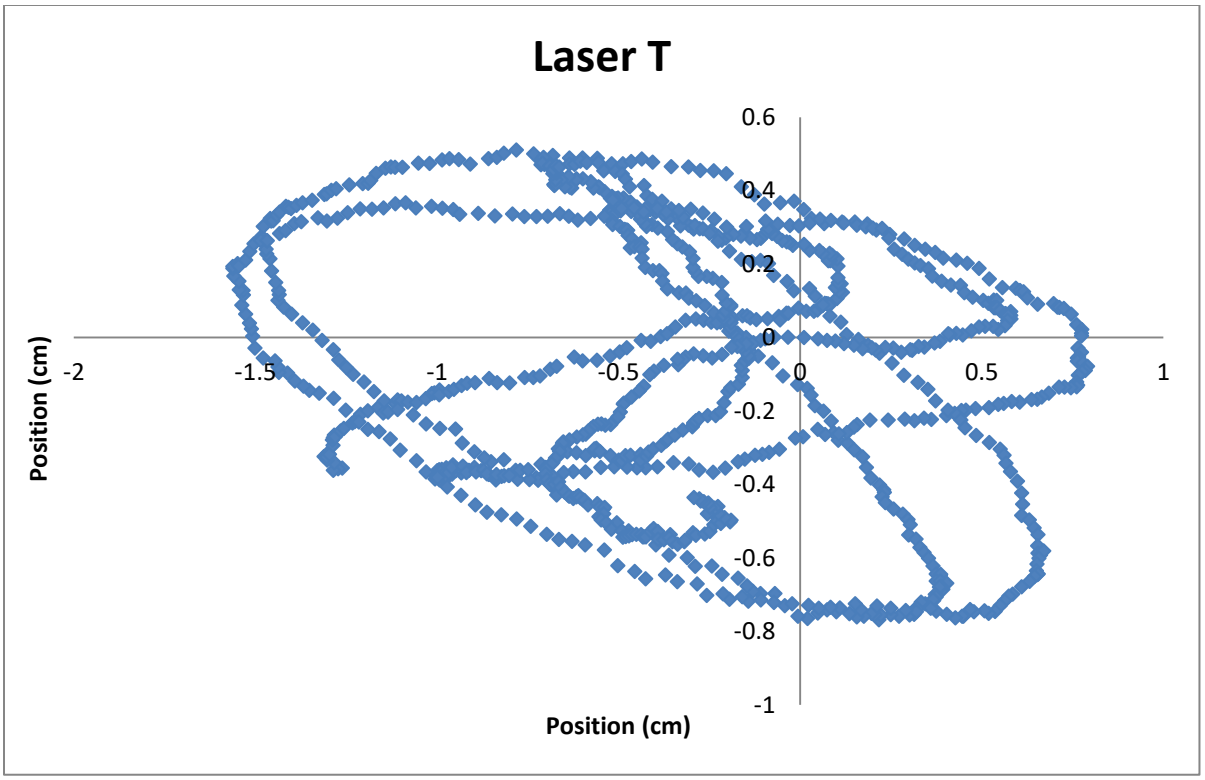

Figure C-21. Position trace of the drill string far from the drill bit from 25s to 26s during the 9V experiment

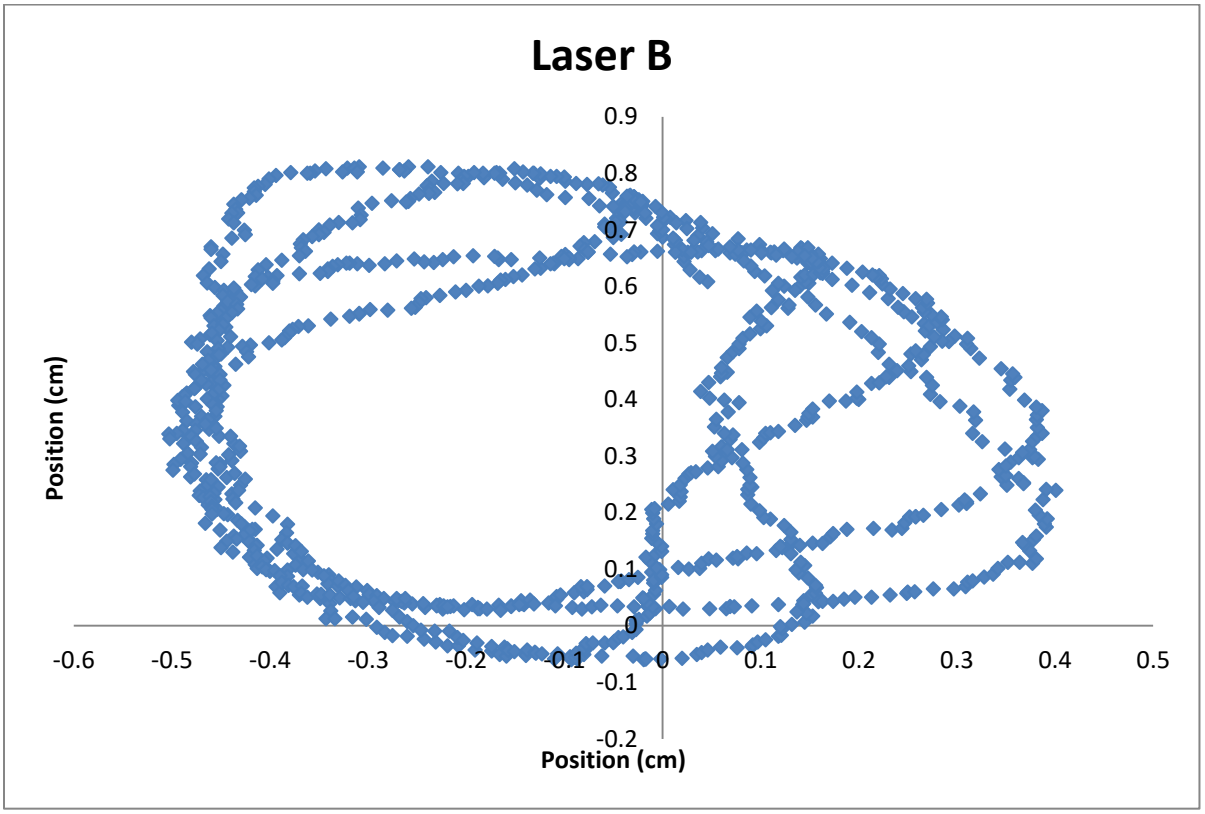

Figure C-22. Position trace of the drill string near the drill bit from 25s to 26s during the 9V experiment

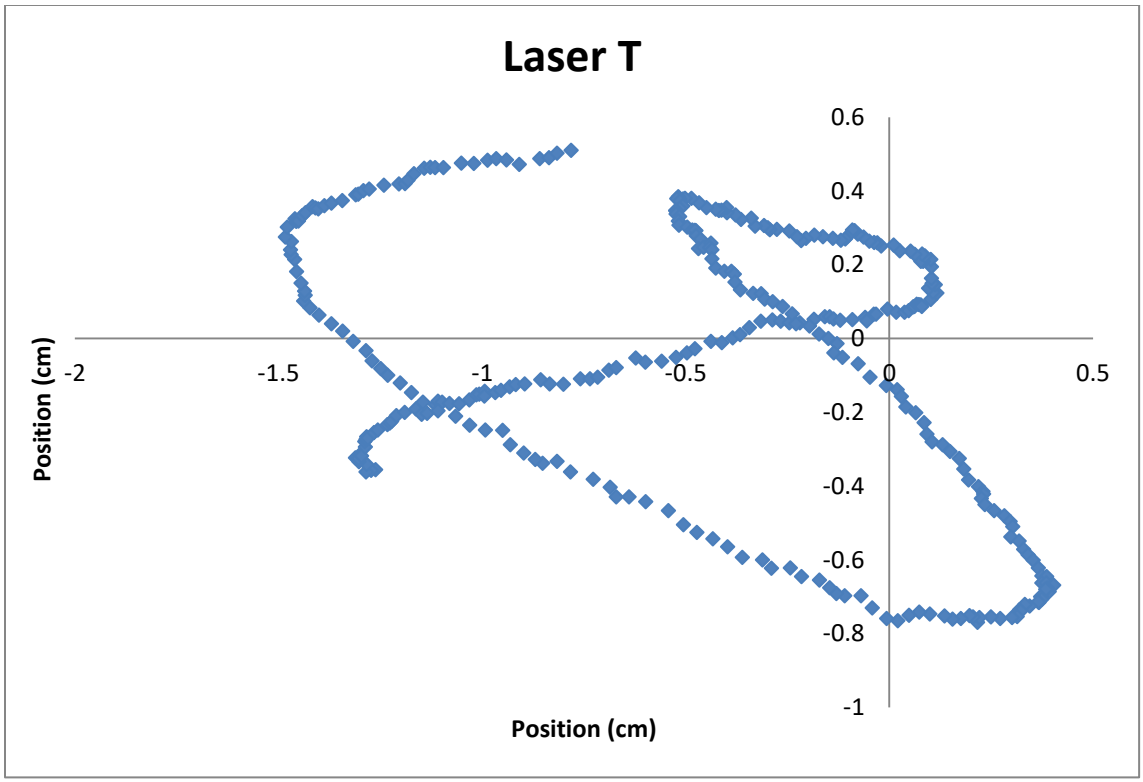

Figure C-23. Position trace of the drill string far from the drill bit from 25s to 25.333s during the 9V experiment

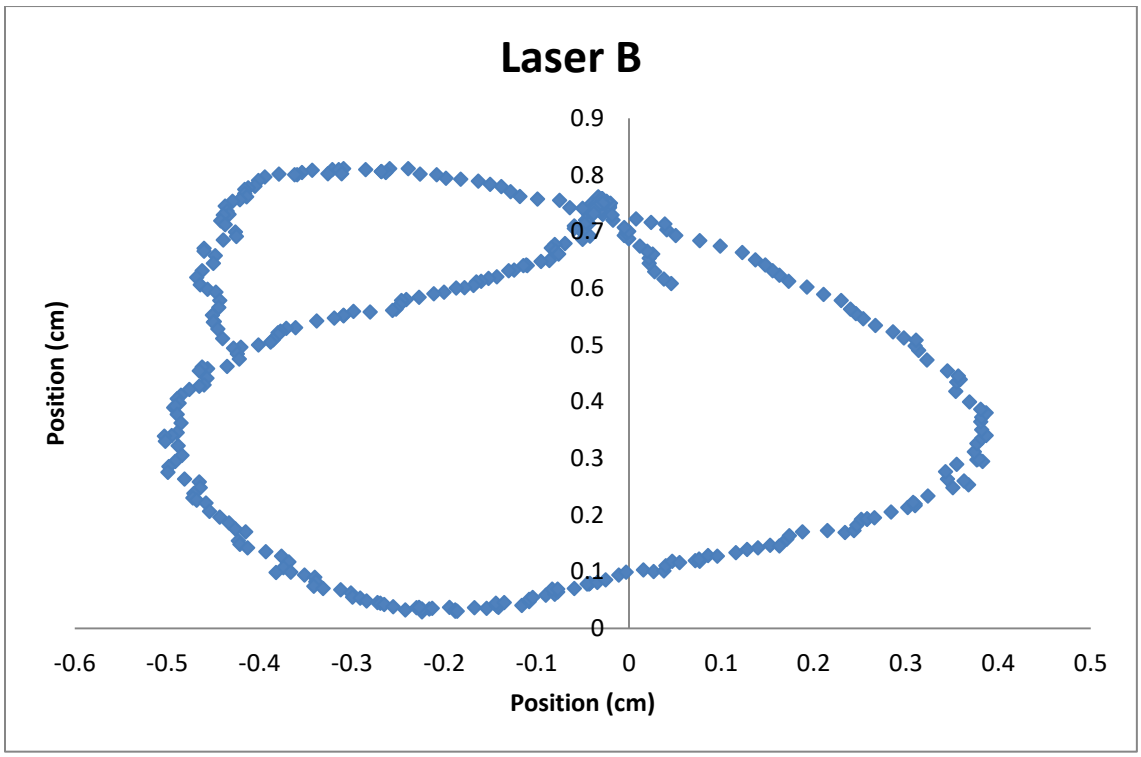

Figure C-24 Position trace of the drill string near the drill bit from 25s to 25.333s during the 9V experiment

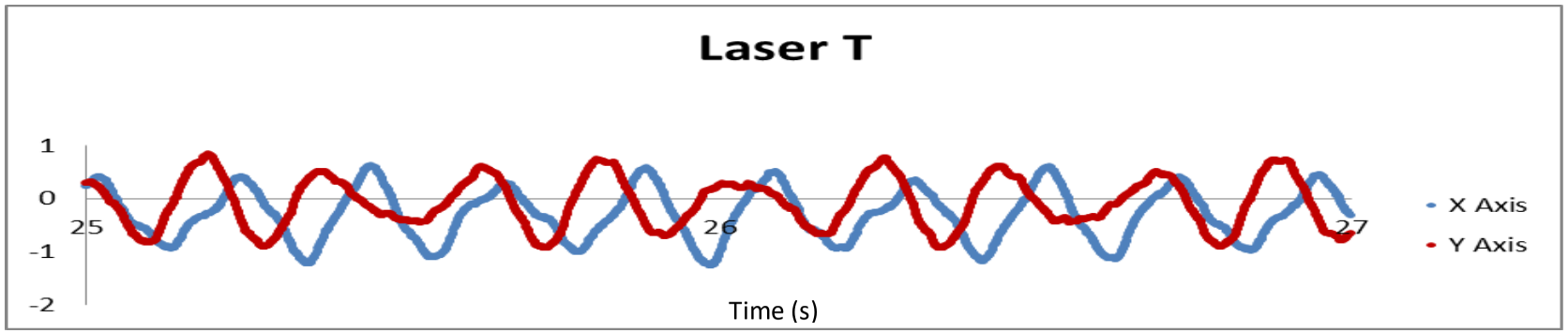

Figure C-25. The behavior of the drill string during the 10V test from 25s to 27s far from the drill bit

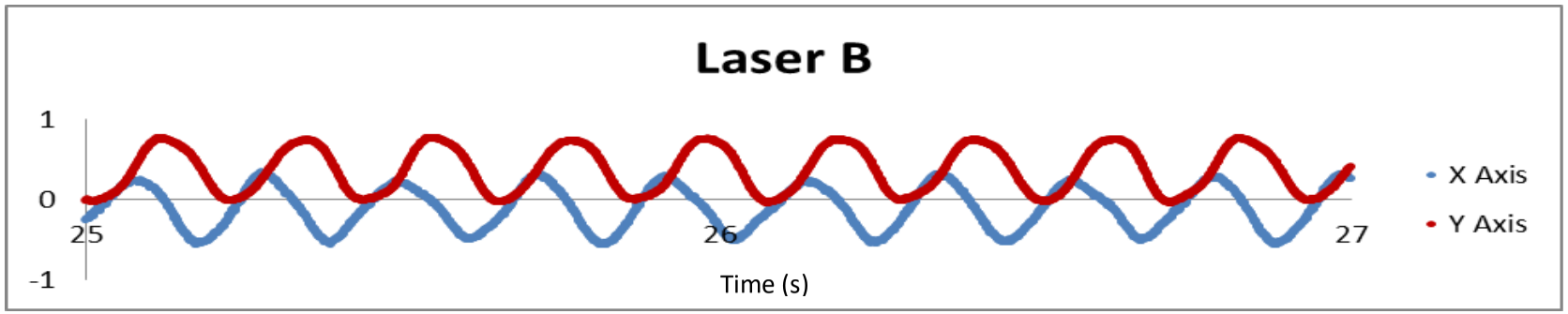

Figure C-26. The behavior of the drill string during the 10V test from 25s to 27s near the drill bit

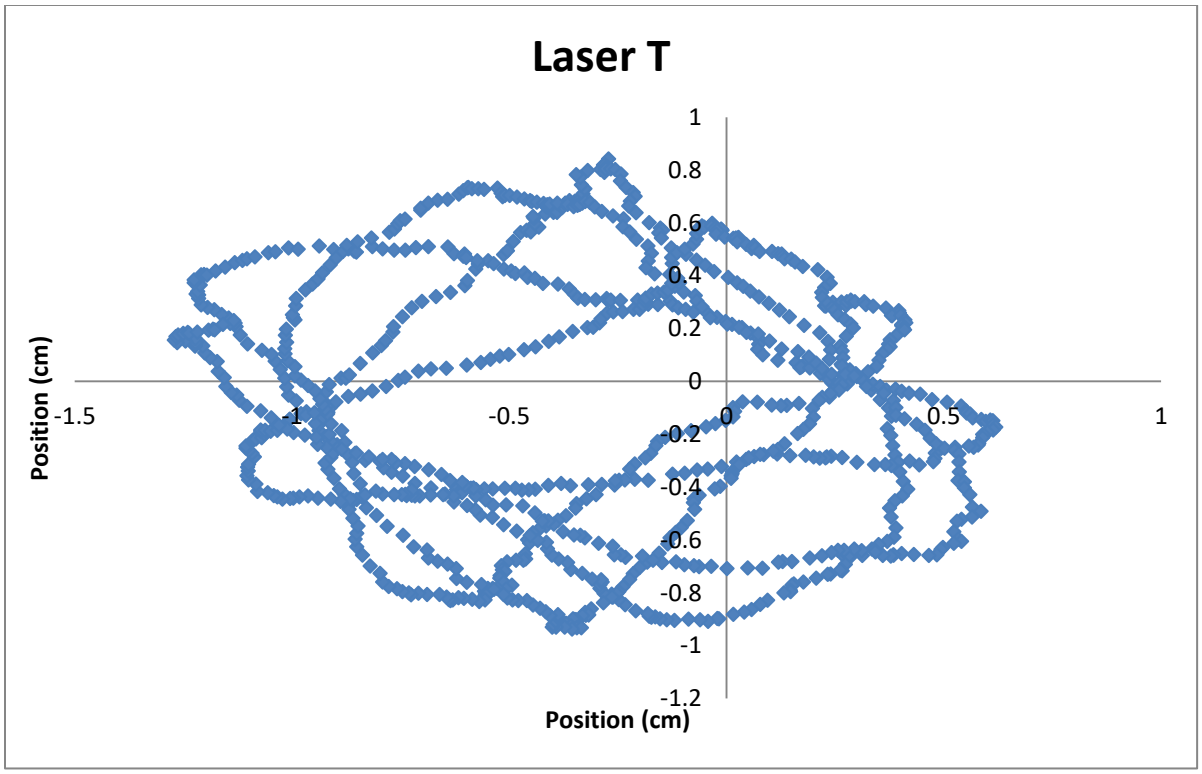

Figure C- 27. Position trace of the drill string far from the drill bit from 25s to 26s during the 10V experiment

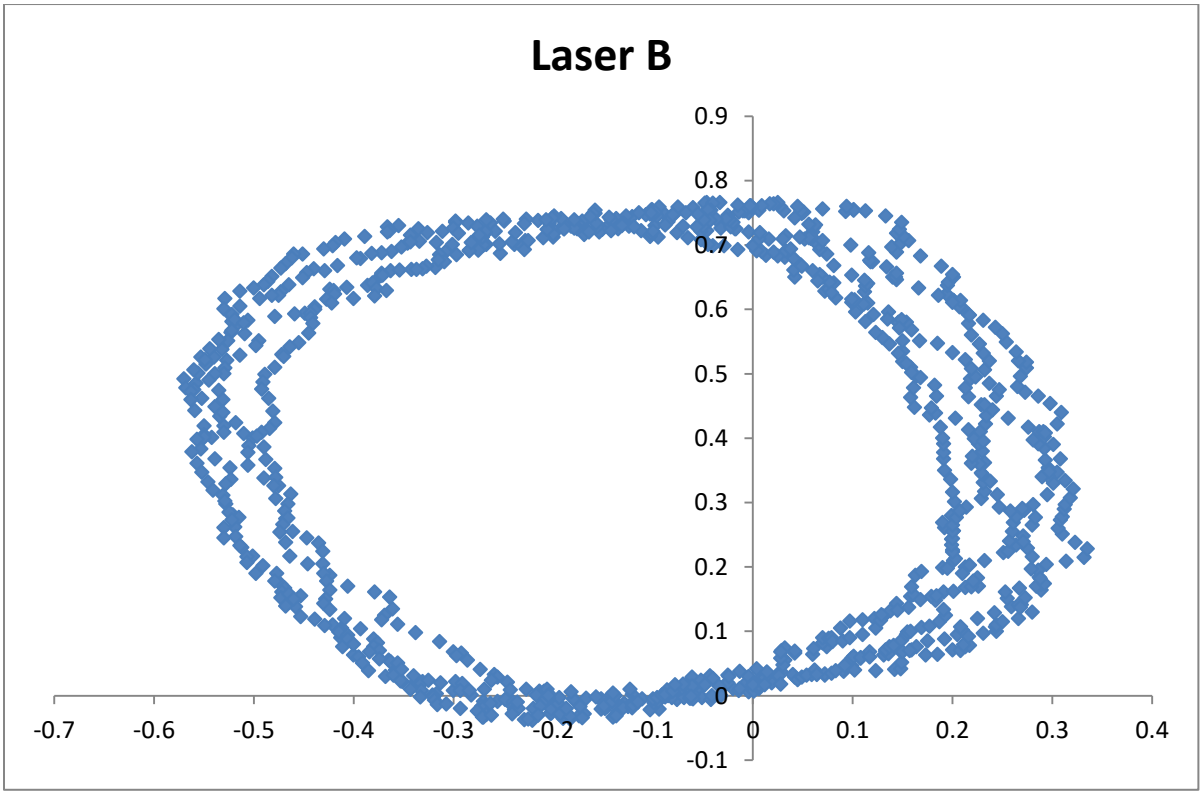

Figure C-28. Position trace of the drill string near the drill bit from 25s to 26s during the 10V experiment

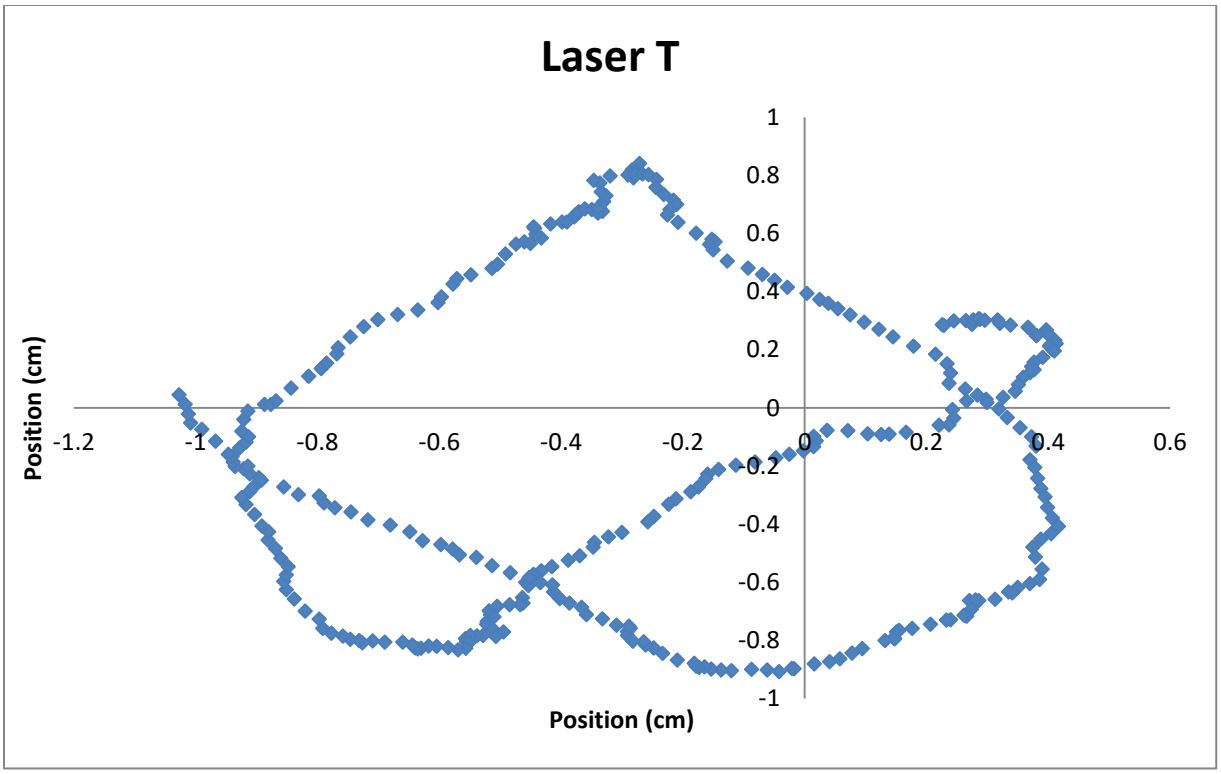

Figure C-29. Position trace of the drill string far from the drill bit from 25s to 25.333s during the 10V experiment

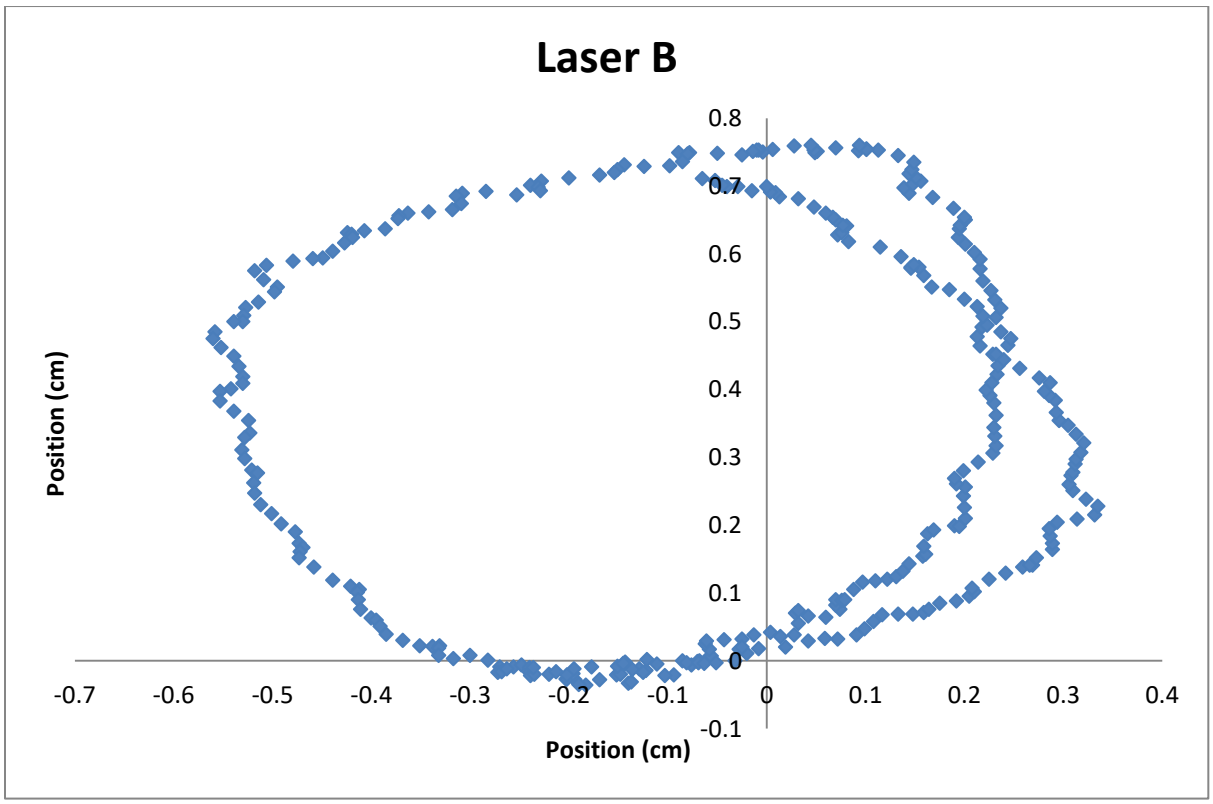

Figure C-30. Position trace of the drill string near the drill bit from 25s to 25.333s during the 10V experiment

Appendix D FFT Plots

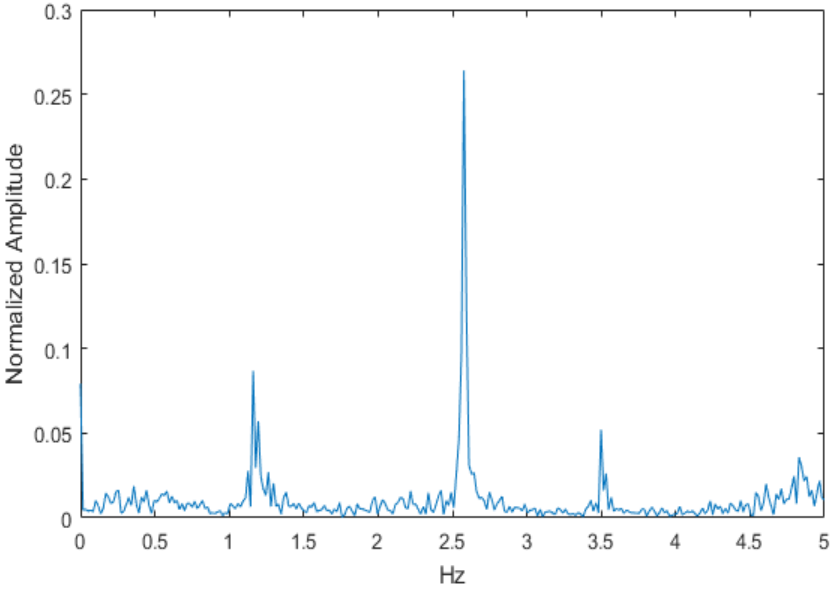

Figure D-1. FFT of the X axis of the bottom laser during the 6V test at 10 Hz

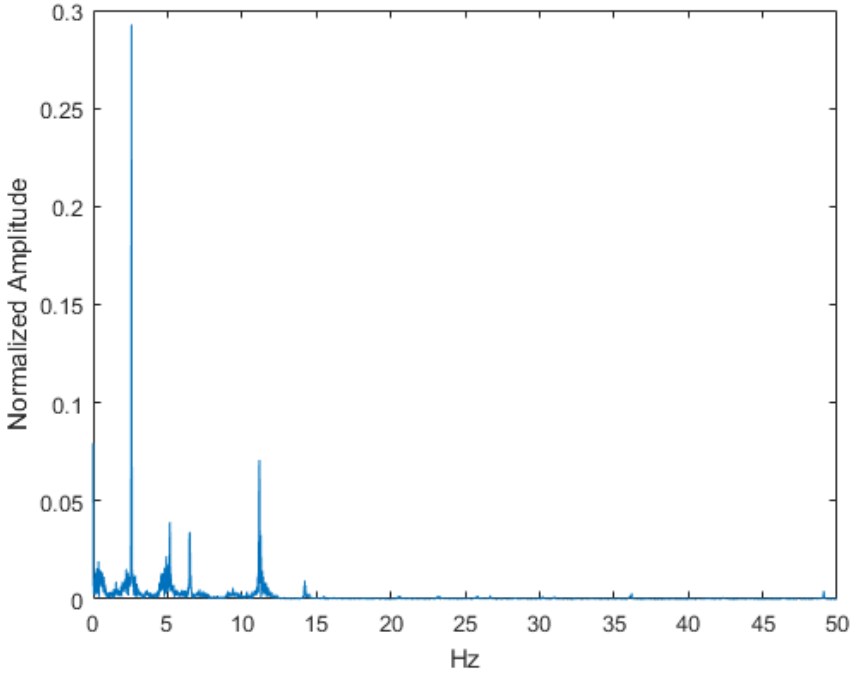

Figure D-2. FFT of the X axis of the bottom laser during the 6V test at 100 Hz

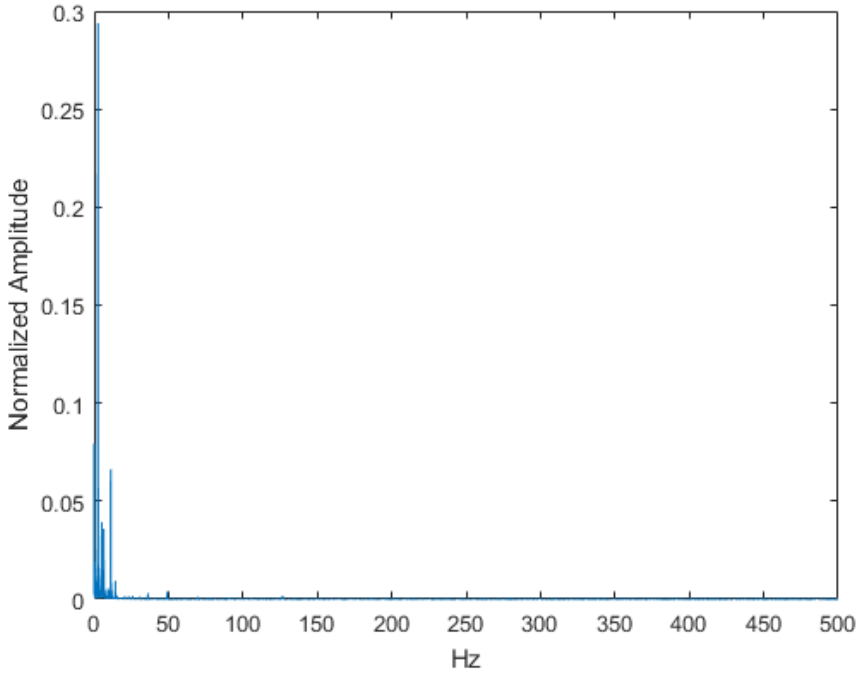

Figure D-3. FFT of the X axis of the bottom laser during the 6V test at 1 kHz

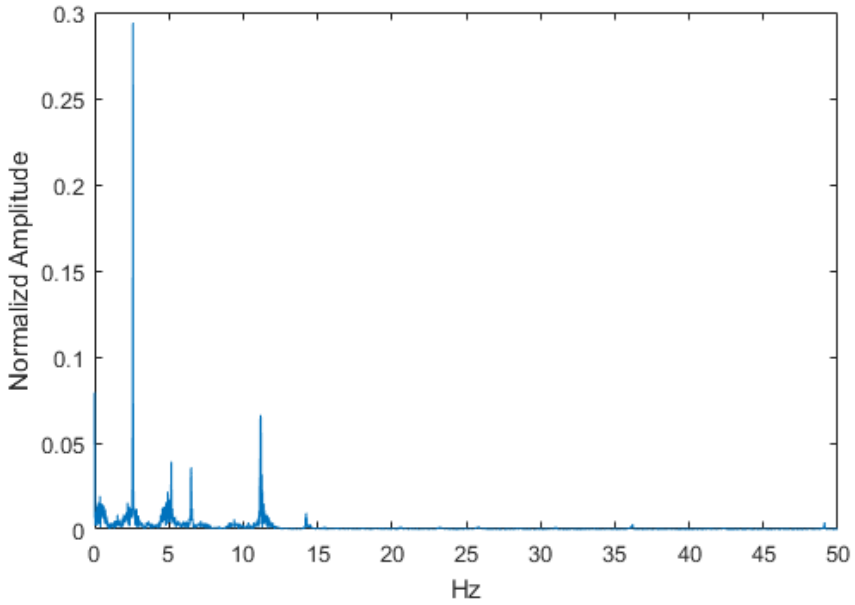

Figure D-4. FFT of the X axis of the bottom laser during the 6V test at 1 kHz zoomed in

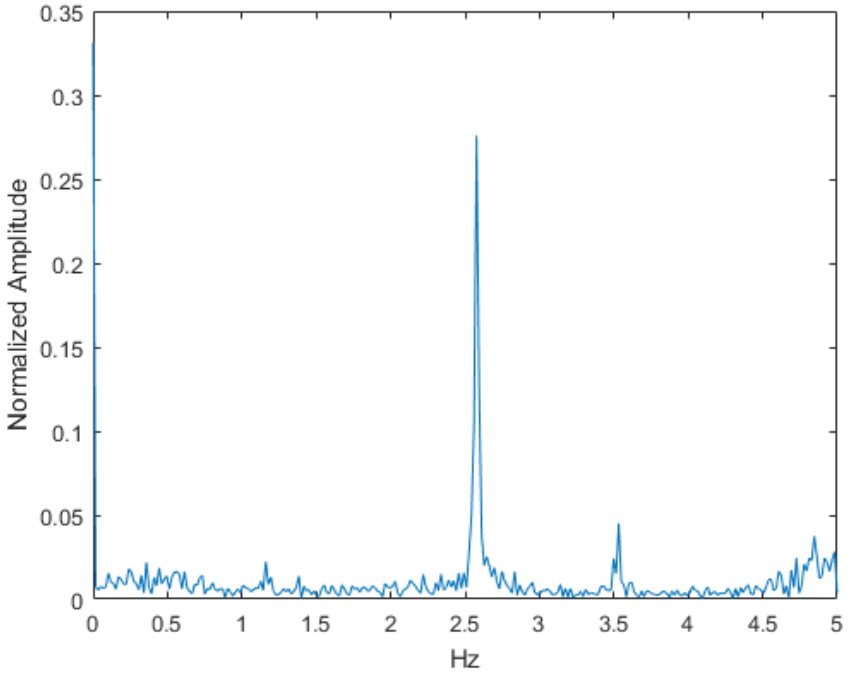

Figure D-5. FFT of the X axis of the bottom laser during the 6V test at 10 Hz

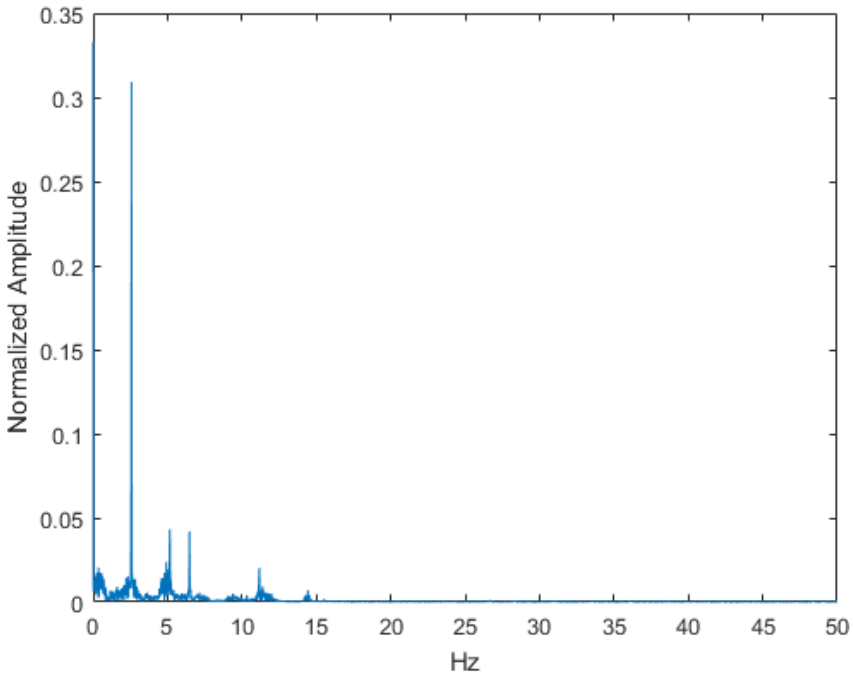

Figure D-6. FFT of the X axis of the bottom laser during the 6V test at 100 Hz

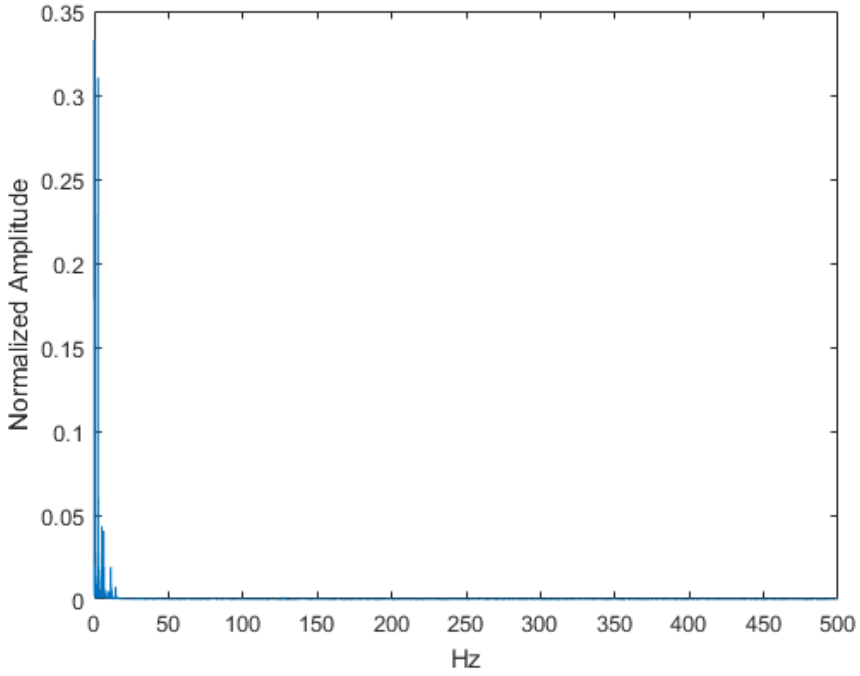

Figure D-7. FFT of the X axis of the bottom laser during the 6V test at 1 kHz

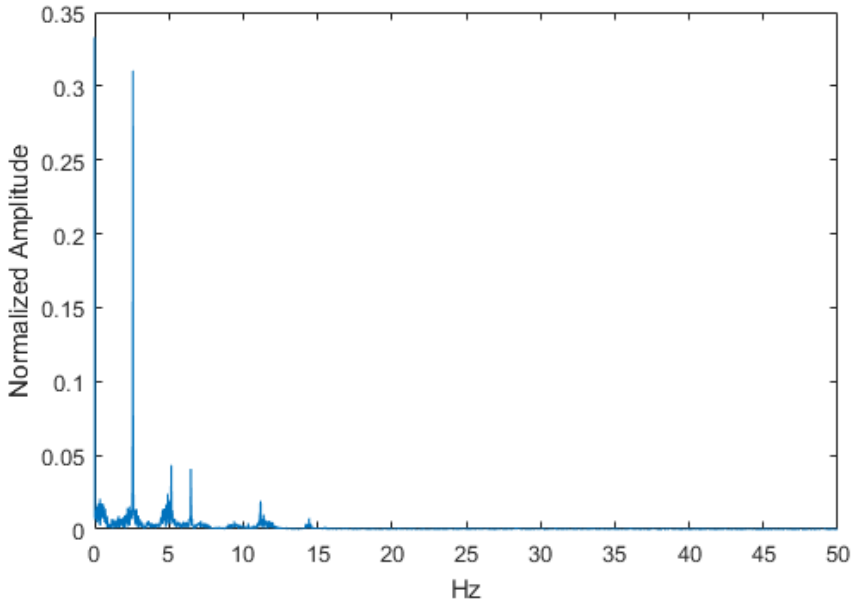

Figure D-8. FFT of the X axis of the bottom laser during the 6V test at 1 kHz zoomed in

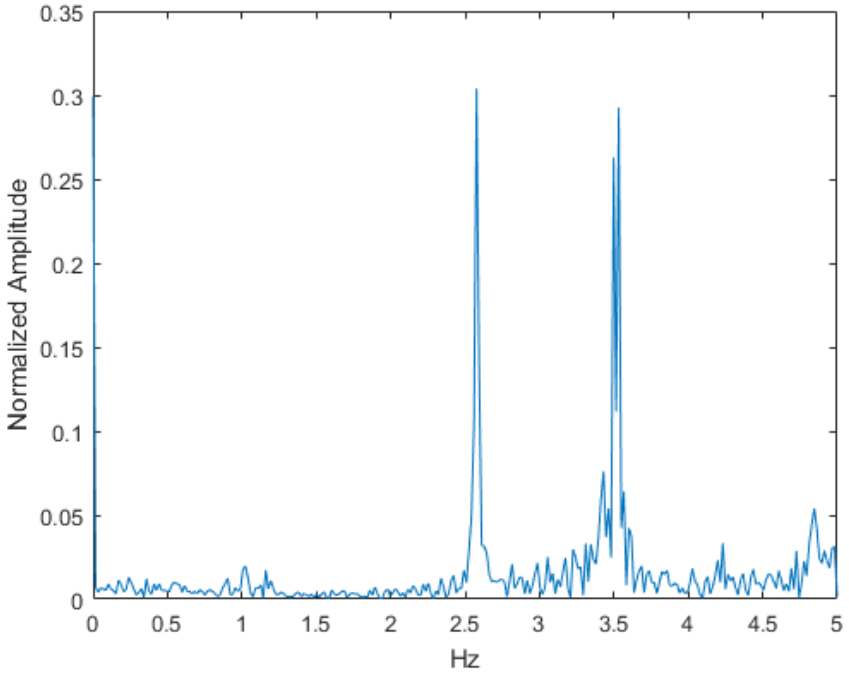

Figure D-9. FFT of the X axis of the top laser during the 6V test at 10 Hz

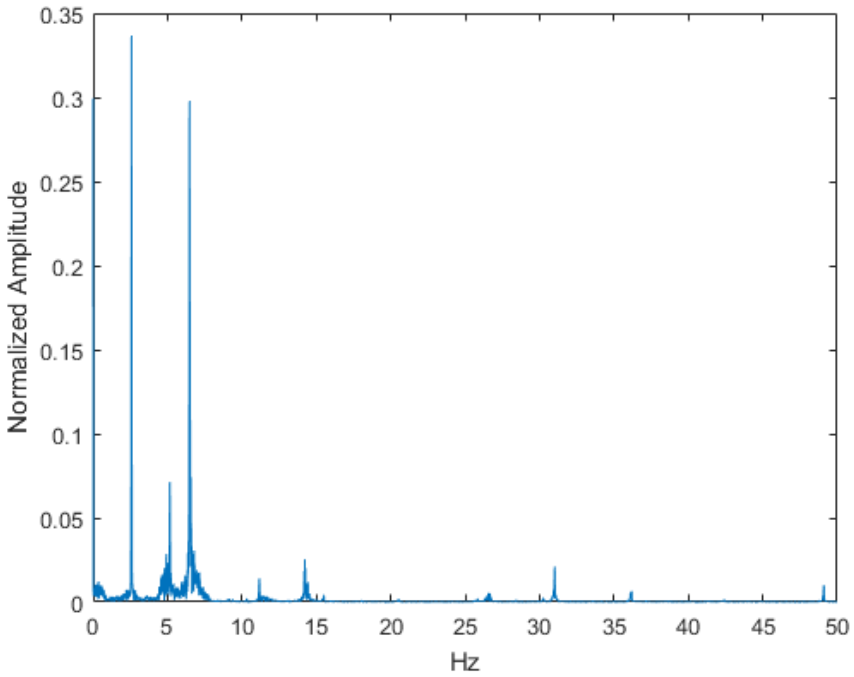

Figure D-10. FFT of the X axis of the top laser during the 6V test at 100 Hz

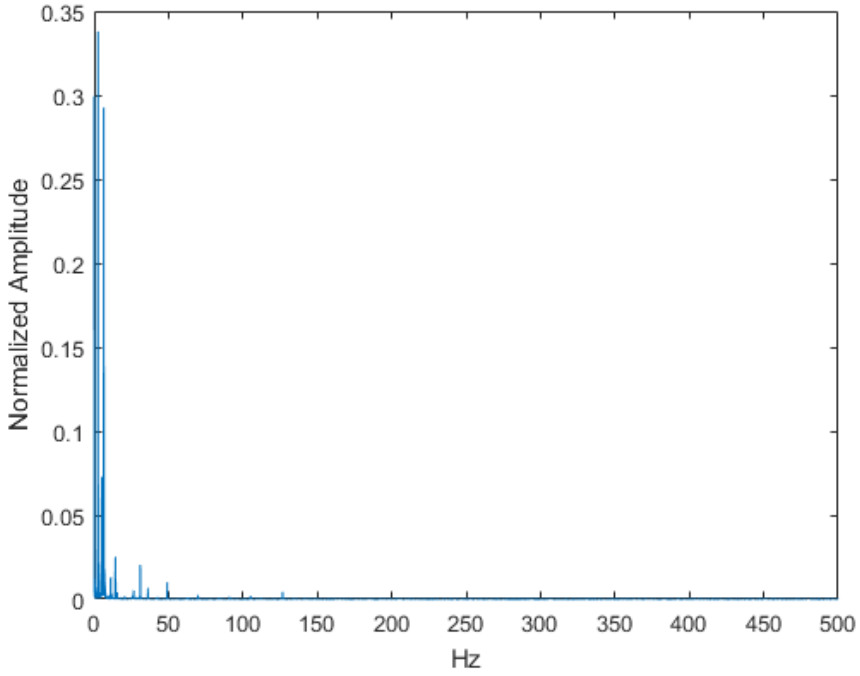

Figure D-11. FFT of the X axis of the top laser during the 6V test at 1 kHz

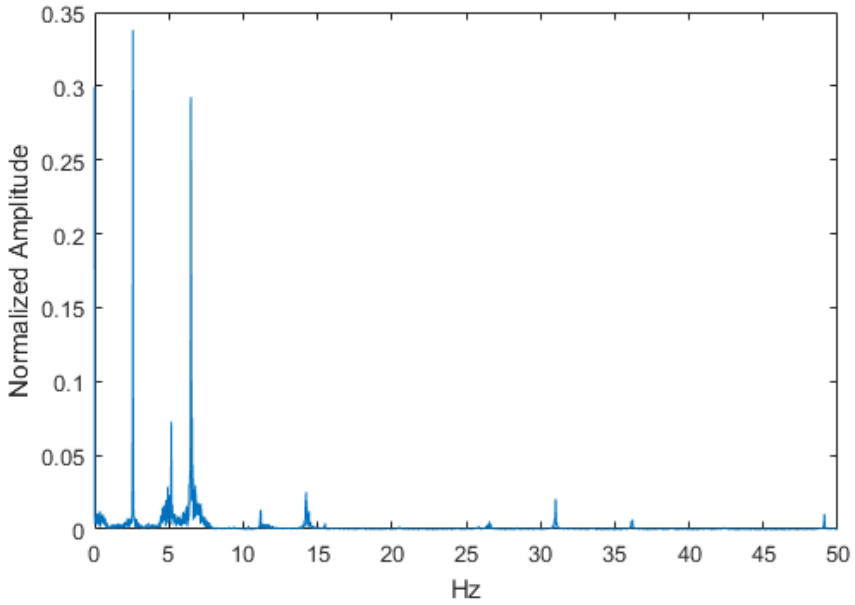

Figure D-12. FFT of the X axis of the top laser during the 6V test at 1 kHz zoomed in

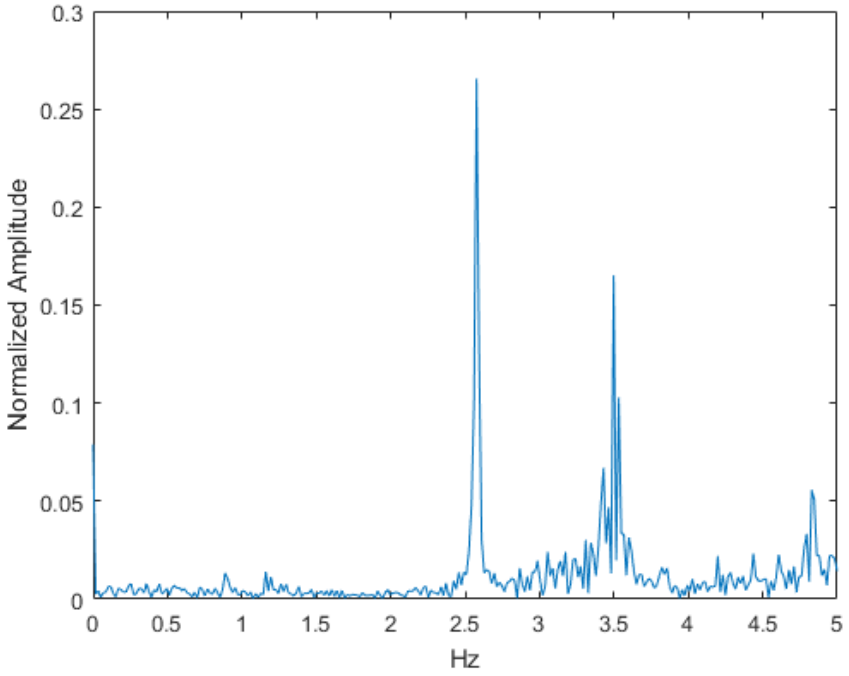

Figure D-13. FFT of the Y axis of the top laser during the 6V test at 10 Hz

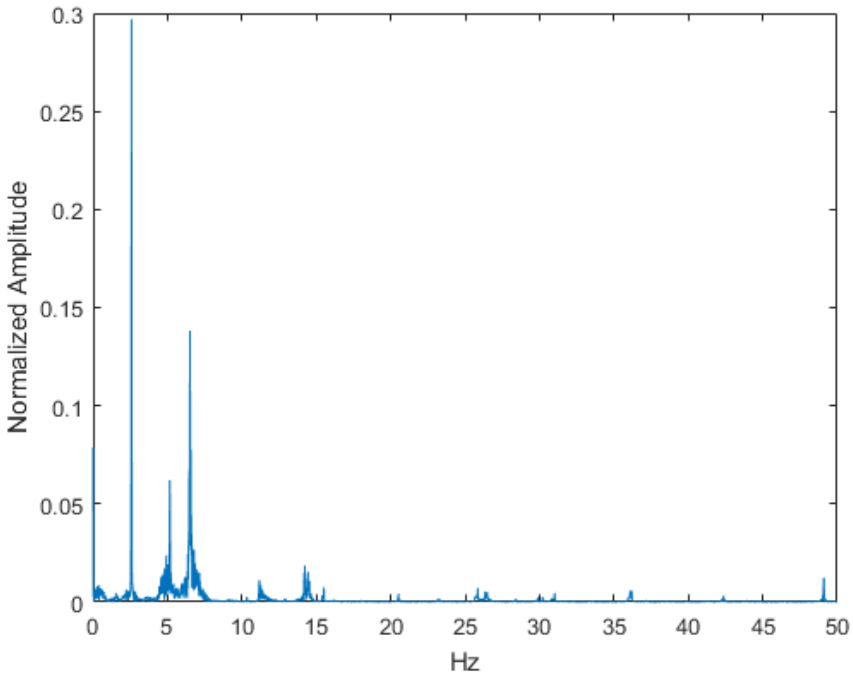

Figure D-14. FFT of the Y axis of the top laser during the 6V test at 100 Hz

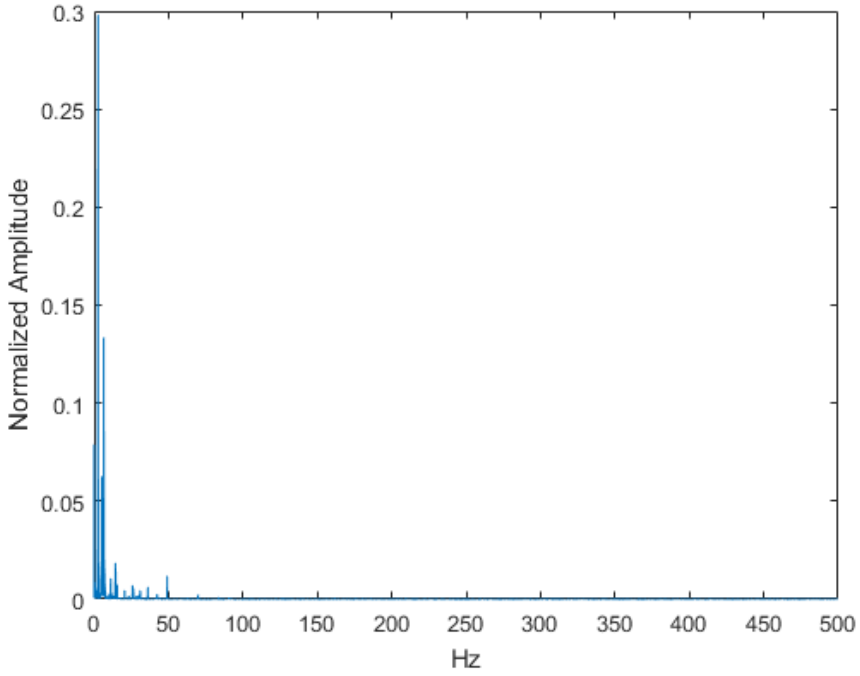

Figure D-15. FFT of the Y axis of the top laser during the 6V test at 1 kHz

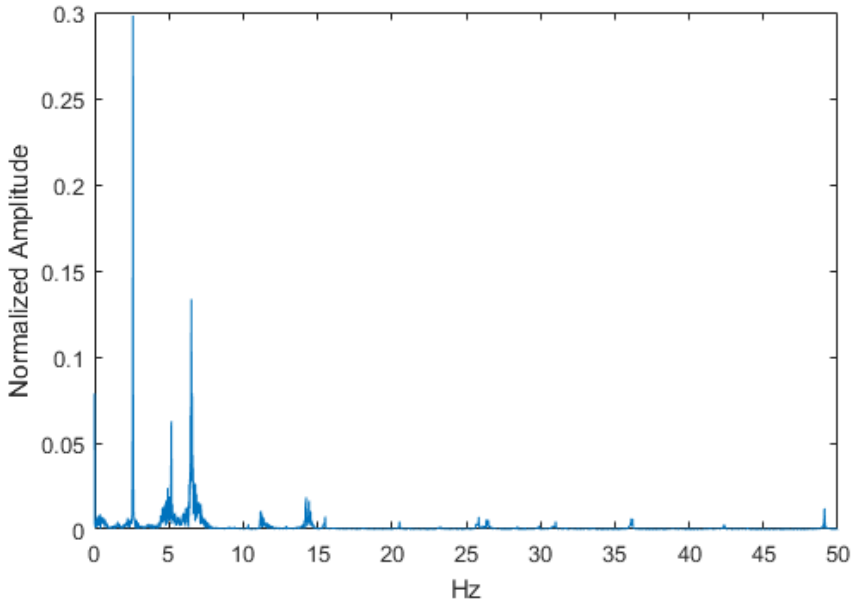

Figure D-16. FFT of the Y axis of the top laser during the 6V test at 1 kHz zoomed in

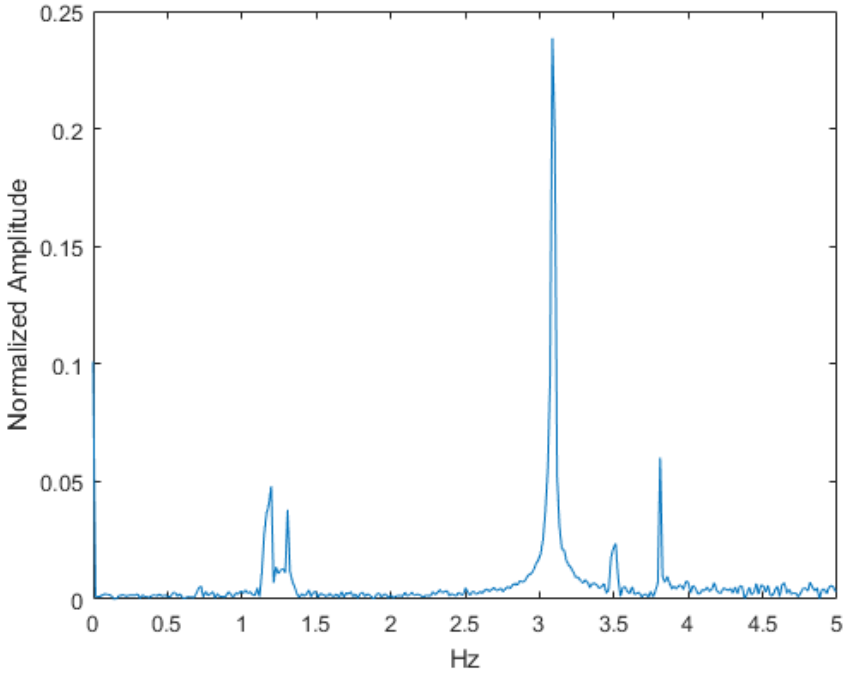

Figure D-17. FFT of the X axis of the bottom laser during the 7V test at 10 Hz

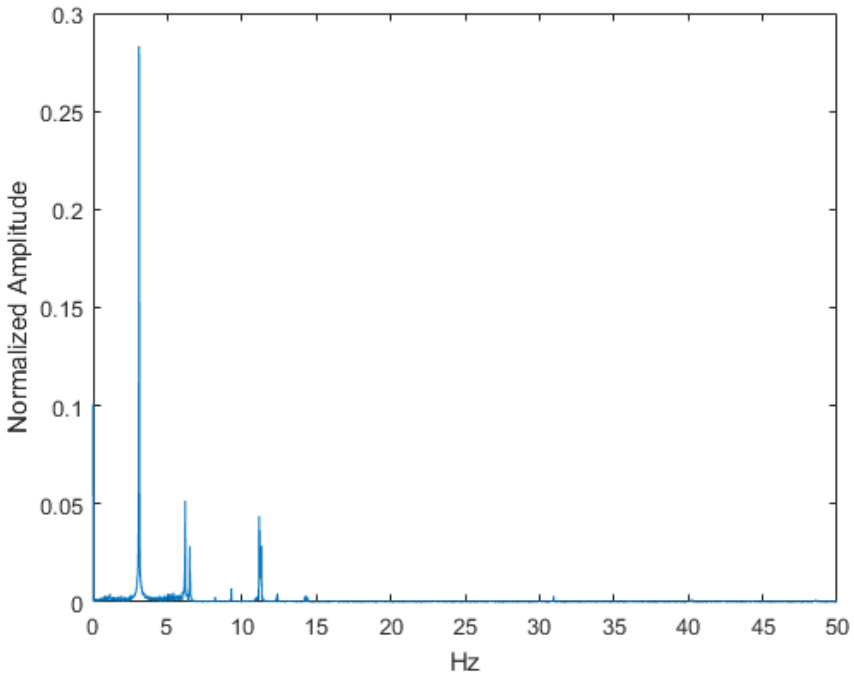

Figure D-18. FFT of the X axis of the bottom laser during the 7V test at 100 Hz

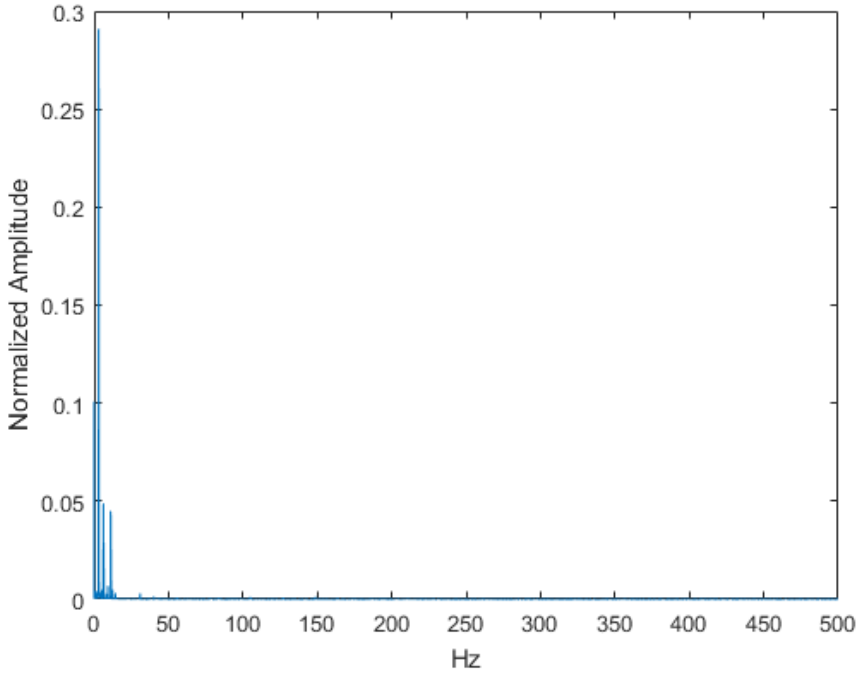

Figure D-19. FFT of the X axis of the bottom laser during the 7V test at 1 kHz

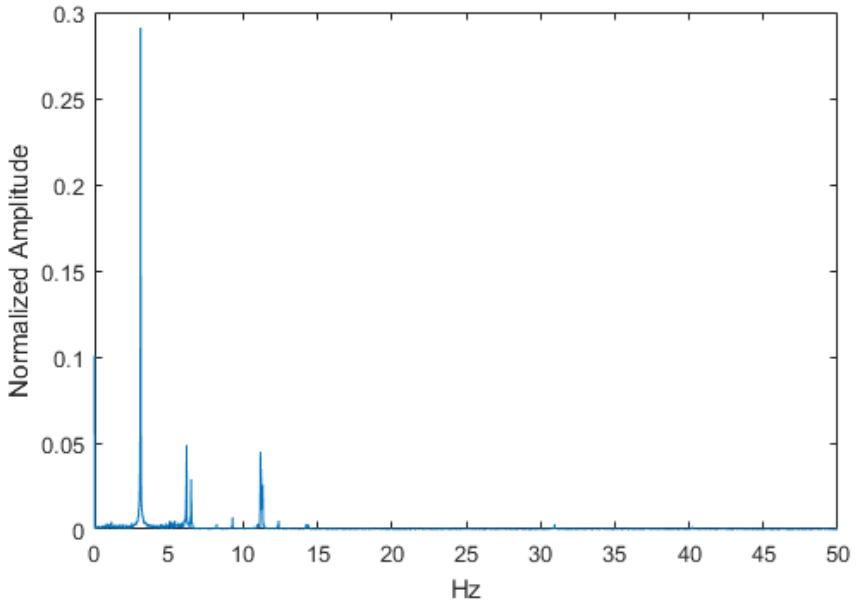

Figure D-20. FFT of the X axis of the bottom laser during the 7V test at 1 kHz zoomed in

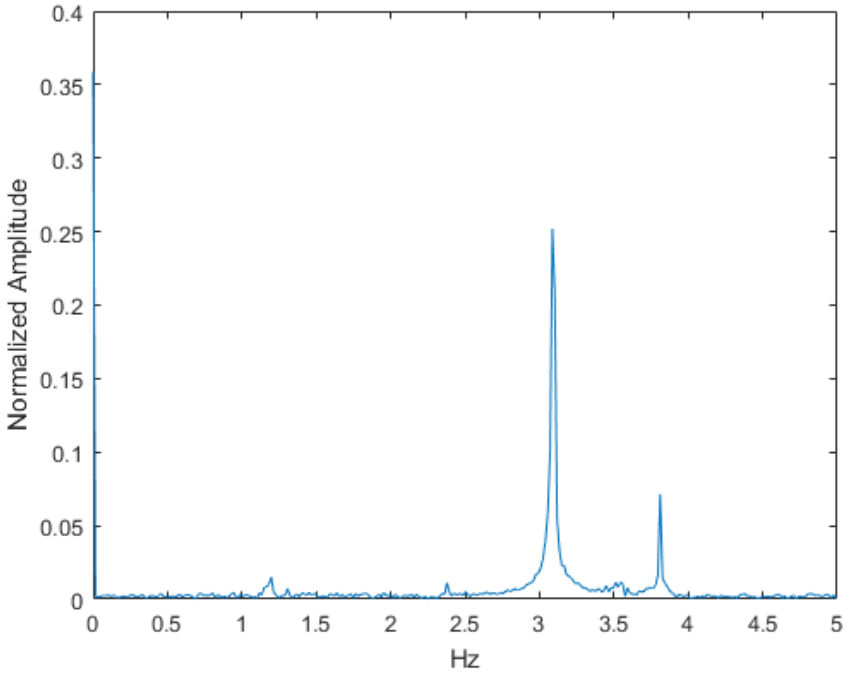

Figure D-21. FFT of the Y axis of the bottom laser during the 7V test at 10 Hz

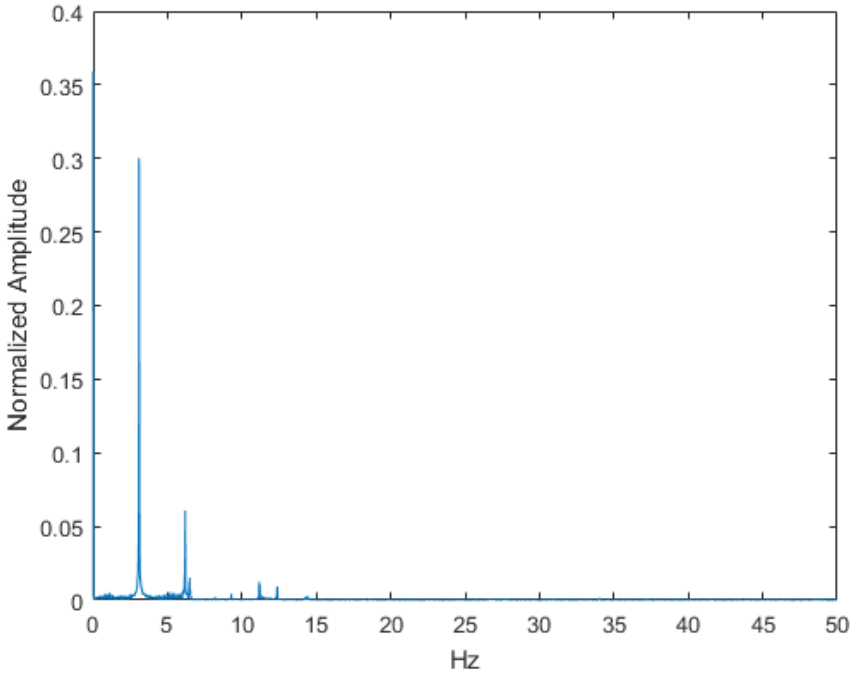

Figure D-22. FFT of the Y axis of the bottom laser during the 7V test at 100 Hz

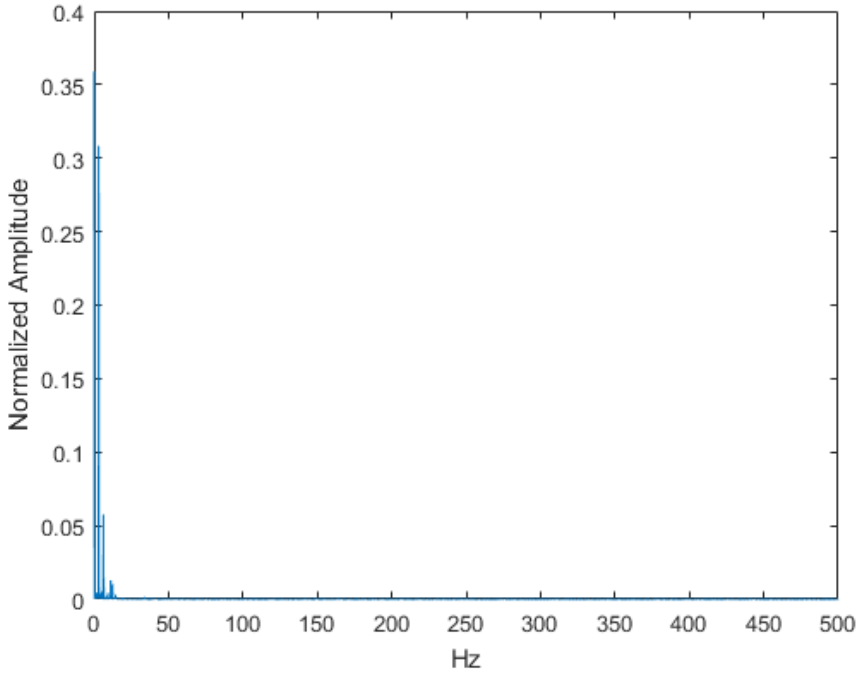

Figure D-23. FFT of the Y axis of the bottom laser during the 7V test at 1 kHz

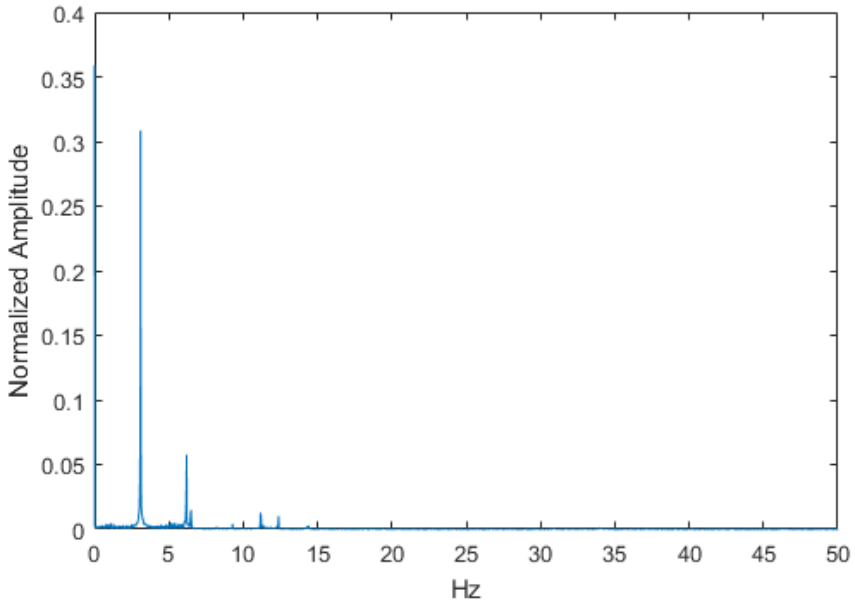

Figure D-24. FFT of the Y axis of the bottom laser during the 7V test at 1 kHz zoomed in

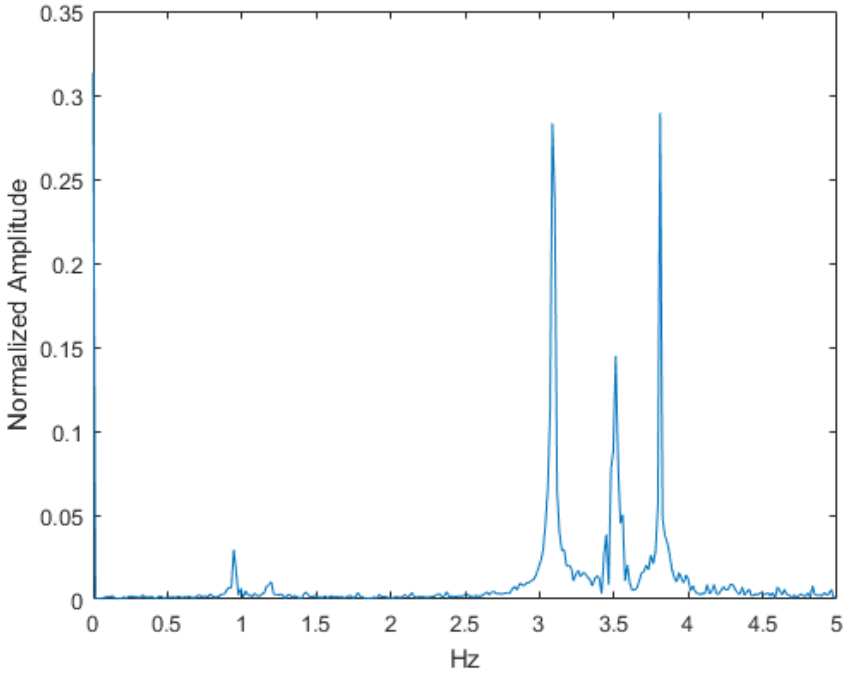

Figure D-25. FFT of the X axis of the top laser during the 7V test at 10 Hz

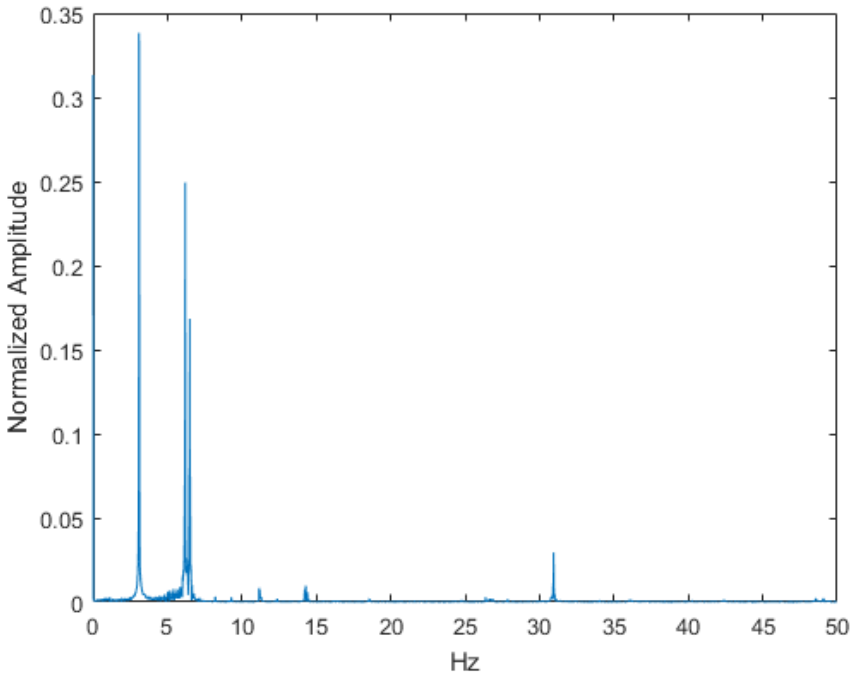

Figure D-26. FFT of the X axis of the top laser during the 7V test at 100 Hz

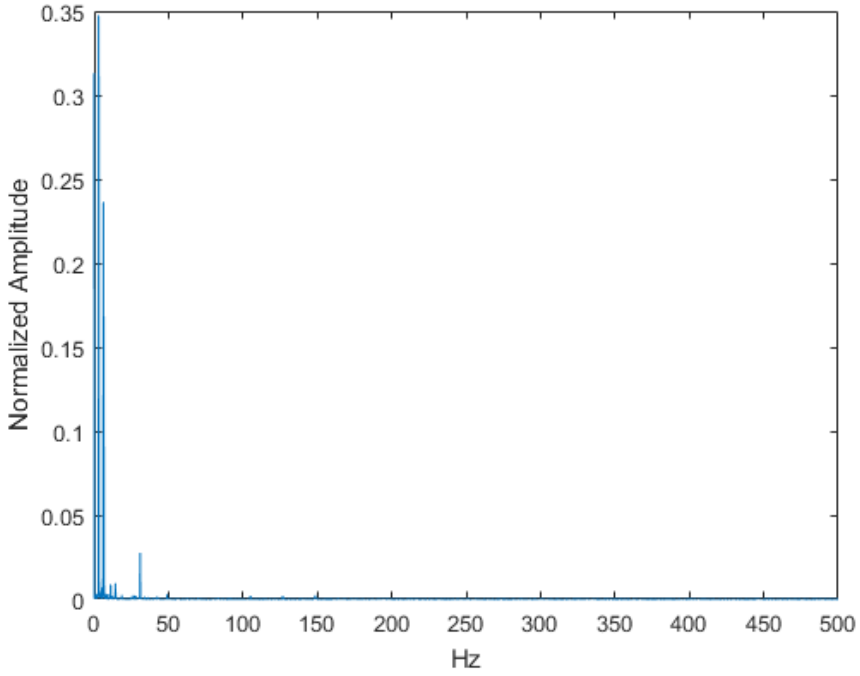

Figure D-27. FFT of the X axis of the top laser during the 7V test at 1 kHz

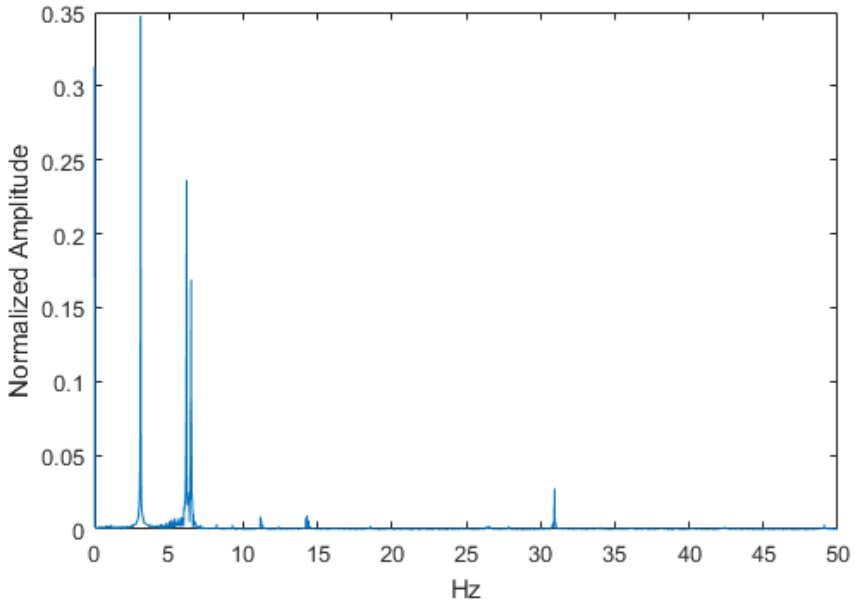

Figure D-28. FFT of the X axis of the top laser during the 7V test at 1 kHz zoomed in

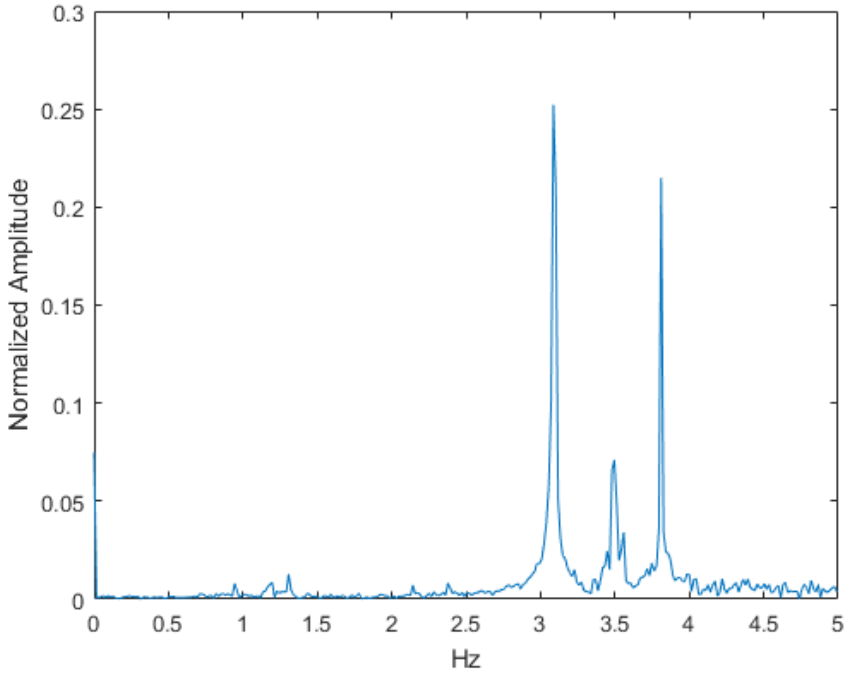

Figure D-29. FFT of the Y axis of the top laser during the 7V test at 10 Hz

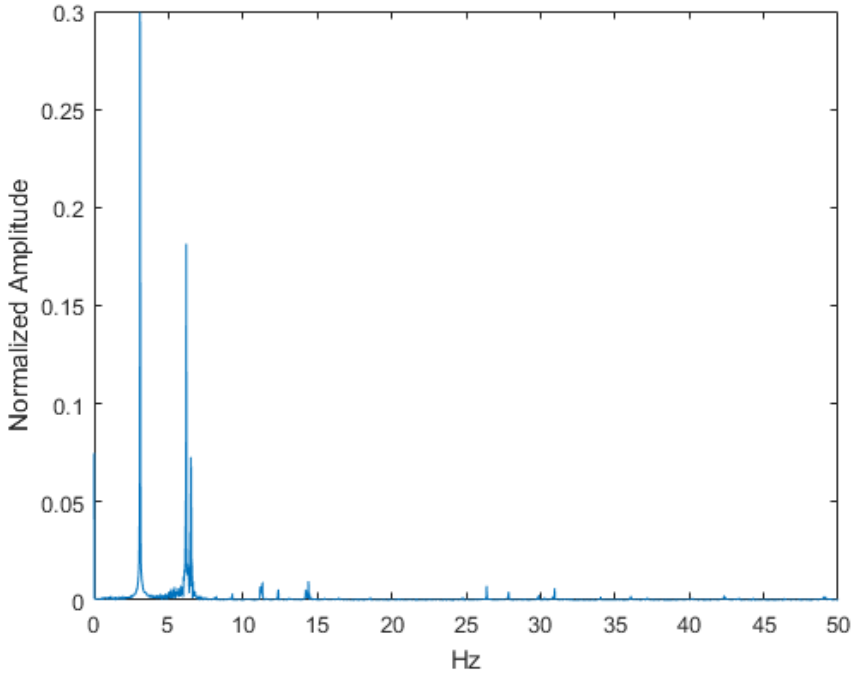

Figure D-30. FFT of the Y axis of the top laser during the 7V test at 100 Hz

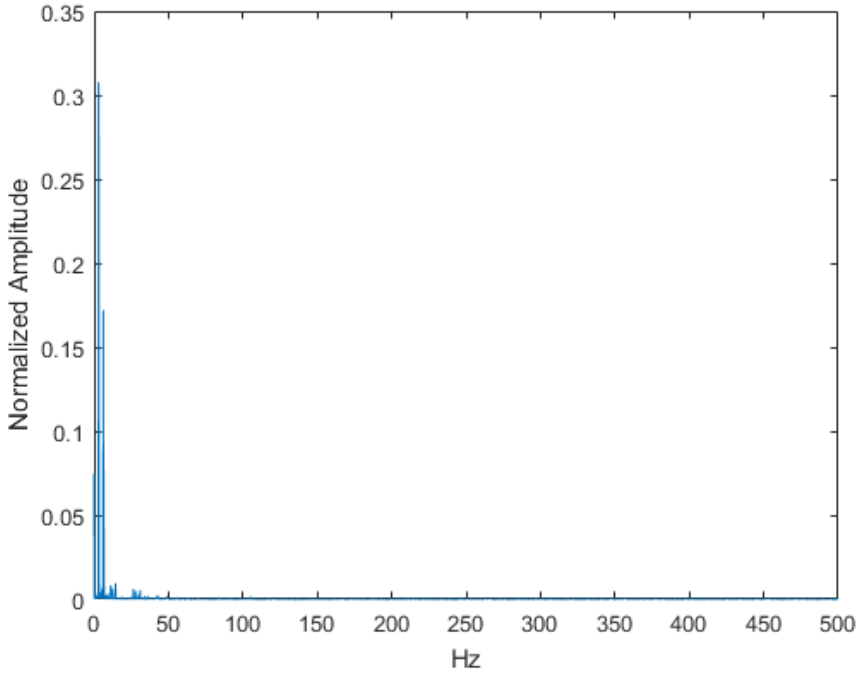

Figure D-31. FFT of the Y axis of the top laser during the 7V test at 1 kHz

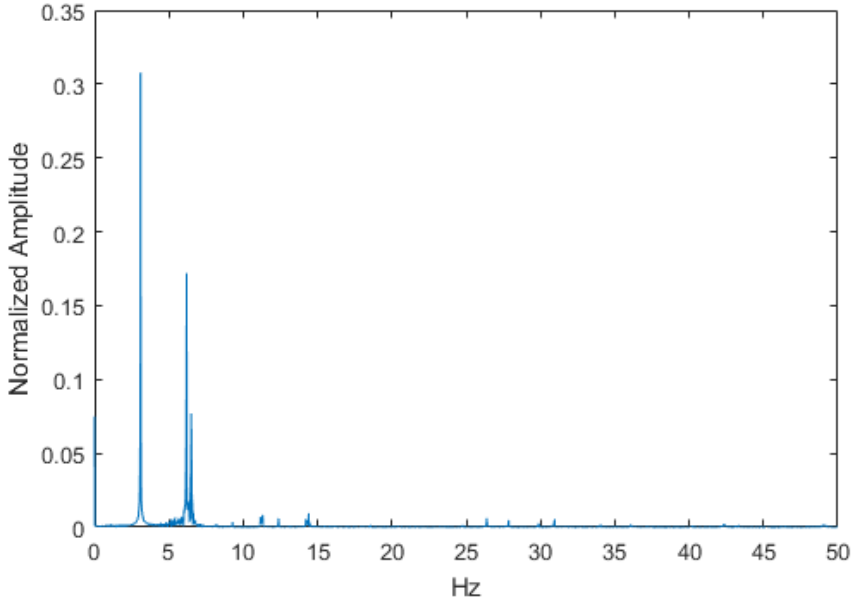

Figure D-32. FFT of the Y axis of the top laser during the 7V test at 1 kHz zoomed in

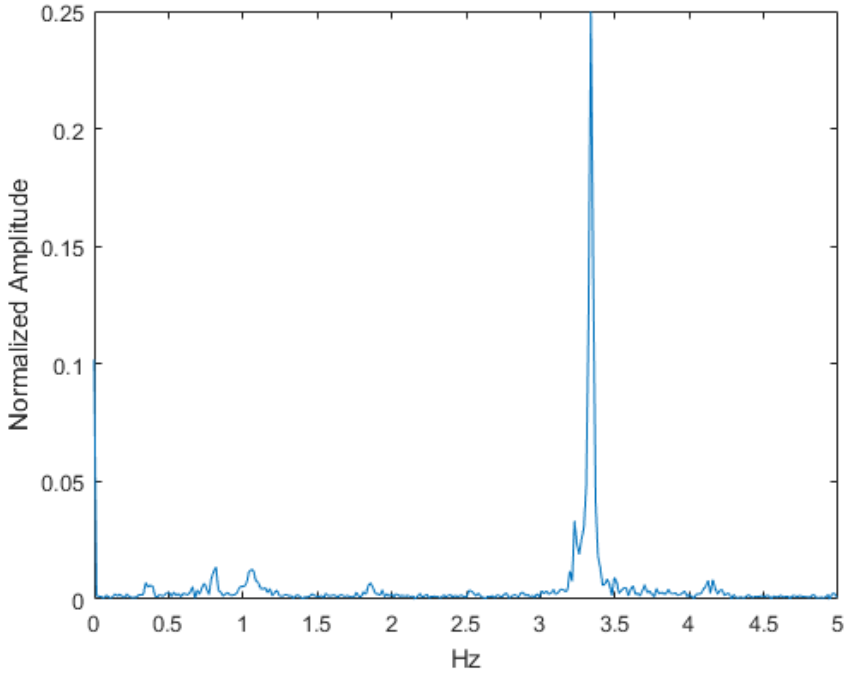

Figure D-33. FFT of the X axis of the bottom laser during the 8V test at 10 Hz

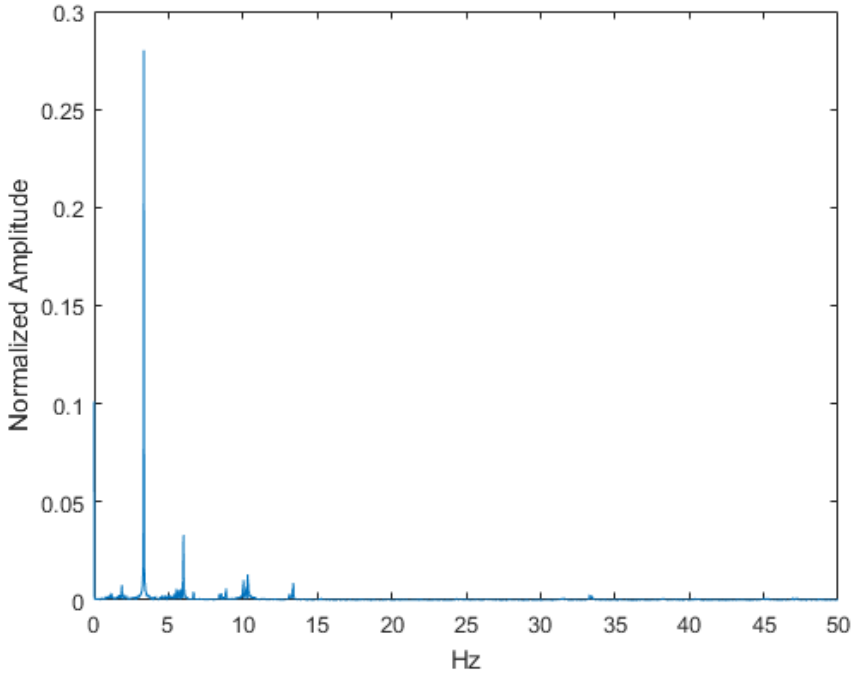

Figure D-34. FFT of the X axis of the bottom laser during the 8V test at 100 Hz

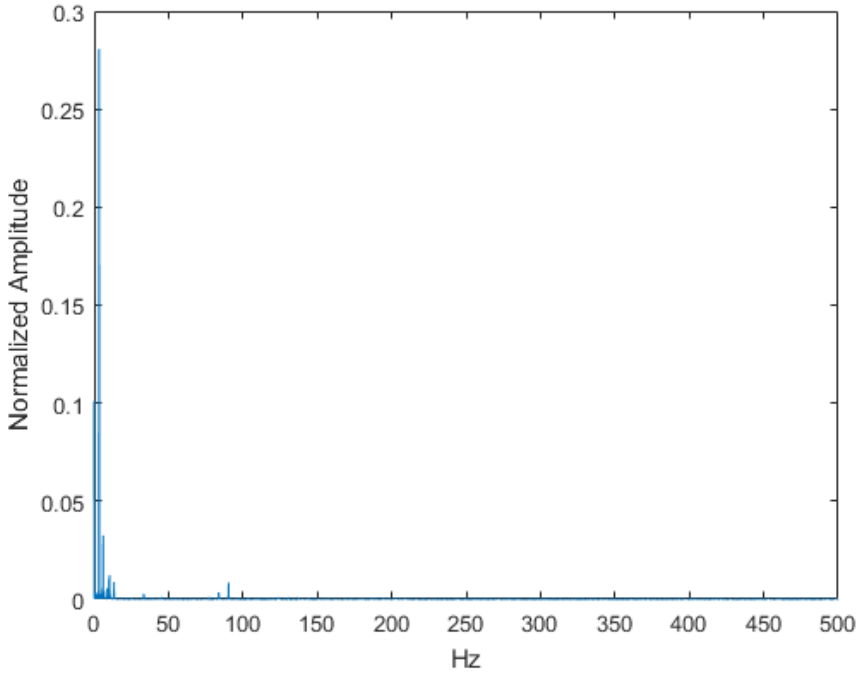

Figure D-35. FFT of the X axis of the bottom laser during the 8V test at 1 kHz

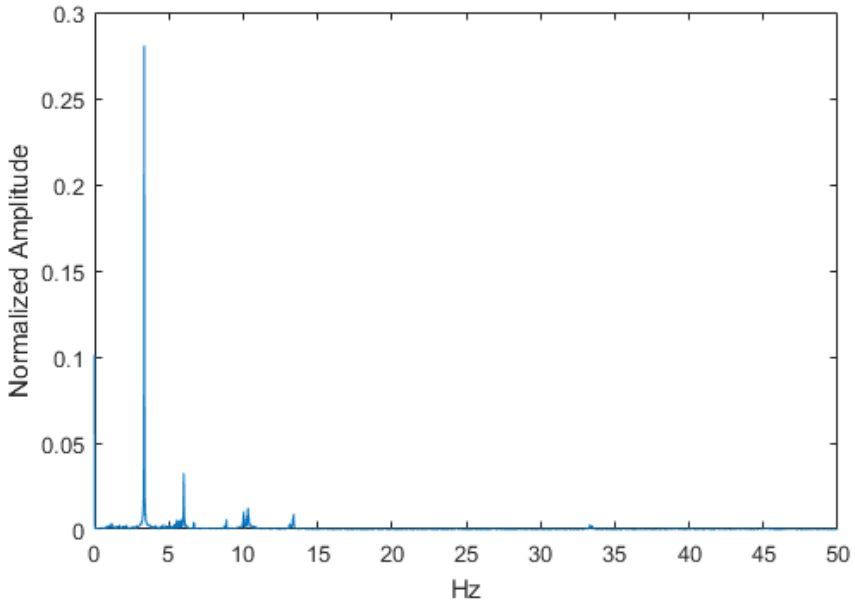

Figure D-36. FFT of the X axis of the bottom laser during the 8V test at 1 kHz zoomed in

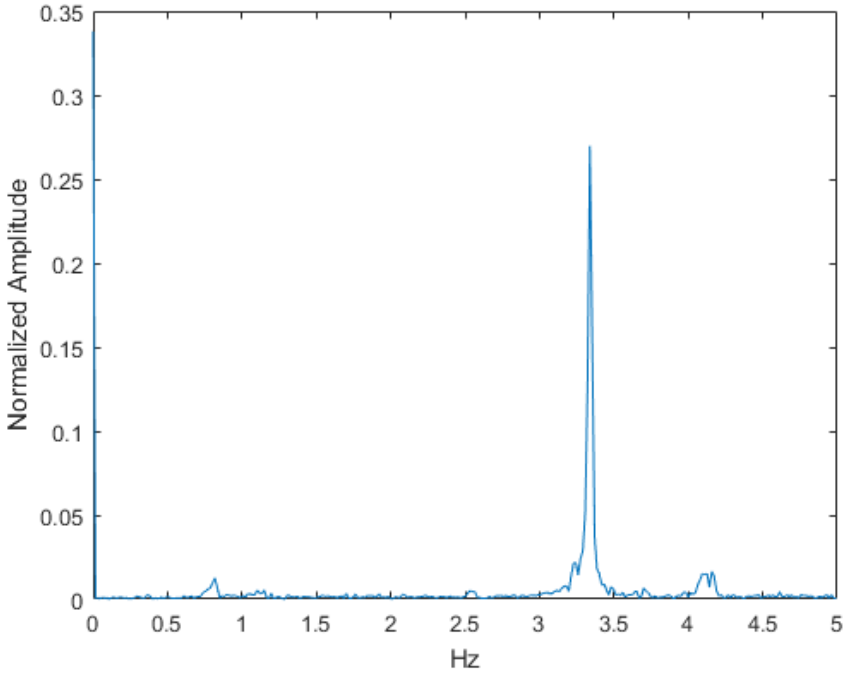

Figure D-37. FFT of the Y axis of the bottom laser during the 8V test at 10 Hz

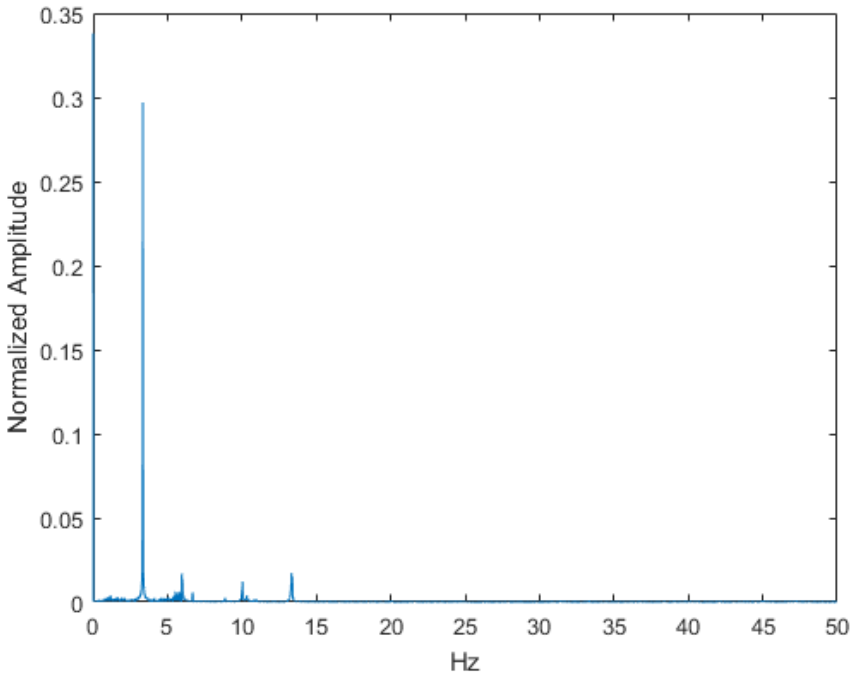

Figure D-38. FFT of the Y axis of the bottom laser during the 8V test at 100 Hz

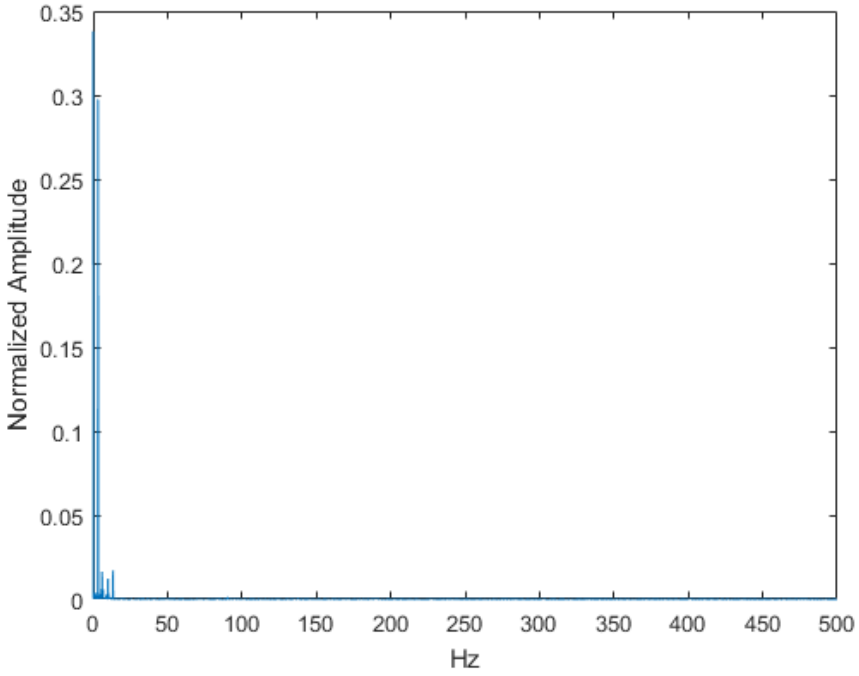

Figure D-39. FFT of the Y axis of the bottom laser during the 8V test at 1 kHz

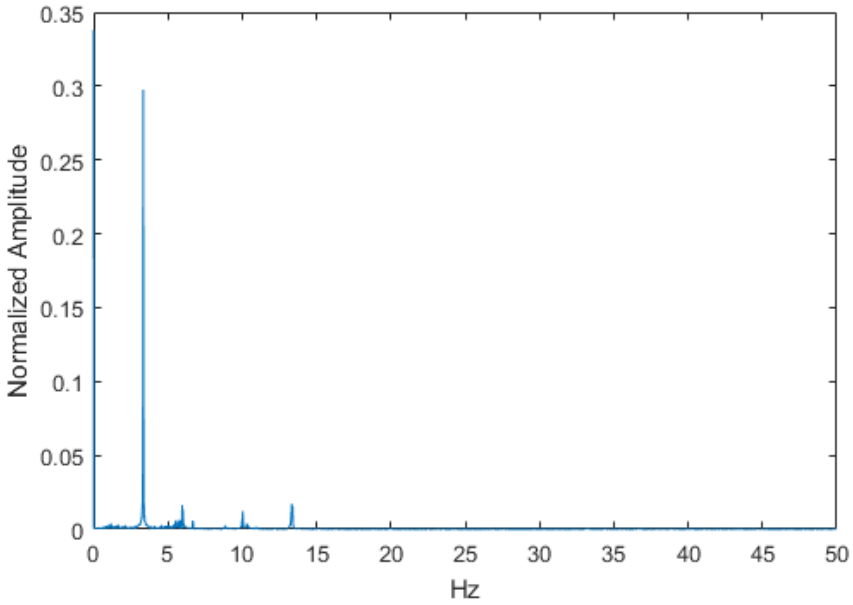

Figure D-40. FFT of the Y axis of the bottom laser during the 8V test at 1 kHz zoomed in

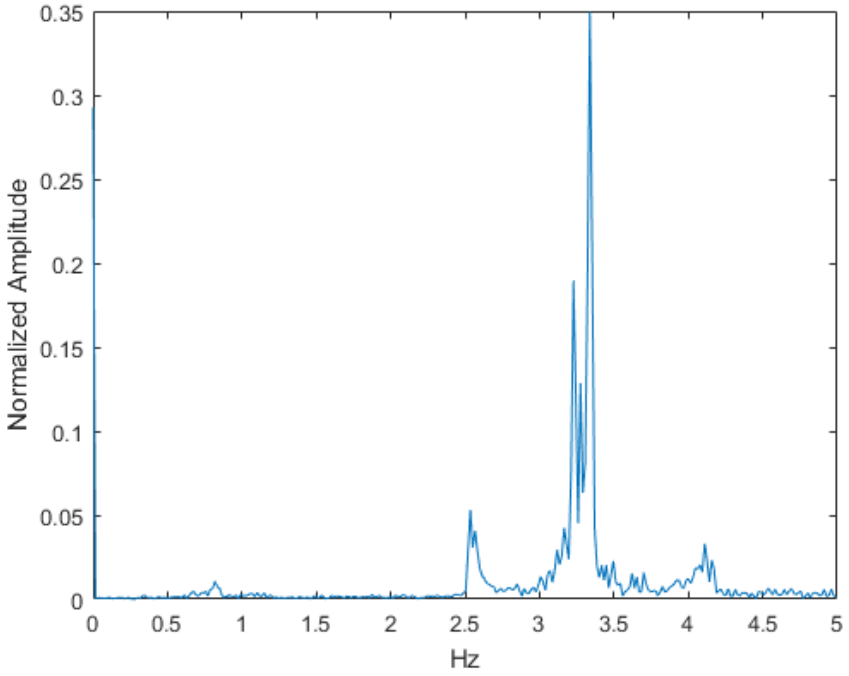

Figure D-41. FFT of the X axis of the top laser during the 8V test at 10 Hz

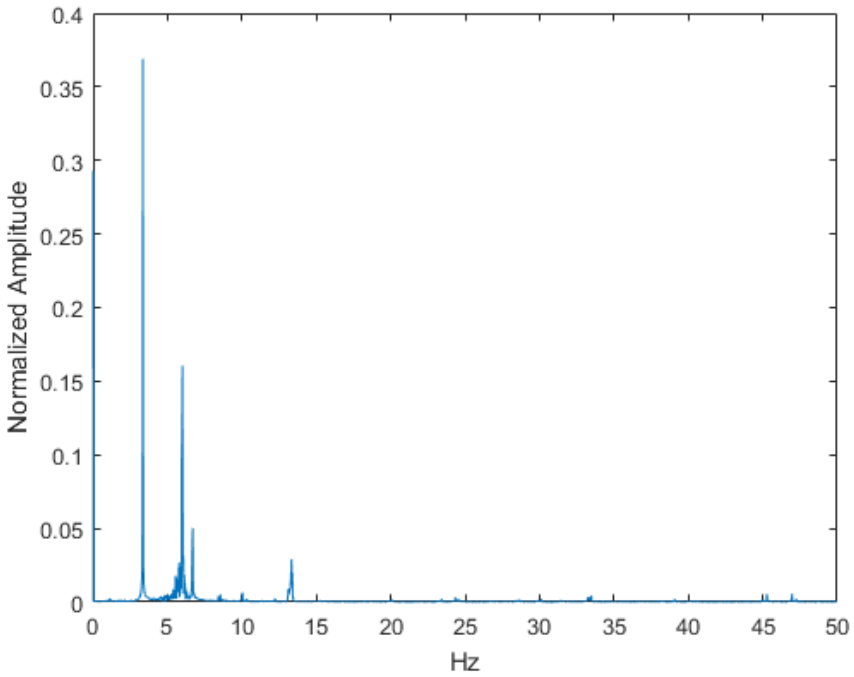

Figure D-42. FFT of the X axis of the top laser during the 8V test at 100 Hz

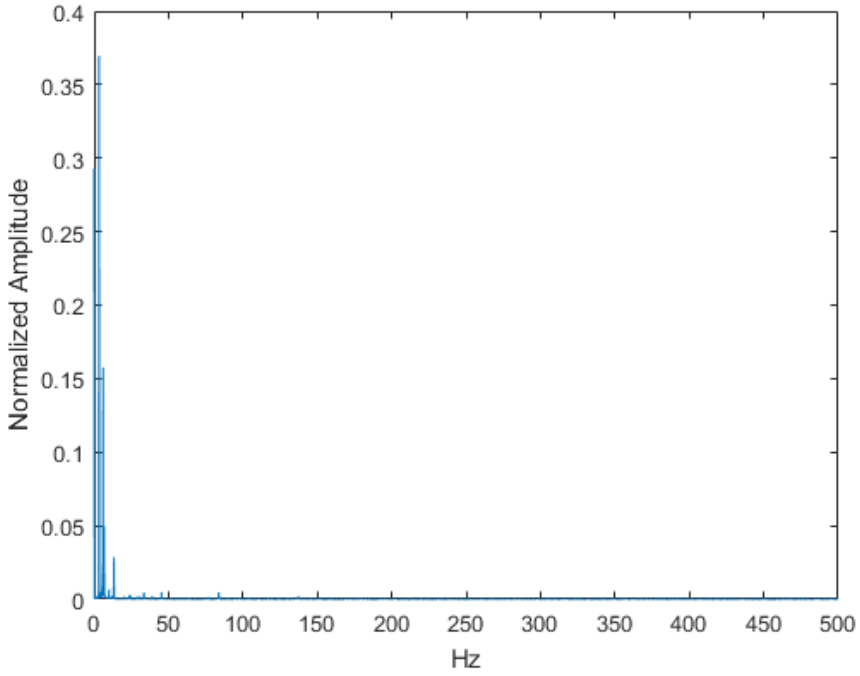

Figure D-43. FFT of the X axis of the top laser during the 8V test at 1 kHz

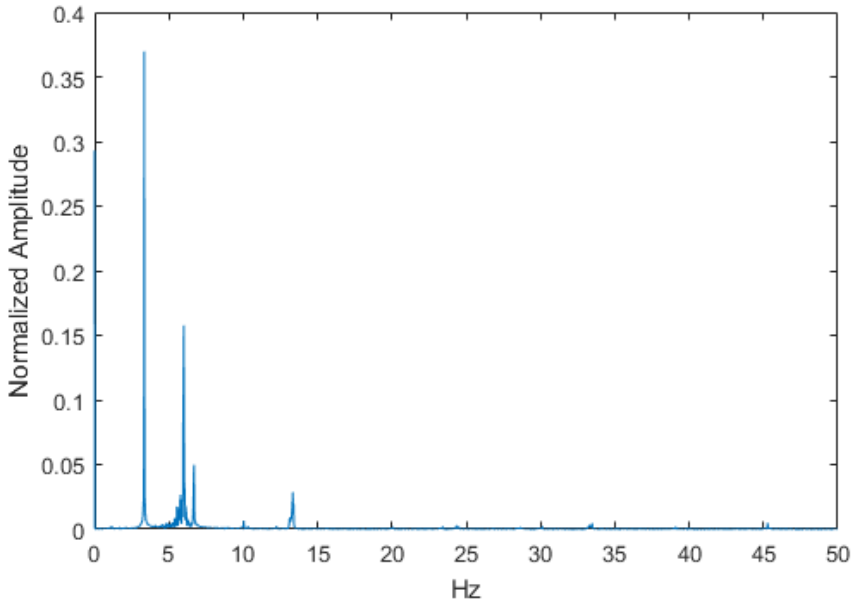

Figure D-44. FFT of the X axis of the top laser during the 8V test at 1 kHz zoomed in

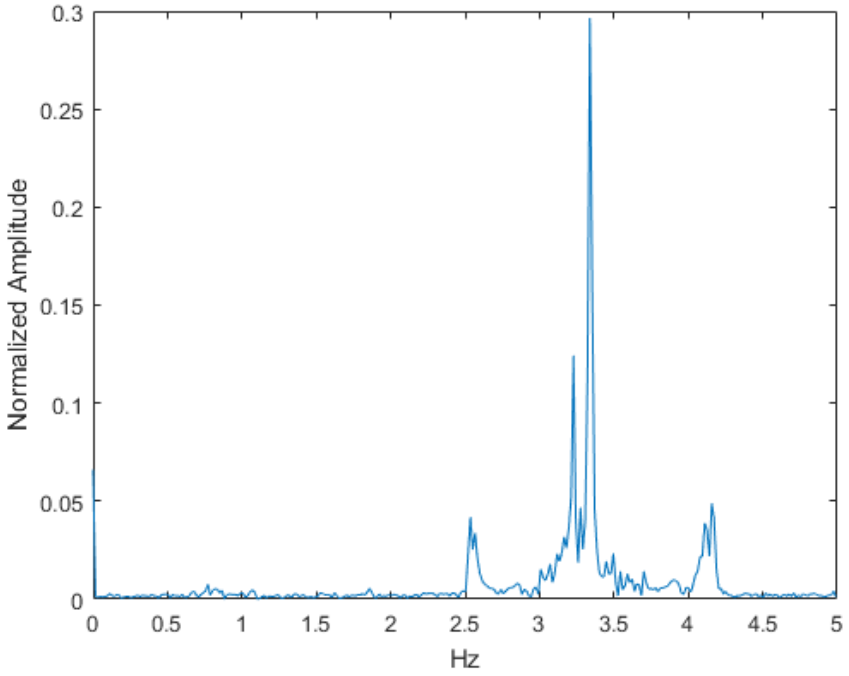

Figure D-45. FFT of the Y axis of the top laser during the 8V test at 10 Hz

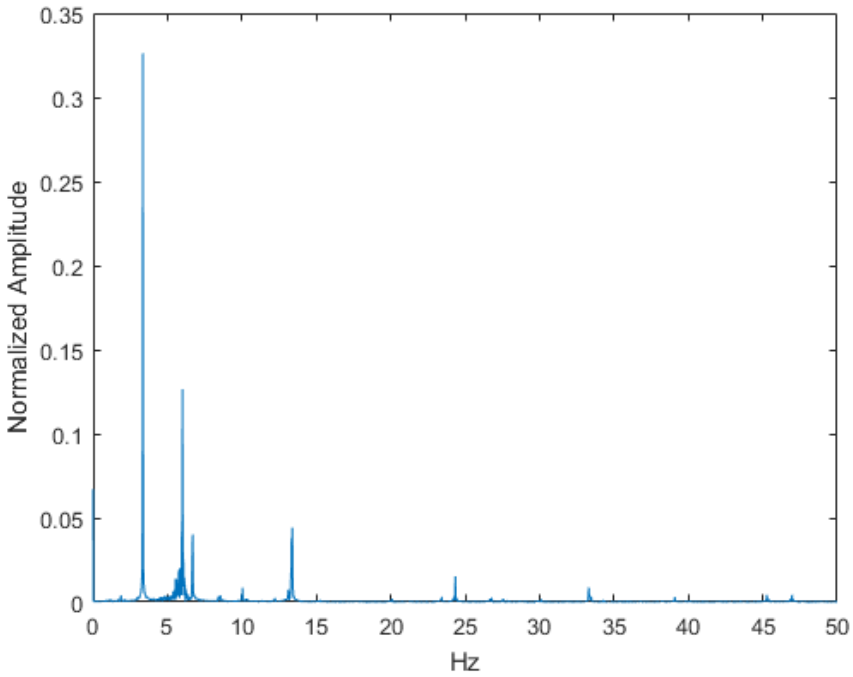

Figure D-46. FFT of the Y axis of the top laser during the 8V test at 100 Hz

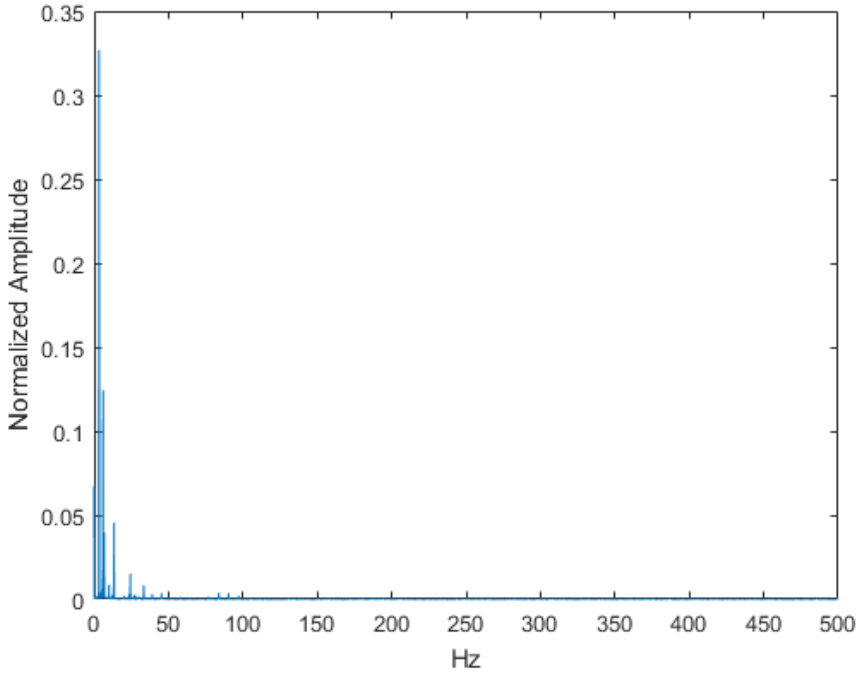

Figure D-47. FFT of the Y axis of the top laser during the 8V test at 1 kHz

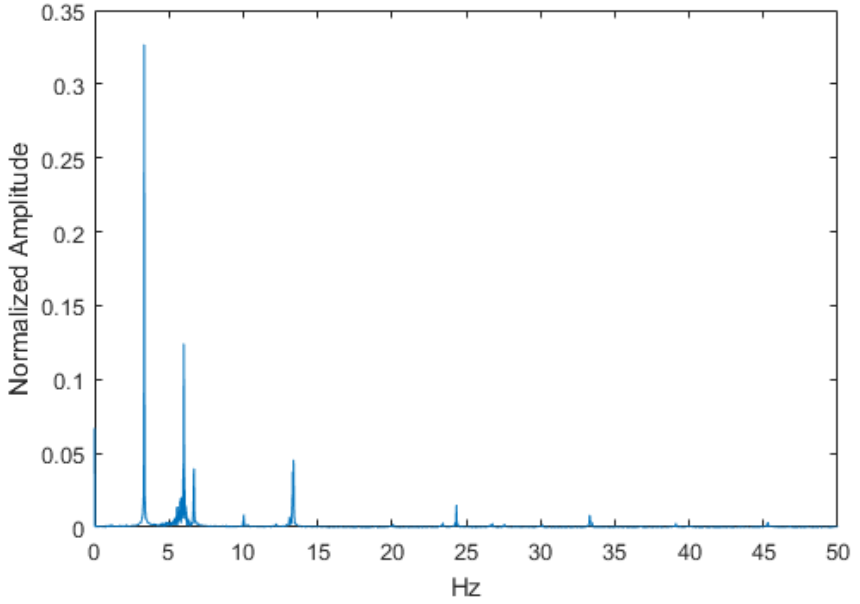

Figure D-48. FFT of the Y axis of the top laser during the 8V test at 1 kHz zoomed in

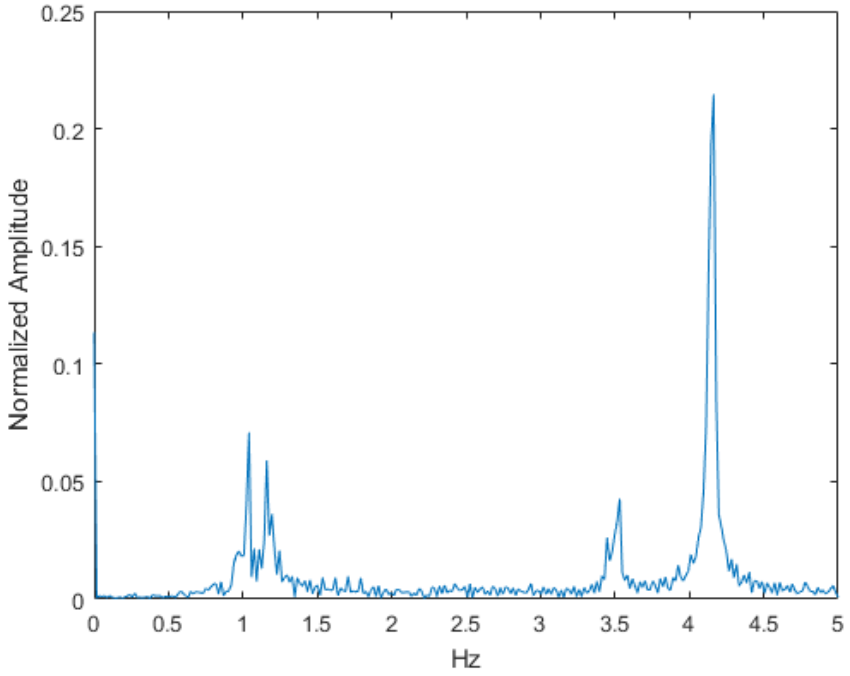

Figure D-49. FFT of the X axis of the bottom laser during the 9V test at 10 Hz

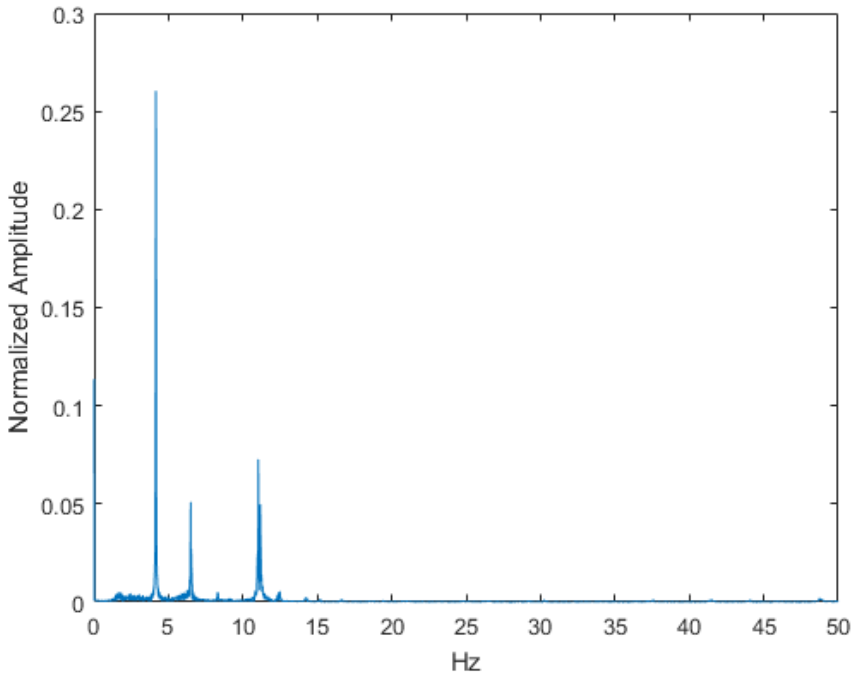

Figure D-50. FFT of the X axis of the bottom laser during the 9V test at 100 Hz

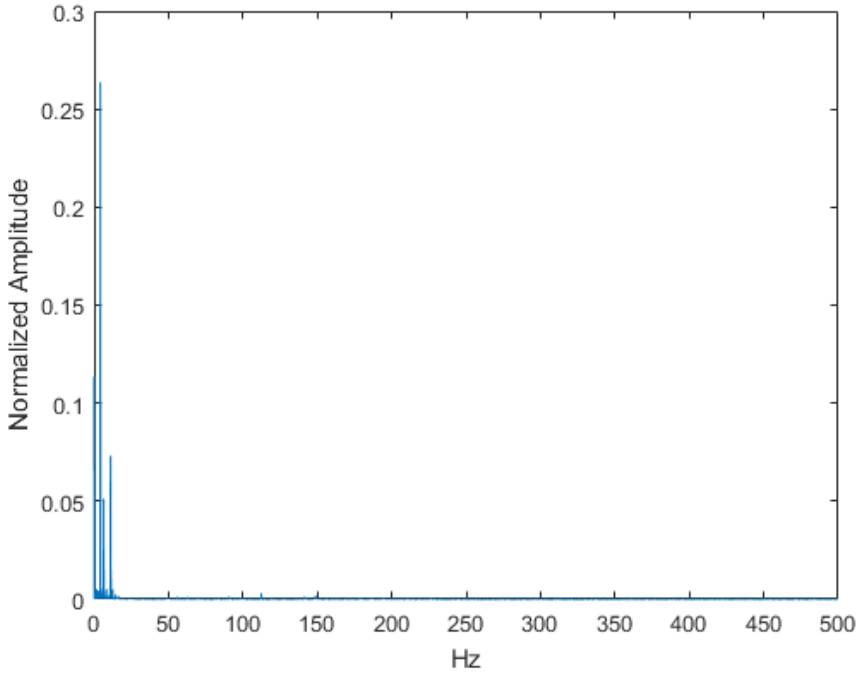

Figure D-51. FFT of the X axis of the bottom laser during the 9V test at 1 kHz

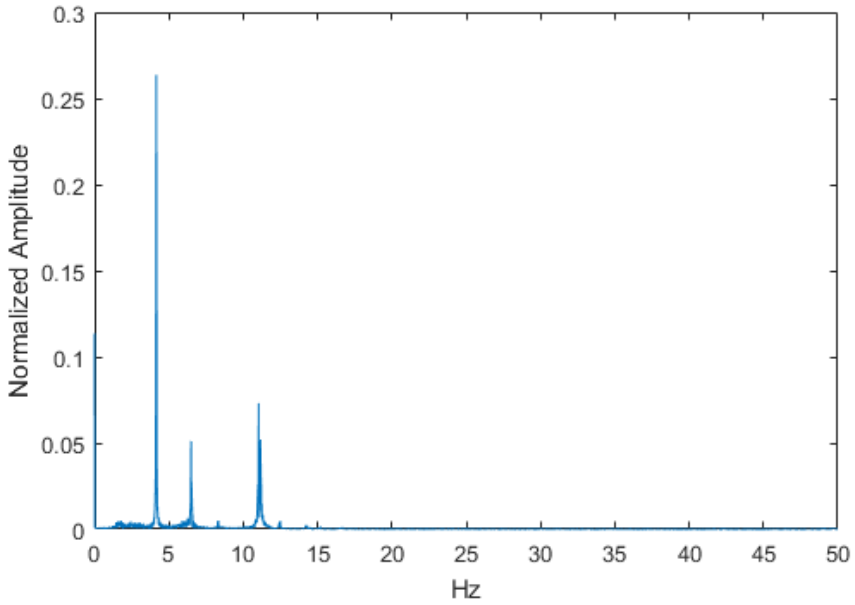

Figure D-52. FFT of the X axis of the bottom laser during the 9V test at 1 kHz zoomed in

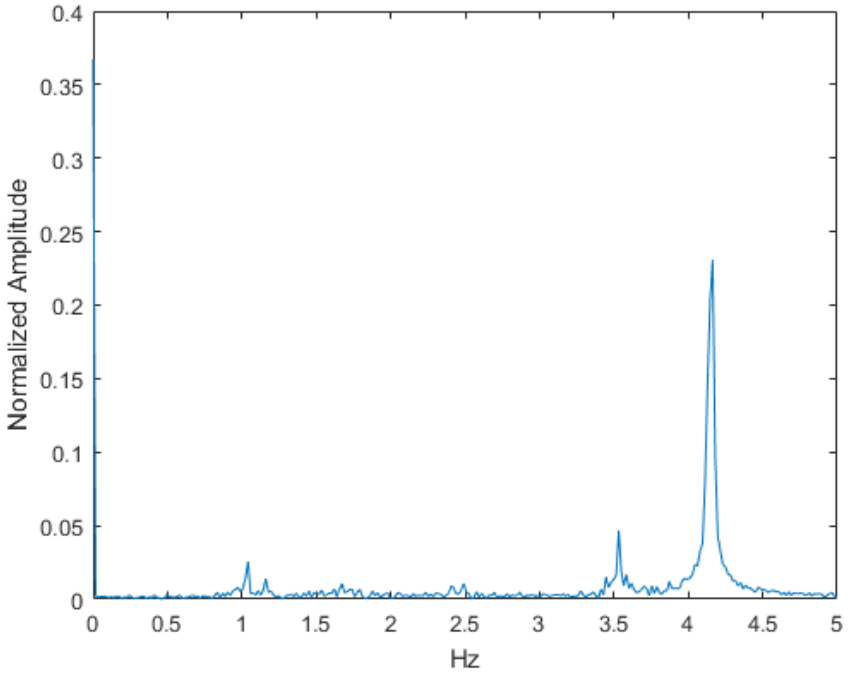

Figure D-53. FFT of the Y axis of the bottom laser during the 9V test at 10 Hz

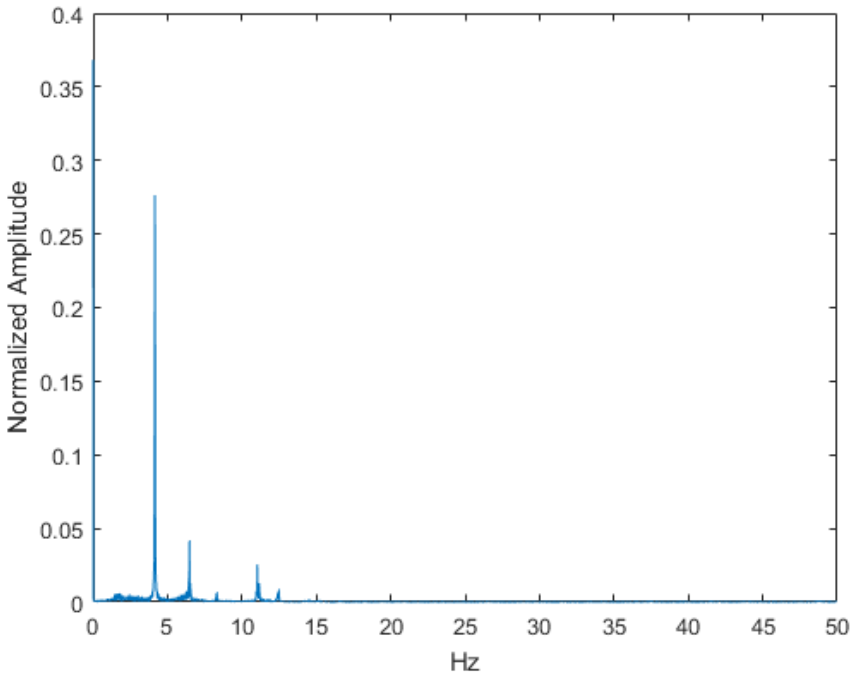

Figure D-54. FFT of the Y axis of the bottom laser during the 9V test at 100 Hz

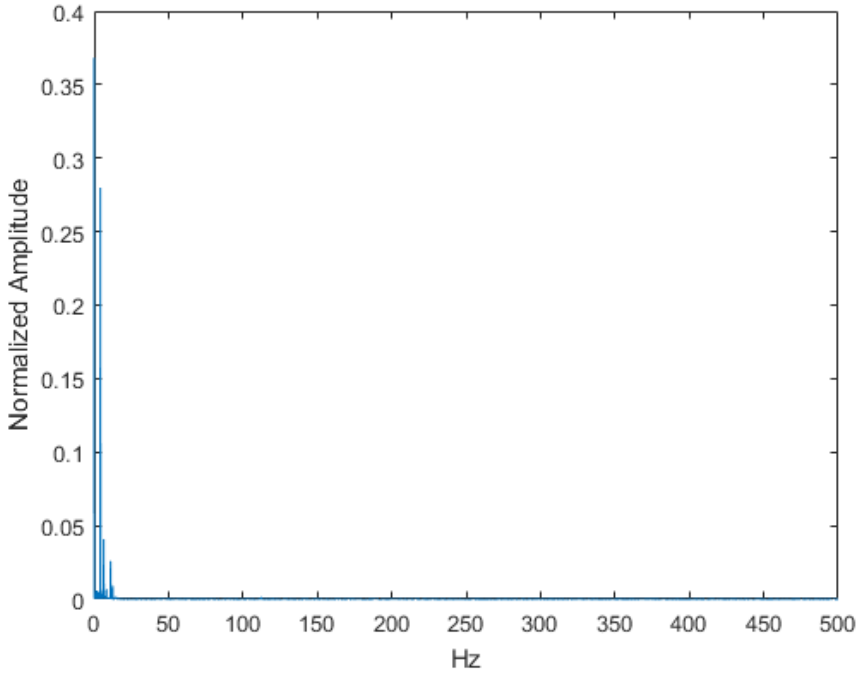

Figure D-55. FFT of the Y axis of the bottom laser during the 9V test at 1 kHz

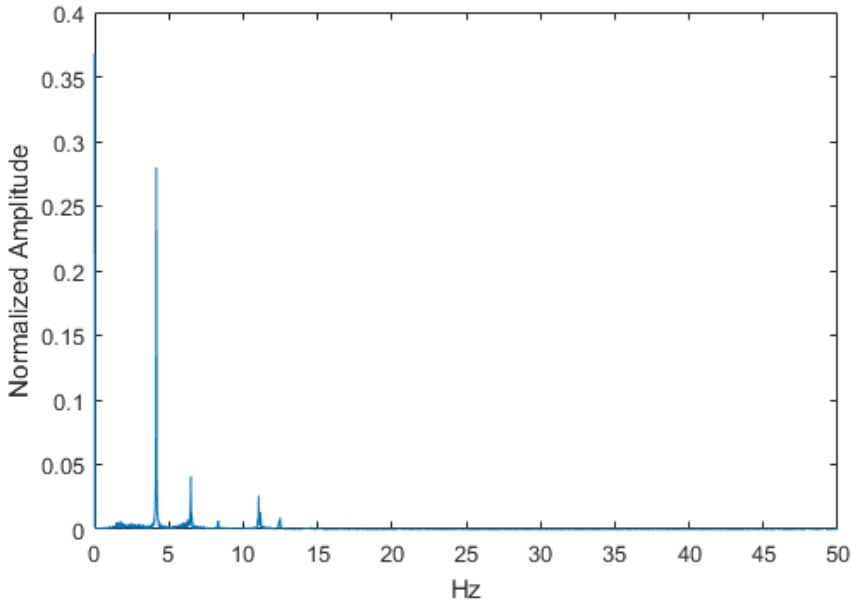

Figure D-56. FFT of the Y axis of the bottom laser during the 9V test at 1 kHz zoomed in

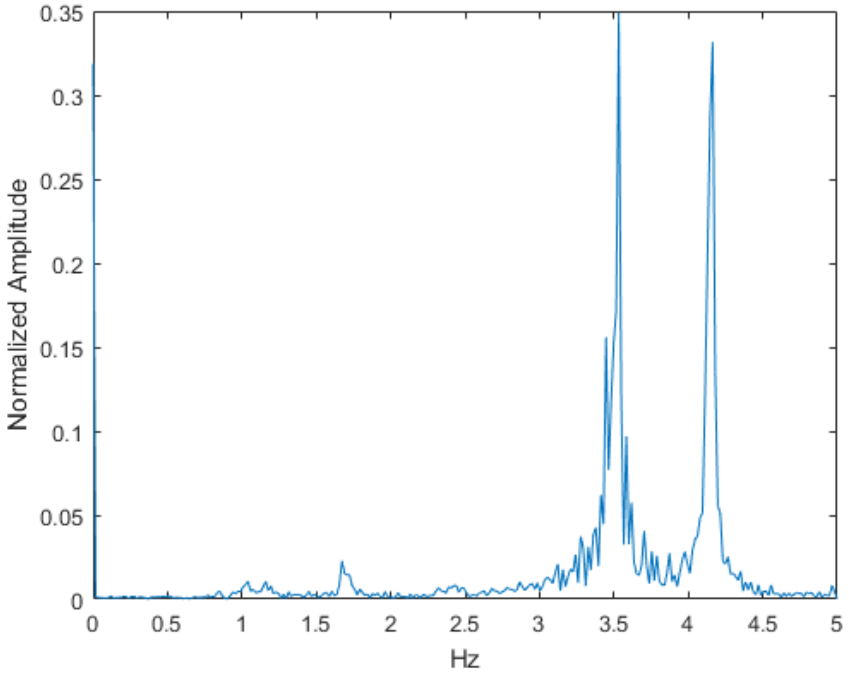

Figure D-57. FFT of the X axis of the top laser during the 9V test at 10 Hz

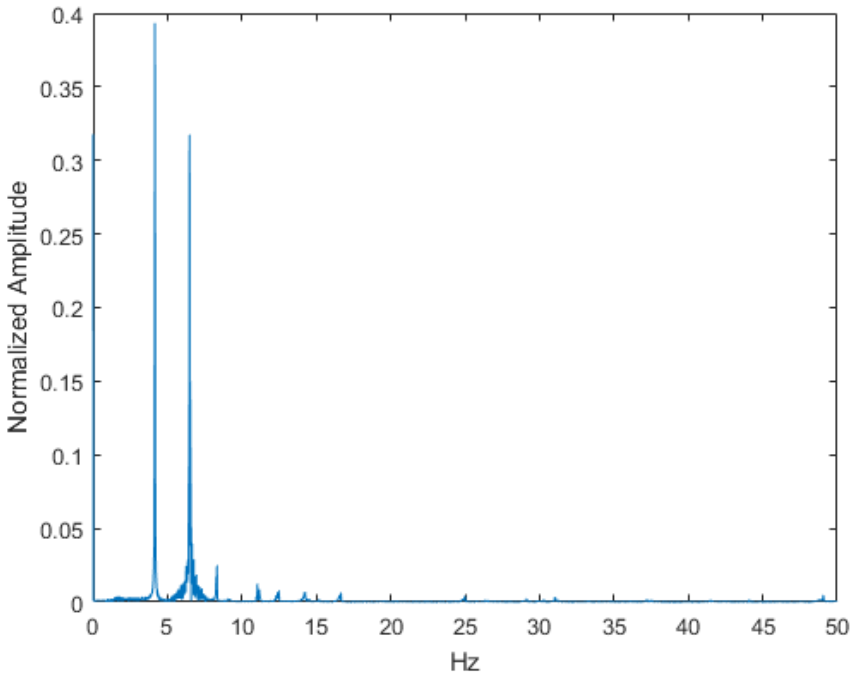

Figure D-58. FFT of the X axis of the top laser during the 9V test at 100 Hz

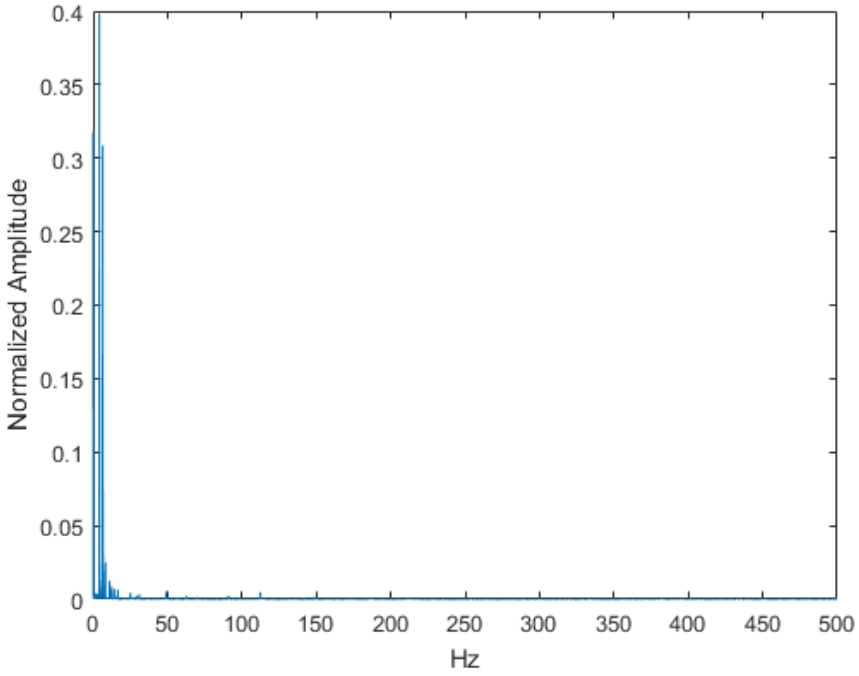

Figure D-59. FFT of the X axis of the top laser during the 9V test at 1 kHz

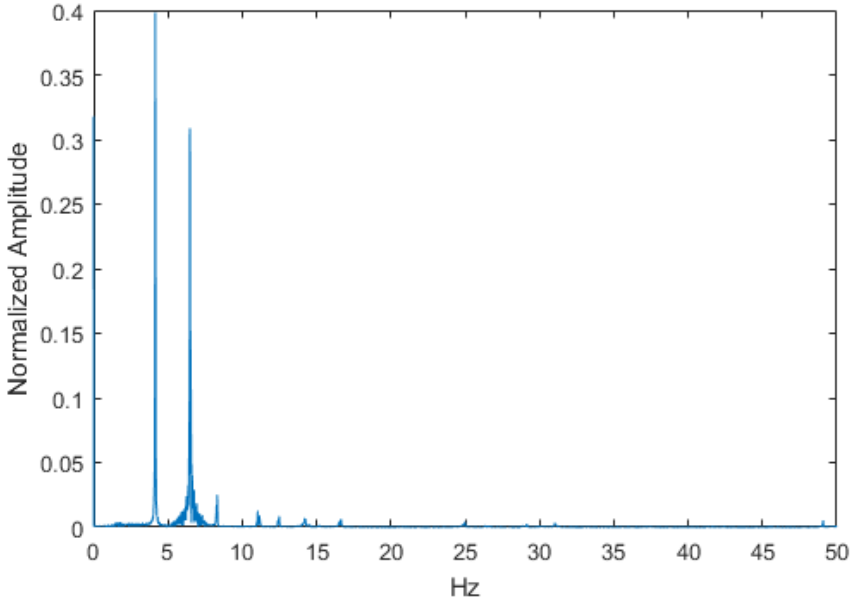

Figure D-60. FFT of the X axis of the top laser during the 9V test at 1 kHz zoomed in

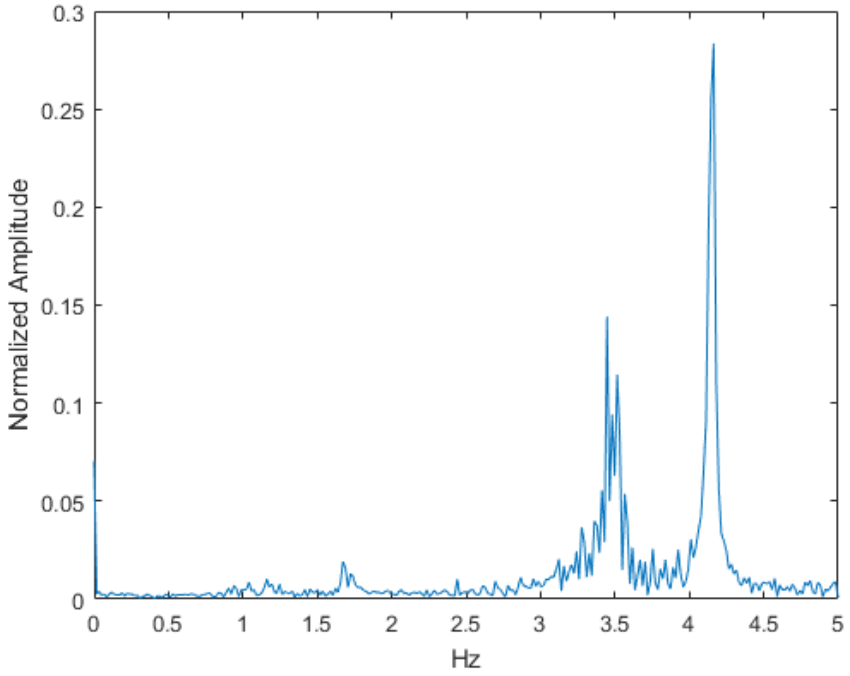

Figure D-61. FFT of the Y axis of the top laser during the 9V test at 10 Hz

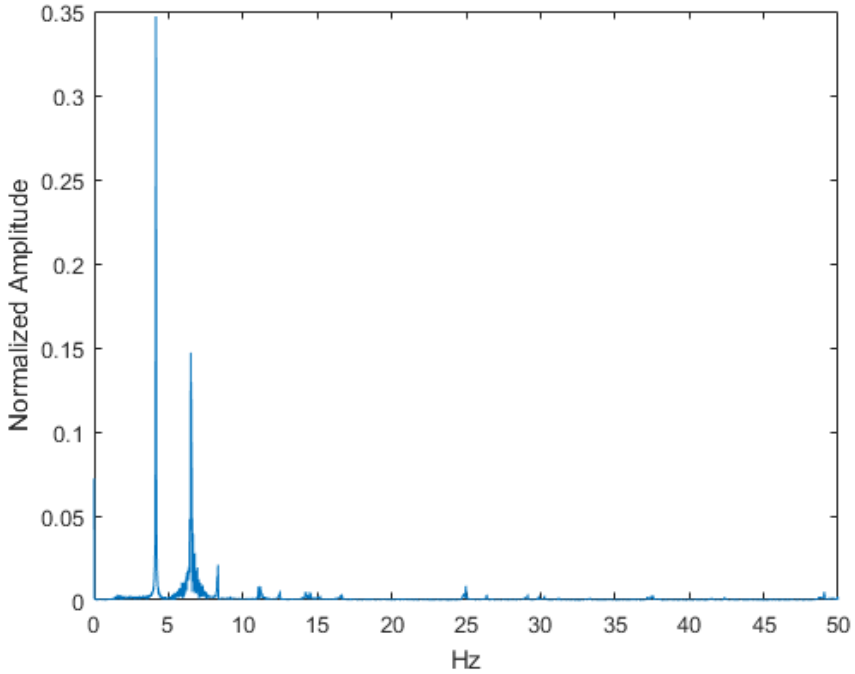

Figure D-62. FFT of the Y axis of the top laser during the 9V test at 100 Hz

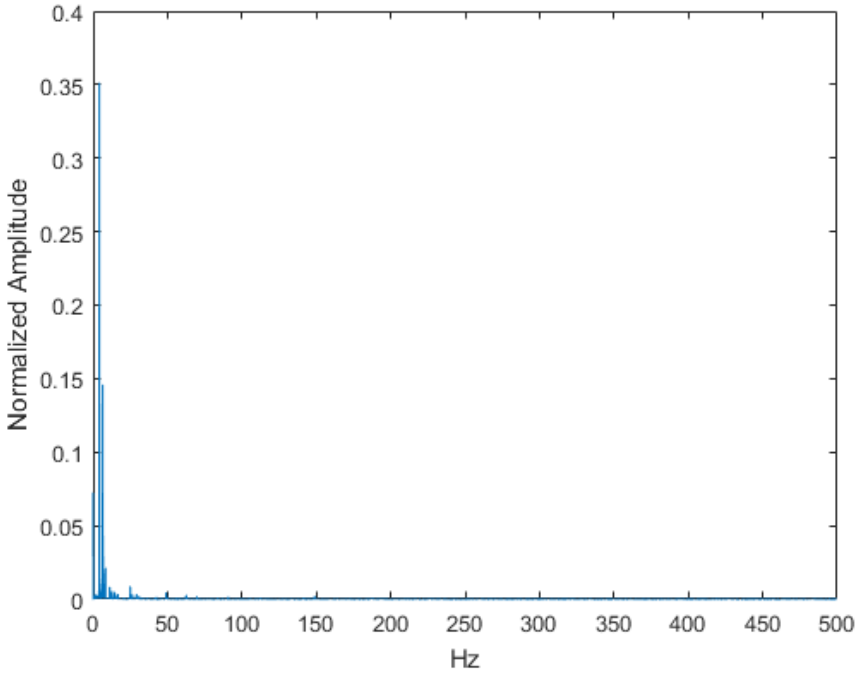

Figure D-63. FFT of the Y axis of the top laser during the 9V test at 1 kHz

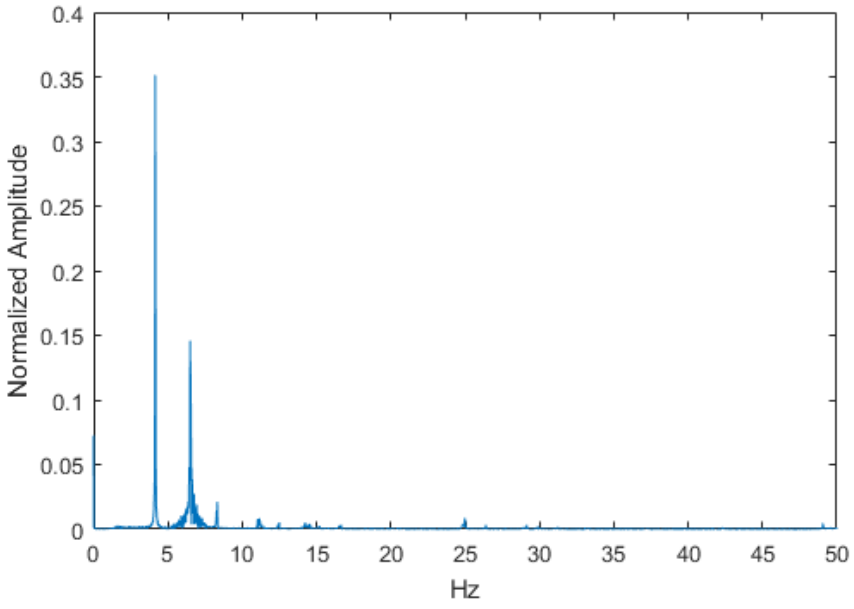

Figure D-64. FFT of the Y axis of the top laser during the 9V test at 1 kHz zoomed in

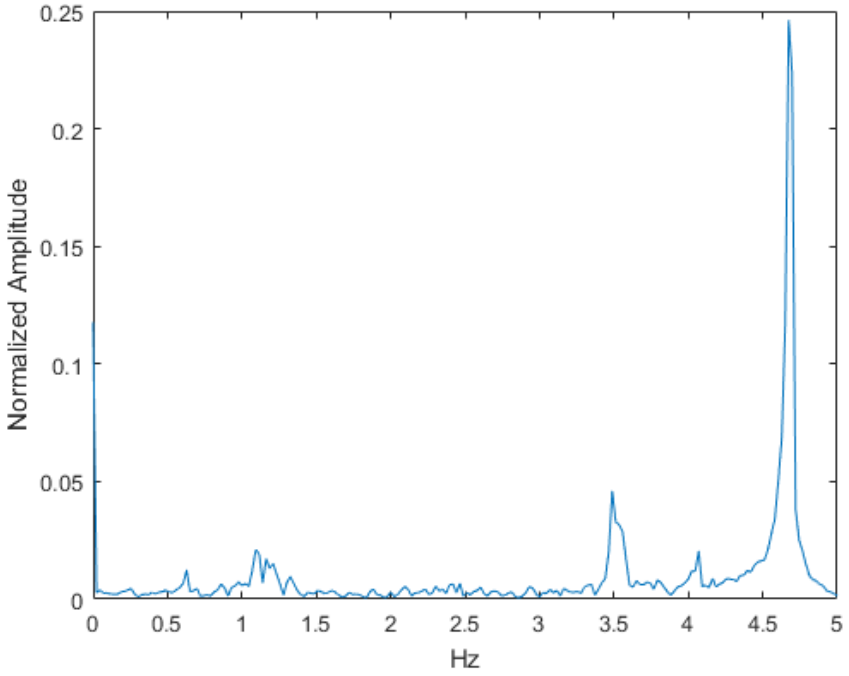

Figure D-65. FFT of the X axis of the bottom laser during the 10V test at 10 Hz

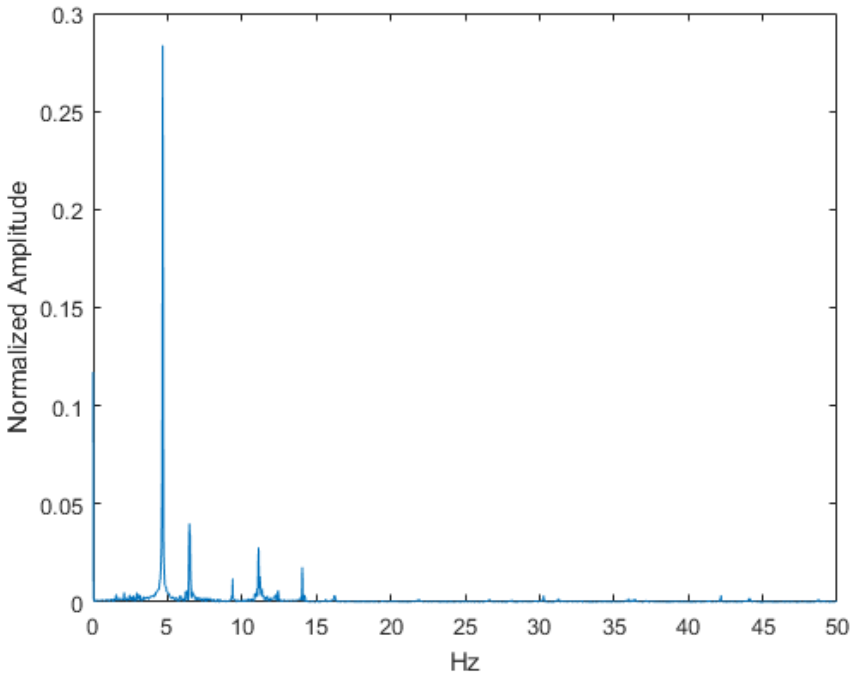

Figure D-66. FFT of the X axis of the bottom laser during the 10V test at 100 Hz

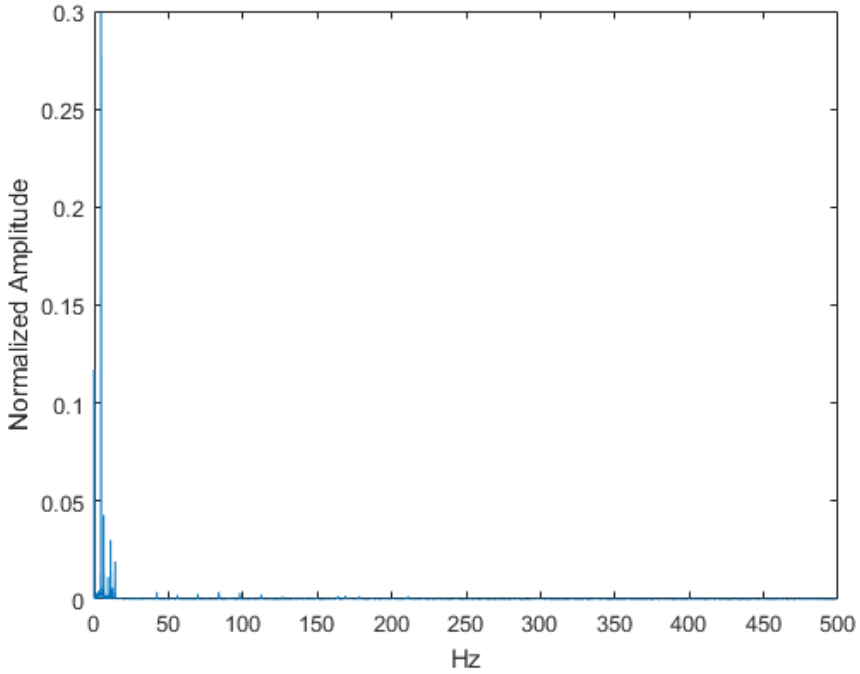

Figure D-67. FFT of the X axis of the bottom laser during the 10V test at 1 kHz

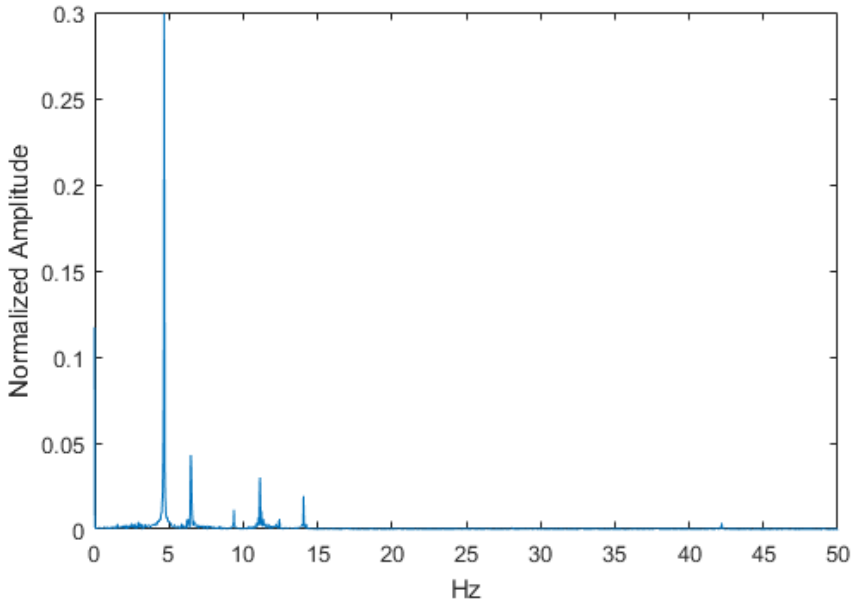

Figure D-68. FFT of the X axis of the bottom laser during the 10V test at 1 kHz zoomed in

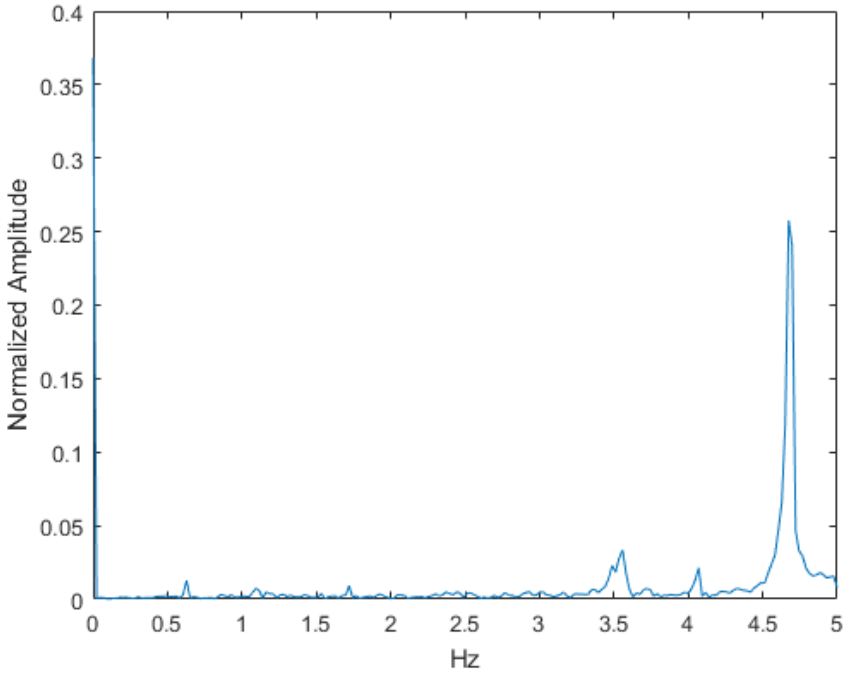

Figure D-69. FFT of the Y axis of the bottom laser during the 10V test at 10 Hz

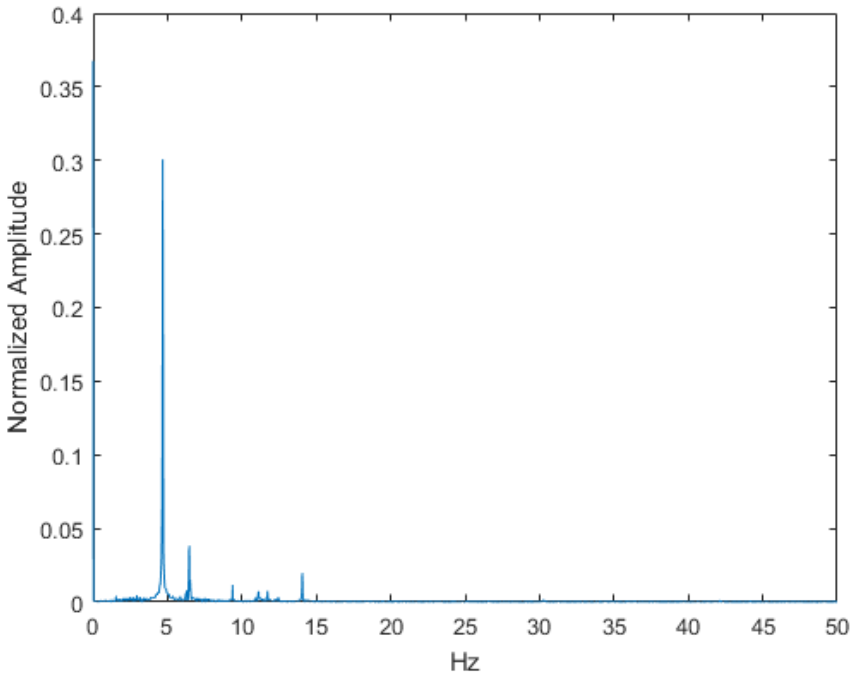

Figure D-70. FFT of the Y axis of the bottom laser during the 10V test at 100 Hz

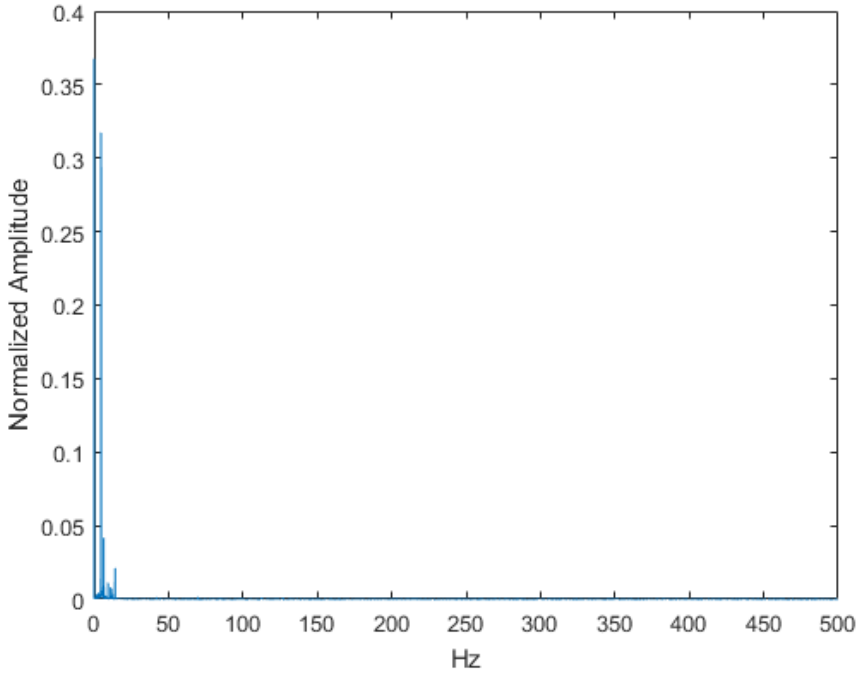

Figure D-71. FFT of the Y axis of the bottom laser during the 10V test at 1 kHz

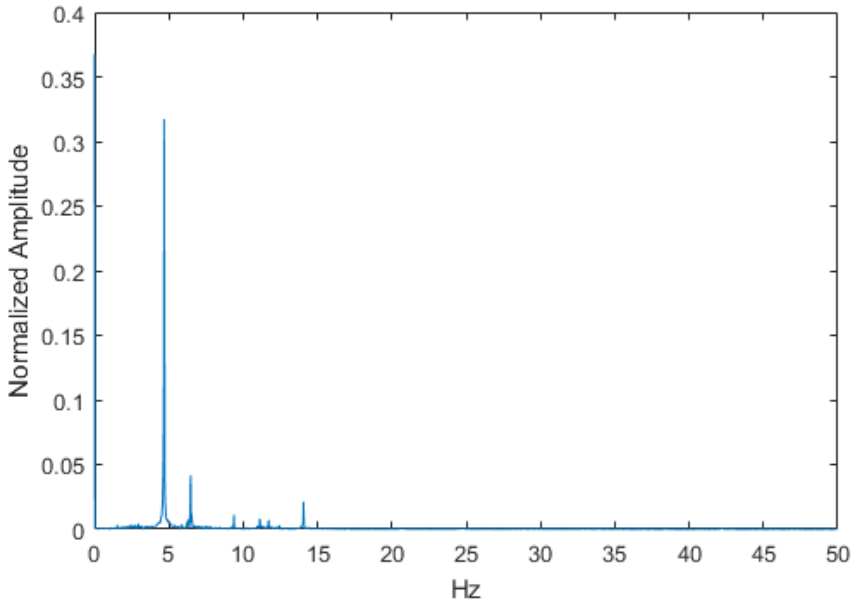

Figure D-72. FFT of the Y axis of the bottom laser during the 10V test at 1 kHz zoomed in

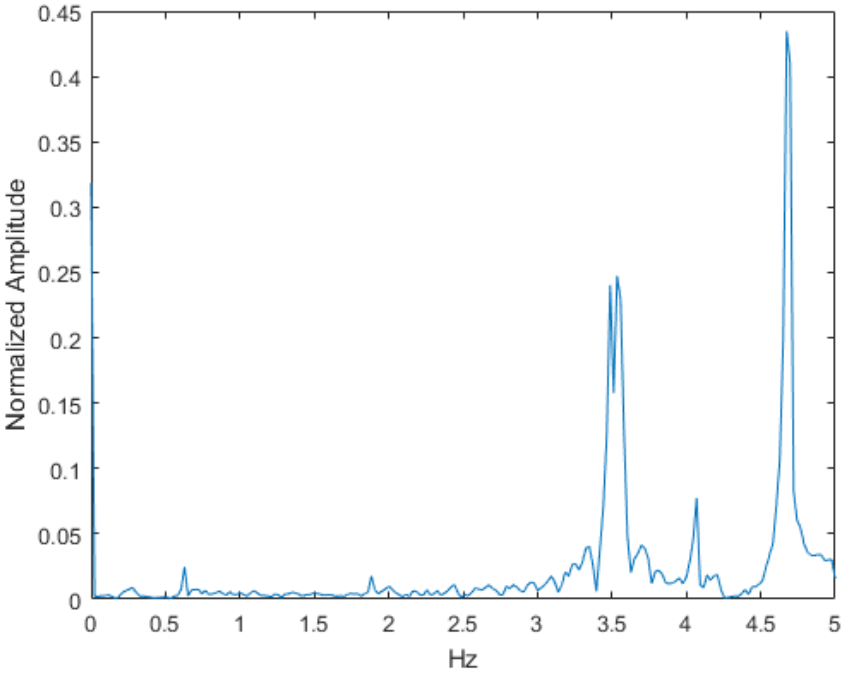

Figure D-73. FFT of the X axis of the top laser during the 10V test at 10 Hz

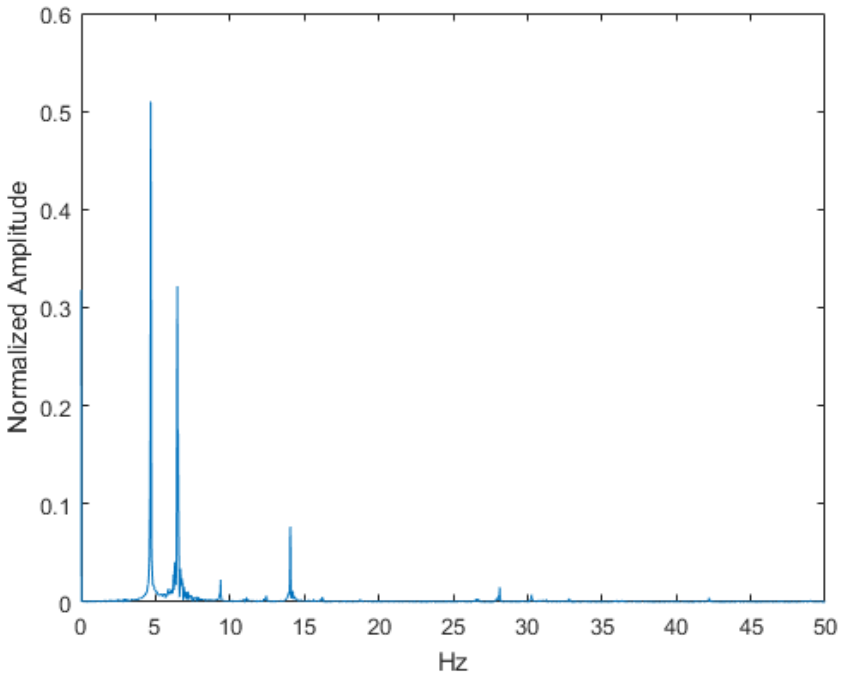

Figure D-74. FFT of the X axis of the top laser during the 10V test at 100 Hz

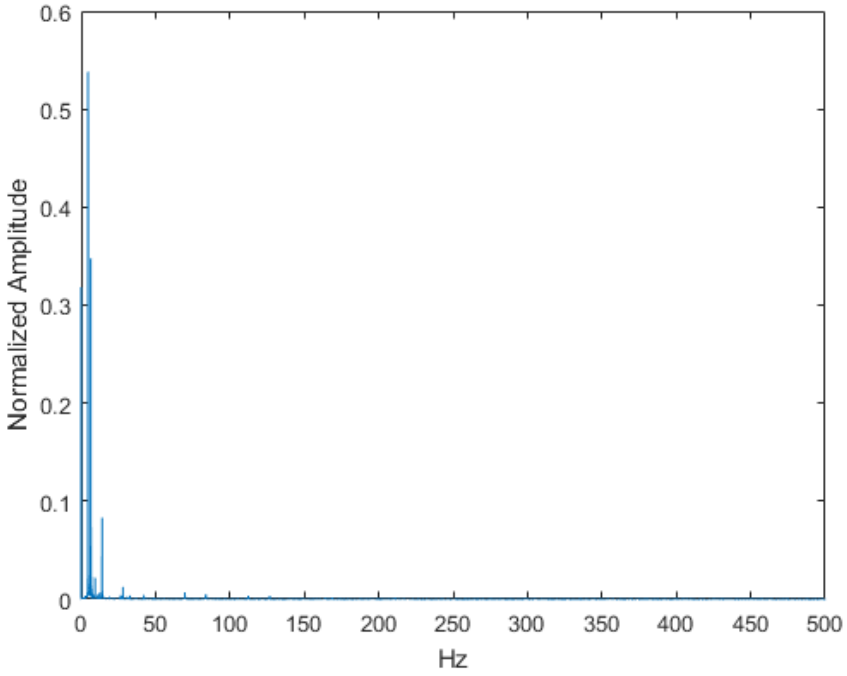

Figure D-75. FFT of the X axis of the top laser during the 10V test at 1 kHz

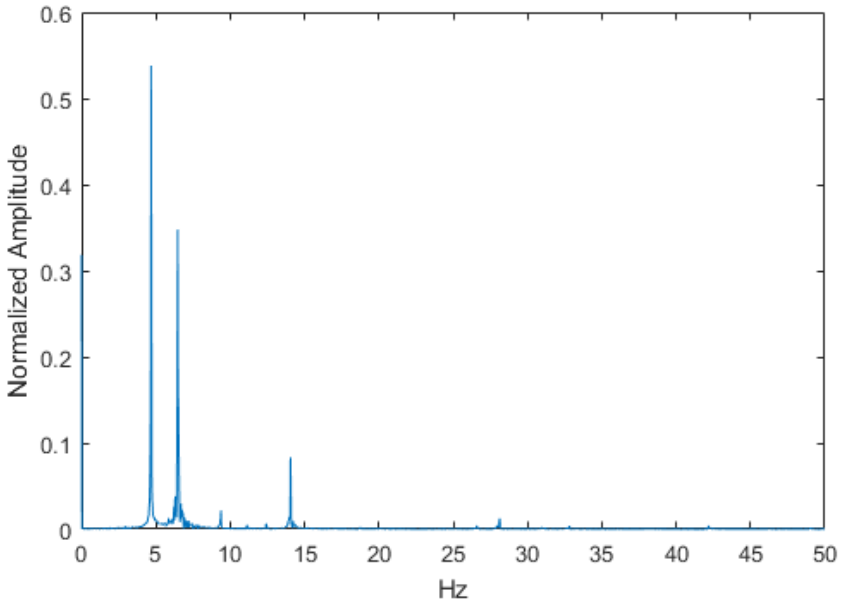

Figure D-76. FFT of the X axis of the top laser during the 10V test at 1 kHz zoomed in

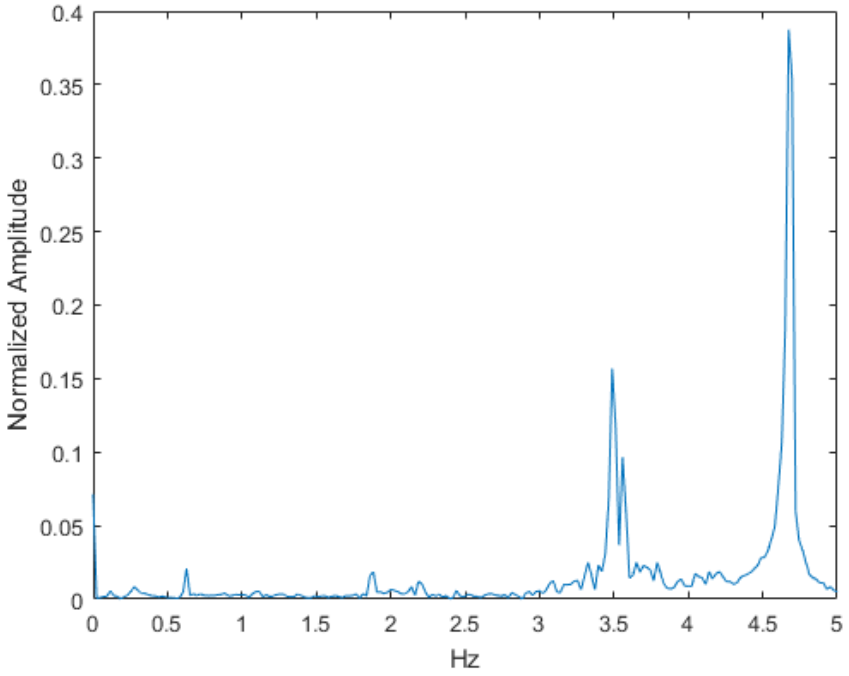

Figure D-77. FFT of the Y axis of the top laser during the 10V test at 10 Hz

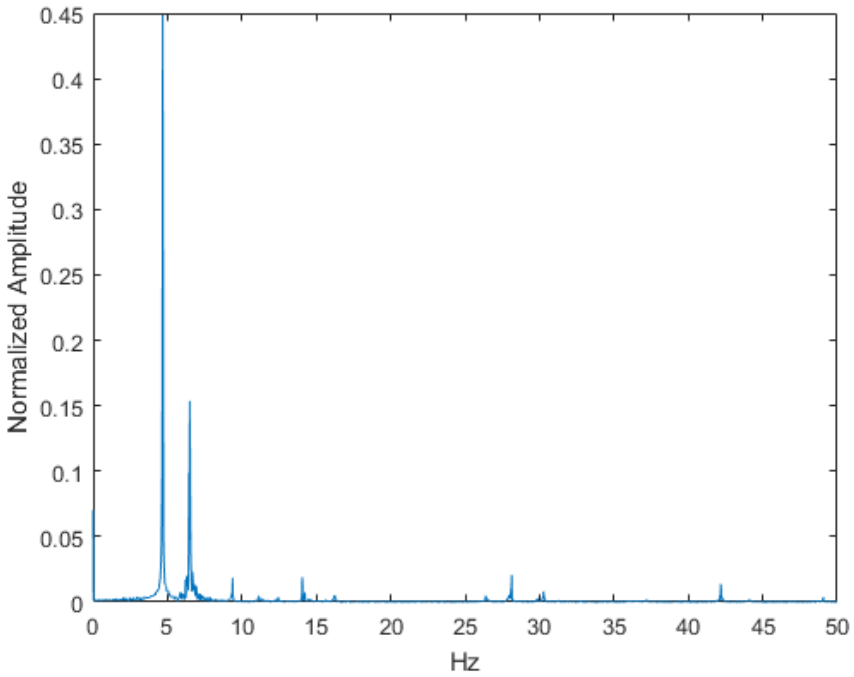

Figure D-78. FFT of the Y axis of the top laser during the 10V test at 100 Hz

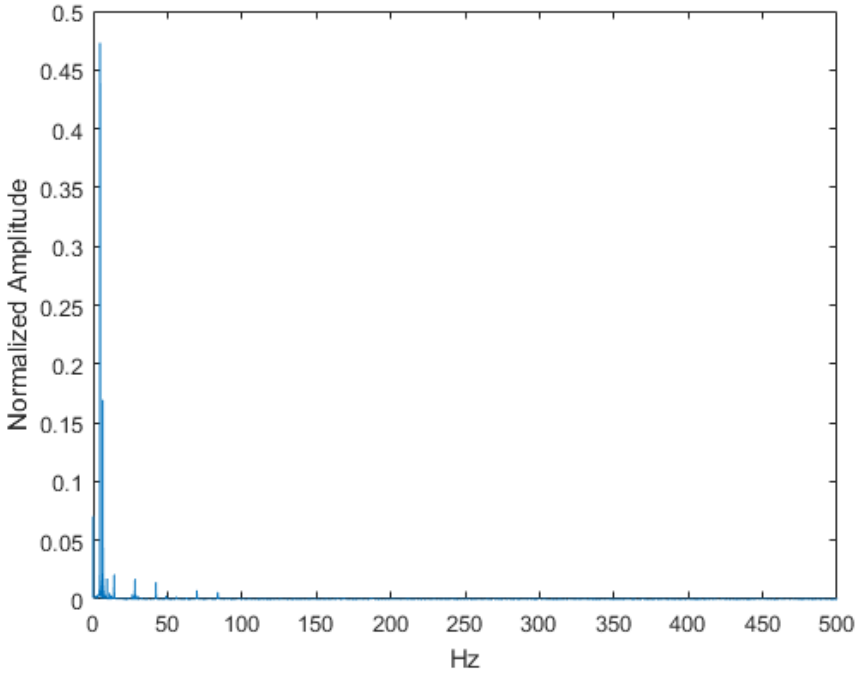

Figure D-79. FFT of the Y axis of the top laser during the 10V test at 1 kHz

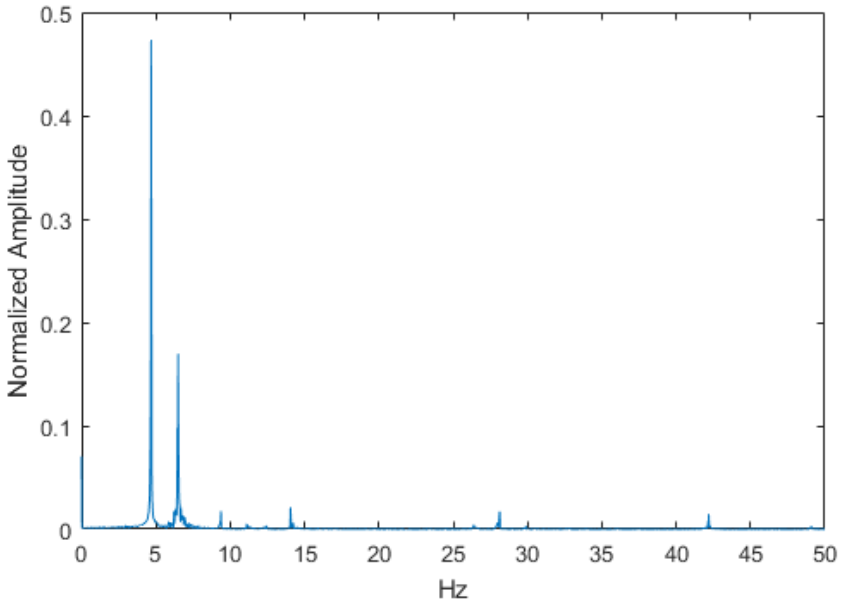

Figure D-80. FFT of the Y axis of the top laser during the 10V test at 1 kHz zoomed in